

TECHNISCHE UNIVERSITÄT MÜNCHEN
Munich School of Engineering
Forschungsgruppe *Energy Efficient and Smart Cities*

Theoretical and Experimental Analysis of Polymer-Based Solar Thermal Drain Back Systems

Mathias Stephan Ehrenwirth

Vollständiger Abdruck der von der *Munich School of Engineering* der *Technischen Universität München* zur Erlangung des akademischen Grades eines

Doktor-Ingenieurs (Dr.-Ing.)

genehmigten Dissertation.

Vorsitzender: Prof. Dr.-Ing. Klaus Peter Sedlbauer
Prüfer der Dissertation: 1. Vicky Albert-Seifried, Ph.D.
2. Prof. Dr.-Ing. Wilfried Zörner
3. Prof. Dr. Thomas Hamacher

Die Dissertation wurde am 10.07.2020 bei der *Technischen Universität München* eingereicht und durch die *Munich School of Engineering* am 07.04.2021 angenommen.

Per aspera ad astra

Acknowledgement

This thesis marks the end of a journey that would not have been possible without the endless support of so many people.

First and foremost, I want to express my deepest gratitude to *Professor Dr.-Ing. Wilfried Zörner* for supervising and mentoring my research. Thank you for always motivating and sharing your ideas with me. I am very grateful to *Dr. Vicky Albert-Seifried* for her guidance and the opportunity to work together with her and the *EESC*-group. Furthermore, I want to thank *Professor Dr. Thomas Hamacher* not only for examining my dissertation but also for providing me the opportunity to be part of the *Munich School of Engineering*.

I am very grateful for all the support I received from all former and current members of the *Institute of new Energy Systems*. Special mention goes to my PhD cohort members *Daniel Beckenbauer* and *Dr. Hermann Riess*: Thank you for all your help and useful comments, especially when I lost the light at the end of the tunnel. In addition, I gratefully acknowledge my mentors *Dr. Christoph Trinkl* and *Dr.-Ing. Michael Klärner* for all your advice and stimulating discussions. I would like to thank all other current and former members of the *Institute of new Energy Systems*, you made this so much more than just a place to work!

I am deeply grateful towards the *Technical University of Munich* as well as the *Munich School of Engineering* for granting me a doctoral scholarship to conduct this research. In particular, I want to thank *Dr. Christiane Hamacher*, not only for organising useful PhD courses and valuable symposia, but for always having an open ear regarding all organisational matters such a PhD project brings with itself.

And finally, last but by no means least, I want to thank my family for all your love and for always encouraging me. Words can hardly describe my gratitude to my love *Antonia*: Thank you so much for joining me on this roller coaster ride called PhD, I owe it all to you! To the greatest gift of my life, *Helena*: Thank you for lighten your parents lives and for your continuous motivation, love you!

Thank you all!

Declaration

Parts and / or results of this thesis were previously published in the following publications:

| | Chapter | | | | | | | |
|---------------------------|---------|---|---|---|---|---|---|---|
| | 1 | 2 | 3 | 4 | 5 | 6 | 7 | 8 |
| Ehrenwirth et al. (2014) | × | × | | | | × | | |
| Ehrenwirth et al. (2015) | × | × | | | | | | |
| Ehrenwirth et al. (2016a) | | × | × | | | | | |
| Ehrenwirth et al. (2016b) | | × | × | | | | | |
| Ehrenwirth et al. (2016c) | | × | × | | × | × | × | |
| Ehrenwirth et al. (2017a) | | × | × | | | | | |
| Ehrenwirth et al. (2017b) | | | × | | × | × | × | |

Abstract

Polymeric solar thermal flat plate collectors promise lower costs compared to conventional, metal-based ones. However, due to their specific material properties (i.e. thermal conductivity, pressure and temperature resistance), they not only require a special absorber structure but also adjustments on the surrounding architecture of the solar thermal system. In this context, so called drain back systems can make a meaningful contribution, as the setup of such systems complement the material characteristics of polymeric solar thermal flat plate collectors.

This thesis aims for a determination of the heat generation costs of drain back systems with polymeric flat plate collectors for application in single-family homes. In contrast to approaches described in scientific literature, which mainly utilise pre-fabricated, semi-finished components (e.g. twin-wall or honeycomb plates) to build polymeric absorbers for solar thermal collectors, a novel manufacturing process called Twin-Sheet-Thermoforming was chosen for producing polymeric absorbers. Based on these polymeric absorbers, different collector prototypes were set up and tested regarding their efficiency. Subsequently, these collector prototypes were implemented into a drain back system to determine both the collector's as well as the system's behaviour under real operation conditions. Based on the collector tests and the system measurements, a simulation model was developed which is able to predict the annual performance of a drain back system with polymeric solar thermal flat plate collectors. By means of the simulation model, the energy savings were determined. Together with the system costs (i.e. investment and operation costs), the heat generation costs of such drain back systems with polymeric flat plate collectors were evaluated.

The results indicate that drain back systems with polymeric solar thermal flat plate collectors can provide heat at competitive costs with respect to systems equipped with metal-based solar flat plate collectors. Extending the application of polymeric materials to other system components (i.e. the heat storage, pipes etc.) can yield further cost savings. Drain back systems with polymeric collectors can therefore make a meaningful contribution towards lower heat generation costs and subsequently to a further dissemination of solar thermal systems.

Contents

| | |
|--|-------------|
| Acknowledgement | i |
| Declaration | ii |
| Abstract | iii |
| Contents | v |
| List of Figures | viii |
| List of Tables | xii |
| List of Abbreviations | xiv |
| List of polymeric materials | xv |
| 1 Background and Introduction | 1 |
| 1.1 Conventional Solar Thermal Systems and Drain Back Systems | 3 |
| 1.2 Research Question and Methodology | 5 |
| 2 Literature Review | 7 |
| 2.1 Collectors | 7 |
| 2.1.1 Efficiency of a Solar Thermal Collector | 7 |
| 2.1.2 Polymeric Materials for Solar Thermal Collectors | 10 |
| 2.1.3 Scientific Investigation of Polymeric Solar Thermal Collectors | 13 |
| 2.1.4 Commercially Available Polymeric Solar Thermal Collectors | 16 |
| 2.1.5 Overheat Protection | 18 |
| 2.1.6 Summary | 20 |
| 2.2 Drain Back Systems | 23 |
| 2.2.1 History and Application Areas of Drain Back Systems | 23 |
| 2.2.2 Advantages and Disadvantages of Drain Back Systems | 24 |
| 2.2.3 Classification of Drain Back Systems | 25 |
| 2.2.4 Operation of Drain Back Systems | 27 |
| 2.2.5 Reliability and Control of Drain Back Systems | 31 |
| 2.2.6 Commercially Available Drain Back Systems | 32 |
| 2.2.7 Summary | 33 |
| 3 Experimental Analysis on Component Level | 36 |
| 3.1 Manufacturing and Testing of Polymeric Absorbers | 36 |
| 3.2 Setup of Polymeric Collector Prototypes | 40 |
| 3.3 Description of the Test Rig for Determining the Collector Efficiency | 43 |
| 3.4 Test Results and Discussion | 46 |

| | | |
|----------|--|------------|
| 4 | Collector Simulation | 50 |
| 4.1 | Background | 50 |
| 4.2 | Description of the Collector Model | 50 |
| 4.3 | Modes of Heat Transfer | 52 |
| 4.3.1 | Thermal Conduction | 53 |
| 4.3.2 | Thermal Convection | 53 |
| 4.3.3 | Thermal Radiation | 60 |
| 4.4 | Collector Optics | 63 |
| 4.4.1 | Reflection Coefficient at the Boundary Surface of the Glazing | 64 |
| 4.4.2 | Absorption of the Glazing | 65 |
| 4.4.3 | Transmission, Reflectance and Absorption Coefficients of the Glazing | 65 |
| 4.4.4 | Transmittance-Absorptance Product | 66 |
| 4.4.5 | Energy Input due to Diffuse Radiation | 68 |
| 4.5 | Model Validation | 68 |
| 4.5.1 | Validation for Steady-State Boundary Conditions | 68 |
| 4.5.2 | Validation for Dynamic Boundary Conditions | 70 |
| 4.6 | Parametric Study | 73 |
| 4.7 | Summary | 75 |
| 5 | Experimental Analysis on System Level | 76 |
| 5.1 | Solar Collector Loop | 78 |
| 5.2 | Backup Heating Loop | 79 |
| 5.3 | Domestic Hot Water Loop | 79 |
| 5.4 | Test Results and Discussion | 80 |
| 6 | Simulation on System Level | 85 |
| 6.1 | Reference Models | 85 |
| 6.1.1 | Conventional Reference System | 87 |
| 6.1.2 | Solar Domestic Hot Water System | 89 |
| 6.1.3 | Solar Combi System | 91 |
| 6.2 | Simulation Model Validation | 93 |
| 6.3 | System Comparison | 96 |
| 6.4 | Simulation Results | 100 |
| 6.5 | Summary | 103 |
| 7 | Economic Evaluation | 105 |
| 7.1 | Methodology | 105 |
| 7.2 | Initial Investment Costs | 106 |
| 7.2.1 | Collectors | 106 |
| 7.2.2 | Heat Storages | 107 |
| 7.2.3 | Other Components | 108 |
| 7.2.4 | Installation | 109 |
| 7.2.5 | Investment Costs of a Solar Domestic Hot Water System located in Würzburg (Germany) | 109 |
| 7.3 | Subsidies | 110 |
| 7.4 | Operation and Maintenance Costs | 110 |
| 7.4.1 | Operation-Related Costs | 111 |

| | | |
|----------|---|-------------|
| 7.4.2 | Demand-Related Costs | 111 |
| 7.4.3 | Operation and Maintenance Costs of a Solar Domestic Hot Water System located in Würzburg (Germany) | 111 |
| 7.5 | Further Parameters | 112 |
| 7.6 | Resulting Levelised Cost of Heat of a Solar Domestic Hot Water System located in Würzburg (Germany) | 114 |
| 7.7 | Parametric Study of the Levelised Cost of Heat | 116 |
| 7.8 | Cost Optimisation Potential for Polymeric Drain Back Systems | 118 |
| 7.8.1 | Installation Costs | 118 |
| 7.8.2 | Investment / Replacement costs | 119 |
| 7.8.3 | Operation-Related and Demand-Related Costs | 120 |
| 7.8.4 | Cost Saving Potential | 120 |
| 7.9 | Summary | 121 |
| 8 | Conclusions and Outlook | 122 |
| 8.1 | Summary of Research Work | 122 |
| 8.2 | Conclusions | 123 |
| 8.3 | Outlook | 124 |
| | Bibliography | xv |
| | Appendices | xxvi |

List of Figures

| | | |
|------|---|----|
| 1.1 | Energy demand in Germany by sectors. | 1 |
| 1.2 | Cost distribution of small solar thermal systems. | 2 |
| 1.3 | Setup of a conventional solar thermal system. | 3 |
| 1.4 | Working principle of a drain back system. | 4 |
| 1.5 | Research methodology. | 6 |
| 2.1 | Heat transfer mechanisms at a solar thermal collector. | 8 |
| 2.2 | Efficiency curve of a single glazed solar thermal flat plat collector. | 10 |
| 2.3 | Setup of conventional vs. polymeric solar thermal FPC. | 11 |
| 2.4 | Polymeric collectors described in scientific papers. | 14 |
| 2.5 | Linear efficiency curves of scientifically investigated polymeric collectors. . . | 15 |
| 2.6 | Unglazed polymeric collectors for pool heating. | 16 |
| 2.7 | <i>One Sun One World</i> solar collector. | 17 |
| 2.8 | <i>Eco Flare 3M</i> collector. | 17 |
| 2.9 | <i>Aventa AS</i> collector. | 18 |
| 2.10 | Efficiency curves of commercially available polymeric collectors. | 19 |
| 2.11 | Different types of DBSs. | 26 |
| 2.12 | Trickle vs. Siphon flow. | 28 |
| 2.13 | Pressure conditions within a drain back system. | 29 |
| 2.14 | Commercially available external drain back reservoir. | 32 |
| 3.1 | Process steps of the twin-sheet-thermoforming process. | 37 |
| 3.2 | Visualisation of the flow distribution inside a polymeric absorber. | 38 |
| 3.3 | Schematic model for the theoretical determination of the pressure drop. . . . | 39 |
| 3.4 | Experimental determination of the pressure drop of a polymeric absorber. . . | 40 |
| 3.5 | Photographs of the collector prototypes. | 41 |
| 3.6 | Schematic layout of the solar simulator. | 44 |
| 3.7 | Efficiency curves of tested polymeric collector prototypes. | 47 |
| 3.8 | Efficiency curves of tested polymeric collectors prototypes in comparison to market available collectors. | 48 |
| 3.9 | Linear efficiency curves of two tested polymeric collector prototypes together with the (linear) efficiency curves of polymeric collector concepts described in literature. | 49 |
| 4.1 | Scheme of solar thermal collector model. | 51 |
| 4.2 | Illustration of convection phenomena inside and outside of a solar thermal flat plate collector. | 58 |
| 4.3 | Wind speed dependent heat transfer coefficient h_{Conv} at the glazing. | 59 |
| 4.4 | Heat transfer coefficient h_{Conv} in the air gap between absorber and glazing. . | 60 |
| 4.5 | Radiative energy exchange between two grey surfaces. | 61 |
| 4.6 | Collector optics. | 63 |
| 4.7 | Transmission, reflection and absorption of a single glazing. | 65 |
| 4.8 | Effective transmission-absorption product of a single-glazed flat plate collector. 67 | |

| | | |
|------|---|-----|
| 4.9 | Validation results for the ABS collector with PUR insulation and PMMA glazing. | 69 |
| 4.10 | Validation results for the PP collector with glasswool insulation and glass glazing. | 69 |
| 4.11 | Validation results for the PP collector with EPS insulation and glass glazing. | 70 |
| 4.12 | Validation results for the PP collector with EPS insulation and glass glazing (including additional frame). | 70 |
| 4.13 | Dynamic validation of a collector array in case of cloudy sky conditions. . . . | 71 |
| 4.14 | Dynamic validation of a collector array in case of clear sky conditions. | 72 |
| 4.15 | Results of a parametric study of a polymeric FPC with a PP absorber. | 74 |
| 4.16 | Comparison of measured and simulated collector prototypes. | 75 |
| 5.1 | Schematic sketch of the system test rig. | 76 |
| 5.2 | Hydraulic setup of the system test rig. | 77 |
| 5.3 | Position of temperature sensors mounted inside the collector prototype. | 78 |
| 5.4 | DHW tapping profile used in the system test rig. | 80 |
| 5.5 | Temperatures inside the collector on 25.06.2016. | 81 |
| 5.6 | Temperatures inside the collector on 26.06.2016. | 81 |
| 5.7 | Temperatures inside the heat storage and states of the hydraulic loops on 25.06.2016. | 82 |
| 5.8 | Temperatures inside the heat storage and states of the hydraulic loops on 26.06.2016. | 83 |
| 6.1 | Weather conditions and heating parameters at the reference location Würzburg (Germany). | 86 |
| 6.2 | Tapping profile L. | 86 |
| 6.3 | Hydraulic setup of the conventional reference system. | 87 |
| 6.4 | Distribution of the fossil fuel demand in case of the conventional reference system (Task 54) located in Würzburg (Germany). | 88 |
| 6.5 | Hydraulic setup of the solar domestic hot water system. | 89 |
| 6.6 | Distribution of the fossil fuel demand / solar yield in case of a solar DHW system (Task 54) located in Würzburg (Germany). | 89 |
| 6.7 | Hydraulic setup of the solar combi system. | 91 |
| 6.8 | Distribution of the fossil fuel demand / solar yield in case of solar combi system with metal-based solar thermal flat plate collectors (FPCs) (Task 54) located in Würzburg (Germany). | 91 |
| 6.9 | Weather conditions on 30.08.2016. | 93 |
| 6.10 | Weather conditions on August 31.08.2016. | 94 |
| 6.11 | Heat production / demand on 30.08.2016. | 94 |
| 6.12 | Heat production / demand on 31.08.2016. | 95 |
| 6.13 | Hydraulic setup of the modified solar combi system. | 98 |
| 6.14 | Distribution of the fossil fuel demand / solar yield in case of the modified solar combi system and a solar DHW system located in Würzburg (Germany). | 99 |
| 6.15 | Correlation between collector area, heat storage volume and fractional energy savings in case of a solar DHW system located in Würzburg (Germany). | 100 |
| 6.16 | Correlation between collector area, heat storage volume and fractional energy savings in case of a modified solar combi system located in Würzburg (Germany). | 101 |

List of Figures

| | | |
|------|---|-----|
| 6.17 | Collector temperatures in case of solar DHW systems located in Würzburg (Germany). | 102 |
| 6.18 | Collector temperatures in case of solar combi systems located in Würzburg (Germany). | 103 |
| 7.1 | Evaluation of specific heat storage costs for DHW storages with one and two heat exchangers available from manufacturer's price lists. | 107 |
| 7.2 | LCoH in case of a solar DBS with polymeric FPCs located in Würzburg (Germany). | 116 |
| 7.3 | LCoH in case of a solar combi system with polymeric FPCs located in Würzburg (Germany). | 117 |
| 7.4 | Cost distribution of a solar thermal DBS with polymeric FPCs located in Würzburg (Germany). | 118 |
| A.1 | Photographs of the Twin-Sheet-Thermoforming process. | A1 |
| A.2 | External view of the system test rig. | A2 |
| A.3 | Collector array. | A2 |
| A.4 | Measurement and control equipment used at the system test rig. | A3 |
| A.5 | Drain back reservoir of the system test rig. | A4 |
| A.6 | Control cabinet inside the system test rig. | A4 |
| A.7 | Indoor solar simulator. | A5 |
| C.1 | Schematic layout of the spectroscopy measurement. | C1 |
| C.2 | Setup of the spectroscopy measurement. | C2 |
| C.3 | Wavelength-dependent transmittance τ of glass and PMMA. | C2 |
| E.1 | Influence of different sky temperature models to the simulated collector outlet temperature in case of cloudy sky conditions ((Date of measurement 30.08.2016). | E1 |
| E.2 | Influence of different sky temperature models to the simulated collector outlet temperature in case of clear sky conditions (Date of measurement 31.08.2016). | E2 |
| F.1 | Weather conditions and heating parameters at the reference location Athens (Greece). | F1 |
| F.2 | Correlation between collector area, heat storage volume and fractional energy savings in case of a solar DHW system located in Athens (Greece). | F2 |
| F.3 | Correlation between collector area, heat storage volume and fractional energy savings in case of a solar combi system located in Athens (Greece). | F3 |
| F.4 | Collector temperatures in case of solar DHW systems located in Athens (Greece). | F4 |
| F.5 | Collector temperatures in case of solar combi systems located in Athens (Greece). | F4 |
| F.6 | LCoH in case of a solar DBS with polymeric collectors located in Athens (Greece). | F5 |
| F.7 | LCoH in case of a solar combi system with polymeric FPCs located in Athens (Greece). | F6 |
| F.8 | Weather conditions and heating parameters at the reference location Davos (Switzerland). | F7 |
| F.9 | Correlation between collector area, heat storage volume and fractional energy savings in case of a solar DHW system located in Davos (Switzerland). | F8 |

| | | |
|------|---|-----|
| F.10 | Correlation between collector are, heat storage volumes and fractional energy savings in case of a solar combi system located in Davos (Switzerland). . . . | F9 |
| F.11 | Collector temperatures in case of solar DHW systems located in Davos (Switzerland). | F10 |
| F.12 | Collector temperatures in case of solar combi systems located in Davos (Switzerland). | F10 |
| F.13 | LCoH in case of a solar DBS with polymeric collectors located in Davos (Switzerland). | F11 |
| F.14 | LCoH in case of a solar combi system with polymeric FPCs located in Davos (Switzerland). | F12 |
| F.15 | Weather conditions and heating parameters at the reference location Stockholm (Sweden). | F13 |
| F.16 | Correlation between collector area, heat storage volume and fractional energy savings in case of a solar DHW system located in Stockholm (Sweden). . . . | F14 |
| F.17 | Correlation between collector area, heat storage volume and fractional energy savings in case of a solar combi system located in Stockholm (Sweden). . . . | F15 |
| F.18 | Collector temperatures in case of solar DHW systems located in Stockholm (Sweden). | F16 |
| F.19 | Collector temperatures in case of solar combi systems located in Stockholm (Sweden). | F16 |
| F.20 | LCoH in case of a solar DBS with polymeric collectors located in Stockholm (Sweden). | F17 |
| F.21 | LCoH in case of a solar combi system with polymeric FPCs located in Stockholm (Sweden). | F18 |
| G.1 | Ratio between collector area and related membrane expansion volume. . . . | G1 |

List of Tables

| | | |
|-----|---|-----|
| 2.1 | Costs and mechanical properties of commonly used polymeric materials compared to metals. | 11 |
| 2.2 | Thermal properties of commonly used polymeric materials compared to metals. | 12 |
| 2.3 | Overview of polymeric collectors described in scientific publications. | 22 |
| 2.4 | Overview of DBS described in scientific publications. | 34 |
| 3.1 | Characterisation of the tested polymeric absorber. | 39 |
| 3.2 | Overview of tested polymeric collectors. | 42 |
| 3.3 | Test conditions for solar thermal collectors. | 44 |
| 3.4 | Comparison of the efficiency of the developed polymeric collector prototypes with market available collectors. | 47 |
| 4.1 | Overview of different formulations for the Nu number in case of forced convection over a flat plate. | 56 |
| 6.1 | System properties of the conventional reference system (Task 54) and comparison with the developed model. | 88 |
| 6.2 | Results of the solar DHW system simulation in comparison to Task 54 results. | 90 |
| 6.3 | Results of the solar combi system simulation. | 92 |
| 6.4 | Setup and results of the tested DBS on 30.08.2016. | 95 |
| 6.5 | Setup and results of the tested DBS on 31.08.2016. | 96 |
| 6.6 | Comparison of a solar thermal DHW system with a solar combi system. . . . | 97 |
| 7.1 | Evaluation of component costs available from manufacturer's price lists. . . . | 108 |
| 7.2 | Comparison of investment costs in case of a solar DHW system located in Würzburg (Germany). | 110 |
| 7.3 | Operation and maintenance costs in case of a solar DHW system located in Würzburg (Germany). | 112 |
| 7.4 | Time series of cash and energy flows in case of a conventional solar DHW system located in Würzburg (Germany). | 114 |
| 7.5 | Time series of cash and energy flows in case of a DBS with polymeric solar thermal FPCs located in Würzburg (Germany). | 115 |
| 7.6 | Influence of investment / replacement cost saving potential on the resulting LCoH. | 120 |
| B.1 | Measurement results for PP absorber with EPS-insulation and glass-glazing (Date of measurement: 22.09.2015). | B1 |
| B.2 | Measurement results for PP absorber with EPS-insulation and glass-glazing (including additional frame) (Date of measurement: 11.02.2016). | B1 |
| B.3 | Measurement results for PP absorber with EPS-insulation and PMMA-glazing (Date of measurement: 18.02.2016). | B2 |
| B.4 | Measurement results for PP absorber with EPS-insulation and PMMA-glazing (including additional frame) (Date of measurement: 22.02.2016). | B2 |

| | | |
|-----|---|-----|
| B.5 | Measurement results for PP absorber with glasswool-insulation and glass-glazing (Date of measurement: 26.02.2016). | B3 |
| B.6 | Measurement results for PP absorber with glasswool-insulation and PMMA-glazing (Date of measurement: 23.02.2016). | B3 |
| B.7 | Measurement results for ABS absorber with PUR-insulation and PMMA-glazing (Date of measurement: 07.07.2017). | B4 |
| D.1 | Measured and simulated results for ABS-collector with PUR-insulation and PMMA-glazing. | D1 |
| D.2 | Measured and simulated results for PP-collector with glasswool-insulation and glass-glazing. | D1 |
| D.3 | Measured and simulated results for PP-collector with EPS-insulation and glass-glazing. | D2 |
| D.4 | Measured and simulated results for PP-collector with EPS-insulation and glass-glazing (including additional frame). | D2 |
| E.1 | Overview of different formulations for the sky temperature. | E1 |
| G.1 | Specific costs and volumes of solar thermal flat plate collectors. | G2 |
| G.2 | Specific costs (without VAT) of monovalent heat storages. | G5 |
| G.3 | Specific costs (without VAT) of bivalent heat storages. | G7 |
| G.4 | Specific costs of membrane expansion vessels. | G9 |
| G.5 | Specific costs for piping. | G13 |
| G.6 | Specific costs of the substructure for solar thermal collectors. | G17 |
| G.7 | Costs for solar stations. | G20 |
| G.8 | Costs for solar controllers. | G21 |
| G.9 | Specific costs for heat transfer fluid. | G22 |

List of Abbreviations

| | |
|------|------------------------------|
| CFD | Computational fluid dynamics |
| CNT | Carbon nanotubes |
| DBS | Drain back system |
| DHW | Domestic hot water |
| ETC | Evacuated tube collector |
| FPC | Flat plate collector |
| HTF | Heat transfer fluid |
| LAC | Large-area collector |
| LCoH | Levelised cost of heat |
| MEV | Membrane expansion vessel |
| TST | Twin-sheet-thermoforming |

List of polymeric materials

| | |
|------|----------------------------------|
| ABS | Acrylonitrile butadiene styrene |
| EPDM | Ethylene propylene diene monomer |
| EPS | Expanded polystyrene |
| HDPE | High density polyethylene |
| LDPE | Low density polyethylene |
| PA | Polyamide |
| PB | Polybutylene |
| PBT | Polybutylene terephthalate |
| PC | Polycarbonate |
| PE | Polyethylene |
| PEEK | Polyether ether ketone |
| PES | Polyether sulfone |
| PET | Polyethylene terephthalate |
| PMMA | Poly(methyl methacrylate) |
| PP | Polypropylene |
| PPO | Polyphenylenoxid |
| PPS | Poly (p-phenylene sulfide) |
| PS | Polystyrene |
| PUR | Polyurethane |
| PVC | Polyvinyl chloride |

1 Background and Introduction

On December 12th 2015, the global community agreed on limiting the worldwide temperature increase to not more than 2 °C with regard to pre-industrial times (United Nations, 2015, p. 2). In order to achieve this objective, it is necessary to reduce greenhouse gas emissions. A significant portion of these greenhouse gases is emitted while generating electricity and heat (Intergovernmental Panel on Climate Change, 2014, p. 9). It is therefore necessary to find cleaner ways to meet these basic needs using renewable energies. The increasing per capita energy demand as well as the increasing world population are additional challenges to achieve this goal. By 2040, the world energy demand will amount to 7.48×10^{20} J (British Petrol, 2019). Given today's level (5.66×10^{20} J), this corresponds to an increase of almost 32 %¹.

Figure 1.1 shows the energy demand of Germany according to sectors and end uses. Most of the energy is in the form of heat and occurs within the sectors private households, trade / commerce / service and industry. As the energy demand is approximately equally distributed over these sectors, the data shows that the largest energy demand in Germany is required in the form of low temperature heat for space heating and domestic hot water (DHW) preparation. To provide this energy demand, low-emission techniques for generating heat efficiently are of major importance to reach the goals of the Paris Agreement.

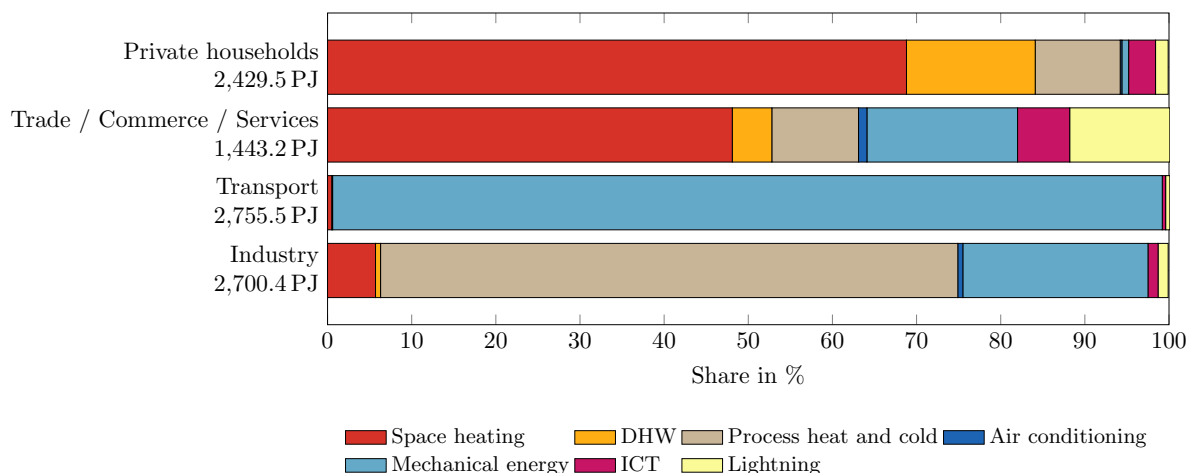


Figure 1.1: Energy demand in Germany by sectors (Data source: Bundesministerium für Wirtschaft und Energie, 2019, table 7a, 7b). DHW = Domestic Hot Water, ICT = Information and Communication Technology.

Heat can be generated by several renewable energy sources. Solar thermal systems convert the energy transmitted by the sun into heat for purposes such as DHW preparation or space heating in private households. This is particularly advantageous, as the annual amount of energy delivered by the sun (3.9×10^{24} J, Quaschnig, 2015, p. 36) is more than 5,000 times

¹ British Petrol (2019) states a total energy of $13,511.17 \times 10^6$ toe in the year 2017. In the year 2040, the study assumes $17,865.82 \times 10^6$ toe as the worldwide, total energy consumption. $1 \text{ toe} \hat{=} 4.19 \times 10^{10}$ J.

1 Background and Introduction

the projected worldwide energy demand for the year 2035. This fact clearly demonstrates the enormous potential of solar energy and illustrates the necessity of sustainable and robust solutions for utilising this source of energy. Although the sun provides energy free of charge, solar thermal systems accounted for only 1.2% in 2013 (Mauthner, Weiss and Spörk-Dür, 2015, p. 6) of the heat supply of buildings due to their relatively high heat generation costs. Available solar thermal systems compete both with conventional (i.e. coal, gas, oil etc.) and renewable (geothermal, heat pumps, PV) energy resources. To increase the market share of solar thermal systems, the heat generation costs must therefore be reduced. As the costs of solar thermal systems for private household application depend on numerous parameters (e.g. size of the collector array, type of the collectors, location of the building, year of construction, number of inhabitants etc.), the heat generation costs found in the literature vary widely from 7.5 €-Ct/(kW h) to 62 €-Ct/(kW h) (Peuser, Remmers and Schnauss, 2002, p. 319; Eicker, 2012, p. 94; Kaltschmitt, 2013, pp. 243; Bundesverband Solarwirtschaft e.V., 2012, pp. 61). In comparison, the costs for heat generated by fossil fuels range between 13 €-Ct/(kW h) and 35.6 €-Ct/(kW h) in case of condensing oil boilers and between 10.5 €-Ct/(kW h) and 32.3 €-Ct/(kW h) in case of condensing gas boilers (Kaltschmitt, 2013, pp. 41). These figures illustrate that the heat generation costs of solar thermal systems for application in households are still relatively high and have to be further reduced in order to become competitive with fossil energy sources.

New materials can play an important role in achieving this goal, as they can contribute to both cost reductions and / or increases in efficiency for solar thermal systems. For example, polymeric materials, which are widely successful in various sectors including automotive, construction, and packaging industry, appear as suitable candidates. Polymers offer several advantages due to their positive engineering properties including low weight, freedom of design, and a broad range of manufacturing techniques. In addition, polymers allow for automated production processes, offering potential for reduced manufacturing costs. (Frick et al., 2014, p. 44)

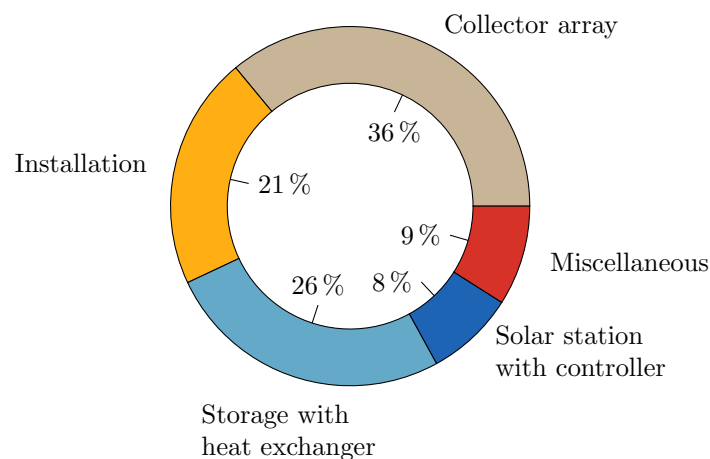


Figure 1.2: Cost distribution of small solar thermal systems (i.e. investment costs ranging between 4,000 € and 5,000 €) (Data source: Eicker, 2012, pp. 93).

As the collector array represents the largest system cost (cf. figure 1.2), several studies have focused on utilising plastics for solar thermal collectors (Reiter et al., 2014; Frick et al.,

2014). However, the application of polymeric FPCs in solar thermal systems is challenging, as standard plastics are typically unable to resist the high pressure and temperatures that typically occur during operation of solar thermal systems. Therefore, a new, holistic system approach is necessary.

1.1 Conventional Solar Thermal Systems and Drain Back Systems

Figure 1.3 shows the setup of a conventional solar thermal system. As soon as the temperature sensor, connected to the solar thermal collector array, detects a higher temperature compared to the heat storage ①, the solar controller ② switches on the pump ③. According to Quaschnig (2015, p. 105-106), typical (specific) volume flow rates for solar thermal systems range between $8\text{ l}/(\text{h m}^2)$ and $25\text{ l}/(\text{h m}^2)$ (low flow systems) and between $30\text{ l}/(\text{h m}^2)$ and $80\text{ l}/(\text{h m}^2)$ (high flow systems). Due to the incident irradiation on the collector ④, the heat transfer fluid (HTF) temperature increases while flowing through the collector. An expansion vessel and a safety valve ⑤ prevent damage from the system in case of high pressure.

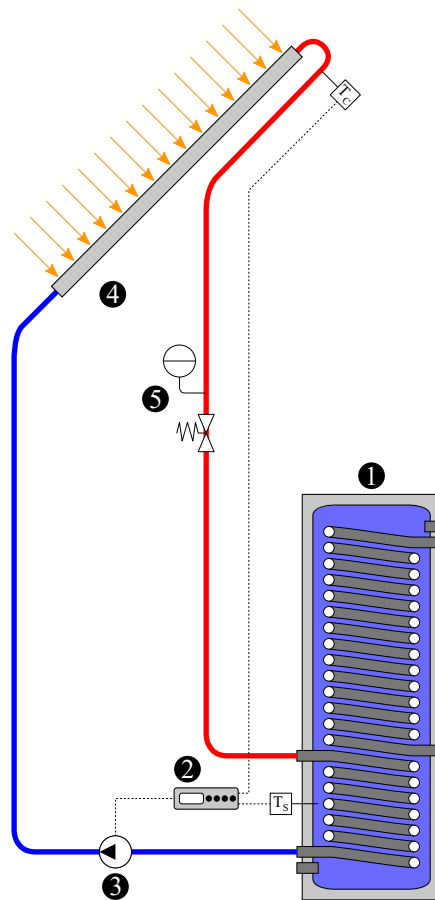


Figure 1.3: Setup of a conventional solar thermal system. ① = heat storage, ② = solar controller, ③ = solar pump, ④ = collector array, ⑤ = safety armatures.

1 Background and Introduction

A well-known problem of solar thermal systems is stagnation, a condition in which the HTF (usually a water-glycol mixture) evaporates. This occurs when a system has a completely charged heat storage tank while high solar irradiation is still present. The pump in the collector loop is switched off, causing the heat transfer from the HTF to come to a standstill. The evaporation of the HTF causes high pressure inside the collector, which is especially in combination with a high temperature load critical for polymeric collectors. Loads on metal-based absorbers caused by stagnation are not critical in general. Polymer-based absorbers usually have a volumetric channel structure to allow for an ideal heat transfer between absorber surface and fluid. However, such a volumetric, typically non-circular-shaped structure has a lower pressure resistance. This can be attributed to the fact that the resulting pressure within the system affects a larger surface area compared to a conventional, metal-based collector. Another disadvantage of closed systems is the degradation of the HTF (better known as 'cracking') which necessitates regular inspections to ensure freezing resistance and adequate fluid volume of the liquid. These problems can be overcome with the open, unpressurised architecture of a drain back system (DBS) (cf. figure 1.4).

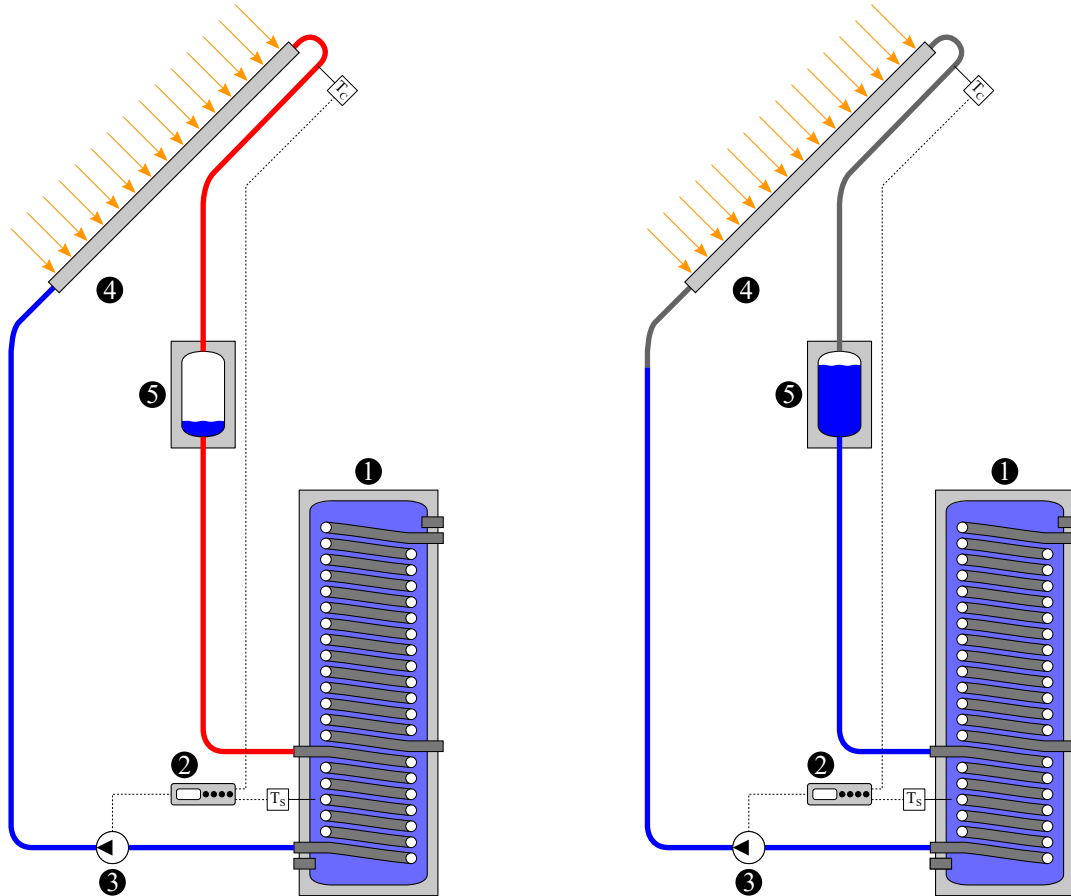


Figure 1.4: Working principle of a DBS. Left: Operating mode. Right: Idle mode. ① = heat storage, ② = solar controller, ③ = solar pump, ④ = collector array, ⑤ = drain back volume.

During normal operation (cf. figure 1.4, left), a pump ③ circulates the HTF through a collector array ④. Afterwards, the HTF flows into a drain back volume ⑤, before the heat

is transferred into the storage tank ①. As soon as the solar controller ② switches off the pump ③ (cf. figure 1.4, right), the solar circuit comes to a standstill. Subsequently, the fluid inside the collector array ④ drains into the drain back volume ⑤ due to gravity and ambient pressure.

The DBS setup has several advantages over a conventional setup: Primarily, it does not require an anti-freeze liquid, because the HTF (in this case water) remains in the drain back vessel when not in operation. Moreover, water has more advantageous fluid properties (e.g. heat capacity, viscosity) compared to a water-glycol mixture. The specific heat capacity of water with $c_{20^\circ\text{C}} = 4.19 \text{ kJ}/(\text{kg K})$ (Verein Deutscher Ingenieure, 2010, p. 155) is about 10 % higher than the specific heat capacity of a 38 % water-glycol mixture ($c_{20^\circ\text{C}} = 3.77 \text{ kJ}/(\text{kg K})$, Verein Deutscher Ingenieure, 2010, p. 449). Due to the kinematic viscosity, the necessary pumping energy for the circulation of the HTF in case of water ($\eta_{20^\circ\text{C}} = 1.00 \times 10^{-3} \text{ Pa s}$, Verein Deutscher Ingenieure, 2010, p. 157) is significantly lower compared to a 38 % water-glycol mixture ($\eta_{20^\circ\text{C}} = 4.56 \times 10^{-3} \text{ Pa s}$, Verein Deutscher Ingenieure, 2010, p. 449). The unpressurised system configuration allows for an utilisation of volumetric absorbers as well as cost-efficient plastic pipes. Due to the special design, essential components that are needed within conventional systems (e.g. expansion vessel, bleeder valve etc.) can be eliminated. However, a DBS also has disadvantages. The most important is the increased installation effort, which results from the fact that a proper inclination (typically $> 10 \text{ mm/m}$, cf. section 2.2.2) of the pipes must be guaranteed in order to prevent any “water pockets”². A detailed overview of the advantages and disadvantages of DBSs will be given in section 2.2.2.

1.2 Research Question and Methodology

In contrast to previous and current research approaches within the solar thermal sector, which mainly deal with improvements on collector level, this study aims for a holistic determination of the heat generation costs of solar thermal DBSs with polymeric FPCs in the context of single family homes. Here, the advantages of polymers and the system characteristics of DBSs perfectly complement each other. The overarching research question of this thesis addresses the issue whether DBSs with polymeric solar thermal FPCs can be a cost-competitive alternative to conventional solar thermal systems. To answer this question, the heat generation costs of such polymer-based DBS have to be determined and evaluated (cf. figure 1.5, lowest entry). Therefore, two important factors have to be determined. Besides investment, operating and maintenance cost, the thermal efficiency of each system has to be identified.

The evaluated literature (cf. chapter 2) reveals typical dimensions and properties of polymeric FPCs. This information is taken into account for the development of a new setup of a polymeric solar thermal FPC. In contrast to polymeric absorbers described in scientific publications, typically utilising semi-finished components (e.g. twin-wall sheets, pipes etc.), a modern processing procedure was used for fabricating cost-effective, polymeric absorbers.

² In case of a discontinuous inclination, residual water remains within the pipes during draining.

1 Background and Introduction

These absorbers are the basis for the development of collector prototypes, which were built-up and subsequently tested regarding their solar thermal efficiency (cf. chapter 3). The determined collector efficiencies were compared with data available from scientific literature. To also determine the collector efficiency of polymeric solar thermal FPCs that have not been tested experimentally, a suitable physical collector model was developed (cf. chapter 4). The previously measured values serve as a basis for validating the collector model. In addition to the solar thermal efficiency, typical temperatures (during operation and in case of stagnation) were evaluated. Therefore, a typical solar thermal DBS was developed and built-up (cf. chapter 5), including the developed collector prototypes. Information available from scientific publications (e.g. inclination and diameter of the pipes, control algorithms, size of collector array etc.) was taken into account during planning of the system test. The measured data are also used for validating the aforementioned collector model in case of dynamic, fluctuating boundary conditions. In the next step, a system simulation model was developed (cf. chapter 6). In this context, the measurement data obtained from the tested DBS was used to validate the simulation model. The collector prototype's efficiency (determined in chapter 3) was incorporated into the model to precisely predict the solar thermal yield of the tested collector array. After validating the simulation model, it was used to predict the annual solar thermal yield of a DBS with polymeric solar thermal FPCs. In this context, the influence of the solar thermal system's architecture as well as its location were evaluated. The aim of chapter 7 is the determination of heat generation costs for the investigated types of DBSs with polymeric solar thermal FPCs. Therefore, both the costs and the annual energetic yield of each system (determined in chapter 6) were evaluated.

The most relevant outcomes of this thesis are summarised subsequently:

- Conception and metrological analysis of different polymeric solar thermal FPC prototypes regarding their efficiency,
- Measurement- and simulation-based evaluation of polymeric solar thermal FPCs's behaviour in case of operation and stagnation within DBSs,
- Determination of heat generation costs for DBSs with polymeric solar thermal FPCs.

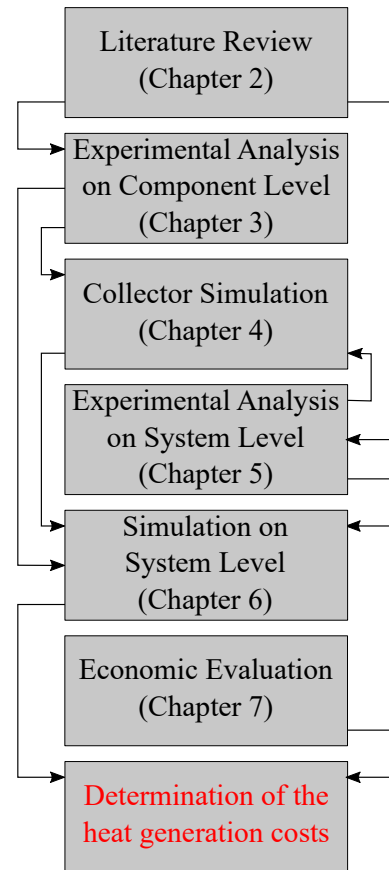


Figure 1.5: Research methodology.

2 Literature Review

In this chapter, the current state of research is presented. As there is hardly any literature regarding solar thermal DBSs with polymeric FPCs available, this review focuses both on solar thermal FPCs and on DBSs.

2.1 Collectors

Solar thermal collectors convert the solar radiation emitted by the sun into heat. They have been subject to scientific research for a long time. Hottel and Woertz (1942) were the first who performed detailed experimental studies regarding the performance of solar thermal FPCs (Duffie and Beckman, 2013, p. 287). Since then, solar thermal collectors have been further developed and are currently used to provide heat for numerous applications (i.e. DHW preparation, space heating / cooling, industrial process heat generation, solar thermal power plants etc.) and temperature ranges (Kalogirou, 2004). Worldwide, FPCs account for 22 %, whereas evacuated tube collectors (ETCs)³ represent the majority (71 %) of solar thermal collectors (Mauthner, Weiss and Spörk-Dür, 2015, p. 7). In Europe, however, FPCs account for 85 % of all solar thermal collectors (Mauthner, Weiss and Spörk-Dür, 2015, p. 7).

2.1.1 Efficiency of a Solar Thermal Collector

Figure 2.1 provides an overview of the heat transfer mechanisms which are present at a solar thermal FPC in case of steady-state conditions. The incoming solar irradiation hits the glazing ① and is divided into several parts. Depending on the optical properties of the glazing, most of the irradiation (e.g. 90 %) can pass through the glazing. Another portion of the irradiation (e.g. 8 %) is reflected at the glazing, whereas the rest (e.g. 2 %) gets absorbed by the glazing, which yields a temperature increase of the glazing. According to the law of conservation of energy, the portions of transmitted (τ), reflected (ρ) and absorbed (α) irradiation add up to one. (Quaschnig, 2015, p. 115)

The transmitted part of the solar irradiation that hits the absorber ③ gets absorbed and is partly reflected back to the glazing. The absorbed irradiation is converted into heat, which is conducted to the HTF flowing through the channels of the absorber. Heat losses of the collector are caused by convection, conduction and radiation. While natural convection is present in the air gap ② between glazing and absorber, both natural and forced convection (e.g. due to wind) cause heat losses at the glazing, the backside ⑤ and the casing ⑥. Conductive and radiative heat losses occur if the FPC's temperature is higher than the ambient temperature.

³ Compared to FPCs, ETCs can typically provide higher temperatures and are therefore used for residential or industrial applications with a high-temperature heat demand.

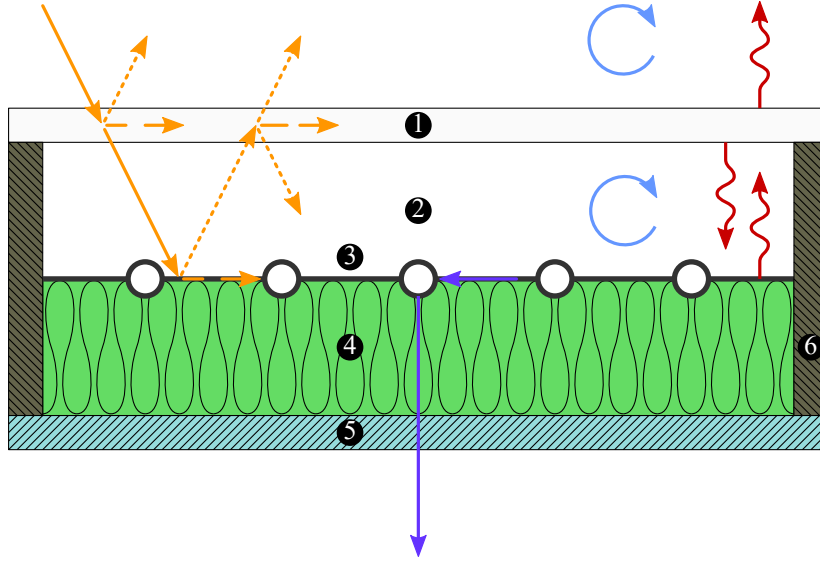


Figure 2.1: Heat transfer mechanisms at a solar thermal collector according to Kaltschmitt (2013, p. 186): Solar radiation (\rightarrow), Solar radiation, reflected ($\cdots\rightarrow$), Solar radiation, absorbed (\dashrightarrow), Conduction (\rightarrow), Convection + Conduction (\rightarrow), Heat radiation (\rightarrow). ① = glazing, ② = air gap, ③ = absorber, ④ = backside insulation, ⑤ = backside, ⑥ = side.

The solar thermal collector's ability to convert irradiation into heat can be expressed by the solar thermal efficiency η . It describes the ratio between utilised thermal output \dot{Q}_{out} and incident irradiation \dot{Q}_{in} (cf. equation 2.1):

$$\eta = \frac{\dot{Q}_{out}}{\dot{Q}_{in}} = \frac{A \cdot [I \cdot \tau \cdot \alpha - U_L \cdot (T_{Abs} - T_{Amb})]}{A \cdot I} = \tau \cdot \alpha - U_L \cdot \frac{T_{Abs} - T_{Amb}}{I} \quad (2.1)$$

where:

- η = Efficiency of the collector
- A = Collector surface area in m^2
- I = Irradiation in W/m^2
- τ = Transmittance of the glazing
- α = Absorption of the absorber
- U_L = Overall collector heat loss coefficient in $W/(m^2 K)$
- T_{Abs} = Absorber temperature in K
- T_{Amb} = Ambient temperature in K

The term $\tau \cdot \alpha$ represents the optical efficiency of the solar thermal collector and is denoted by η_0 . The second term of equation 2.1 represents the thermal losses of the collector to the environment. As the temperature distribution over the absorber area is not constant, the determination of T_{Abs} requires a significant amount of measurement data. Therefore,

the absorber temperature is expressed as an average temperature difference between the collector inlet and outlet and the collector efficiency factor F' . (Eicker, 2012, p. 97)

$$\begin{aligned}\eta &= F' \cdot \tau \cdot \alpha - F' \cdot U_L \cdot \frac{T_{Mean} - T_{Amb}}{I} \\ &= \eta_{0,eff} - F' \cdot U_L \cdot \frac{T_{Mean} - T_{Amb}}{I}\end{aligned}\quad (2.2)$$

where:

| | |
|----------------|---|
| η | = Efficiency of the collector |
| $\eta_{0,eff}$ | = Optical efficiency of the collector |
| F' | = Collector efficiency factor |
| U_L | = Overall collector heat loss coefficient in W/(m ² K) |
| T_{Mean} | = Average absorber temperature in K |
| T_{Amb} | = Ambient temperature in K |

As the overall collector heat loss coefficient U_L is temperature dependent, a linear relation between U_L and the temperature difference is assumed (cf. equation 2.3) (Eicker, 2012, p. 97).

$$F' \cdot U_L = a_1 - a_2 \cdot (T_{Mean} - T_{Amb}) \quad (2.3)$$

where:

| | |
|------------|---|
| a_1 | = Y-intercept in W/(m ² K) |
| a_2 | = Slope in W/(m ² K ²) |
| T_{Mean} | = Average absorber temperature in K |
| T_{Amb} | = Ambient temperature in K |

Inserting equation 2.3 into equation 2.2 yields the correlation between collector efficiency and temperature difference ΔT :

$$\begin{aligned}\eta &= \eta_{0,eff} - [a_1 - a_2 \cdot (T_{Mean} - T_{Amb})] \cdot \frac{T_{Mean} - T_{Amb}}{I} \\ &= \eta_{0,eff} - a_1 \cdot \frac{T_{Mean} - T_{Amb}}{I} - a_2 \cdot \frac{(T_{Mean} - T_{Amb})^2}{I}\end{aligned}\quad (2.4)$$

The efficiency curve of a single glazed flat plat collector is shown in figure 2.2. Depending on its purpose, the working range of a solar thermal collector varies (e.g. 0.02 K m²/W – 0.06 K m²/W for DHW preparation, cf. figure 2.2). Eicker (2012, pp. 97-98), Kaltschmitt (2013, p. 201) and Kalogirou (2004, p. 266) provide an detailed overview of different collectors, their specific efficiency curves and working ranges.

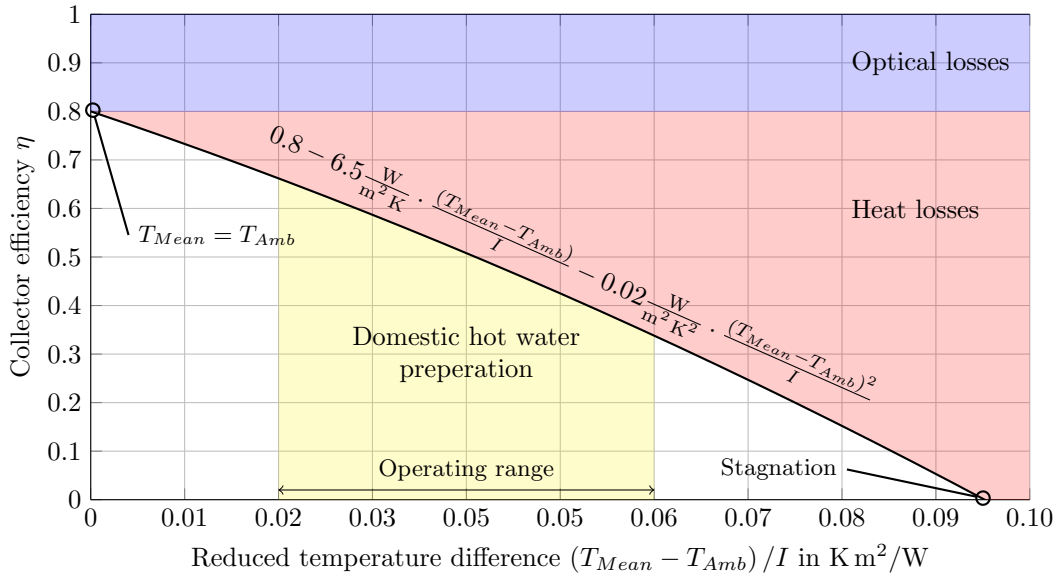


Figure 2.2: Efficiency curve of a single glazed FPC.

If $T_{Mean} = T_{Amb}$ (i.e. intersection of the efficiency curve with the y-axis), no thermal losses are present. Therefore, only optical losses (due to the optical properties of the glazing and the absorption properties of the absorber) limit the maximum efficiency of the FPC ($\eta_{max} = \eta_{0,eff}$). With increasing collector temperature, the thermal losses become more important. At the intersection of the efficiency curve with the x-axis (i.e. $\eta = 0$), the maximum temperature (also called stagnation temperature) is reached. The efficiency of FPCs can be increased by various measures, such as novel absorber materials and designs (e.g. bionic absorber structures) (Hermann, 2012), special coatings (Zhang et al., 2017) and many others. However, the purpose of any solar thermal system is to minimise the heat generation costs, therefore it can be advantageous to use less efficient collectors if their costs are significantly lower (Duffie and Beckman, 2013, p. 238).

2.1.2 Polymeric Materials for Solar Thermal Collectors

Figure 2.3 (left) shows a sectional view of a typical FPC with a metallic absorber, commonly made of copper or aluminium (Kalogirou, 2004, p. 243). Due to their high thermal conductivity ($\lambda_{Aluminium} = 222 \text{ W}/(\text{m K})$, $\lambda_{Copper} = 388 \text{ W}/(\text{m K})$, Callister and Rethwisch, 2020, p. A22), a variety of processing techniques (such as welding, soldering etc.) and semi-finished products (e.g. pipes, metal sheets etc.), these materials are well suited for applications in solar thermal collectors. The applicability of polymers as a suitable material for collector components has been investigated over the past few years. Figure 2.3 (right) shows a sectional view of a FPC with a polymeric absorber. Compared to the design of the metal-based absorber, a polymeric absorber typically has rectangular flow channels instead of tubular riser pipes.

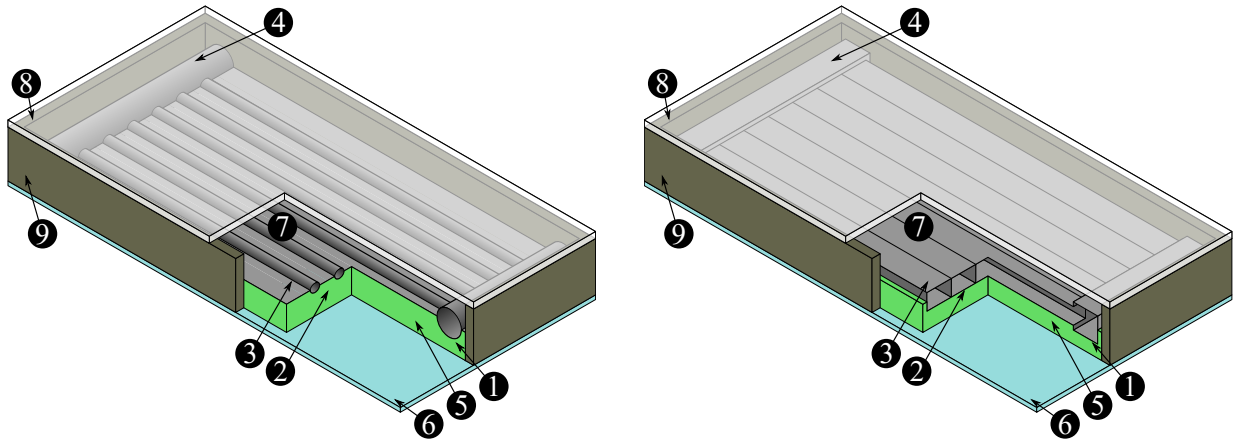


Figure 2.3: Setup of conventional vs. polymeric solar thermal FPC. Left: Conventional FPC with metal absorber made of circular riser pipes bonded to a fin-shaped absorber-sheet. Right: Flat plate collector with polymeric absorber made of volumetric riser channels. A HTF enters the collector and flows into the first header tube / manifold ①. Here, the flow gets separated into several risers ②. The purpose of these risers is to conduct the heat absorbed by the absorber ③ to the HTF. Afterwards, the separate flows converge at the second header tube ④. An insulation ⑤ minimises the heat losses towards the backside ⑥. An air gap ⑦ between the absorber and a transparent glazing ⑧ reduces the heat losses towards the front side. All parts are enclosed by a casing ⑨.

Table 2.1: Costs and mechanical properties of commonly used polymeric materials compared to metals. C_{Mat} = material costs, ρ = density, E = Young’s modulus, ν = Poisson’s ratio, σ = yield stress. Cost information according to Callister and Rethwisch (2020, pp. A33-A35), mechanical properties according to Callister and Rethwisch (2020, pp. A3-A15). Empty cells indicate that there is no information available.

| | | C_{Mat} in €/kg ¹ | ρ in kg/m ³ | E in GPa | ν | σ in MPa |
|----------|---------------|--------------------------------|-----------------------------|-------------|-------------|-----------------|
| Metals | Aluminium | 0.68 – 2.70 | 2,710 | 69 | 0.33 | 34 |
| | Copper | 5.86 – 9.01 | 8,500 | 115 | 0.33 | 96 |
| | Stainl. Steel | 1.35 – 3.88 | 8,000 | 193 | 0.30 | 205 |
| Polymers | LDPE | 0.90 – 2.48 | 923 | 0.17 – 0.28 | 0.33 – 0.40 | 9 – 15 |
| | HDPE | 0.81 – 2.39 | 959 | 1.08 | 0.46 | 26 – 33 |
| | PMMA | 0.72 – 3.24 | 1,190 | 2.24 – 3.24 | 0.37 – 0.44 | 54 – 73 |
| | PP | 0.63 – 2.34 | 905 | 1.14 – 1.55 | 0.40 | 31 – 37 |
| | PS | 0.72 – 2.66 | 1,050 | 2.28 – 3.28 | 0.33 | 25 – 69 |
| | PVC | 0.72 – 2.30 | 1,300 – 1,580 | 2.41 – 4.14 | 0.38 | 41 – 45 |
| | PBT | 0.81 – 2.75 | 1,340 | 1.93 – 3.00 | | 57 – 60 |
| | PC | 0.72 – 4.78 | 1,200 | 2.38 | 0.36 | 62 |
| | PET | 0.63 – 2.16 | 1,350 | 2.76 – 4.14 | 0.33 | 59 |
| | PEEK | 90.13 – 252.37 | 1,310 | 1.10 | | 91 |

¹ Callister and Rethwisch (2020) specified the raw material costs in \$/kg (data collected in January 2015). 1€ $\hat{=}$ 1.11\$ (average exchange rate in 2015) (European Central Bank, 2020).

2 Literature Review

Table 2.2: Thermal properties of commonly used polymeric materials compared to metals. T_{ST} / T_{LT} = short / long term operating temperature in °C, λ = thermal heat conductivity, c = heat capacity, β = coefficient of thermal expansion. Operating temperature information according to Verein Deutscher Ingenieure (2010, p. 567), thermal properties according to Callister and Rethwisch (2020, pp. A21-A26). Empty cells indicate that there is no information available.

| | | T_{ST} in °C | T_{LT} in °C | λ in W/(m K) | c in J/(kg K) | β in 10^{-6} 1/K |
|----------|---------------|----------------|----------------|----------------------|-----------------|--------------------------|
| Metals | Aluminium | | | 222 | 0.90 | 24 |
| | Copper | | | 338 | 0.39 | 17 |
| | Stainl. Steel | | | 16 | 0.50 | 17 |
| Polymers | LDPE | 70 – 80 | 60 – 80 | 0.33 | 2.30 | 180 – 400 |
| | HDPE | 90 – 120 | 60 – 80 | 0.48 | 1.85 | 106 – 198 |
| | PMMA | 85 – 100 | 60 – 90 | 0.17 – 0.25 | 1.46 | 90 – 162 |
| | PP | 140 | 80 – 100 | 0.12 | 1.93 | 146 – 180 |
| | PS | 60 – 80 | 50 – 70 | 0.13 | 1.17 | 90 – 150 |
| | PVC | 80 | 70 | 0.15 – 0.21 | 1.05 – 1.46 | 90 – 180 |
| | PBT | | | 0.18 – 0.29 | 1.17 – 2.30 | 108 – 171 |
| | PC | 135 | 100 – 120 | 0.20 | 0.84 | 122 |
| | PET | | | 0.15 | 1.17 | 117 |
| | PEEK | | | | | 72 – 85 |

On the one hand, this particular design allows for a better conversion of the incident irradiation into heat, as the normal thermal resistance of the rectangular riser pipes is lower compared to the in-plane thermal resistance of an absorber sheet. On the other hand, volumetric absorbers in combination with polymeric materials are of major importance to compensate the lower heat conductivity ($\lambda_{PP} = 0.12 \text{ W/(m K)}$, Callister and Rethwisch, 2020, p. A23) of these materials. While such a design can theoretically also be realised with metals, the production costs would be higher compared to polymers. According to Bonnet (2014, p. 72), polymers can be divided into three groups: Standard plastics (e.g. LDPE, HDPE, PMMA, PP) can resist temperatures up to 100 °C (cf. table 2.2) and cost between 2 €/kg and 2 €/kg . Engineering plastics (e.g. PA, PC, PBT, PPO) are able to withstand temperatures up to 150 °C and cost between 2.50 €/kg and 3.50 €/kg . High-performance plastics (e.g. PES, PEEK) can resist temperatures above 150 °C with prices ranging between 5 €/kg and 20 €/kg (and above). An overview of commonly used polymeric materials for solar thermal applications together with their material costs and properties in comparison to metals is shown in tables 2.1 and 2.2. Due to the variety of polymers and their manufacturing techniques, different setups of polymeric collectors have been discussed in the scientific literature. Subsequently, an overview of various aspects regarding such collectors will be given.

2.1.3 Scientific Investigation of Polymeric Solar Thermal Collectors

Martinopoulos et al. (2010) determined the efficiency of a polymeric solar thermal collector (absorber surface = 1.252 m^2) both experimentally and by means of a computational fluid dynamics (CFD) simulation. For the absorber, a transparent, UV-stabilised, honeycombed, 10 mm thick plate made of PC was used (cf. figure 2.4, left). The rear insulation also consisted of a honeycombed, 10 mm thick sheet of PC. Here, a special nano-gel was used to limit the heat losses to $0.018\text{ W}/(\text{m}^2\text{ K})$. The glazing was made of a UV-stabilised, transparent, 3 mm thick plate of PC⁴. A circumferential, 30 mm thick PUR-insulation minimised the heat losses to the side of the collector ($\lambda = 0.03\text{ W}/(\text{m}^2\text{ K})$). Black coloured water was used as the HTF. The results showed a considerable accordance between the measured and simulated values. The maximum efficiency of the investigated prototype was around 64%. The (linear) curve of thermal efficiency is shown in figure 2.5 (black curve).

The previously validated CFD-model of Martinopoulos et al. (2010) was the basis for the work of Missirlis et al. (2014), who investigated the influence of different manifold configurations to the collector efficiency. The highest efficiencies could be determined for a configuration where both the inlet and outlet pipes are aligned to the orientation of the extruded riser channels of the absorber. This setup yields a more uniform flow and temperature distribution compared to other configurations, resulting in lower heat losses and a higher efficiency, respectively. The (linear) curve of thermal efficiency for this arrangement of inlet and outlet is shown in figure 2.5 (blue curve).

Ariyawiriyanan et al. (2013) investigated the efficiency of five different, unglazed polymeric collectors. Three absorbers (made of PVC-B, PB and PP-R) had the same aperture area of 1.3 m^2 , while the remaining absorbers (made of PVC-CB) had different aperture areas (1.8 m^2 and 2.0 m^2 , respectively). The authors showed a relation between the thermal heat conductance of the absorber material and the collector efficiency. Furthermore, a dependency between the size of collector and its efficiency was found. The curve of the most efficient polymeric collector is shown in figure 2.5 (grey curve). The maximum efficiency of this prototype was 50%.

Mintsa Do Ango, Medale and Abid (2013) performed CFD simulations of a polymeric solar thermal collector with a 4 mm-thick absorber made of PC. The 0.2 m-wide collector was glazed with a transparent PC cover on the frontside. On the backside, a 30 mm-thick insulation made of glass wool minimised the heat losses to the ambient. The authors investigated the influence of several parameters on the efficiency of the collector. The study showed that there is no relation between the length of the collector and its efficiency. This result contrasts with the study of Ariyawiriyanan et al. (2013), who found a dependency between the area of a collector and its efficiency. Mintsa Do Ango, Medale and Abid (2013) identified an optimal thickness of the air gap between the glazing and absorber (which is 10 mm). Furthermore, the authors identified a correlation between the mass flow rate and the FPC's efficiency: Increasing the mass flow rate leads to a lower temperature difference between the collector's inlet and outlet and hence, *ceteris paribus*, to lower heat losses / a higher collector efficiency.

⁴ The absorber plate, the backside insulation as well as the frontside glazing were made from LEXAN[®], a transparent PC material.

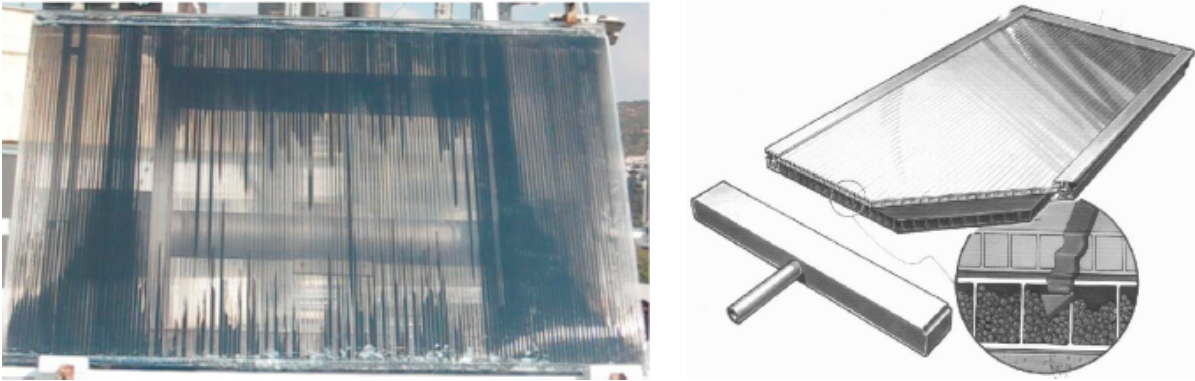


Figure 2.4: Polymeric collectors described in scientific papers. Left: Transparent polymeric collector prototype by Martinopoulos et al. (2010, p. 1508) filled with black coloured water as a HTF. The photograph shows an unequal flow distribution inside the absorber structure. Right: Photorealistic representation of the *SolarNor* collector described by Sandnes and Rekstad (2002, p. 64). The detail shows the riser channels of the absorber filled with ceramic granulate.

Cristofari et al. (2002) developed a simulation model to identify the influence of several parameters (insulation thickness, mass flow rate and fluid layer thickness) on the efficiency of a solar thermal collector with a PP absorber based on a 10 mm-thick twin-wall plate. For the insulation thickness, the authors identified optimal values between 20 mm and 30 mm. Furthermore, they proposed that the ideal fluid layer should be < 10 mm. Based on a system simulation, Cristofari et al. (2002) report an ideal mass flow rate of $2.65 \times 10^{-3} \text{ kg}/(\text{m}^2 \text{ s})$. Compared to the volume of the storage tank ($V = 150 \text{ l}$), this equals an hourly 12% exchange of the storage's volume. The authors estimate the costs for a 2 m^2 collector to be approximately $\text{€}54/\text{m}^2$ ⁵.

Chen et al. (2015) utilised the concept of a twin-wall plate as basis for a polymeric absorber. The investigated PC absorber had an absorber area of 1.16 m^2 and an overall thickness of 8 mm. A 16 mm air gap is present between the absorber and the 4 mm-thick glazing made of PC (twin-wall plate). In order to minimise the heat losses at the backside, a 20 mm poly-foam insulation was used. In their study, the authors report about the disadvantages which came along with the utilisation of twin-wall plates. Due to different thermal expansion factors between the extruded absorber plate and the header tubes, leakages can occur at high temperatures. Another aspect of this study dealt with the coating of the absorber. As transparent twin-wall plates were used as an absorber, the authors investigated the application of a black coating both on the top and on bottom surface of the twin-wall plate. In the first case, the incoming irradiation hits the black top surface where it gets converted into heat and conducted through the twin-wall plate into the collector fluid. In the second case, the sun rays hit the upper side of the absorber (where they get partly absorbed) and pass through the transparent collector fluid. The light is absorbed on the lower side of the twin-wall plate and converted into heat. By comparing the solar thermal yields of both concepts, the authors report that there is no significant difference between both concepts. The (linear) curve of thermal efficiency is shown in figure 2.5 (green curve).

⁵ Cristofari et al. (2002) specified costs of $\text{\$/m}^2$. $1 \text{ €} \hat{=} 0.95 \text{ \$}$ (average exchange rate in 2002) (European Central Bank, 2020).

Sandnes and Rekstad (2002) performed experimental investigations on a PV/T collector⁶ (absorber area = 0.48 m²). A twin-wall plate made of a modified PPO was used as an absorber. The individual channels of the twin-wall plate were filled with a ceramic granulate in order to increase the heat transfer between the absorber and the HTF (cf. 2.4, right). The authors used a 4 mm-thick front cover made of glass ($\tau \approx 0.9$) at a distance of 12 mm from the absorber. The HTF was pumped to the upper header tube, where it flowed downwards the absorber due to gravitational force. The (linear) curve of thermal efficiency of the tested collector (pure solar thermal without PV) is shown in figure 2.5 (orange curve).

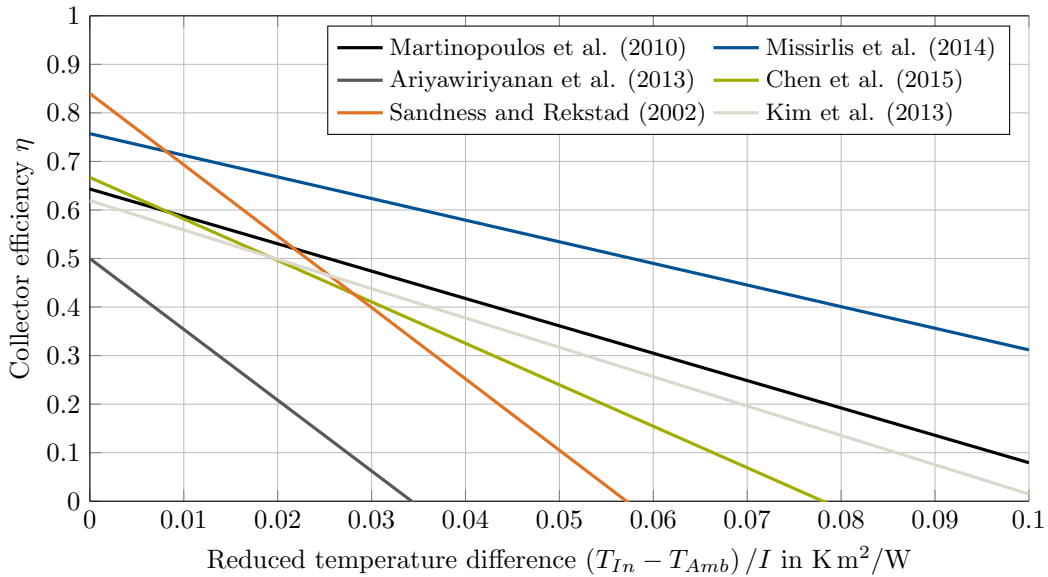


Figure 2.5: Linear efficiency curves of scientifically investigated polymeric collectors according to ASHRAE 93-1986 (pp. 11-12). In contrast to European testing standards (cf. section 3.3), the American standard ASHRAE 93-1986 neglects the non-linear heat losses of solar thermal FPCs (cf. equation 2.4, last term). The resulting efficiency curve can therefore mathematically be described as a linear function. Although the second-order polynomial formulation of the European standards EN ISO 9806:2013 / DIN EN 12975-2:2006 allows for a more precise description of a solar thermal FPC's efficiency, the straight-line equation provided by ASHRAE 93-1986 can be found much more frequently in scientific publications.

Kim et al. (2016) investigated the utilisation of carbon nanotubes (CNT) in a solar thermal collector with an absorber made of PC. Due to the high thermal conductivity of CNT ($\lambda_{CNT} = 2,000 \text{ W/(m K)} - 6,000 \text{ W/(m K)}$) and a very high aspect ratio (i.e. the ratio between a CNT's length to its diameter), even small amounts of this material ($> 1.5\%$) can have a positive effect on the heat conductivity of polymeric absorbers. The authors compared the efficiency of both a polymeric solar thermal collector with and without a 2%-concentration of CNT. Measurements with a solar simulator revealed a 2.5 times higher

⁶ A PV/T collector is a combination of a PV-module and a solar thermal FPC and is therefore able to provide both electricity and heat. By circulating a HTF through an absorber-structure mounted to the backside of a PV-module, the thermal losses of the PV-module can be utilised (e.g. for DHW preparation or space heating). At the same time, the electricity production is increased due to lower operating temperature of the PV-module.

maximum efficiency of the CNT-impregnated absorber compared to the absorber without CNT. Furthermore, the absorptivity of the investigated PC absorber filled with CNT was more than three times higher compared to the absorber without CNT. The authors also investigated the influence of the absorber length to the efficiency of the collector. The result indicates a lower efficiency for longer absorbers, which can be attributed to a higher mean temperature of the longer absorber, resulting in higher heat losses. The (linear) curve of thermal efficiency is shown in figure 2.5 (ivory curve).

2.1.4 Commercially Available Polymeric Solar Thermal Collectors

The application of polymeric materials in the solar thermal energy sector has already been successfully demonstrated. Most often, single components are replaced by polymers in order to utilise their advantages. A typical application area of polymeric collectors is the preparation of hot water for swimming pools. In case of such unglazed collectors, the pool water is directly pumped through the absorber without a heat exchanger. For this reason, the materials used for the absorbers must resist potential additives (e.g. chlorine) of the pool water. The maximum achievable collector temperatures for unglazed pool absorbers range between 20 °C and 30 °C (depending on the area of the collector array and the environmental conditions). As the system is open to the atmosphere, the maximum pressure is usually limited to 1.2 bar – 1.5 bar (Köhl, Meir and Papillon, 2013, p. 221). Due to the comparatively low pressure and temperature in case of stagnation, commodity plastics (e.g. UV-resistant PP, PVC, PE and EPDM) are suitable materials for unglazed pool heating absorbers. To prevent frost damage on the absorbers, they must be emptied or disassembled during winter. Pool heating absorbers are either rigid, volumetric (cf. figure 2.6, left) or flexible, mat-shaped structures (cf. figure 2.6, right).



Figure 2.6: Unglazed polymeric collectors for pool heating. Left: OKU[®] absorber with integrated header tube (Oku Obermaier GmbH, 2018). Right: SunStar pool heating absorber (UMA Solar, 2016).

In addition to the pool heating absorbers described above, some solar thermal FPCs with polymeric absorbers are commercially available for hot water preparation and space heating.

The *One Sun One World* solar collector has a gross collector area of 0.95 m^2 and uses a honeycomb-structure as absorber. This structure is welded with two header tubes and enables a volumetric flow throughout the absorber. The frame of this collector consists of several welded plastic parts. A special characteristic of this collector is a transparent honeycomb-matrix between the absorber and the glazing (cf. figure 2.7, left, pos. 38).

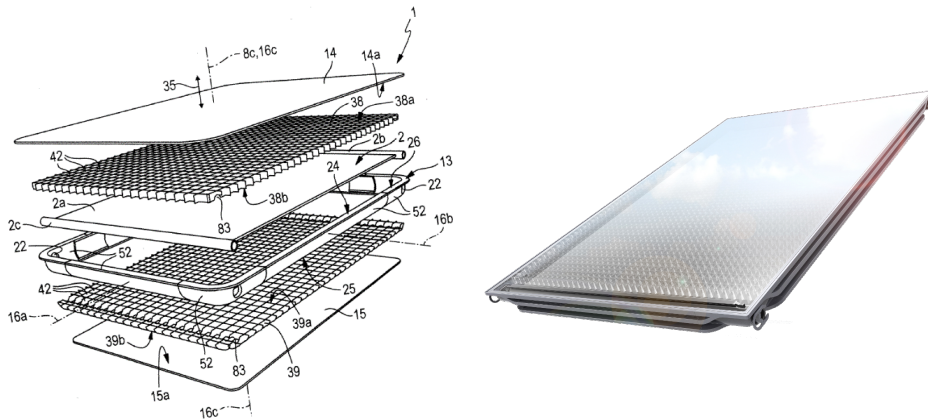


Figure 2.7: *One Sun One World* solar collector. Left: Exploded assembly drawing (Buchinger and Barek, 2015, fig. 8). Right: Photo-realistic representation (Internationales Design Zentrum Berlin e. V., 2015).

Hollands (1965) was the first one who investigated the utilisation of honeycomb-structures to reduce convective heat losses. A further advantage of that matrix is the support of the 3 mm thick glazing. The same type of honeycomb-structure is used behind the absorber (cf. figure 2.7, left, pos. 39) to minimise the heat losses to the environment. A photorealistic image of the *One Sun One World* solar collector is shown in figure 2.7 (right). The collector efficiency curve of the *One Sun One World* collector was determined according to EN ISO 9806:2013 and is shown in figure 2.10 (black curve).

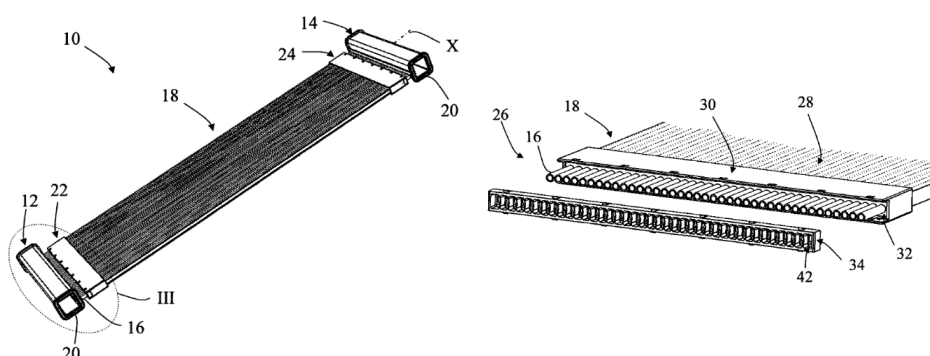


Figure 2.8: *Eco Flare 3M* collector. Left: General view. Right: Detailed view of the clasp (Sessler, Waisman and Plaschkes, 2011, fig. 1 and 5).

The absorber of the *Eco Flare 3M* collector (absorber area = 2.25 m^2) consists of numerous polymeric pipes (cf. figure 2.8, right, pos. 16). These pipes are arranged in a special clasp

(cf. figure 2.8, right, pos. 34) and connect both manifolds, which have a rectangular cross-section (cf. figure 2.8, left, pos. 12 and 14). The collector efficiency curve of this collector was determined according to DIN EN 12975-2:2006 and is shown in figure 2.10 (blue curve).

The Norwegian manufacturer *Aventa AS* uses an extruded twin-wall plate made of PPS as an absorber (Rekstad, 2012). A special feature of this collector (surface area = 2.65 m²) is the arrangement of hydraulic connections, which are both located at the lower part of the absorber (cf. figure 2.9, top right, pos. 51 and 52). A twin-wall plate made of PC is used as the cover (cf. figure 2.9, bottom right). The distance between the cover, absorber and the backside insulation (mineral wool) is ensured by suitable aluminium profiles. The efficiency curve of the collector was determined according to DIN EN 12975-2:2006 and is shown in figure 2.10 (orange curve).

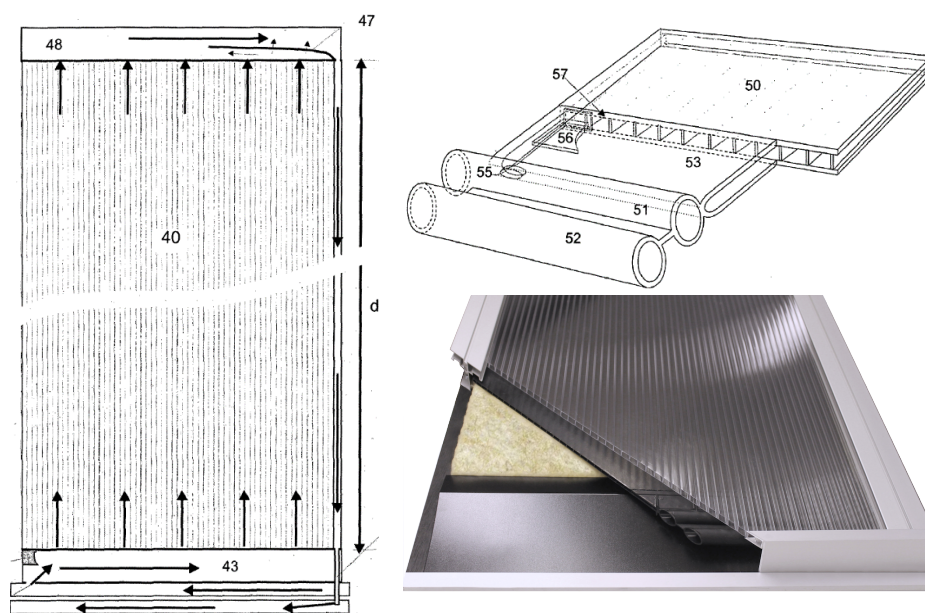


Figure 2.9: *Aventa AS* collector. Left: Top view (Rekstad, 2012, fig. 7). Right (top): Detail view (Rekstad, 2012, fig. 8). Right (bottom): Cutaway model of the collector (*Aventa AS*, 2016).

2.1.5 Overheat Protection

The main challenges for polymeric collectors are both high temperatures and pressures which occur during operation. In this context, many research activities aim for a temperature limitation of the collector. Typical stagnation temperatures for conventional, metal-based FPCs range from 150 °C to 300 °C, depending on the type of coating (Duffie and Beckman, 2013, p. 311). According to Gladen, Davidson and Mantell (2014, p. 43), overheating-protection measures can be classified in two categories: Measures of the first category try to restrict the maximum temperature of the collector by increasing the thermal losses (e.g. by using a cooling agent, venting the collector, utilising evaporative cooling mechanisms or reducing the insulation thickness). Approaches associated to the second category aim for a decrease of the incident radiation to the absorber.

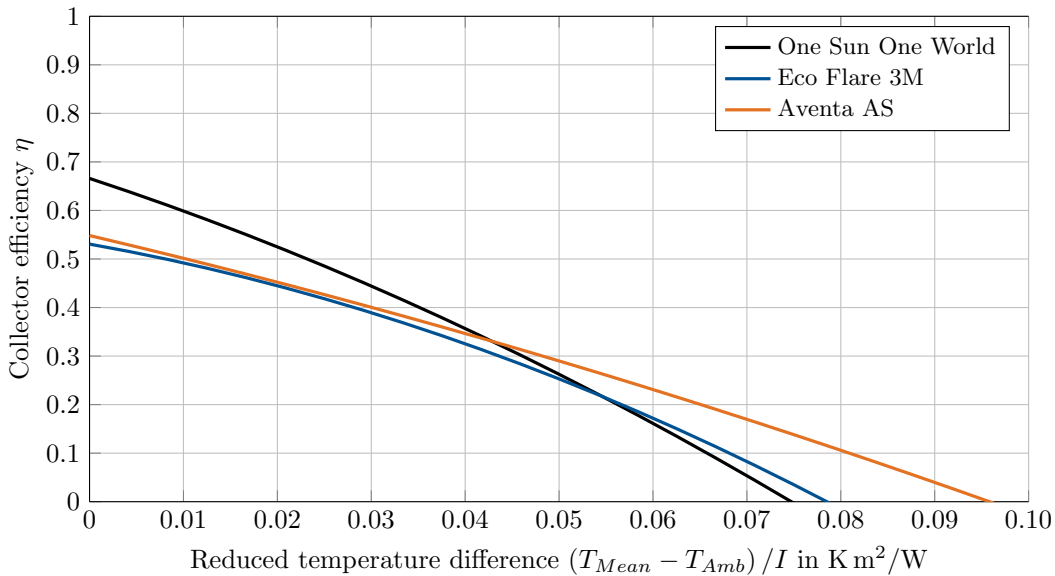


Figure 2.10: Efficiency curves of commercially available polymeric collectors (data source: DIN CERTO, 2015, DIN CERTO, 2011 and DIN CERTO, 2014). The efficiency of the *One Sun One World* solar collector was determined according to EN ISO 9806:2013, the efficiency of the *Eco Flare 3M* and *Aventa AS* according to DIN EN 12975-2:2006. To compare the efficiency curves determined according to different standards, the parameters η_0 , a_1 and a_2 were scaled by the ratio of the aperture surface area to the gross collector area in the case of the *Eco Flare 3M* and *Aventa AS* collectors.

In order to assess the maximum temperatures, which arise during operation, Piekarczyk et al. (2016) performed long-term measurements of polymeric collectors at three different locations: Dessert Negev (Israel), Gran Canaria (Spain) and Freiburg (Germany). The absorbers made of PP or PPS (fabricated from an extruded twin-wall plate) had a mineral wool backside insulation and transparent frontside glazing (also an extruded twin-wall plate). All parts were integrated into an aluminium frame. For more than 200 days, temperatures were recorded at different locations of the polymeric collectors. The maximum absorber temperatures at Freiburg were ranging between 120 °C and 130 °C. Within the monitored period, these temperatures occurred between 50 h and 100 h. For the investigated material, an absorber temperature of 85 °C was considered as a critical temperature. Temperatures >85 °C were recorded in 15 % (Freiburg), 16 % (Gran Canaria) and 27 % (Dessert Negev) of the cases.

In order to limit the maximum collector temperature, Kearney, Davidson and Mantell (2005) investigated how air vents at different positions affect the maximum temperature of a polymeric collector. Such air vents can be operated either actively (e.g. with actuator motors) or passively (e.g. by utilising shape memory alloy springs, Kessentini et al., 2014) and can be regarded as overheating-protection measure of category I. Depending on the location of the air vent, the authors detected a decrease in the maximum collector temperature ranging between 26 °C and 31 °C. The study also investigated the usage of a wetted pad (which is in contact with the absorber) in combination with venting. In this case, a temperature decrease of 79 °C could be observed. Taking into account the maximum temperature of 149 °C of the

2 Literature Review

investigated collector, only the application of a wetted pad in combination with venting will drop the temperature below the maximum operating temperature of commonly used plastics.

Hintringer, Richtfeld and Hauer (2014) as well as Thür, Neyer and Streicher (2014) investigated the behaviour of a heat exchanger which is placed behind (and outside) a polymeric solar thermal collector (i.e. overheating-protection measure of category I). During normal operation, this collector acts like a conventional solar thermal collector. In case of stagnation, a valve bypasses the hot water to the heat exchanger behind the absorber. Here, the heat is emitted to the environment. As a consequence, the HTF will be cooled and prevents the collector from overheating. The heat carrier circulates due to the thermosiphonic effect until the valve switches back to normal operation.

Thermotropic layers for limiting the maximum temperature of polymeric absorbers were investigated extensively by Wallner, Resch and Hausner (2008), Resch, Wallner and Hausner (2009) and Gladen, Davidson and Mantell (2015). These layers have the ability to switch from a transparent state to an opaque state at a certain temperature. Their behaviour can be regarded as an overheating protection measure of category II.

A further approach for limiting the incident irradiation (i.e. overheating protection measure of category II) is the utilisation of prismatic structures (Slaman and Griessen, 2009), which can be incorporated into the glazing. In case of direct irradiation, which causes the highest temperature loads to the collector, the light rays are reflected by the prismatic structure. In case of oblique incident irradiation, the energy emitted by the sun can pass through the prismatic structure and is absorbed.

2.1.6 Summary

An overview of polymeric collectors described in scientific publications is shown in table 2.3. The scientific publications presented above show that a lot of research has been performed on collector level. Most studies aimed for an improved collector efficiency, trying to identify the most influencing parameters. All concepts utilise pre-fabricated, semi-finished components (e.g. twin-wall or honeycombed plates) to build polymeric absorbers for solar thermal collectors. This approach was adopted by the few manufacturers of commercially available polymeric collectors. The utilisation of semi-finished components has several advantages: As they are widely used across many industries, twin-wall plates are fabricated on a large scale. Furthermore, manufacturers of polymeric solar thermal FPCs can buy these components as supply parts. Both facts yield low costs for such semi-finished components.

On the other hand, the usage of twin-wall plates for solar thermal applications is limited. Several steps are necessary in order to transform such a twin-wall plate into a fully functional absorber, requiring substantial effort by additional components and services for manufacture and assemblage. As mentioned by Chen et al. (2015), merging other polymeric parts to a twin-wall plate may cause leakage at higher temperatures due to different coefficients of thermal expansion. Even more steps are necessary to transform such a polymeric absorber into a solar thermal collector.

Although the commercially available collectors use polymeric materials, they are not fully taking advantage of the wide range of design / manufacturing opportunities that modern plastic processing offer.

The overheating measures described in the scientific literature require additional measures to ensure fail-safe operation of the collectors. Therefore it is questionable whether these approaches can usefully contribute to cost-effective polymeric FPCs. An alternative solution is to use less efficient collectors which do not risk critical temperatures.

The literature presented above reveals some typical dimensions for polymeric collectors. The collector area ranges between 0.3 m^2 and 2.0 m^2 . Generally, either glass or UV-resistant PC is used as a front cover, typically 3 mm – 4 mm thick. The backside insulation (5 mm – 50 mm thick) usually consists of polymeric or fibre materials. The evaluated scientific publications lack information concerning the collector costs (in terms of €/m²). In order to determine these costs, detailed information about the manufacturing processes of a polymeric solar thermal FPC is necessary. Furthermore, the review reveals that there are only a few investigations available on system level.

Table 2.3: Overview of polymeric collectors described in scientific publications. Empty cells indicate that there is no information available, crossed-out cells (—) indicate that the corresponding collector does not include the indicated component / property (▨ = honeycomb-structure, ▤ = Twin-wall plate, □ = transparent plate, ▥ = transparent twin-wall plate).

| | (a) | (b) | (c) | (d) | (e) | (f) | (g) | |
|---------------|--|------------------------------|--|-----------------------------|-----------------------|-----------------------------|--------------------|--|
| | Martinopoulos et al. (2010) Missirlis et al. (2014) | Ariyawiriyaman et al. (2013) | Mintsa Do Argo, Medale and Abid (2013) | Cristofari et al. (2002) | Chen et al. (2015) | Sandnes and Rektstad (2002) | Kim et al. (2016) | |
| Absorber | area | 1.3 m ² | 1.3 - 2.0 m ² | 0.05 - 1.8 m ² | 2.0 m ² | 1.2 m ² | 0.5 m ² | 0.3 m ² , 0.8 m ² |
| | thickness | 10 mm | | 4 mm | 3 - 52 mm | 8 mm | | 10 mm |
| | material | PC | PVC-B, PB, PP-R, PVC-CB | PC | PP | PC | PPO | PC + CNT |
| type | ▨ | | ▤ | ▥ | ▥ | ▥ | ▥ | |
| Insulation | thickness (back) | 10 mm | | 30 mm | 5 - 50 mm | 20 mm | 50 mm | 50 mm |
| | material (back) | PC + nanogel | | glass wool | PUR | polyfoam | mineral wool | PUR |
| | thickness (side) | 30 mm | | — | 5 - 50 mm | — | — | — |
| | material (side) | PUR | | — | PUR | — | — | — |
| Cover | thickness | 3 mm | — | | 4 mm | 4 mm | 4 mm | 4 mm |
| | material | PC | — | | glass | PC | glass | PC |
| | type | □ | — | | □ | ▥ | □ | ▥ |
| Misc. | air gap thickness | | | 3 - 13 mm | | 16 mm | 12 mm | 10 mm |
| | fluid | water (colored) | water | water | water | water | water | water |
| | costs | | | | ≈ 54 €/m ² | | | |
| type of study | simulation / measurement | measurement | simulation | simulation / measurement | measurement | measurement | measurement | |

2.2 Drain Back Systems

A brief description of the functionality of a DBS is given in section 1.1. Compared to conventional solar thermal systems, the main difference of the DBS is the open, unpressurised architecture.

2.2.1 History and Application Areas of Drain Back Systems

The principle of solar thermal drain back systems has been known for decades. The *MIT Solar House #1* is one of the very first examples of a DBS (Hesselschwerdt, 1954). This house was built to demonstrate the utilisation of solar thermal collectors for space heating and hot water preparation. A total collector area of 37.2 m^2 is connected to a 4,500l storage tank, which is horizontally placed below the roof of the building. In comparison to the net floor area of the building (approximately 56.5 m^2), the large collector array could cover a significant portion of the heat demand (ranging between 63 % and 100 % during October 1951 and April 1952).

An increasing interest in solar thermal systems, particularly in DBSs, arose after the Arab oil embargo in 1973 (Botpaev et al., 2015, p. 43). During that time, an increasing number of patent application both in the US and Europe could be observed, aiming for an effective anti-freeze protection. Special drinking water regulations prohibiting the use of additives within solar collector loops led to a widespread use of DBSs in the Netherlands (Bokhoven, van Dam and Kratz, 2001, p. 349) in the mid of 1980s.

Initial efforts towards DBSs with polymeric collectors were made in the mid of 1980s (Kutscher et al., 1984, p. 151). According to Botpaev et al. (2015, p. 44), DBSs in combination with polymeric solar thermal collectors were further investigated in Norway in the 1990s. Rekestad et al. (2000) describe a DBS with polymeric collectors made of PPO. According to the authors, the climate conditions in Norway require solar thermal systems which are able to cover an increased space heating demand compared to the DHW demand. The relatively low temperatures of floor heating systems (e.g. $30 \text{ }^\circ\text{C}$) enable the application of polymeric solar thermal collectors. However, due to the lower efficiency of these collectors in combination with the cold climate of Norway, a relatively large collector array (i.e. 28.2 m^2) in combination with a 2,000l storage tank is necessary to provide a single family home (floor heating area 180 m^2) with heat. To minimise the costs, heat exchangers for separating the solar from the floor heating loop were neglected, demanding pure water as the HTF.

Besides applications in single-family homes, large DBSs are nowadays used for providing process heat. Bokhoven, van Dam and Kratz (2001, pp. 350-351) note that typical, small DBSs for DHW preparation in the Netherlands use a storage volume of 100l in combination with a collector area of 2.75 m^2 . Based on this ratio between collector area and heat storage volume, a large scale DBS with a collector area of $2,400 \text{ m}^2$ consisting of large-area collector

(LAC)s⁷ and a storage volume of 95 m³ was installed for generating industrial heat (cf. table 2.4-a).

Louvet, Botpaev and Vajen (2015) describe a DBS for hay bales drying. This system consists of a 127 m² array of FPCs in combination with a 42 m³ heat storage. Due to the unpressurised setup of the system, cost-effective PP was used as the heat storage material.

DBSs are also used to provide larger buildings with heat. Engeler and Salerno (2006) describe a system with 45 m² collector array for hot water preparation of a combined residential building and a workshop. The authors report total / specific costs of approximately 41,400 € / 920 €/m²⁸.

2.2.2 Advantages and Disadvantages of Drain Back Systems

An extensive list of advantages and disadvantages of DBSs is presented by Botpaev et al. (2015, p. 44). The most important advantages of DBSs with respect to polymeric solar thermal collectors are:

- Unpressurised system architecture: As the typical pressure loads⁹ are not present within a DBS, polymeric materials with a low pressure resistance can be utilised (e.g. for the collectors, pipes, heat exchangers etc.), enabling a cost saving potential. Pressure-related components like membrane expansion vessels and pressure relief valves, which are typically used in conventional solar thermal systems, are unnecessary, yielding further cost savings.
- Inherently fail-safe: If ambient temperature may cause freezing of the HTF, the system controller will switch off the system. As a consequence, the HTF drains back into the drain back storage, preventing the pipes and other components from frost damages. If the collector / storage temperature exceeds a critical value (in case of high solar irradiation in combination with no heat demand), the system controller also shuts off the pump, preventing the HTF from boiling. In case of a defect (e.g. at the pump and / or the controller), the HTF will also drain back into the drain back storage, preventing damage of the system.

The self-draining of a DBS eliminates the need for a so called “gravity brake”, which is a typical component in conventional solar thermal systems. Such a one-way valve / gravity break is necessary to prevent cooling of the heat storage during night time due to a thermosiphonic flow within the solar collector loop (Eicker, 2012, p. 69). Since the collector circuit is emptied during night time, this particular component is unnecessary in case of a DBS, yielding an equivalent cost saving.

⁷ A LAC is significantly larger than a conventional solar thermal FPC (e.g. 10 m² in case of a LAC vs. 2 m² in case of a FPC). The major benefits of LACs over standard FPCs are lower specific installation costs (in terms of €/m²) as well as the lower heat losses due to a better ratio between absorber area and edge surfaces. A potential field of application for LACs are solar-assisted district heating networks.

⁸ Engeler and Salerno (2006) specified total / specific costs of 65,000 CHF / 1,437 CHF/m². 1 € ≐ 1.57 CHF (average exchange rate in 2006) (European Central Bank, 2020).

⁹ Eicker (2012, p. 67) indicates a typical pressure level of 3 bar – 6 bar inside a solar thermal system. This is consistent with information provided by Köhl, Meir and Papillon (2013, p. 36), who specify a working pressure up to 7 bar for forced-circulation systems.

- HTF: In addition to the aforementioned cost saving potentials, further benefits arise from utilising pure water as a HTF. Typically, a water-glycol-mixture is used as a HTF in conventional solar thermal systems to prevent frost damages. By comparison, pure water is cheaper, has a lower environmental hazard potential and better fluid properties (cf. section 1.1).

The most important drawbacks of DBSs are:

- Special requirements regarding system setup: To ensure a safe draining of the system, a careful selection and installation of all relevant components is of major importance for correct system functioning. Bokhoven, van Dam and Kratz (2001, p. 3) report about a typical slope of 10 mm/m for the pipes to ensure a safe draining of the system. Weiss (2003, p. 185) recommended a minimum inclination of 10 mm/m, preferably 15 mm/m – 30 mm/m for the pipes, whereas Perers et al. (2015) observed safe draining also in the case of almost horizontal pipes. Botpaev, Orozaliev and Vajen (2014, p. 2476) experimentally determined that safe draining is also feasible with horizontal pipes. The formation of “water pockets” must be prevented, both within the piping and the collector / absorber. As a consequence, harp-shaped absorbers should be preferred over meander-shaped absorbers.
The pump must be able to overcome the static height difference between the water level inside the drain back storage and the highest point within the system. In order to remove the air inside the system, a pump-speed of 40 l/h – 80 l/h is recommended during the startup of the system (Weiss, 2003, p. 187). The pump may not prevent a backflow.
- Air ingress: The infiltration of the system with oxygen may yield corrosion in case of steel components (Weiss, 2003, p. 186). However, this phenomenon may be of minor importance for polymeric system components. As described in Botpaev et al. (2015, p. 44), the formation of organic matter might prevent the system from functioning properly. Furthermore, Bokhoven, van Dam and Kratz (2001, p. 351) report about clogged pipes after operating a large DBS for approximately 6 months due to the formation of Fe_3O_4 (magnetite), which is assumed to be the result of a reaction of free oxygen with the steel pipes.
- Operation: The increased effort for the installation of a DBS can cause higher costs compared to a conventional solar thermal system. As the pump has to overcome the height difference between the water level inside the drain back storage and the highest point whenever the system re-starts, a higher power demand for the pump might be required, yielding higher operating costs of a DBS. Botpaev et al. (2015, p. 44) also mention a potential undesirable noise level as a result from the HTF flowing back into the drain back volume.

2.2.3 Classification of Drain Back Systems

In contrast to solar thermal collectors, which are classified according to their efficiency, different DBSs can be compared with respect to various factors. According to Kutscher (1985, p. 1), DBSs can be distinguished between open and closed systems. They can further be divided with respect to the location of the heat exchanger. In case of a load-side heat

exchanger, the HTF is directly mixed with the fluid inside the storage tank (e.g. as shown in figure 2.11, left), which is prevented in case of a collector-side heat exchanger (e.g. as shown in figure 2.11, right). Botpaev and Vajen (2014a, p. 85) suggest another classification regarding the position of the volume of the HTF when the DBS is shut down. In this context, figure 2.11 (left) shows a system where the heat storage is also the drain back storage, whereas figure 2.11 (right) represents a system with external drain back reservoir. A detailed overview of different DBSs is provided by Kutscher et al. (1984) and Botpaev et al. (2015).

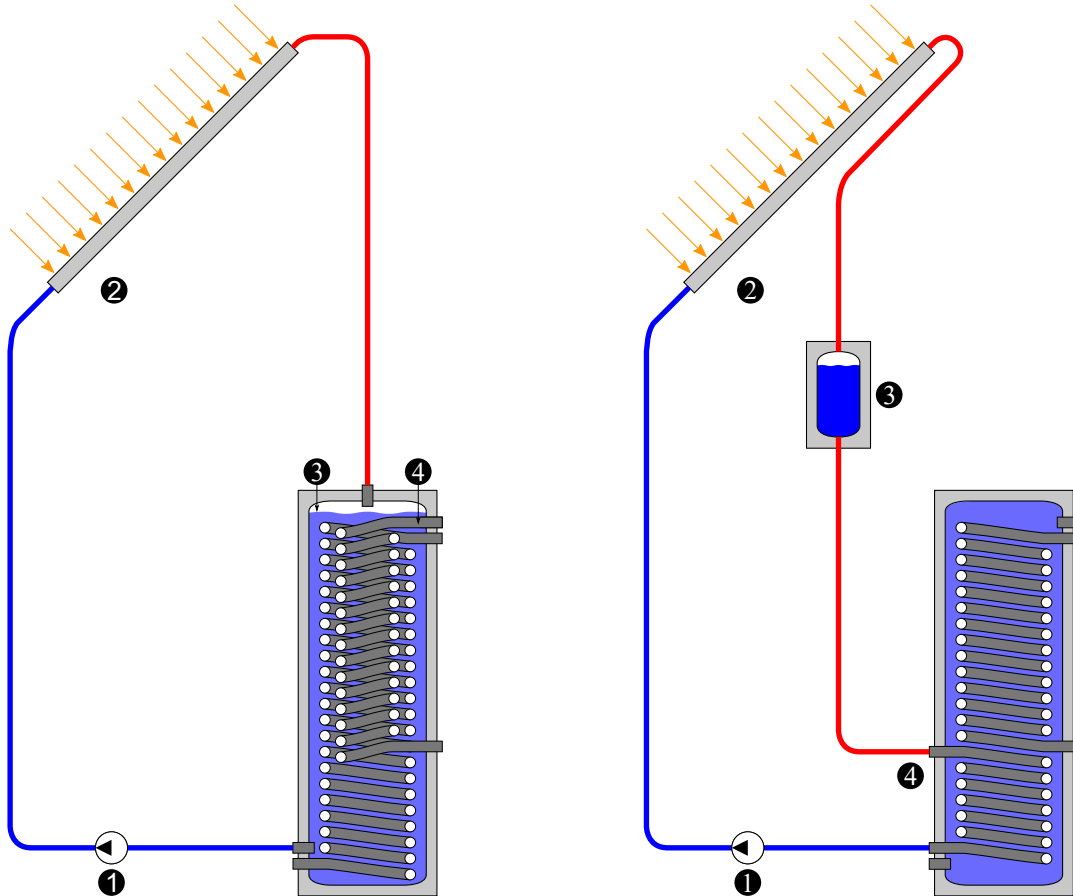


Figure 2.11: Different types of DBSs. Left: Load-side heat exchanger. Right: Collector-side heat exchanger. The pump ① circulates the fluid through the collector ②, before it flows into the drain back reservoir ③, either an internal (left) or external volume (right). In case of a load-side heat exchanger ④ (left), the solar fluid is identical with the fluid inside the heat storage. In case of a collector-side heat exchanger ④ (right), the water inside the heat storage is separated from the solar fluid.

The evaluation of several different DBSs indicates that load-side heat exchangers seem to be more widespread in large systems (e.g. for industrial heat generation), whereas collector-side heat exchangers are more common in smaller systems (e.g. single-family homes) (cf. table 2.4).

2.2.4 Operation of Drain Back Systems

Botpaev et al. (2015, pp. 48-54) divide the operation of DBSs into three different phases: Filling, operating and draining. As the solar controller switches on the pump, the water has to overcome the elevation head. According to the conservation of energy, the elevation head is defined by the difference in height between the highest point within the system and the water level of the drain back reservoir. This energy must be provided by the solar pump (cf. equation 2.5).

$$P_{Pump} = \frac{E_{Pot}}{t} = \dot{m} \cdot g \cdot (h_{Top} - h_{Water}) \quad (2.5)$$

where:

| | |
|-------------|--|
| P_{Pump} | = Power in W |
| E_{Pot} | = Potential energy in J |
| t | = Time in s |
| \dot{m} | = Mass flow rate of the fluid in kg/s |
| g | = Gravitational acceleration, i.e. 9.81 m/s ² |
| h_{Top} | = Position of the highest point within the system in m |
| h_{Water} | = Position of the water level in m |

As shown in figure 2.11, there is a potentially larger difference in height in case of systems which utilise the heat storage as the drain back reservoir (exception: the heat storage is located close to the collector array, e.g. below the rooftop of the house). In order to minimise the power consumption of the solar pump, it is preferable to place the drain back reservoir at the highest possible point inside the frost-protected building envelope. The height difference is of major importance in the selection of the solar pump, as it defines the necessary pressure of the pump. Besides its capability to overcome the height difference during the startup phase, the pump must be sufficiently powerful to remove all air inside the piping. Kutscher (1985, p. 1) describes two different types of operation modes for circulating water within a DBS:

- Trickle flow (cf. figure 2.12, left): In this case, the pump is not able to completely displace the air inside the pipes, as the volume flow rate speed of the pump is too low for establishing a full siphon. As a result, the pump constantly has to overcome the height difference and has therefore a higher power demand compared to a closed loop system.
- Siphon flow (cf. figure 2.12, right): In this case, the pump is able to completely flush the system. According to Kutscher et al. (1984, p. 58), a minimum flow rate of 0.21 m/s is necessary to maintain a siphon flow in a 12.7 mm copper pipe. Perers et al. (2015, p. 301) experimentally determined a velocity between 0.3 m/s and 0.5 m/s to establish a siphon. Other studies also examined necessary velocities for different pipe diameters to establish a siphon flow, described in detail by Botpaev et al. (2015, p. 49).



Figure 2.12: Trickle vs. Siphon flow. Left: Trickle flow. Right: Siphon flow.

Louvet, Botpaev and Vajen (2015) evaluated the electric energy demand for both trickle and siphon flow. In case of the trickle flow, the pump has to continuously overcome the difference in height, therefore, the electric energy demand is 108 % higher compared to a siphon flow. However, the ratio between necessary electric energy for operating the pump and energy gain delivered by the collector array is relatively small (0.8 % in case of a siphon and 1.6 % in case of a trickle flow). This indicates that minimising the electrical energy demand of the solar pump is of minor importance if the heat delivered by the collector array can be maximised. It is worth mentioning that the power demand of the pump (i.e. 280 W) is slightly lower during filling compared to normal operation (285 W) (Louvet, Botpaev and Vajen, 2015). These results are in contradiction with Weiss (2003, pp. 187-188), stating that the power demand of the pump during operation should be lower compared to the filling phase.

After start-up of the system, the behaviour of a DBS can be explained with Bernoulli's equation (cf. equation 2.6). According to Bernoulli's principle (which is a special form of energy conservation), the total energy between two points along a streamline remains constant:

$$H = \frac{v_1^2}{2g} + \frac{p_1}{\rho \cdot g} + z_1 = \frac{v_2^2}{2g} + \frac{p_2}{\rho \cdot g} + z_2 + h_L \quad (2.6)$$

where:

- H = Total energy head in m
- v = Velocity in m/s
- g = Gravitational acceleration, i.e. 9.81 m/s²
- p = Pressure in Pa
- ρ = Density of the fluid in kg/m³
- z = Height in m
- h_L = Head loss in m

Figure 2.13 shows a cut-out from a DBS with external drain back reservoir. Bernoulli's equation applies between the highest point of the system ① and the transition into the drain back reservoir ②. As the drain back reservoir is open to the atmosphere, atmospheric pressure (p_{Atm}) is present inside the volume. Assuming a constant velocity, equation 2.6 simplifies to 2.7. As the height z_1 is greater than z_2 , the pressure at point ① is lower than

the atmospheric pressure at point ②.

$$\begin{aligned} \frac{p_1}{\rho \cdot g} + z_1 &= \frac{p_{Atm}}{\rho \cdot g} + z_2 + h_L \\ p_1 &= p_{Atm} - \rho \cdot g \cdot (z_1 - z_2 + h_L) \end{aligned} \quad (2.7)$$

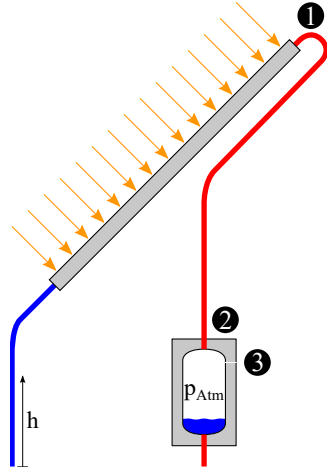


Figure 2.13: Pressure conditions within a DBS. ① = highest point of the system, ② = transition into drain back reservoir, ③ = opening to atmosphere.

As mentioned by Kutscher et al. (1984, pp. 42-43), the resulting vacuum point ② causes the water to boil within the system at temperatures below 100 °C (depending on the ambient atmospheric pressure). The volume expansion inside the system caused by the boiling of the water yields an increase in the system's overall pressure. As a result, the collector efficiency decreases due to the lower mass flow rate. Furthermore, the siphon flow can be disturbed. To solve these problems, the authors suggest to either pressurise the system periodically or to utilise a vacuum breaker¹⁰.

Boiling of the HTF was also observed by Louvet, Botpaev and Vajen (2015) during measurements within a large DBS with a 127 m² collector array. Due to the boiling, the authors noticed a reduction in the volume flow rate of 0.0281/(s K) for temperatures higher than 83 °C.

Botpaev and Vajen (2014b) experimentally investigated the filling and draining process of DBSs. Therefore, two different types of systems were built up in the laboratory. Both systems had a 130 l, unpressurised heat storage made of PP with a transparent front plate, allowing for a view inside the storage tank. The meander-shaped, transparent absorber made of a PVC-tube was placed 6 m above ground. For the first setup, the collector could directly drain back into the heat storage (cf. table 2.4-g), whereas the second setup included an external, 24 l transparent drain back reservoir (cf. table 2.4-h). For the first system, the

¹⁰ A vacuum breaker enables the surrounding air to enter a hydraulic system in case of a pressure below atmosphere. Vacuum breakers can be controlled either passively (e.g. by utilising a spring) or actively (e.g. by externally triggering a solenoid valve) and are typically used to stop a siphon flow within hydraulic systems.

2 Literature Review

difference in height between the water surface and the highest point within the system was 4.7 m. During operation, a total pressure of 60 kPa (i.e. 40 kPa below ambient pressure) was measured at the highest point of the system. In the second system, the maximum difference in height was 2 m. For this setup, a total pressure of 83 kPa (i.e. 17 kPa below ambient pressure) was measured at the highest point (Botpaev and Vajen, 2014b; Botpaev et al., 2015). The results experimentally prove the linear correlation between the level of under-pressure at the highest point of a DBS and the maximum distance between this location and the drain back reservoir (cf. equation 2.7).

As soon as the solar controller switches off the pump, the DBS starts to drain. During draining, the flow direction gets reversed (so called siphon draining), experimentally observed e.g. by Botpaev, Orozaliev and Vajen (2014). The time required to drain the whole system depends on the pipe length and diameters / cross-sections within the system. According to Kutscher et al. (1984, p. 51), pipes with diameters greater than 10 mm can empty themselves, whereas pipes with smaller or equal diameters are not able to drain independently due to the surface tension. Self emptying of a vertical, 1 m pipe with a 14 mm diameter took 12 s, whereas a 3 m pipe with 14 mm drained within 29 s. This indicates a nearly linear relation between pipe length and draining time. On the other hand, a vertical 1 m pipe with a 10 mm diameter did not drain at all (Kutscher et al., 1984, p. 51).

Botpaev, Orozaliev and Vajen (2014) experimentally investigated the draining of DBSs both with an external (24l) and an integrated drain back reservoir (130l). Both systems needed approximately 40 s for draining. However, in case of draining into an external reservoir, due to the lower difference in height (maximum difference in height = 2 m), the velocity of the volume drainage was much lower (5 l/min in case of an external drain back volume compared to 10 l/min in case of directly draining into the heat storage).

The transition between the flow pipe and the drain back vessel (either as separate reservoir or integrated into the heat storage) has been subject of many different patents (Botpaev et al., 2015). In the simplest case, the fluid directly flows into the drain back reservoir, e.g. shown in figure 2.11. Although this approach is easy to implement and enables reliable draining, the resulting noise level due to the splashing water might be unacceptable for a commercially available system. Depending on the fluid level and the velocity, an ingress of air bubbles into the system can be a further consequence of the splashing water (Botpaev and Vajen, 2014b, p. 7). Engeler and Salerno (2006, p. 9) report about such an ingress of air into the system, yielding a noise generation within the solar pump. However, the proper functionality of the system was not affected. In order to minimise the noise generation, the difference in height between the pipe and the free water surface should be reduced. Botpaev, Orozaliev and Vajen (2014, p. 10) report about successfully draining a DBS with a difference in height of only 10 mm. However, if the distance between pipe and water level is too small, the rising water level in the reservoir may block the pipe, preventing further draining of the system (Perers et al., 2015, p. 310). As a consequence, the remaining fluid inside the pipe can be pressed up or sucked into the collector, yielding freeze damages during winter / cold nights. ASHRAE 1990 (p. 43) suggests the drain back reservoir should be filled between 3/4" – 7/8" in case of switched-off systems and 1/8" – 1/2" during regular operation.

More advanced approaches utilise pipes which end below the water level of the drain back reservoir (Botpaev et al., 2015, p. 12). To initialise draining, additional valves (or other

components) are necessary, opening the system to atmosphere in case of a pump shut-off. Although these approaches may be able to overcome problems like noise generation or air ingress, additional components yield further costs and potential of malfunction.

2.2.5 Reliability and Control of Drain Back Systems

Thornton and Shannon (1984) performed a study among 122 solar thermal systems for DHW preparation, including 24 DBSs. Two different categories were defined for problems regarding solar thermal systems. Category 1 problems cause a major defect to the system due to a problem with one of the main system components (controller, pump etc.) or problems that lead to a frost damage. Furthermore, any defect causing replacement costs higher than 50 \$ was also assigned to category 1. Problems of category 2 were defined as minor defects to the system, e.g. due to a leaking fitting or a failure of less important components like air vents or control valves. The evaluation of different solar thermal systems (like closed loop, drain back or drain down) reveals that DBSs had the highest reliability (i.e. least amount of category 2 problems) out of all types of solar thermal systems. The majority of defects can be traced back to installation problems. To overcome these problems, Perers et al. (2015, p. 310) emphasise the importance of installer training.

The evaluation of several scientific publications reveals different strategies to control a DBS. At the *MIT Solar House #1*, a special control algorithm was applied to switch on / off the solar pump: Besides the collector array, an additional, identical (dry) collector was installed on the south-facing roof, hydraulically not connected with the rest of the collector array. Whenever the temperature difference between the dry collector and the storage tank exceeds a threshold of 5 °F, the solar pump was switched on. This setup was chosen to reduce the heat capacity loss of the overall collector array. (Hesselschwerdt, 1954, p. 99)

Louvet, Botpaev and Vajen (2015, p. 8) used a temperature differential controller with two temperature sensors to control the system. If the difference between collector and storage temperature exceeded 12 K, the pump started. If the difference between the two sensors dropped below 3 K, the pump was switched off. The authors mention that finding the correct parameters for a control strategy is difficult: If the switch-on condition / temperature is too low, the collectors may be cooled down by the HTF, yielding unstable fillings of the systems. If the switch-on condition is too high, the risk of (partial) boiling increases.

Gaspar and Michalconok (2016, p. 146) emphasise that a control algorithm for DBSs should be capable of detecting and preventing oscillations of the pump. Such an oscillation can occur if the pump is shut off. As a result, the collector heats up significantly (dry stagnation). If the controller switches on the pump, the fluid might evaporate as it comes in contact with the heated up collector / pipes. The temperature of the hot steam may be detected by a sensor, yielding the next shut-down of the pump. The hot steam occurring during these oscillations can harm the collectors and / or reduce their lifetime. The authors suggest the installation of an irradiation sensor in addition to temperature sensors (located at the flow and return of the collector array, inside the storage tank and on the shadowed side of the collector to detect the ambient temperature) and a flow sensor. Access to meteorological forecast data and the possibility of changing controller parameters during runtime may be a further enhancement.

Rekstad et al. (2000, p. 267) describe a solar controller for a DBS with a polymeric FPC. The authors suggest a combination of an irradiation sensor and a collector temperature sensor to compensate the poor thermal conductivity of the polymeric material.

Perers et al. (2015, p. 310) mention that an adopted control algorithm is necessary for DBSs. During startup, the pump should be operated at a higher velocity to reliably flush out the air inside the system. After establishing a siphon flow, the pump speed may be reduced to decrease the pump's power demand. The controller should further be capable of detecting the ambient temperature to prevent the system from starting at extremely cold temperatures. The authors emphasise the correct mounting of the collector temperature sensor, as its proper function is of major importance for the whole system.

In order to prevent the system's startup at very low temperatures, Engeler and Salerno (2006, p. 10) included an ambient temperature sensor into the control algorithm of the DBS. If the temperature dropped below 15 °C, the system could not start.

2.2.6 Commercially Available Drain Back Systems

A detailed overview of commercially available DBSs is given by Berner (2012). According to Botpaev and Vajen (2014a, p. 87), 86 % of commercially available DBSs are equipped with FPCs. The majority (96 %) of the systems utilise a centrifugal pump.

The major distinction is the position of the drain back reservoir, either an external volume or directly integrated into the storage tank. In case of external drain back reservoirs, manufacturers of DBSs often try to merge the drain back reservoir with other parts (e.g. pump, solar controller, safety valves etc.) into one unit, aiming at cost savings during installation (cf. figure 2.14).



Figure 2.14: Commercially available external drain back reservoirs. Left: PAW GmbH & Co. KG (2017). Centre: STI Solar-Technologie-International GmbH (2017). Right: Vaillant GmbH (2017).

Further cost savings can be realised by installing the drain back reservoir close to the collector array (e.g. in the frost-protected attic of the building). Due to the small difference in height,

the power demand of the pump can be minimised during the start-up of the system. Another advantage is that the necessary slope of the pipes has to be ensured over a shorter distance, yielding lower installation costs. Disadvantages of external drain back reservoirs result from the fact that these systems may suffer from higher heat losses compared to storage-integrated drain back reservoirs.

In case of integrated drain back reservoirs, two approaches are widespread. One option is to integrate an over-sized heat exchanger or an additional volume into the heat storage. As soon as the pump stops, the water drains back into the storage tank and replaces the air inside the heat exchanger. This approach has several advantages: Compared to closed, pressurised systems, the additional effort is limited to the increased material demand of the over-sized heat exchanger. Furthermore, the system can be installed without any additional parts. Depending on the difference in height between the drain back reservoir and the collector array, this type of system may require a high power demand of the pump. Another disadvantage is the limited volume of the drain back reservoir which can limit the size of the collector array.

The second type of integrated drain back reservoirs requires unpressurised heat storages, enabling direct draining into the storage tank (cf. figure 2.11, left). Due to the non-required pressure stability of the heat storage, cost-effective materials can be used (e.g. polymers), yielding lower investment costs. Furthermore, the lower weight of such a heat storage may contribute to lower installation costs. However, the greater difference in height between the heat storage and the collector array yields an increased power demand of the pump during start-up of the system.

2.2.7 Summary

A summary of DBSs described in literature is shown in table 2.4, revealing information about typical collector array areas, inclination and diameters of pipes etc.. The evaluation of the examined literature shows that there has been much progress in understanding fundamental processes of DBSs. In addition, successful implementation and realisation of DBSs were described by several authors. Although the publications provide valuable information (e.g. regarding necessary pipe diameters, typical operating pressures within the system), generally applicable statements regarding the economic performance of these systems compared to conventional, pressurised solar thermal systems are lacking. This includes particularly information regarding investment, installation, maintenance and operating costs.

Table 2.4: Overview of DBSs described in scientific publications. Empty cells indicate that there is no information available. Orientation: 0° = North, 90° = East, 180° = South, 270° = West. Control algorithm: ΔT = Temperature differential based controller, I = Irradiation based controller.

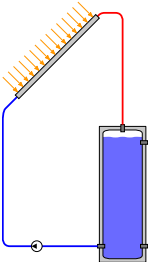
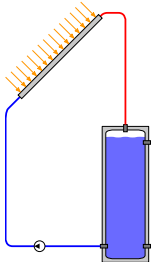
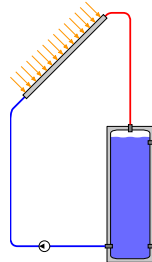
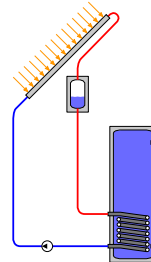
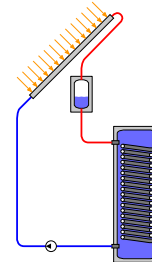
| | (a) | (b) | (c) | (d) | (e) | |
|-------------|--|--|--|---|---|--|
| | Bokhoven, van Dam and Kratz (2001) | Hesseltschwerdt (1954) | Louvet, Botpaev and Vajen (2015) | Gaspar and Michalconok (2016) | Perers et al. (2015) | |
| type of DBS |  |  |  |  |  | |
| Collector | type size tilt angle orientation HTF | LAC 2,400 m ² 180° water | FPC approx. 37.2 m ² 57° 180° water | FPC 127 m ² water | ETC 3.4 m ² 55° water | ETC 6.1 m ² / 12.2 m ² 45° / 27° 195° / 240° water |
| System | purpose storage size DB storage size pipe diameter pipe inclination ΔH control algorithm | industrial heat 95,000 l = heat storage 1° 6 m ΔT | DHW + heat approx. 4,500 l = heat storage 3/8" 6.5 m ΔT | industrial heat 42,000 l = heat storage ΔT | DHW ΔT | DHW + heat 500 l / 750 l 100 l / 150 l 22 mm / 12 mm $\approx 0^\circ$ ΔT |

Table 2.4: Overview of DBSs described in scientific publications. Empty cells indicate that there is no information available. Orientation: 0° = North, 90° = East, 180° = South, 270° = West. Control algorithm: ΔT = Temperature differential based controller, I = Irradiation based controller. **(Continued)**

| | (f) | (g) | (h) | (i) |
|-------------|--|--|--|--|
| | Rekstad et al. (2000) | Botpaev, Orozaliev and Vajen (2014) | Botpaev, Orozaliev and Vajen (2014) | Engeler and Salerno (2006) |
| type of DBS | | | | |
| Collector | type size tilt angle orientation HTF | FPC 28.2 m ² 27° 180° water | FPC, unglazed approx. 1.2 m ² variable water (colored) | FPC 45 m ² 30° 180° water |
| System | purpose storage size DB storage size pipe diameter pipe inclination ΔH control algorithm | DHW + heat 2,000 l = heat storage = heat storage 9 mm / 19 mm 4.7 m ΔT / I | experiment 130 l 24 l 9 mm / 19 mm 2 m | DHW 3x 1,250 l 90 l 22 mm ΔT |

3 Experimental Analysis on Component Level

Scientific publications presented in chapter 2 show a variety of concepts and prototypes of polymeric solar thermal FPCs. In contrast to other manufacturing approaches, which most often assemble polymeric absorbers from semi-finished components (cf. chapter 2), the absorbers described below were produced by utilising the twin-sheet-thermoforming (TST) process. With this manufacturing process, semi-finished products like plates or films are processed by means of pressure and temperature. Potential materials are both amorphous (e.g. PS, ABS, PMMA, PC etc.) as well as semi-crystalline thermoplastics (Hopmann and Michaeli, 2015, pp. 243-244).

3.1 Manufacturing and Testing of Polymeric Absorbers

The TST process enables a highly scalable, automated production of polymeric absorbers. Compared to other manufacturing processes for mass production of polymeric components (e.g. injection moulding, extrusion, blow moulding, single-sheet-thermoforming), the major advantages of TST are the low unit costs and both the tool and machine reliability (Ehrenwirth et al., 2016c, p. 27). The necessary steps for producing a polymeric absorber using the TST are described in figure 3.1. To enable the process, a tool with an upper and a lower mould half is necessary. At the initial position, the upper and lower parts of the tool are open (cf. figure 3.1-a). In the first step, two sheets are clamped to a mount, covering both the upper and lower half of the tool (cf. figure 3.1-b). Afterwards, two radiators heat up both polymeric sheets (cf. figure 3.1-c), yielding a change of their mechanical properties. As soon as the sheets reach the necessary processing temperature, the radiators are removed from the TST machine to not impede the moulding halves (cf. figure 3.1-d). In the next step, a vacuum is applied both in the upper and lower half of the tool (cf. figure 3.1-e, blue marked zones), yielding the heated sheets to be aspirated into the mould halves (cf. figure 3.1-f). While the plates are still hot, the two halves close and seal together the upper and lower sheet (cf. figure 3.1-g). After opening both halves and cooling down the final part (cf. figure 3.1-h), surplus material is removed from the absorber (cf. figure 3.1-i). By assembling a backside insulation and a frontside cover to the absorber, the solar thermal FPC is completed (cf. figure 3.1-j). Photographs of the TST process are shown in the appendix (cf. figure A.1).

In order to obtain a high thermal efficiency as well as a minimum pressure drop, a uniform flow distribution inside the polymeric absorbers is of major importance. To evaluate the flow distribution, one polymeric absorber was heated to constant temperature of approximately 70 °C. Subsequently, cold water was suddenly fed into the absorber. The resulting cooling sequence was recorded by means of a thermography camera. The results of the thermography measurements (cf. figure 3.2) show a uniform flow through the absorber.

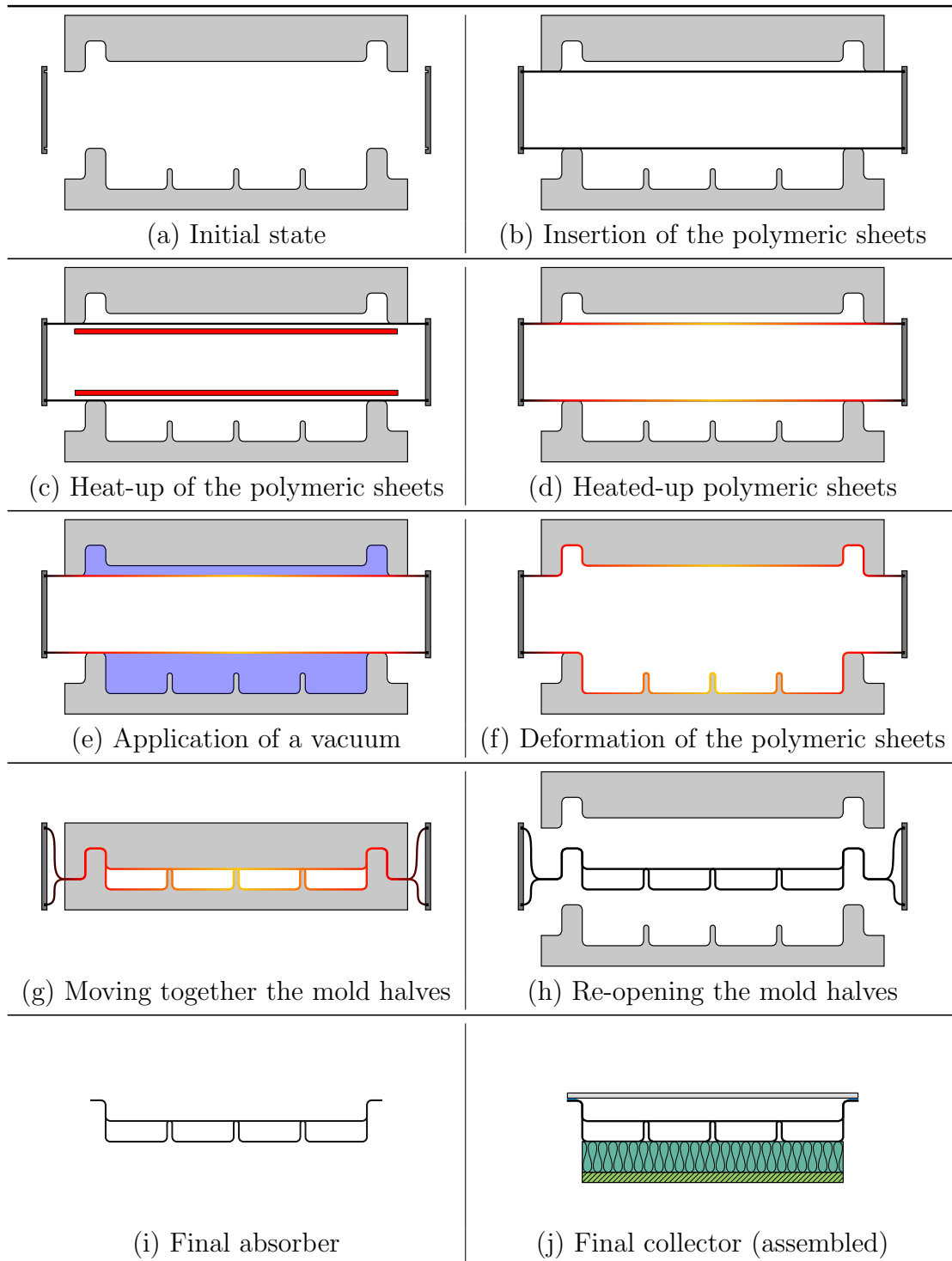


Figure 3.1: Necessary steps during manufacturing of a polymeric solar thermal FPC with the TST process according to Ehrenwirth et al. (2016c, p. 25).

The HTF is divided equally at the transition between the lower header and the riser channels. The cold water enters the absorber on the lower right part connector (cf. figure 3.2-a). At that time, the temperature in the centre of the collector is 58.9°C . 77s later (cf. figure 3.2-b), the lower part of the absorber already cooled down compared to the upper part, the

3 Experimental Analysis on Component Level

temperature in the centre reports a value 51.5 °C. Another 74 s later, the temperature in the centre of the absorber is 46.4 °C (cf. figure 3.2-c). In the end of the measurement (cf. figure 3.2-d), the temperature is uniformly distributed across the absorber at a temperature of approximately 43.1 °C.

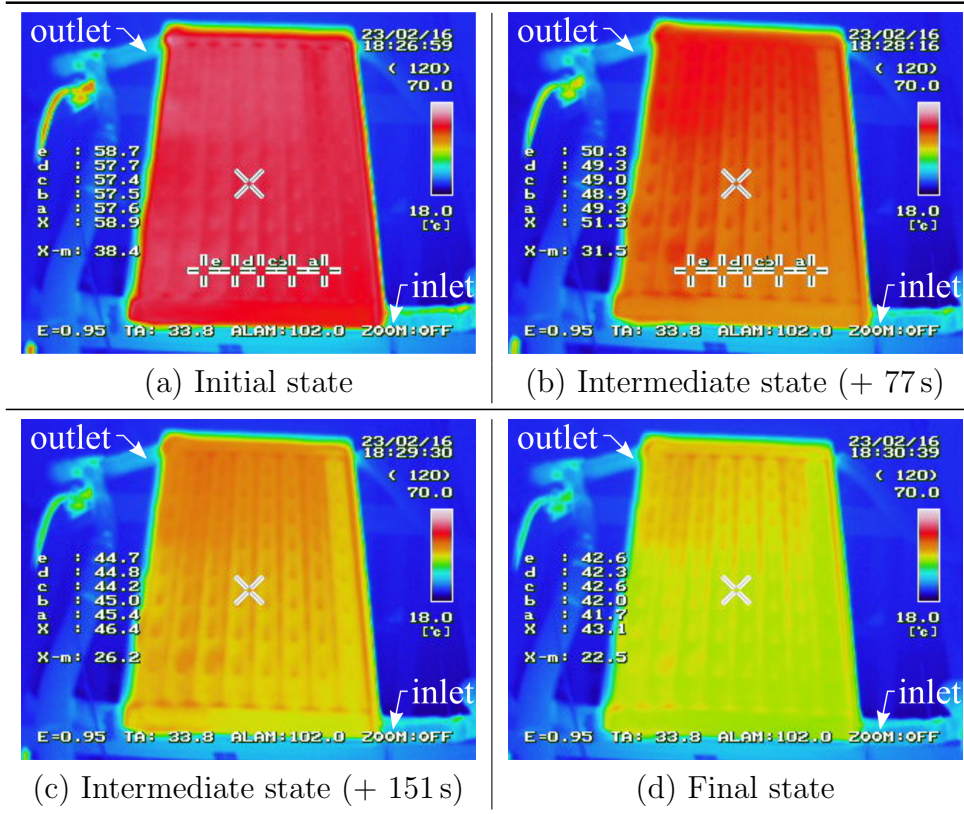


Figure 3.2: Visualisation of the flow distribution inside a polymeric absorber at four different time steps by means of a thermography camera.

In addition to the flow distribution, the pressure drop of the absorber was experimentally evaluated. Therefore, the pressure was measured by means of a differential pressure sensor connected to both the inlet and outlet of the absorber (cf. figure 3.3-a). The volume flow rate was varied in increments of 50 l/h up to 400 l/h. The pressure drop was evaluated for different inlet temperatures (20.2 °C, 28.4 °C, 40.2 °C and 59.9 °C). Following the experiment, a mathematical model of the absorber was developed with MATLAB / Simscape, accounting for the different components of the absorber (e.g. nozzles, diffusers, pipe segments). Every component is represented by a local hydraulic resistance (cf. figure 3.3-b), taking into account the local flow phenomena and the pressure loss coefficients (ζ -values), which are described in scientific literature (e.g. Idel'cik, 1996). The mathematical model accounts for transitional effects from laminar to turbulent flow as well as temperature dependent material properties of the fluid (density, viscosity). The parameters of the tested absorber are shown in table 3.1, the results of both the experimental and simulated pressure drop determination are shown in figure 3.4.

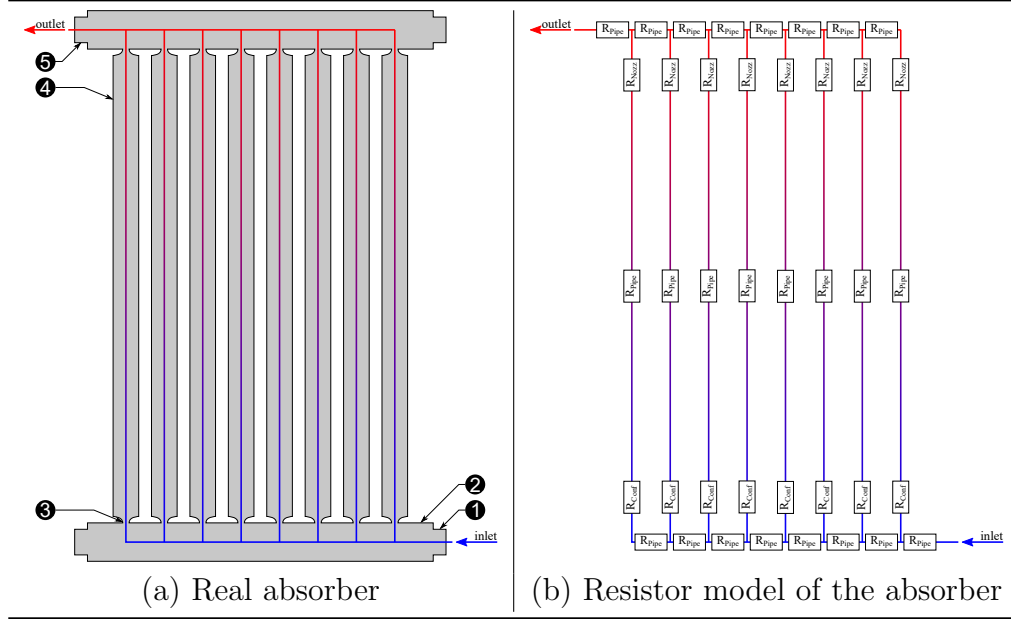


Figure 3.3: Schematic model for the theoretical determination of the pressure drop. ① = inlet , ② = header, ③ = transition to riser channel, ④ = riser channel, ⑤ = outlet.

The pressure loss relates inversely proportional to the inlet temperature (cf. figure 3.4). This can be attributed to the decreasing viscosity of the HTF (in this case water) with increasing temperature (Verein Deutscher Ingenieure, 2010, p. 154).

Table 3.1: Characterisation of the tested polymeric absorber. The indicated cross-sectional areas can be found in figure 3.3.

| Sensor accuracy | | |
|-----------------|---|------------------------|
| General | overall width | 560 mm |
| | overall length | 1,050 mm |
| | surface roughness k | 2.5×10^{-5} m |
| Header | number of header channels n_{header} | 2 |
| | length of header channel l_{header} | 0.45 m |
| | cross-sectional area inlet and outlet $A_{in-/outlet}$ ① / ⑤ | 254 mm^2 |
| | cross-sectional area header channel A_{header} ② | 688 mm^2 |
| Riser | number of riser channels n_{riser} | 8 |
| | length of riser channel l_{riser} | 0.92 m |
| | cross-sectional area transition to header $A_{transition,header}$ ③ | 9 mm^2 |
| | cross-sectional area riser channel A_{riser} ④ | 180 mm^2 |

According to figure 3.4, the simulated pressure loss is higher than the measured one for low flow rates. With increasing flow rate, the difference between measurement and simulation becomes smaller. Furthermore, the results indicate a higher deviation between simulated and measured values in case of higher fluid temperatures. The recorded data show that the

3 Experimental Analysis on Component Level

differential pressure sensor used in the experimental setup displays values close to 0 Pa for volume flow rates smaller than 100 l/h. Therefore, the difference between measurement and simulation is attributed to a potential inaccuracy of the sensor.

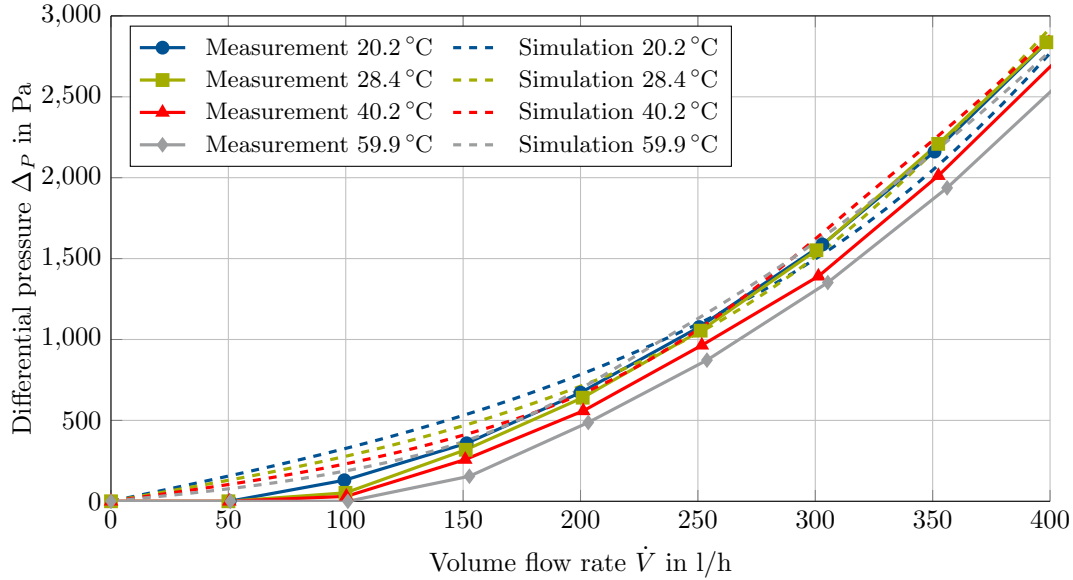


Figure 3.4: Experimental determination of the pressure drop of a polymeric absorber.

According to Eicker (2012, p. 70), pressure losses for conventional collector arrays smaller than 10 m² typically are lower than 2,000 Pa, yielding a specific pressure loss of 200 Pa/m². Assuming a typical flow rate of 40 l/(h m²) (Quaschnig, 2015, p. 106) and a gross area of the investigated absorber of 0.59 m² (cf. table 3.2), a specific pressure loss lower than 100 Pa/m² can be determined by simulation. The pressure loss of a real 10 m² collector array strongly depends on the hydraulic setup (either serial or parallel) and the final dimensions of one individual collector. Nonetheless, a cost saving potential can be concluded from these results, as the lower pressure loss of the collector array allows for the selection of a smaller pump (assuming that the pump is able to overcome the initial height difference during the filling phase, cf. section 2.2.4). As a consequence, both investment and operating costs can be reduced.

3.2 Setup of Polymeric Collector Prototypes

Based on the polymeric absorbers described above, different prototypes of polymeric collectors were set up (cf. table 3.2). Typically, market available solar thermal FPC have gross areas ranging between 2.0 m² and 2.4 m² (Wesselak et al., 2013, p. 313). Scientific literature shows typical dimensions of polymeric solar FPC of 0.3 m² – 2.0 m² (cf. table 2.3). Due to the high tool cost related to the TST process, two batches of small-scale absorbers were produced. The first batch of absorbers was manufactured in 2016. A PP absorber (gross area = 0.59 m²) with eight volumetric riser channels was the basis for six different prototypes. Type and thickness of the backside insulation, the glazing material and the air gap thickness were

changed to determine their influence on the efficiency curve. For the backside insulation, two different setups were defined: On the one hand, a 70 mm thick insulation made of EPS was used to minimise the backside losses (cf. table 3.2-a and figure 3.5-a/b). On the other hand, a 30 mm thick glass wool layer in combination with a 10 mm wooden plate was used (cf. table 3.2-c and figure 3.5-c). The wooden plate is not intended to minimise the heat losses but to mechanically stabilise the collector. To investigate the influence of the air gap thickness (the distance between the absorber and the glazing), an additional, 28 mm thick wooden frame was placed between the polymeric absorber and the glazing (cf. figure 3.5-b and figure 3.5-b).

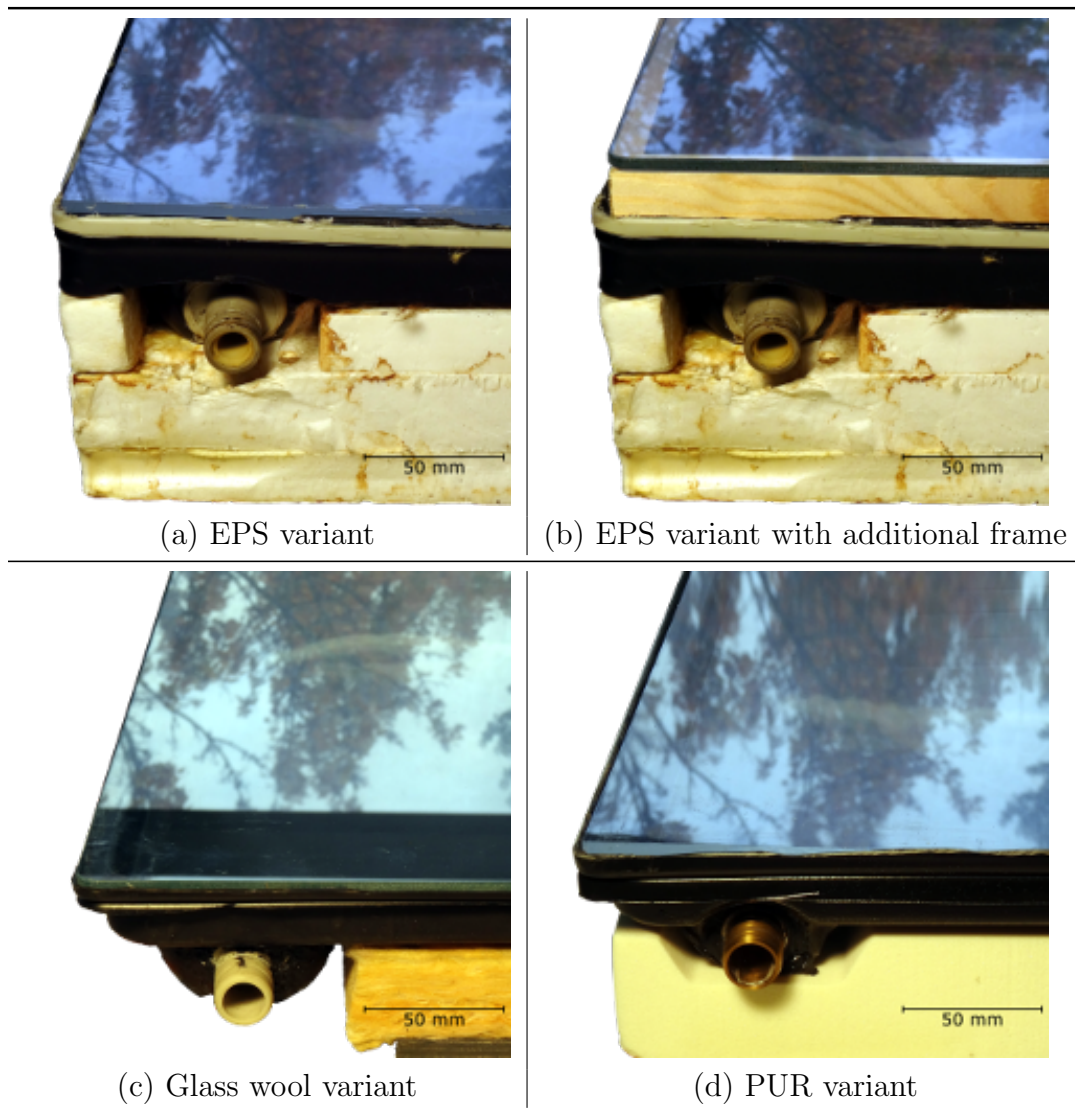
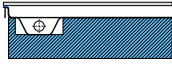
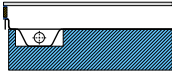
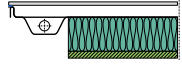
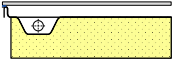


Figure 3.5: Photographs of the collector prototypes.

Table 3.2: Overview of tested polymeric collectors. Material properties of PP according to Dominghaus et al. (2012, pp. 226, 228). Material properties of ABS according to Bonten (2014, p. 199) and Dominghaus et al. (2012, pp. 374-375). Material properties of EPS, glass wool and PUR according to Spitzner et al. (2007, pp. 9-10, 23). Thermal properties of PMMA according to Dominghaus et al. (2012, pp. 485-486), thermal properties of glass according to Verein Deutscher Ingenieure (2010, p. 611). Transmission properties of PMMA and glass were experimentally determined by means of a spectroscopy measurement, cf. appendix (chapter C).

| | (a) EPS variant | (b) EPS variant with additional frame | (c) glass wool variant | (d) PUR variant | |
|------------|--|--|--|--|--|
| |  |  |  |  | |
| Absorber | overall width overall length overall height number of riser channels riser width thickness (plate) thickness (fluid) material operating temperature heat conductivity specific heat capacity | 560 mm 1,050 mm 41 mm 8 58 mm 3 mm 3 mm PP ~ 100 °C 0.22 W/(m K) 1.7 kJ/(kg K) | 560 mm 1,050 mm 41 mm 8 58 mm 3 mm 3 mm PP ~ 100 °C 0.22 W/(m K) 1.7 kJ/(kg K) | 560 mm 1,050 mm 41 mm 8 58 mm 3 mm 3 mm PP ~ 100 °C 0.22 W/(m K) 1.7 kJ/(kg K) | |
| Insulation | thickness material heat conductivity specific heat capacity | 70 mm EPS 0.035 W/(m K) – 0.040 W/(m K) 1.5 kJ/(kg K) | 70 mm EPS 0.035 W/(m K) – 0.040 W/(m K) 1.5 kJ/(kg K) | 30 mm + 10 mm glass wool + wooden plate 0.035 W/(m K) – 0.045 W/(m K) 0.84 kJ/(kg K) – 1.00 kJ/(kg K) | 50 mm PUR 0.024 W/(m K) – 0.030 W/(m K) 1.40 kJ/(kg K) – 1.50 kJ/(kg K) |
| Cover | thickness material transmission heat conductivity specific heat capacity | 4 mm glass / PMMA 89.7% / 91.7% 1.00 W/(m K) / 0.19 W/(m K) 0.75 kJ/(kg K) / 1.5 kJ/(kg K) | 4 mm glass / PMMA 89.7% / 91.7% 1.00 W/(m K) / 0.19 W/(m K) 0.75 kJ/(kg K) / 1.5 kJ/(kg K) | 4 mm glass / PMMA 89.7% / 91.7% 1.00 W/(m K) / 0.19 W/(m K) 0.75 kJ/(kg K) / 1.5 kJ/(kg K) | 4 mm glass 89.7% 1.00 W/(m K) 0.75 kJ/(kg K) |
| Misc. | air gap thickness year of manufacture | 20 mm 2016 | 48 mm 2016 | 20 mm 2016 | |

A second batch of absorbers was manufactured in 2017. Compared to the absorber described above, this second generation of polymeric absorbers has a gross area of 1.32 m² and eleven riser channels (cf. table 3.2-d and figure 3.5-d). The absorbers made of ABS were equipped with a 50 mm thick PUR insulation and a 4 mm thick glass cover. Reviewing the properties of the different prototypes such as absorber, insulation and glazing with information available from scientific literature (cf. table 3.2) reveals a comparable setup of the prototypes tested, ensuring comparability of the results.

3.3 Description of the Test Rig for Determining the Collector Efficiency

To quantify the efficiency of different collector prototypes, an indoor solar simulator according to the standard EN ISO 9806:2013 was used. The purpose of such a solar simulator is to determine the difference between inlet and outlet temperature at a fixed irradiation to the solar thermal collector. The resulting instantaneous efficiency can be determined according to equation 3.1. A photograph of the solar simulator can be found in the appendix (cf. figure A.7). 228 lamps provide a uniform level of irradiation ranging between 600 W/m² and 1,100 W/m² with a light spectrum comparable to the sunlight. A solar thermal FPC (maximum possible dimensions 1.4 m (width) × 2.3 m (height), not shown in the photograph) is placed below the lamp field at an angle of inclination of 45°. Fans above the lamp field provide an airflow to prevent the lamps from overheating. During operation, the test rig demands an electric power of approximately 30 kW.

$$\eta = \frac{\dot{V} \cdot \rho \cdot c_p \cdot (T_{out} - T_{in})}{A \cdot I} \quad (3.1)$$

where:

| | |
|-----------|---|
| η | = Instantaneous efficiency of the collector |
| \dot{V} | = Volume flow rate in m ³ /s |
| ρ | = Density of the HTF in kg/m ³ |
| c_p | = Specific heat capacity in J/(kg K) |
| T_{out} | = Collector outlet temperature in K |
| T_{in} | = Collector inlet temperature in K |
| A | = Collector gross area in m ² |
| I | = Irradiation in W/m ² |

The standard EN ISO 9806:2013 (pp. 52-53, 58-69) specifies both the setup (cf. figures A.7 and 3.6) of such a solar simulator as well as the testing procedure. The efficiency of each collector has to be determined at four different inlet temperatures, evenly distributed over the operating temperature range of the collector.

3 Experimental Analysis on Component Level

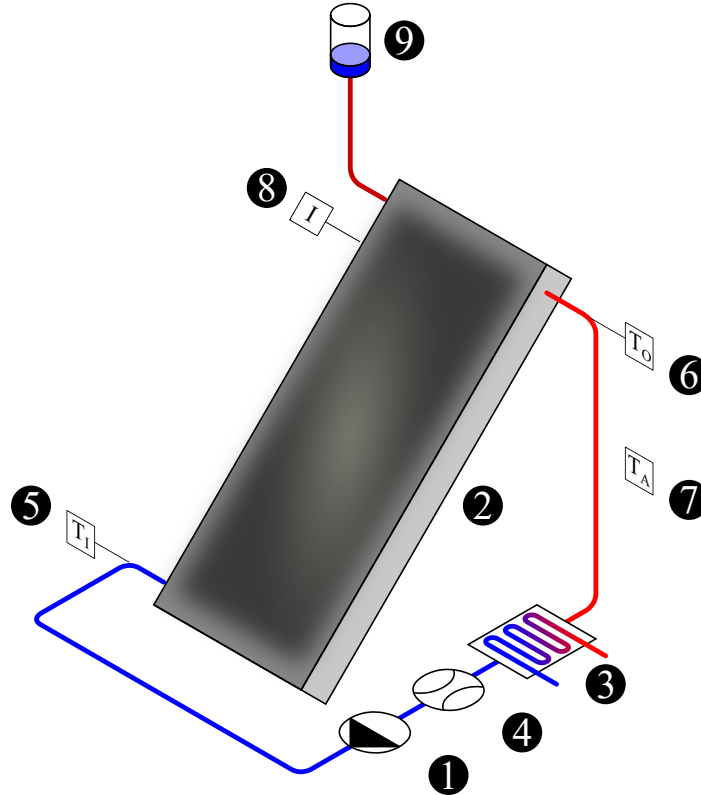


Figure 3.6: Schematic layout of the solar simulator. ① = pump, ② = collector prototype, ③ = heat exchanger, ④ = volume flow meter, ⑤ = collector inlet temperature sensor, ⑥ = collector outlet temperature sensor, ⑦ = ambient temperature sensor, ⑧ = pyranometer, ⑨ = external reservoir.

In case of an indoor test, at least two measurements have to be performed at each inlet temperature, yielding a minimum of eight data points. Table 3.3 shows the requirements of the testing standard with respect to the physical quantities.

Table 3.3: Testing conditions for liquid FPCs according to EN ISO 9806:2013 (pp. 59-60, 65). The last column indicates the accuracy of each sensor to be achieved.

| Physical quantity | Measurement value | Fluctuation range | Sensor accuracy |
|------------------------------|---------------------------------------|------------------------------|-----------------|
| Mass flow of HTF | $\sim 0.02 \text{ kg}/(\text{s m}^2)$ | +/- 1 % | +/- 0.5 % |
| Collector inlet temperature | | +/- 0.1 K | +/- 0.1 % |
| Collector outlet temperature | | +/- 0.5 K | +/- 0.1 % |
| Ambient temperature | | +/- 1.5 K | +/- 0.5 % |
| Collector surface area | | +/- 0.3 % | +/- 0.3 % |
| Global irradiation | $> 700 \text{ W}/\text{m}^2$ | +/- 50 W/m^2 | +/- 2.0 % |
| Wind speed | 3 m/s | +/- 1 m/s | |

To quantify the collector's efficiency, the mass flow rate is evaluated with an electromagnetic flow meter ④. Both the collector inlet and outlet temperatures ⑤ / ⑥ as well as the ambient temperature ⑦ are measured with appropriate sensors. A pyranometer ⑧ detects

the incident irradiation on the collector. In deviation from the testing standard, an external reservoir ⑨ is integrated into the test rig. This reservoir ensures that there is no overpressure that can damage the polymeric collector. As the reservoir is open to the atmosphere, the static height defines the maximum internal pressure inside the system.

The determination of each data point is associated with a certain measurement error, which is caused by the uncertainty of the sensors. The incident irradiation is measured with a pyranometer fulfilling the *secondary standard* classification according to ISO 9060:1990. The uncertainty of such pyranometers is affected by the calibration accuracy, the ambient temperature, the spectral sensitivity of the sensor, the orientation of the sensor and further effects. In case of high quality pyranometers, the World Meteorological Organization (2012, p. I.7-12) specifies the achievable uncertainty (within a 95 % confidence level) for a daily measurement to 2 % (cf. table 3.3). This figure is in accordance with values published by Myers et al. (2002, p. 50) (2.5 % – 3 %), Reda (2011, p. 15) (4.1 %) and Myers (2013, p. 34) (3 % – 5 %). PT100 resistance thermometers are used for measuring the ambient, inlet and outlet temperatures. The error of such a temperature sensor is composed of a temperature-independent and a temperature-dependent part. Depending on the achievable uncertainty of the sensor, the standard DIN EN 60751:2009 (p. 13) specifies different accuracy classes. For determining the ambient temperature, a 1/3 *class B* sensor is used. For a theoretical maximum ambient temperature of 35 °C, the measurement error is smaller than 0.5 % (cf. table 3.3). In case of the inlet and outlet temperature sensors, two 1/10 *class B* sensors are used. Assuming a theoretical maximum inlet and outlet temperature of 80 °C, the uncertainties are less than 0.1 % (cf. table 3.3). As both sensors are used for determining the difference between collector inlet and outlet, the uncertainty has to be determined for the temperature difference. A maximum difference of 8 K between inlet (19.17 °C) and outlet (27.17 °C) was measured for the PP collector with EPS insulation and glass-glazing (cf. table B.1).

$$\Delta\eta = \left| \frac{\partial\eta}{\partial\dot{V}} \right| \Delta\dot{V} + \left| \frac{\partial\eta}{\partial\rho} \right| \Delta\rho + \left| \frac{\partial\eta}{\partial c_p} \right| \Delta c_p + \left| \frac{\partial\eta}{\partial(T_{out} - T_{in})} \right| \Delta(T_{out} - T_{in}) + \left| \frac{\partial\eta}{\partial A} \right| \Delta A + \left| \frac{\partial\eta}{\partial I} \right| \Delta I \quad (3.2)$$

where:

| | |
|----------------------------|--|
| $\Delta\eta$ | = Uncertainty of the instantaneous efficiency of the collector |
| $\Delta\dot{V}$ | = Uncertainty of the volume flow rate |
| $\Delta\rho$ | = Uncertainty of the density of the HTF |
| Δc_p | = Uncertainty of the specific heat capacity |
| $\Delta(T_{out} - T_{in})$ | = Uncertainty of the temperature difference between collector outlet and inlet |
| ΔA | = Uncertainty of the collector gross area |
| ΔI | = Uncertainty of the irradiation |

In this case, the uncertainty equals 0.6 %. A minimum temperature difference of 1.81 K between inlet (69.61 °C) and outlet (71.42 °C) was measured for the PP collector with glasswool-insulation and glass-glazing (cf. table B.5). In this case, the uncertainty equals 7.8 %. Similar to the temperature sensors, the error of the volume flow rate can be divided into a flow rate-independent and a flow rate-dependent fraction. The standard EN ISO 9806:2013 (p. 60)

3 Experimental Analysis on Component Level

specifies the specific mass flow rate as $0.02 \text{ kg}/(\text{s m}^2)$ (cf. table 3.3). In combination with the minimal surface area of the tested prototypes ($1.05 \text{ m} \times 0.56 \text{ m} = 0.59 \text{ m}^2$, cf. table 3.2), the diameter of the flow sensor (4 mm) and the density of the HTF, a minimal velocity of 0.94 m/s is present inside the sensor, yielding an error of 0.5% (Krohne Messtechnik GmbH, 2004, p. 10). The prototype's dimensions were measured with a ruler whose uncertainty is $\pm 1 \text{ mm}$. As a result, the relative error increases in case of smaller surface areas. In case of the aforementioned collector dimensions ($1.050 \text{ m} \times 560 \text{ mm}$), the resulting uncertainty is 0.3% (cf. table 3.3). The temperature-dependent material properties ρ and c_p were determined experimentally. Instead, regression polynomials provided by EN ISO 9806:2013 (pp. 120-122) have been used. The uncertainties of these polynomials are smaller than 0.02% in case of the density ρ and smaller than 0.04% in case of the specific heat capacity c_p . The total uncertainty of the instantaneous efficiency (cf. equation 3.1) can be determined according to equation 3.2.

Depending on the temperature difference between collector inlet and outlet, the uncertainty of the instantaneous η ranges between 3.5% and 10.7% . It must be emphasised that this total error summarises all individual errors under worst case conditions. Therefore, the overall uncertainty is lower for a particular efficiency curve. These levels of uncertainty are in accordance with information published by Sillmann and Rockendorf (2001, p. 261), who determined a typical deviation of $\pm 1.8 \%$ for the η_0 -value and $\pm 5.0 \%$ for the linear heat loss coefficient a_1 in case of a selective FPC. Mathioulakis, Voropoulos and Belessiotis (1999, p. 347) report an uncertainty up to 5% in case of efficiency measurements according to EN ISO 9806:2013, indicating a similar order of deviation.

3.4 Test Results and Discussion

The results of the collector efficiency determination are shown in figure 3.7. The parameters of the efficiency curves are shown in table 3.4, the underlying measurement data can be found in the appendix (cf. tables B.1 to B.7). According to EN ISO 9806:2013 (p. 65), the specific mass flow rate of the HTF (approx. $0.02 \text{ kg}/(\text{s m}^2)$) must not deviate more than $\pm 1 \%$ (cf. table 3.3). This requirement could not be met for all measurements, as the relatively small gross collector area yields a low absolute tolerable deviation. However, the mass flow rate deviates from the mean value with $+2.2 \%$ / -2.4% (cf. table B.1 to B.7).

The comparison of the collectors with glass and PMMA cover shows that prototypes with the latter option achieve higher efficiencies than collectors with glass covers (cf. figure 3.7). On the one hand, this can be explained with the lower thermal conductivity of PMMA ($\lambda_{PMMA} = 0.19 \text{ W}/(\text{K m})$, Dominghaus et al., 2012, p. 485) compared to glass ($\lambda_{Glass} = 1.00 \text{ W}/(\text{K m})$, Verein Deutscher Ingenieure, 2010, p. 611). On the other hand, the higher transmission (and therefore lower absorption) of PMMA compared to glass positively contributes to the higher efficiency of the collectors with PMMA covers ($\tau_{PMMA} = 91.7 \%$, $\tau_{Glass} = 89.7 \%$, cf. table 3.2). The evaluation of the prototypes with the additional frame indicates a slightly higher efficiency compared to the versions without a smaller air gap (cf. figure 3.7). This can be explained with the higher insulation effect of the air gap. However, the air gap thickness cannot be infinitely increased, as the thermal losses of the additional frame counterbalance the benefit of the air gap.

Comparing the type of backside insulation (glasswool vs. EPS) reveals higher efficiencies of the prototypes with EPS / ABS insulation (cf. figure 3.7). One reason is the increased thickness of the EPS insulation compared to the glasswool insulation ($t_{EPS} = 70$ mm, $t_{glasswool} = 30$ mm + 10 mm wooden plate).

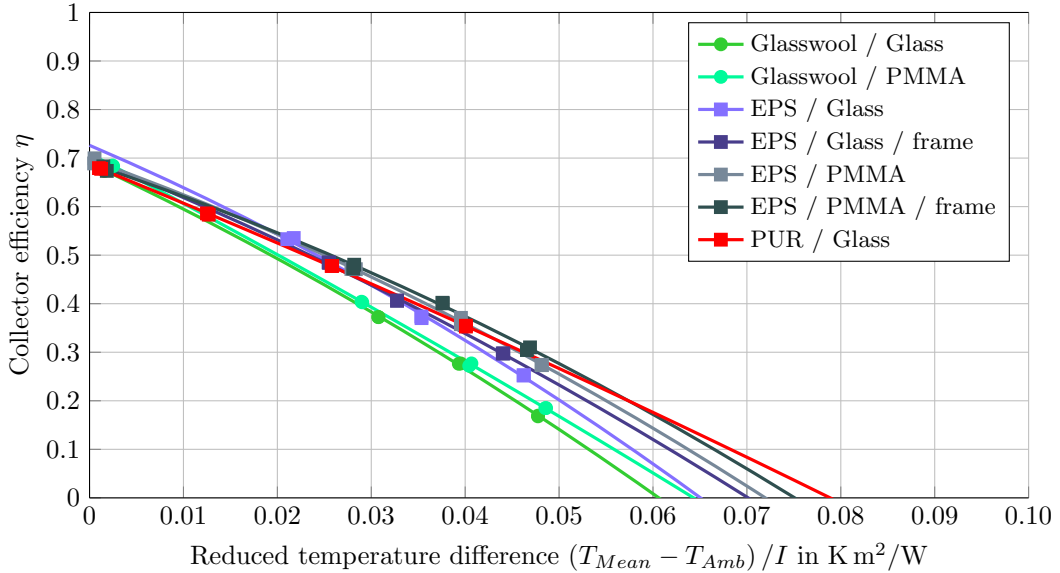


Figure 3.7: Efficiency curves of tested polymeric collector prototypes. The data points indicate the measured values, the polynomials represent the resulting collector efficiency curves.

Table 3.4: Comparison of the efficiency of the developed polymeric collector prototypes with market available collectors. The efficiency is evaluated at an irradiation of $1,000 \text{ W/m}^2$.

| | Collector | η_0 | a_1 | a_2 | η at $0.05 \text{ K m}^2/\text{W}$ | rank |
|------------|---------------------|----------|--------|--------|---|------------------|
| Prototypes | EPS / Glass | 0.7263 | 7.1796 | 0.0387 | 27.1 % | 6 th |
| | EPS / Glass / frame | 0.6995 | 7.0347 | 0.0285 | 27.7 % | 5 th |
| | EPS / PMMA | 0.6976 | 6.0963 | 0.0338 | 30.8 % | 3 rd |
| | EPS / PMMA / frame | 0.6886 | 5.6472 | 0.0329 | 32.4 % | 2 nd |
| | Glasswool / Glass | 0.6896 | 8.0417 | 0.0335 | 20.4 % | 10 th |
| | Glasswool / PMMA | 0.7092 | 8.9720 | 0.0124 | 23.0 % | 9 th |
| | PUR / Glass | 0.6870 | 6.7227 | 0.0089 | 32.9 % | 1 st |
| Ref. | One World One Sun | 0.6660 | 6.3700 | 0.0340 | 26.3 % | 7 th |
| | Magen eco energy | 0.5307 | 3.4447 | 0.0422 | 25.3 % | 8 th |
| | Aventa Solar | 0.5483 | 4.5618 | 0.0121 | 29.0 % | 4 th |

Furthermore, the shape of the insulation is of major importance for the correct function. While the glasswool insulation does not cover the riser channels at all, the EPS insulation minimises the heat losses from the riser channels to the ambient (cf. figure 3.5 and table 3.2). In case of the specially shaped PUR insulation, the highest efficiency of all prototypes

3 Experimental Analysis on Component Level

could be observed, although the thickness is thinner than the EPS insulation ($t_{PUR} = 50$ mm, $t_{EPS} = 70$ mm).

In order to compare the measurement results with data of market available FPC, the efficiency was evaluated at $0.05 \text{ K m}^2/\text{W}$ (cf. table 3.4), a representative operating point for DHW applications (cf. figure 2.2).

Evaluating the solar thermal efficiency of both the tested prototypes and market available polymeric collectors at a reduced temperature of $0.05 \text{ K m}^2/\text{W}$ (cf. table 3.4) indicates a mean efficiency of 27.5%. All collectors deviate within an absolute range of +5.4 p.p. / -7.1 p.p.¹¹ (relative deviation: +17.9% / -25.8%). The results indicate that the chosen insulation and glazing are of major importance, yielding the solar thermal efficiency either significantly higher or lower compared with the efficiency of market available polymeric FPCs.

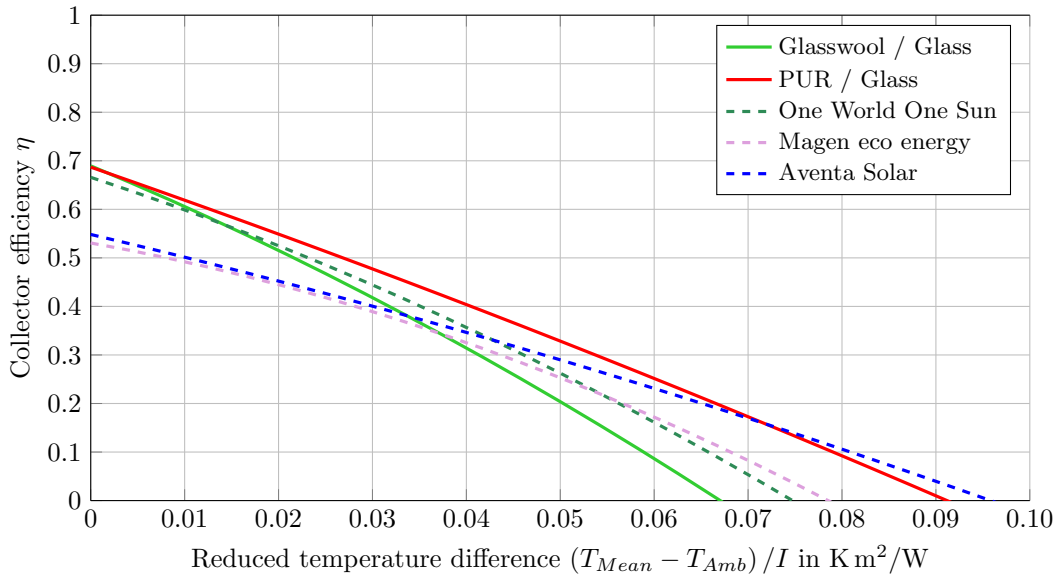


Figure 3.8: Efficiency curves of tested polymeric collector prototypes with the lowest and highest efficiency in comparison to market available FPCs. The efficiency is evaluated at an irradiation of $1,000 \text{ W}/\text{m}^2$.

The efficiency curves of the prototype with the lowest (PP absorber with glasswool insulation and glass cover, 10th rank) and the highest efficiency (ABS absorber with PUR insulation and glass cover, 1st rank) are shown together with the efficiency curves of market available FPCs in figure 3.8. The results indicate that the prototype with PUR insulation and glass cover yield a higher solar thermal efficiency compared to market available collectors for reduced temperatures $(T_{Mean} - T_{Amb}) / I < 0.07 \text{ K m}^2/\text{W}$.

The prototypes with the lowest and highest efficiency are compared to efficiency data available from scientific literature (cf. figure 3.9). The efficiency curve of the PUR / glass variant is most comparable with the results reported by Kim et al. (2016) and Martinopoulos et al.

¹¹ The abbreviation “p.p.” stands for “percentage points” and indicates the absolute difference between two percentage values. Example: The absolute difference between 50% and 55% equals 5 p.p., whereas the relative percentage variance is 10%.

(2010). According to the advices given by Missirlis et al. (2014, p. 719), the efficiency of the prototypes can be improved by means of an adjusted arrangement of the inlet and outlet pipe into / out of the manifolds.

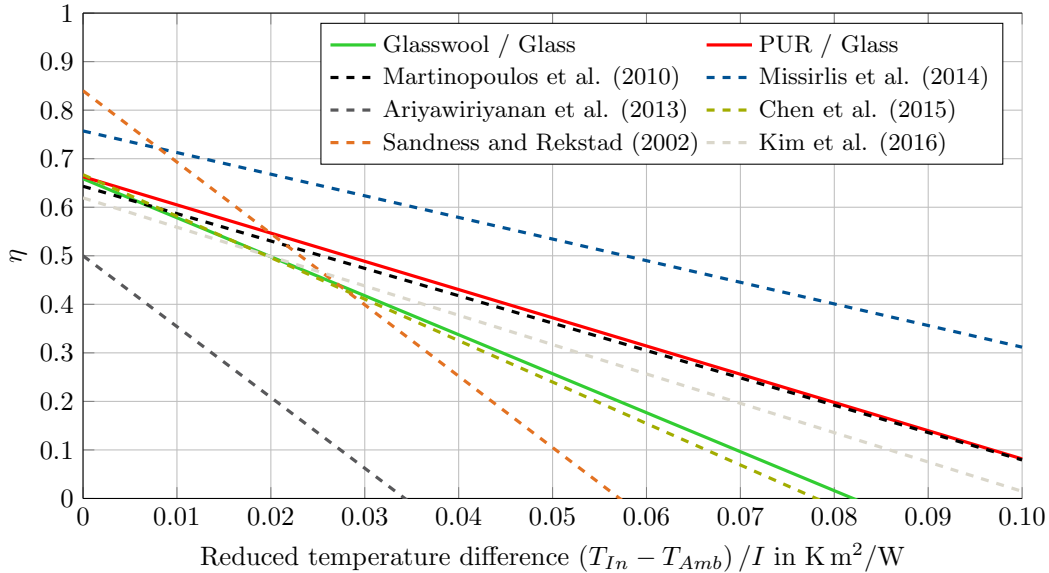


Figure 3.9: Linear efficiency curves of two tested polymeric collector prototypes together with the (linear) efficiency curves of polymeric collector concepts described in literature. The efficiency is evaluated at an irradiation of $1,000 \text{ W/m}^2$.

In conclusion, the results show a considerable technical potential of polymeric FPCs manufactured with the TST process. The developed prototypes are able to reach similar solar thermal efficiencies compared to market available collectors. A further increase of the solar thermal efficiency can therefore be expected in case of a serial production of polymeric FPCs manufactured with the TST process. A further improvement can be achieved by increasing the mass flow rate. Due to the relatively large cross-sectional area of the riser channels, the standard mass flow rate according to EN ISO 9806:2013 (p. 60) (approx. $0.02 \text{ kg}/(\text{s m}^2)$) yields a very low Reynolds number (ranging between 15 and 60), depending on the temperature of the HTF. According to Hausner and Fechner (1999, p. 1), the solar thermal efficiency of a typical solar FPC can be increased by 3% – 8% when switching from laminar to turbulent flow conditions. In accordance to findings from Ariyawiriyanan et al. (2013), the measured results indicate the highest solar efficiency in case of the largest prototype (1.32 m^2 ABS absorber with PUR insulation and glass cover). This can be attributed to the fact that heat losses towards ambient across the side walls become less dominant in case of a larger collectors. Increasing the collector gross area to more common values of $2.0 \text{ m}^2 - 2.4 \text{ m}^2$ (Wesselak et al., 2013, p. 313) is expected to further increase of the solar thermal efficiency.

4 Collector Simulation

Obtaining experimental results for the thermal efficiency of polymeric solar thermal FPCs is both time-consuming and cost-intensive, as each design iteration of the absorber results in revised mould halves when utilising the TST manufacturing process. To cope with this, a mathematical model of a solar thermal FPC was developed, enabling a fast and cost-effective prediction of collector efficiency curves.

4.1 Background

Mathematical models of conventional solar thermal FPCs are widely described in scientific literature. An extensive review of models developed within the last 40 years is presented by Tagliafico, Scarpa and Rosa (2014), who defined different categories of solar thermal collector models. Steady state models neglect thermal capacities of different parts of the collector (such as glazing, insulation, absorber etc.), yielding low computational costs. These models are well suited to predict the efficiency of a solar thermal collector as well as the temperatures of the different parts of the collector. However, due to the missing thermal capacities, steady state models are usually unable to account for dynamic effects. Dynamic models are able to compensate for this drawback by including thermal capacities for each component of the collector. Simple dynamic models account for one-dimensional heat transfer through the collector, e.g. described by Reiter et al. (2015) or Herrero López et al. (2015). More complex dynamic models account for multi-dimensional heat transfer mechanisms and are therefore able to evaluate potential temperature distributions, e.g. within the absorber (Oliva, Costa and Segarra, 1991). CFD-models further discretise the geometry of solar thermal collectors. This results in more detailed information regarding the heat flow and temperature distribution but also an exponential increase in the computational costs.

Approaches described in scientific literature most often aim to predict the efficiency and typical component temperatures of conventional solar thermal FPC with sheet-pipe absorbers (cf. figure 2.3). Therefore, in order to account for the behaviour of a polymeric collector with a volumetric absorber, modelling approaches described in scientific literature were reviewed and integrated into an appropriate collector model, which is described in detail below.

4.2 Description of the Collector Model

The primary purpose of the collector model subsequently described is the determination of the efficiency curve. Therefore, a multi-layer model was developed which is shown in figure 4.1. Each layer (cf. figure 4.1, highlighted areas) represents one physical component of a polymeric solar thermal FPC (e.g. glazing, absorber, insulation), which is further divided into several nodes. Within one layer, these nodes are connected by thermal resistors and /

or capacitors. The latter option accounts for the thermal mass of each layer, represented by the specific heat capacity and the mass of the layer.

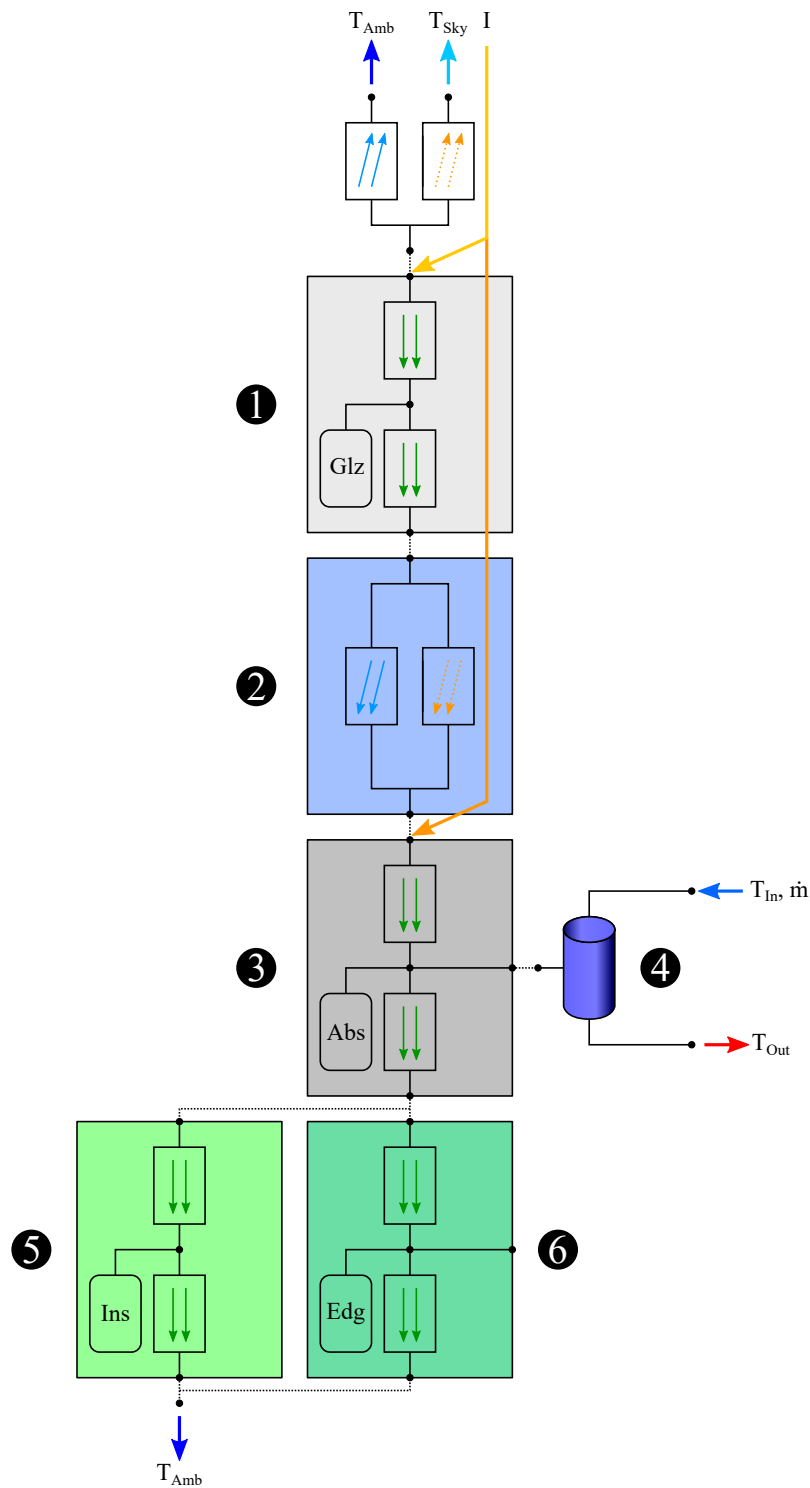


Figure 4.1: Scheme of solar thermal collector model. ① = Glazing. ② = Air, ③ = Absorber, ④ = Fluid, ⑤ = Backside insulation, ⑥ = Edge insulation. Modes of heat transfer: \Rightarrow = Thermal conduction, \Rightarrow = Thermal convection, \Rightarrow = Thermal radiation.

4 Collector Simulation

The second layer, representing the air gap between the absorber and the frontside glazing, does not include a thermal mass, as it is considered to be negligible compared to the thermal masses of the other layers. Including the thermal capacities of each component allows for an evaluation of the collector's behaviour in case of dynamic boundary conditions (apart from determining the collector's efficiency curve), enabling an integration of this model into more complex system models. Thermal resistors account for the different phenomena of heat transfer such as conduction, convection and radiation. Connecting the different layers results in a complete thermal network of a polymeric solar thermal FPC.

Apart from specific properties of the collector such as material properties and dimensions, boundary conditions have to be applied to determine the efficiency curve. These boundary conditions can be divided into sources and sinks of energy (cf. figure 4.1). Two energy sources are present in this model: On the one hand, solar irradiation hits both the glazing ① and the absorber ③. On the other hand, the HTF enters the absorber with a specific inlet temperature (T_{In}) and mass flow rate (\dot{m}) ④. The incident irradiation hits the upper node of the absorber and is converted into heat. After halfway conducted through the absorber, the heat can be exchanged with the fluid, yielding a certain outlet temperature T_{Out} . Due to thermal losses to ambient, only a certain portion of the heat is transferred into the fluid. The remaining is conducted through the backside ⑤ and side insulation ⑥. Here, an energy sink is specified by assuming a constant ambient temperature boundary condition T_{Amb} . In addition, heat is exchanged between the absorber and the glazing due to thermal convection and radiation in the air gap ②. The glazing absorbs part of the incident irradiation. Two boundary conditions (energy sinks) are applied here: On the one hand, heat can be transferred to the ambient due to a combination of free and forced convection. On the other hand, energy can be exchanged to the sky by means of long-wave radiative heat transfer.

The model was set up with MATLAB / Simscape. The Simscape library allows for multidirectional energy flow; thus, the direction of energy flow does not have to be specified in advance. The predefined external boundary conditions act as energy potentials of the model, yielding an energy flow throughout all layers. Thus, for example, the ambient can either represent a heat sink (in case of the collector temperature is higher than the ambient temperature) or as a heat source (in case the ambient temperature is higher than the collector temperature). This behaviour is of major importance, as it reflects the physics behind a polymeric solar thermal FPC. Herrero López et al. (2015) followed the same approach when developing a collector model utilising the Modelica programming language.

4.3 Modes of Heat Transfer

The mechanisms of heat transfer (thermal conduction, convection and radiation) present in the model described in section 4.2 are explained subsequently.

4.3.1 Thermal Conduction

The random collision of molecules in solids, liquids and gases yields an exchange of energy (Verein Deutscher Ingenieure, 2010, p. 18). This phenomenon is known as thermal conduction. Due to an increasing molecular movement at higher temperatures, the heat flux corresponds proportionally to an increasing temperature gradient between the medium and its surrounding. Thermal conduction is present within the solid components of the collector (glazing, absorber, back and side insulation). The one-dimensional, steady state conductive heat transfer through a wall can be described by Fourier's law (Verein Deutscher Ingenieure, 2010, p. 20):

$$\dot{Q}_{Cond} = h_{Cond} \cdot A \cdot \Delta T = \frac{\lambda}{t} \cdot A \cdot \Delta T \quad (4.1)$$

where:

| | |
|------------------|--|
| \dot{Q}_{Cond} | = Heat flux due to conduction in W |
| h_{Cond} | = Conductive heat transfer coefficient in W/(m ² K) |
| A | = Effective surface area in m ² |
| ΔT | = Temperature difference in K |
| λ | = Thermal heat conductivity in W/(m K) |
| t | = Thickness in m |

The same surface area is assumed for the glazing, absorber and back side insulation. For these components, the surface area is identical to the gross collector area. In case of the side insulation, the surface area is represented by the collector's perimeter multiplied by the height of the side insulation. Apart from the surface area, the thickness of each component as well as the thermal heat conductivity is taken into account. The component dimensions and the thermal conductivity can be combined into the conductive heat transfer coefficient h_{Cond} .

4.3.2 Thermal Convection

In contrast to thermal conduction, thermal convection is caused by a macroscopic fluid flow (Verein Deutscher Ingenieure, 2010, p. 18). In addition to the material properties and characteristic dimensions, the boundary conditions of the fluid movement strongly affect the amount of heat being transferred. Thermal convection is present both inside the air gap between the absorber and glazing (natural convection) and outside the glazing (combined free and forced convection). The Nusselt (Nu) number correlates the convective heat transfer coefficient h_{Conv} with a characteristic length L and the thermal heat conductivity λ of the fluid (Verein Deutscher Ingenieure, 2010, p. 20). Therefore, thermal conduction is already part of thermal convection within the fluid and must not be considered separately. The convective heat transfer can be determined according to equation 4.2:

4 Collector Simulation

$$\dot{Q}_{Conv} = h_{Conv} \cdot A \cdot \Delta T = \frac{Nu \cdot \lambda}{L} \cdot A \cdot \Delta T \quad (4.2)$$

where:

| | |
|------------------|--|
| \dot{Q}_{Conv} | = Heat flux due to convection in W |
| h_{Conv} | = Convective heat transfer coefficient in W/(m ² K) |
| A | = Effective surface area in m ² |
| ΔT | = Temperature difference in K |
| Nu | = Nusselt number |
| λ | = Thermal heat conductivity in W/(m K) |
| L | = Characteristic dimension in m |

As the effective surface area A , the characteristic dimension L and the thermal heat conductivity λ are known properties, the Nu number has to be determined to calculate the convective heat transfer. The determination of the Nu number depends on the particular flow conditions. While forced flow is the major mode of heat transfer between the HTF and the absorber, free (or natural) convection is present inside the air gap between absorber and glazing. A combination of both phenomena is responsible for the heat transfer from the glazing to the ambient.

Forced Convection inside the Absorber

The fluid flow through the absorber structure is modelled by utilising the pipe model from Simscape's thermal liquid (TL) library. Neither fluid compressibility, elevation gains nor inlet effects are considered. The Nu number depends on the type of fluid flow inside the absorber (either laminar or turbulent). The decisive criteria to determine the flow type is the Reynolds (Re) number:

$$Re = \frac{\rho \cdot v \cdot L}{\mu} = \frac{v \cdot L}{\nu} \quad (4.3)$$

where:

| | |
|--------|--|
| Re | = Reynolds number |
| ρ | = Density of the fluid in kg/m ³ |
| v | = Velocity of the fluid in m/s |
| L | = Characteristic dimension in m |
| μ | = Dynamic viscosity of the fluid in kg/(m s) |
| ν | = Kinematic viscosity in of the fluid in m ² /s |

To account for an internal flow inside non-circular, channel-like structures, the characteristic dimension L is represented by the hydraulic diameter d_h (Mills, 1999, p. 306).

$$d_h = 4 \cdot \frac{A}{U} \quad (4.4)$$

where:

| | |
|-------|--|
| d_h | = Hydraulic diameter in m |
| A | = Cross-sectional area of the absorber in m ² |
| U | = Perimeter of the cross-sectional area in m |

The high width-height-ratio of the absorber (width = 60 mm, height = 3 mm) in combination with a constant axial wall heat flux yields a Nu_{lam} number of 5.385 in case of a laminar flow ($Re < 2,300$) (Mills, 1999, p. 307). For $Re > 10^4$, the Nu number directly correlates with the Re number (Gnielinski, 1975, p. 11), taking into account the formulation of the friction factor f by Haaland (1983, p. 90). If $2,300 < Re < 10^4$, the Nu number is interpolated (Verein Deutscher Ingenieure, 2010, p. 696).

$$Nu_{Abs} = \begin{cases} 5.385 & \text{for } 0 < Re < 2,300 \rightarrow Nu_{lam} \\ \frac{f/8 \cdot (Re-1,000) \cdot Pr}{1+12.7\sqrt{f/8}(Pr^{2/3}-1)} & \text{for } Re \geq 10^4 \rightarrow Nu_{turb} \\ (1-\gamma)Nu_{lam,Re=2,300} + \gamma Nu_{turb,Re=10^4} & \text{for } 2,300 \leq Re \leq 10^4 \rightarrow Nu_{trans} \end{cases} \quad (4.5)$$

with

$$\frac{1}{\sqrt{f}} = -1.8 \log \left[\left(\frac{6.9}{Re} \right) + \left(\frac{K}{3.75 \cdot d_h} \right)^{1.11} \right], \quad \gamma = \frac{Re - 2,300}{10^4 - Re}$$

where:

| | |
|------------|---|
| Nu_{Abs} | = Nusselt number due to forced convection inside the absorber |
| Re | = Reynolds number |
| Pr | = Prandtl number |
| f | = Friction factor |
| K | = Surface roughness in m |
| d_h | = Hydraulic diameter in m |
| γ | = Interpolation factor |

The determination of the Nu number allows for the evaluation of the convective heat transfer between the absorber and the HTF (cf. equation 4.2).

Combined Natural and Forced Convection at the Glazing

A combination of forced convection (resulting from an external airflow over the glazing) and natural convection (resulting from the temperature difference between the glazing and the surrounding) applies for the heat transfer between glazing and ambient environment. To account for the heat transfer between the cover and the ambient due to forced convection, equation 4.2 applies. In this context, the characteristic length L as well as the Nu number

4 Collector Simulation

have to be determined. Scientific literature is lacking a unique definition of these numbers. Eicker (2012, p. 113) and Reiter et al. (2015, p. 8) follow the description of Verein Deutscher Ingenieure (2010, p. 714) regarding the formulation of the Nu number (cf. table 4.1, first to third row). In this context, Eicker (2012, p. 113) defines L to be equal to the longer side of the plate, assuming an air flow from the bottom to the top of the glazing. In contrast, Reiter et al. (2015, p. 9) specify the shorter dimensions of the plate as the characteristic length L , implying the wind flowing from the left to the right of the collector (or vice versa). Reiter et al. (2015, p. 8) also do not restrict the formulation of the Nu number for certain Re numbers. This is in contradiction to Verein Deutscher Ingenieure (2010, p. 714), which limits the validity of the Re number to $5 \cdot 10^5 < Re < 10^7$. Sparrow, Ramsey and Mass (1979, pp. 202-203) use a different equation for the Nu number, taking into account a characteristic length $L = 4 \cdot A/U$ (where A is the surface area of the glazing in m^2 and U the corresponding perimeter in m), stating validity for $2 \cdot 10^4 < Re < 9 \cdot 10^4$. Duffie and Beckman (2013, p. 163) suggest to extended the range of validity of this formula to $2 \cdot 10^4 < Re < 10^6$ (cf. table 4.1, fifth row). Due to the wide range of valid Re numbers, this formulation was chosen for the Nu number. The different formulations (with their specific range of validity) are shown in table 4.1.

Table 4.1: Overview of different formulations for the Nu number in case of forced convection over a flat plate. Empty cells indicate that there is no information available, crossed-out cells (—) indicate that the corresponding publication did not restrict the range of validity.

| Source | Characteristic length L | Formulation of Nu number | Range of validity |
|--|---------------------------|--|------------------------------------|
| Verein Deutscher Ingenieure (2010, p. 714) | | | $5 \cdot 10^5 < Re < 1 \cdot 10^7$ |
| Eicker (2012, p. 113) | Longer side | $\frac{0.037 \cdot Re^{0.8} \cdot Pr}{1 + 2.443 \cdot Re^{-0.1} (Pr^{2/3} - 1)}$ | — |
| Reiter et al. (2015) | Shorter side | | — |
| Sparrow, Ramsey and Mass (1979) | | | $2 \cdot 10^4 < Re < 9 \cdot 10^4$ |
| Duffie and Beckman (2013, p. 163) | $4 \cdot \frac{A}{U}$ | $0.86 \cdot Re^{1/2} \cdot Pr^{1/3}$ | $2 \cdot 10^4 < Re < 1 \cdot 10^6$ |

Besides formulations taking into account the Nu number, direct correlations between the wind speed v and the convective heat transfer coefficient h_{Conv} are widely described in literature, usually in an expression of $h_{Conv} = a + b \cdot v$. One example is the formulation of MacAdams (1954, p. 249), who states $h_{Conv} = 5.7 + 3.8v^{1.2}$. These relations are typically obtained from wind-tunnel experiments. The resulting heat transfer coefficient h_{Conv} (in $W/(m^2 K)$) is therefore usually limited to the dimensions of the investigated specimen as well as the type of boundary condition (wind speed and direction) and may therefore not be generalised (Duffie and Beckman, 2013, p. 164). Due to the constant part of the equation ($h_{Conv} = \underline{a} + b \cdot v$), a convective heat transfer is present even in case of windless conditions.

¹² MacAdams (1954, p. 249) specified the formula in imperial units, a conversion into SI-units was been done by Palyvos (2008, p. 803).

It is therefore questionable if these relations are valid for pure forced convection or whether other effects (e.g. natural convection, radiation) are also included. A comprehensive overview of overall wind convection coefficients is given by Palyvos (2008).

As the density of air decreases with increasing temperature, the hot air close to the glazing has a lower density compared to the ambient air, yielding a movement based on the density difference. This phenomenon is known as natural (or free) convection (Mills, 1999, p. 325). In case of free convection, the Rayleigh (Ra) number is used to determine whether the type of flow is laminar or turbulent. The Ra number (which is defined as the product of the Grashof (Gr) and the Prandtl (Pr) number) can be determined according to equation 4.6 (Mills, 1999, p. 325).

$$Ra = Gr \cdot Pr = \frac{\beta \cdot \Delta T \cdot g \cdot \cos \theta \cdot L^3}{\nu^2} \cdot Pr = \frac{\Delta T \cdot g \cdot \cos \theta \cdot L^3}{T_{Mean} \cdot \nu^2} \cdot Pr \quad (4.6)$$

where:

| | |
|------------|--|
| Ra | = Rayleigh number |
| Gr | = Grashof number |
| Pr | = Prandtl number |
| β | = Volumetric coefficient of expansion = $1/T_{Mean}$ |
| T_{Mean} | = Absolute mean temperature between glazing and ambient air in K |
| ΔT | = Temperature difference between glazing and ambient air in K |
| g | = Gravitational acceleration, i.e. 9.81 m/s^2 |
| Θ | = Angle of inclination of the collector in $^\circ$ |
| L | = Characteristic dimension in m |
| ν | = Kinematic viscosity of the air in m^2/s |

Equation 4.6 is valid for collector inclination angles $\theta \leq 60^\circ$, which seems to be an acceptable boundary condition for most solar thermal FPCs. Furthermore, equation 4.6 implies that the temperature of the glazing is higher than the ambient temperature. The characteristic dimension L in case of free convection is defined as the longer side of the plate (Verein Deutscher Ingenieure, 2010, p. 668).

The Nusselt number for natural convection is a function of the Rayleigh number (cf. equation 4.7). The transition between laminar and turbulent flow occurs at $Ra \approx 10^9$ (Mills, 1999, p. 325).

$$Nu_{Glz,free} = \begin{cases} 0.68 + 0.67 (Ra \cdot \psi)^{1/4} & \text{for } Ra \leq 10^9 \rightarrow Nu_{lam} \\ 0.68 + 0.67 (Ra \cdot \psi)^{1/4} \cdot \left(1 + \frac{Ra \cdot \psi}{1.6 \cdot 10^8}\right)^{1/12} & \text{for } Ra > 10^9 \rightarrow Nu_{turb} \end{cases} \quad (4.7)$$

4 Collector Simulation

with

$$\psi = \left[1 + \left(\frac{0.492}{Pr} \right)^{9/16} \right]^{-16/9}$$

where:

$Nu_{Glz,free}$ = Nusselt number due to free convection outside the glazing
 Ra = Rayleigh number
 ψ = Prandtl number function

To equally account for both forced and natural convection, the Nu numbers of forced and natural convection are superimposed (cf. equation 4.8), assuming the same direction of these physical phenomena (Verein Deutscher Ingenieure, 2010, p. 671). This assumption implies that the wind is flowing parallel to the long side of the FPC and that the temperature of the glazing is higher than the ambient temperature (cf. figure 4.2).

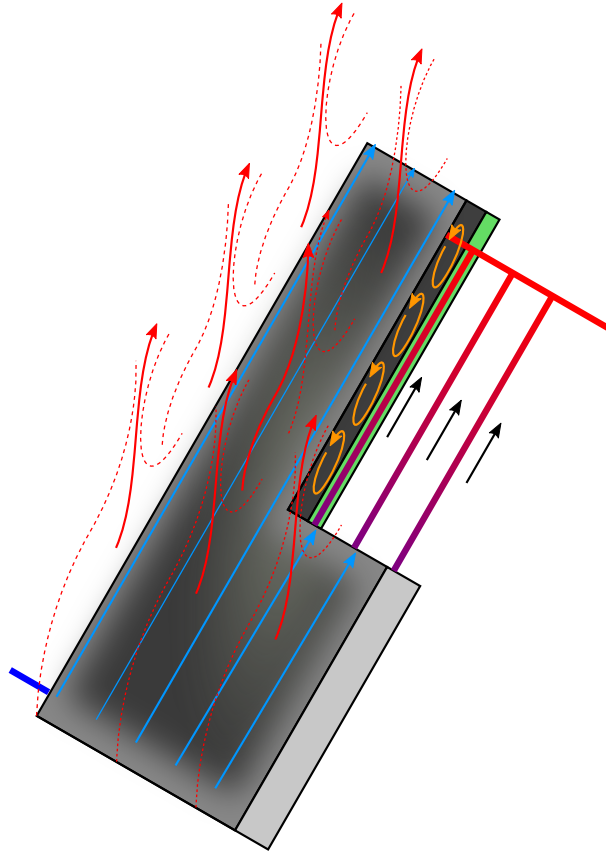


Figure 4.2: Illustration of convection phenomena inside and outside of a solar thermal FPC: Forced convection due to internal flow of HTF (\rightarrow), Forced convection due to external airflow (\rightarrow), Free convection between glazing and ambient (\rightarrow), Free convection between absorber and glazing (\rightarrow).

These conditions are not always fulfilled (e.g. in case of a south-oriented FPC subjected to west / east wind). Nevertheless, equation 4.8 is applied in absence of formulations for

non-uniform superimposition (Verein Deutscher Ingenieure, 2010, p. 671).

$$Nu_{Glz} = \sqrt[3]{Nu_{Glz,forced}^3 + Nu_{Glz,free}^3} \quad (4.8)$$

where:

- Nu_{Glz} = Superimposed Nusselt number outside of the glazing
- $Nu_{Glz,forced}$ = Nusselt number due to forced convection
- $Nu_{Glz,free}$ = Nusselt number due to natural convection

Based on the Nu number of forced ($Nu_{Glz,forced}$) and free ($Nu_{Glz,free}$) convection, the overall Nu_{Glz} number is calculated according to equation 4.8. As a result, the convective heat transfer coefficient can be determined according to equation 4.2. The overall convective heat transfer coefficient h_{Conv} due to forced and natural convection for a typical $2\text{ m} \times 1\text{ m}$ FPC is shown in figure 4.3. Material properties (Pr number, kinematic viscosity ν and thermal conductivity λ) are evaluated for an air temperature of 20°C . The temperature of the glazing (angle of inclination = 45°) is assumed to be 50°C . Due to the latter mentioned boundary conditions, the fraction of natural convection is constant and independent of the wind speed v (cf. figure 4.3, red shaded area). With increasing wind speed, the fraction of forced convection to the overall heat transfer coefficient h_{Conv} becomes more dominant.

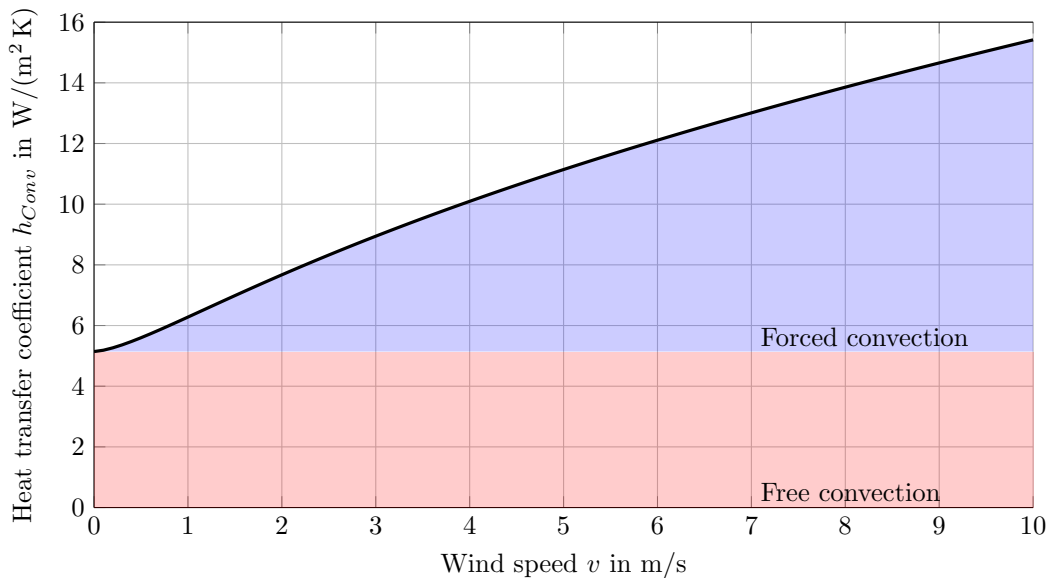


Figure 4.3: Wind speed dependent heat transfer coefficient h_{Conv} at the glazing.

Natural Convection inside the Air Gap

To account for the temperature-driven natural convection in the air gap between absorber and glazing, equation 4.9 applies (Hollands et al., 1976, p. 192). The “+” exponent indicates

4 Collector Simulation

that statements in square brackets are only considered if these terms are greater than zero. Otherwise, these statements are set to zero.

$$Nu_{AirGap} = 1 + 1.44 \left[1 - \frac{1,708 (\sin 1.8\beta)^{1.6}}{Ra \cos \beta} \right] \left[1 - \frac{1,708}{Ra \cos \beta} \right]^+ + \left[\left(\frac{Ra \cos \beta}{5,830} \right)^{1/3} - 1 \right]^+ \quad (4.9)$$

where:

- Nu_{AirGap} = Nusselt number due to free convection in the air gap
- Ra = Rayleigh number, cf. equation 4.6
- β = Volumetric coefficient of expansion = $1/T_{Mean}$
- T_{Mean} = Absolute mean temperature between glazing and absorber in K

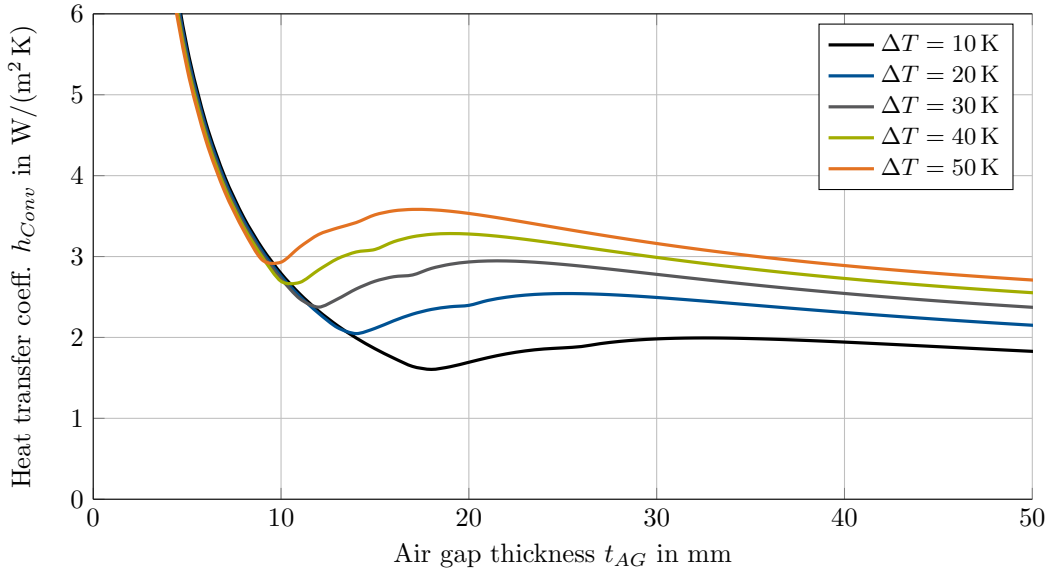


Figure 4.4: Heat transfer coefficient h_{Conv} in the air gap between absorber and glazing.

4.3.3 Thermal Radiation

Every body with a temperature higher than 0 K emits radiation to its surrounding (Verein Deutscher Ingenieure, 2010, p. 20). Such a radiative heat transfer can be described by the law of Stefan-Boltzmann (Stefan, 1879; Boltzmann, 1884). To keep compatibility with the formulation in case of thermal conduction and convection (cf. equations 4.1 and 4.2), Duffie and Beckman (2013, p. 148) define the radiative heat transfer between two surfaces according to equation 4.10. The radiative energy exchange between both surfaces is a function of their respective emissivities (ϵ_1, ϵ_2) and the view factor F_{12} between those surfaces (A_1, A_2), cf. figure 4.5 (Duffie and Beckman, 2013, p. 147). A detailed derivation of equation 4.10 is

given by Eicker (2012, pp. 109-111), a list of view factors is presented by Mills (1999, pp. 541-543).

$$\dot{Q}_{Rad} = A_1 \cdot h_{Rad} \cdot (T_2 - T_1) \quad (4.10)$$

with

$$h_{Rad} = \frac{\sigma (T_1^2 + T_2^2) (T_1 + T_2)}{\frac{1 - \epsilon_1}{\epsilon_1} + \frac{1}{F_{12}} + \frac{(1 - \epsilon_2) A_1}{\epsilon_2 A_2}}$$

where:

| | |
|--------------------------|--|
| \dot{Q}_{Rad} | = Heat flux due to radiation in W |
| h_{Rad} | = Radiative heat transfer coefficient in W/(m ² K) |
| σ | = Stefan-Boltzmann constant, i.e. 5.67×10^{-8} W/(m ² K ⁴) |
| ϵ_1, ϵ_2 | = Emissivity of the surface ($0 \leq \epsilon \leq 1$) |
| A_1, A_2 | = Effective surface areas in m ² |
| T_1, T_2 | = Temperatures of the surfaces in K |

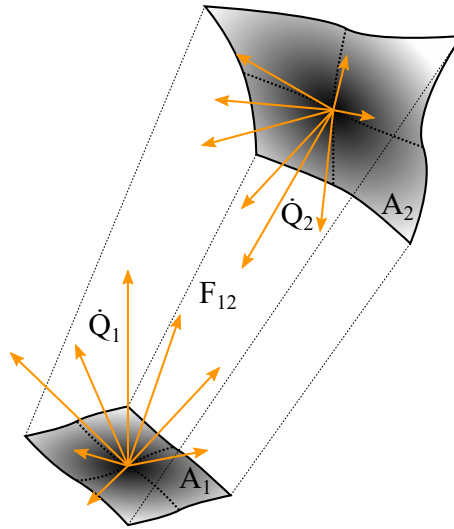


Figure 4.5: Radiative energy exchange between two grey surfaces according to Eicker (2012, p. 109).

Radiative Heat Exchange to the Sky

Equation 4.10 is applied to account for the radiative heat exchange between a horizontally placed glazing (A_1) and the sky (A_2). As the sky totally absorbs the radiation emitted by the glazing, the view factor $F_{12} = 1$. The sky is significantly larger than the surface area

4 Collector Simulation

of the glazing, therefore $A_1/A_2 \approx 0$. Inserting these boundary conditions into equation 4.10 yields the following definition of the radiative heat transfer coefficient:

$$h_{Rad, Sky} = \frac{\sigma (T_{Glz}^2 + T_{Sky}^2) (T_{Glz} + T_{Sky})}{\frac{1 - \epsilon_{Glz}}{\epsilon_{Glz}} + 1} \quad (4.11)$$

where:

| | |
|------------------|--|
| $h_{Rad, Sky}$ | = Radiative heat transfer coefficient between glazing and sky in $W/(m^2 K)$ |
| σ | = Stefan-Boltzmann constant, i.e. $5.67 \times 10^{-8} W/(m^2 K^4)$ |
| T_{Glz} | = Temperature of the glazing in K |
| T_{Sky} | = Temperature of the sky in K |
| ϵ_{Glz} | = Emissivity of the glazing |

The sky temperature T_{Sky} is related to the sky conditions. Models that correlate T_{Sky} with meteorological data (such as ambient temperature, water vapour pressure, dew point temperature, dry bulb temperature etc.) are widely described in scientific literature (Duffie and Beckman, 2013, p. 148). A comprehensive list of the most common relations is presented by Eicker (2012, p. 54). Swinbank (1963) correlates the sky temperature with the ambient temperature (cf. equation 4.12). This formulation is implemented in the collector model. More complex models can be applied if sufficient data are available.

$$T_{Sky} = 0.0552 \cdot T_{Amb}^{1.5} \quad (4.12)$$

where:

| | |
|-----------|-------------------------------|
| T_{Sky} | = Temperature of the sky in K |
| T_{Amb} | = Ambient temperature in K |

Radiative Heat Exchange between Absorber and Glazing

To account for the radiative heat exchange between the absorber (A_1) and the glazing (A_2), equation 4.10 is applied, assuming sufficient comparability with the (theoretical) case of radiation between two infinitely large, parallel surfaces. In this context, the view factor $F_{12} = 1$. In addition, both surfaces have the same area ($A_1 = A_2$), the radiative heat transfer coefficient can therefore be determined according to equation 4.13:

$$h_{Rad,Gap} = \frac{\sigma (T_{Abs}^2 + T_{Glz}^2) (T_{Abs} + T_{Glz})}{\frac{1 - \epsilon_{Abs}}{\epsilon_{Abs}} + 1 + \frac{1 - \epsilon_{Glz}}{\epsilon_{Glz}}} \quad (4.13)$$

where:

| | |
|------------------|---|
| $h_{Rad,Gap}$ | = Radiative heat transfer coefficient between glazing and absorber in $W/(m^2 K)$ |
| σ | = Stefan-Boltzmann constant, i.e. $5.67 \times 10^{-8} W/(m^2 K^4)$ |
| T_{Abs} | = Temperature of the absorber in K |
| T_{Glz} | = Temperature of the glazing in K |
| ϵ_{Glz} | = Emissivity of the glazing |
| ϵ_{Abs} | = Emissivity of the absorber |

4.4 Collector Optics

The principle of conservation of energy may be applied to describe the optical effects both at the glazing and the absorber. For a particular wavelength λ , the incident irradiation I gets partly absorbed by, transmitted through and reflected at the transparent glazing (cf. equation 4.14 and figure 4.6, left). As the absorber is opaque (that is $\tau_{\lambda, Abs} = 0$), no energy is transmitted through the absorber (cf. figure 4.6, right).

$$I_{\lambda} = \alpha_{\lambda} I_{\lambda} + \rho_{\lambda} I_{\lambda} + \tau_{\lambda} I_{\lambda} \rightarrow 1 = \alpha_{\lambda} + \rho_{\lambda} + \tau_{\lambda} \quad (4.14)$$

where:

| | |
|--------------------|--|
| I_{λ} | = Wavelength dependent incident irradiation in W/m^2 |
| α_{λ} | = Wavelength dependent absorption |
| ρ_{λ} | = Wavelength dependent reflection |
| τ_{λ} | = Wavelength dependent transmittance |

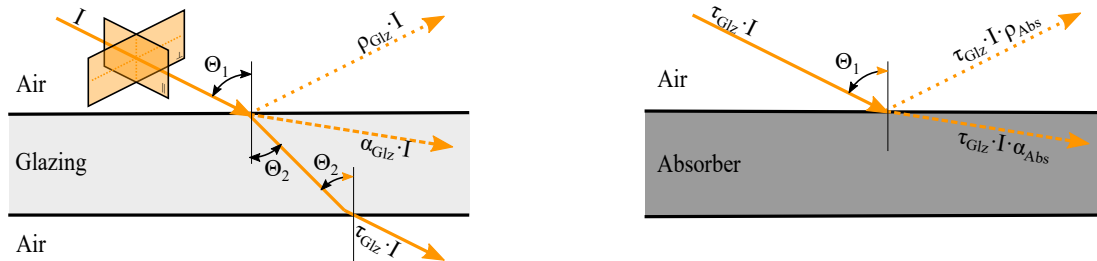


Figure 4.6: Collector optics according to Eicker (2012, p. 115) and Reiter et al. (2015, p. 6): Incident solar radiation (\rightarrow), Solar radiation, reflected ($\cdots\rightarrow$), Solar radiation, absorbed ($- \rightarrow$).

4 Collector Simulation

The ratio between absorption, reflection and transmittance depends on the angle of incidence θ_1 , the material properties (represented by the extinction coefficient K and the refractive indices n_{Air}, n_{Glz}) as well as on the thickness L of the glazing. In general, both the extinction coefficient K and the refractive indices n are wavelength-dependent properties, which are assumed to be constant within the scope of this collector model. According to Duffie and Beckman (2013, p. 202), this assumption holds true especially for glass.

4.4.1 Reflection Coefficient at the Boundary Surface of the Glazing

To account for the reflection at the boundary surface of the glazing, in case of smooth surfaces, Fresnel's equations may be applied (Duffie and Beckman, 2013, p. 202). The overall reflection coefficient is the average of the parallel and perpendicular part of the unpolarised, incident irradiation (cf. equation 4.15 and figure 4.6, left).

$$r_{Glz} = \frac{I_{refl,Glz}}{I} = \frac{r_{\perp} + r_{\parallel}}{2} \quad (4.15)$$

with:

$$r_{\perp} = \frac{\sin^2(\theta_2 - \theta_1)}{\sin^2(\theta_2 + \theta_1)}, \quad r_{\parallel} = \frac{\tan^2(\theta_2 - \theta_1)}{\tan^2(\theta_2 + \theta_1)}$$

where:

| | |
|----------------------------|---|
| r_{Glz} | = Reflection coefficient at the glazing |
| $I_{refl,Glz}$ | = Reflected part of incident irradiation at the boundary surface of the glazing in W/m ² |
| I | = Incident irradiation in W/m ² |
| r_{\perp}, r_{\parallel} | = Reflection coefficient for perpendicular / parallel portion of incident irradiation |
| θ_1, θ_2 | = Angle of incidence / reflection in ° |

According to Snell's law, the ratio between the angle of incidence and the angle of reflection correlates with the refractive indices of the glazing and the surrounding air (Duffie and Beckman, 2013, p. 203). In case of normal irradiation, the angle of incidence / reflection as well as the reflection coefficients r_{\perp} and r_{\parallel} are zero. Taking into account Snell's law, the reflection of the unpolarised irradiation perpendicular to the glazing can be expressed according to equation 4.16 (Eicker, 2012, p. 115).

$$r_{Glz,0} = \left(\frac{n_{Air} - n_{Glz}}{n_{Air} + n_{Glz}} \right)^2 \quad (4.16)$$

where:

| | |
|--------------------|---|
| $r_{Glz,0}$ | = Reflection coefficient at the glazing in case of normal irradiation |
| n_{Air}, n_{Glz} | = Refractive indices |

4.4.2 Absorption of the Glazing

The absorption of a transparent material is defined as the ratio of transmitted to incident irradiation. It depends on the extinction coefficient K and the path-length through the glazing (cf. figure 4.6, left). Integrating Bouguer's law with respect to the path-length yields equation 4.17 (Duffie and Beckman, 2013, p. 206).

$$\tau_\alpha = \frac{I_{trans,Glz}}{I} = e^{-\frac{K_{Glz}L_{Glz}}{\cos\theta_2}} \quad (4.17)$$

where:

| | |
|-----------------|---|
| τ_α | = Transmittance without reflection at the glazing |
| $I_{trans,Glz}$ | = Transmitted part of incident irradiation in W/m^2 |
| I | = Incident irradiation in W/m^2 |
| K_{Glz} | = Extinction coefficient of the glazing in $1/m$ |
| L_{Glz} | = Thickness of the glazing in m |
| θ_2 | = Angle of reflection $^\circ$ |

4.4.3 Transmission, Reflectance and Absorption Coefficients of the Glazing

The incident irradiation hitting the transparent cover is partly reflected at the upper boundary surface. The remaining part of the light gets either absorbed by or transmitted through the transparent cover. A certain portion of the irradiation leaves the glazing from the bottom side (cf. figure 4.7). Depending on the angle of incidence θ_1 and the path-length of the beam, another portion of the energy is reflected back to the upper boundary, yielding an infinite series of transmission, reflection and absorption at the glazing (Eicker, 2012, p. 117).

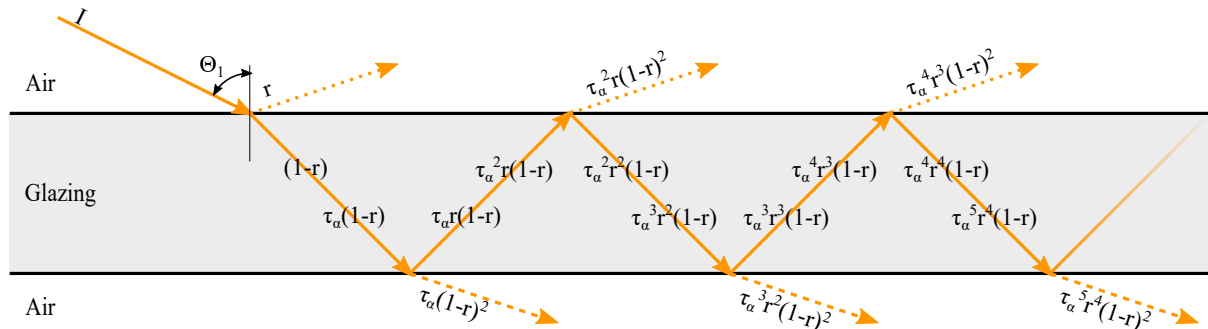


Figure 4.7: Transmission, reflection and absorption of a single glazing according to Eicker (2012, p. 117) and Reiter et al. (2015, p. 7): Incident solar radiation (\rightarrow), Solar radiation, reflected at upper boundary surface ($\cdots\rightarrow$), Solar radiation, transmitted through lower boundary surface ($-\rightarrow$).

4 Collector Simulation

Ray-tracing techniques may be used to account for the transmission, reflection and absorption coefficient of the glazing (cf. equations 4.18 - 4.20), including both reflection and absorption losses (Duffie and Beckman, 2013, p. 206).

$$\tau = \frac{\tau_{\perp} + \tau_{\parallel}}{2} \quad \text{with} \quad \tau_{\perp} = \frac{\tau_{\alpha}(1 - r_{\perp})^2}{1 - (r_{\perp}\tau_{\alpha})^2}, \quad \tau_{\parallel} = \frac{\tau_{\alpha}(1 - r_{\parallel})^2}{1 - (r_{\parallel}\tau_{\alpha})^2} \quad (4.18)$$

$$\rho = \frac{\rho_{\perp} + \rho_{\parallel}}{2} \quad \text{with} \quad \rho_{\perp} = r_{\perp} \cdot (1 + \tau_{\alpha}\tau_{\perp}), \quad \rho_{\parallel} = r_{\parallel} \cdot (1 + \tau_{\alpha}\tau_{\parallel}) \quad (4.19)$$

$$\alpha = \frac{\alpha_{\perp} + \alpha_{\parallel}}{2} \quad \text{with} \quad \alpha_{\perp} = (1 - \tau_{\alpha}) \left(\frac{1 - r_{\perp}}{1 - r_{\perp}\tau_{\alpha}} \right), \quad \alpha_{\parallel} = (1 - \tau_{\alpha}) \left(\frac{1 - r_{\parallel}}{1 - r_{\parallel}\tau_{\alpha}} \right) \quad (4.20)$$

where:

| | |
|--------------------------------------|---|
| τ | = Transmission coefficient of the glazing |
| $\tau_{\perp}, \tau_{\parallel}$ | = Perpendicular / parallel portion of transmission coefficient |
| ρ | = Reflection coefficient of the glazing |
| $\rho_{\perp}, \rho_{\parallel}$ | = Perpendicular / parallel portion of reflection coefficient |
| α | = Absorption coefficient of the glazing |
| $\alpha_{\perp}, \alpha_{\parallel}$ | = Perpendicular / parallel portion of absorption coefficient |
| τ_{α} | = Transmittance without reflection at the glazing |
| r_{\perp}, r_{\parallel} | = Reflection coefficient for perpendicular / parallel portion of incident irradiation |

The resulting direct, angle-dependent energy input to the glazing can be determined according to equation 4.21:

$$\dot{Q}_{Glz,dir} = A_{Glz} \cdot I_{dir} \cdot \alpha \quad (4.21)$$

where:

| | |
|---------------------|---|
| $\dot{Q}_{Glz,dir}$ | = Energy input to the glazing due to direct incident irradiation in W |
| A_{Glz} | = Surface area of the glazing in m ² |
| I_{dir} | = Incident irradiation in W/m ² |
| α | = Absorption coefficient of the glazing |

4.4.4 Transmittance-Absorptance Product

After passing through the transparent cover (with a particular transmission coefficient τ , cf. equation 4.18), the incident irradiation gets absorbed by the absorber. The absorber surface has a specific, material-dependent absorption coefficient α , which is wavelength-dependent and assumed to be constant within the scope of this model. Due to multiple reflections between the lower boundary surface of the glazing and the absorber (cf. figure

4.8), the effective transmittance-absorptance product $(\tau\alpha)_{eff}$ can be determined according to equation 4.22 (Eicker, 2012, p. 119). In this context, this effective transmittance-absorptance product may be interpreted as a property of a specific cover-absorber combination (Duffie and Beckman, 2013, p. 213).

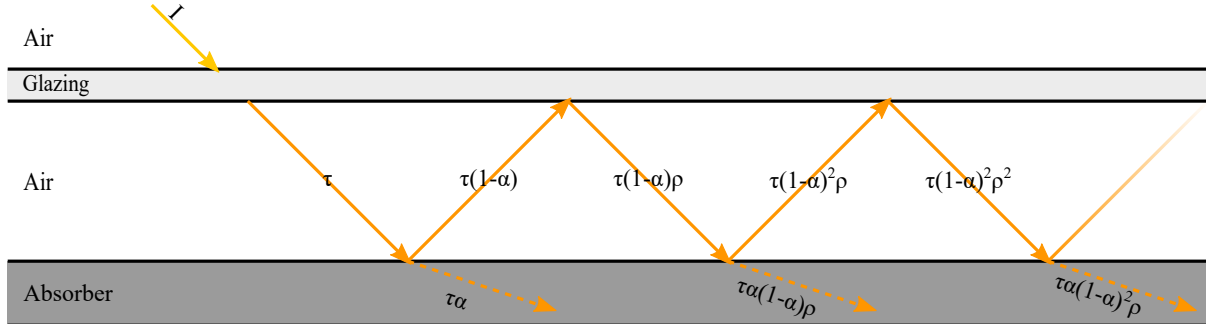


Figure 4.8: Effective transmittance-absorptance product of a single-glazed FPC according to Eicker (2012, p. 119), Duffie and Beckman (2013, p. 213) and Reiter et al. (2015, p. 7): Incident solar radiation (\rightarrow), Solar radiation, absorbed ($- \rightarrow$).

$$\dot{Q}_{Abs} = (\tau\alpha)_{eff} \cdot I \cdot A \quad \text{with} \quad (\tau\alpha)_{eff} = \tau\alpha \sum_{n=0}^{\infty} ((1-\alpha)\rho)^n = \frac{\tau\alpha}{1-(1-\alpha)\rho} \quad (4.22)$$

where:

- \dot{Q}_{Abs} = Energy input to the absorber due to incident irradiation in W
- $(\tau\alpha)_{eff}$ = Effective transmission-absorption product
- τ = Transmission coefficient of the glazing
- α = Absorption coefficient of the absorber
- ρ = Reflection coefficient of the lower boundary surface
- I = Irradiation in W/m²
- A = Surface area of the collector in m²

The resulting direct, angle-dependent energy input to the absorber can be determined according to equation 4.23.

$$\dot{Q}_{Abs,dir} = A_{Abs} \cdot I_{dir} \cdot (\tau\alpha)_{eff} \quad (4.23)$$

where:

- $\dot{Q}_{Abs,dir}$ = Energy input to the absorber due to direct irradiation in W
- A_{Abs} = Surface area of the absorber in m²
- I_{dir} = Incident irradiation in W/m²
- $(\tau\alpha)_{eff}$ = Effective transmission-absorption product

4.4.5 Energy Input due to Diffuse Radiation

Besides the energy input due to angle-dependent irradiation, a further source of energy results from angle-independent, diffuse irradiation (Duffie and Beckman, 2013, p. 212). Based on empirical studies, Brandemuehl and Beckman (1980, p. 512) identified the isotropic, diffuse irradiation to be equally effective as the beam radiation hitting the collector at an angle of approximately 60°. To account for different angles of inclination, the authors formulated a correction angle for the diffuse irradiation (cf. equation 4.24):

$$\theta = 59.68 - 0.1388\beta + 0.001497\beta^2 \quad (4.24)$$

where:

- θ = Equivalent angle of incidence for diffuse irradiation in °
- β = Angle of inclination of the collector in °

Based on the equivalent angle of incidence for diffuse irradiation, the additional energy input to both the glazing and the absorber can be determined according to equations 4.21 and 4.23.

4.5 Model Validation

In order to assess the developed collector model's accuracy, it was both validated under steady-state and dynamic boundary conditions.

4.5.1 Validation for Steady-State Boundary Conditions

The collector model was validated with data obtained from the tests using the indoor solar simulator (cf. chapter 3). In total, four different prototypes with polymeric absorbers were simulated and evaluated with measurement data. The properties of the tested prototypes are listed in table 3.2. In order to compare the measured data with the numerical results from the simulation model, the absolute difference between the efficiency were evaluated for each measurement point.

The results are shown in figure 4.9 - 4.12, the underlying measurement data can be found in the appendix (cf. table D.1 to D.4). A maximum deviation of 5.8 p.p. between measured and simulated data can be identified. The results indicate that the simulation model slightly overestimates the efficiency. This can be attributed to the fact that the collector model does not cover all physical phenomena which are present in reality. A further source of uncertainty is caused by the measurement error of the solar simulator, which ranges between 3.5 % and 10.7 % (cf. section 3.3). Reiter et al. (2015, p. 14) obtained a maximum deviation between their collector model and measured data of 3.1 %. In addition to that, Reiter et al. (2015) give an overview about deviations of other collector models: Matuska and Zmrhal (2009,

p. 48) reported differences of 3% – 4%, Cadafalch (2009, p. 2162) obtained deviations between measured and simulated values < 2%. Taking this information into account, the aforementioned maximum deviation of 5.8% can be interpreted as a tolerable value.

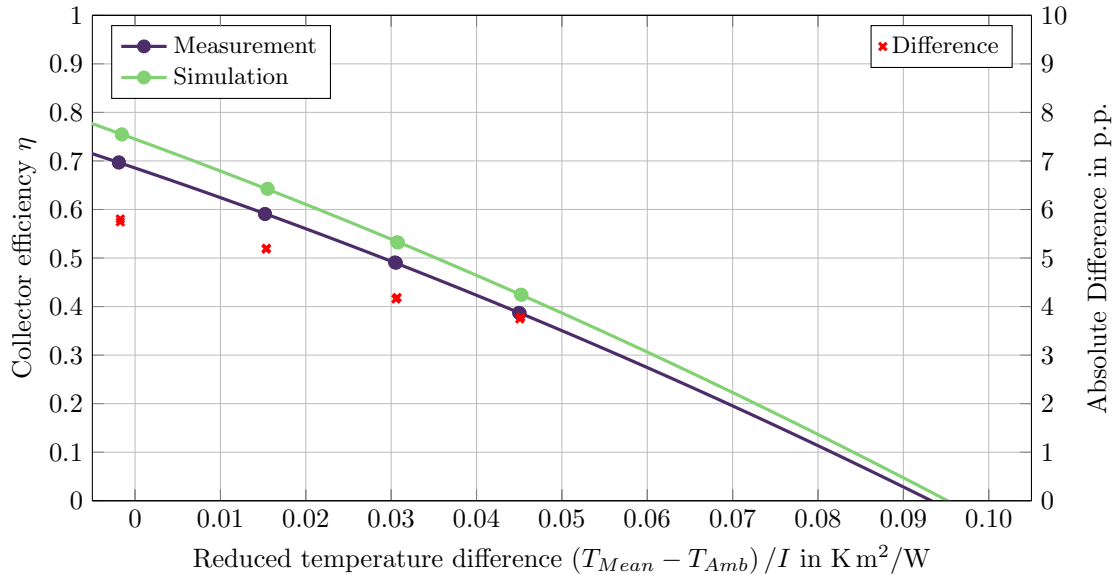


Figure 4.9: Validation results for the ABS collector with PUR insulation and PMMA glazing. Maximum deviation between simulated and measured data: 5.8 p.p..

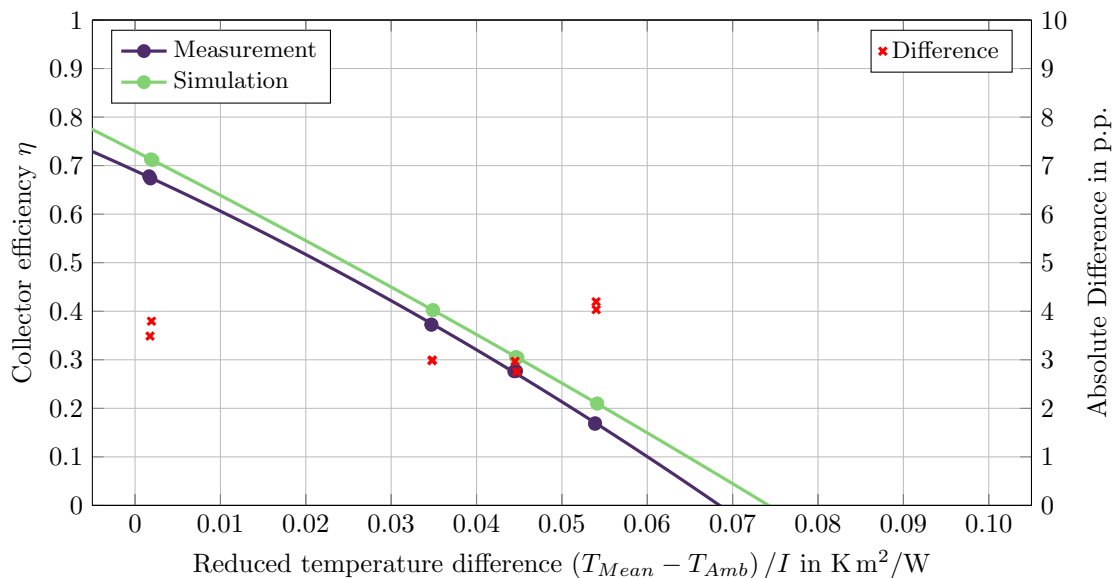


Figure 4.10: Validation results for the PP collector with glasswool insulation and glass glazing. Maximum deviation between simulated and measured data: 4.2 p.p..

4 Collector Simulation

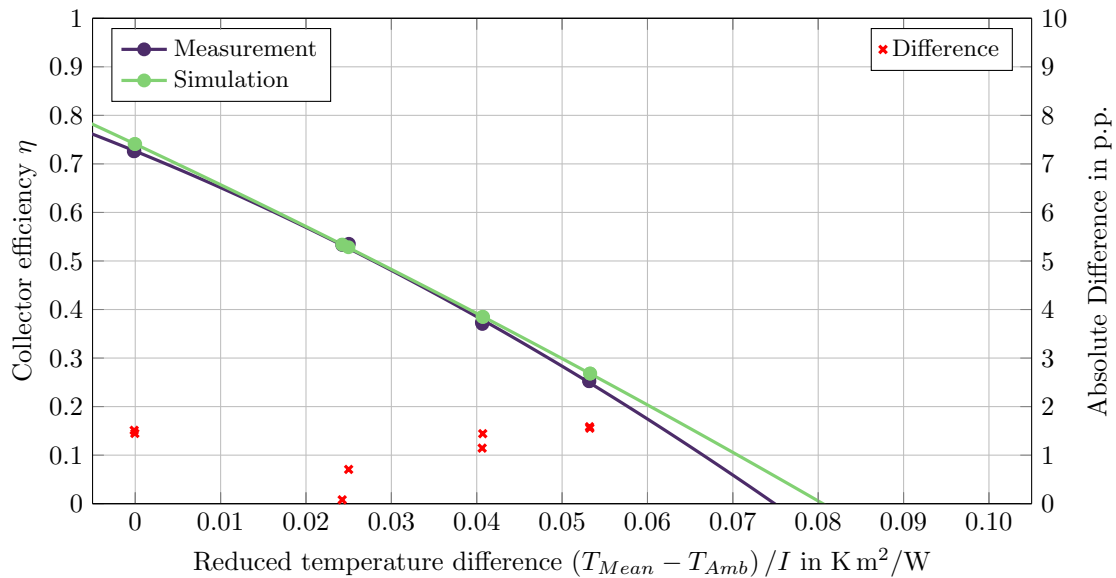


Figure 4.11: Validation results for the PP collector with EPS insulation and glass glazing. Maximum deviation between simulated and measured data: 1.6 p.p..

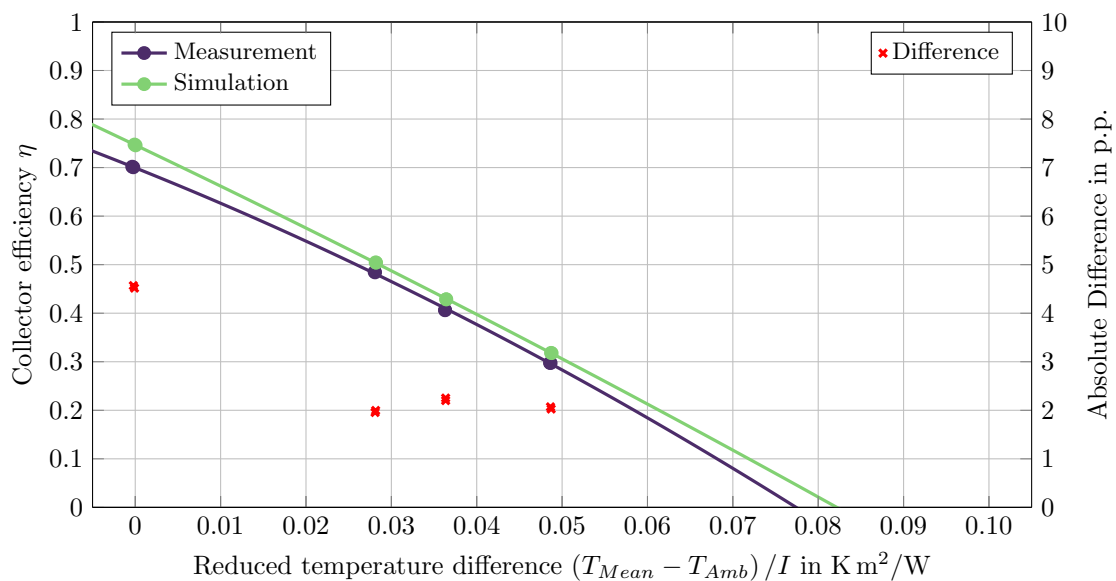


Figure 4.12: Validation results for the PP collector with EPS insulation and glass glazing (including additional frame). Maximum deviation between simulated and measured data: 4.6 p.p..

4.5.2 Validation for Dynamic Boundary Conditions

After validating the simulation model under steady-state boundary conditions, the dynamic behaviour was investigated based on measurement data monitored at an outdoor test-rig (cf. chapter 5). Four identical PP collectors with glasswool insulation and glass glazing were mounted under 45° inclination (south oriented). The overall collector area amounted

to 2.37 m^2 . For validating the model, two consecutive days were chosen: The first day represents a summer day with several clouds passing by throughout the day, whereas the second day had clear sky conditions (cf. figures 4.13 and 4.14, yellow curve). Between 10:45 and 10:50 AM, the pump starts to circulate the HTF (in this case water) through the collector array with a volume flow rate of approximately 150 l/h . Around 5:30 PM, the pump stops (cf. figures 4.13 and 4.14, lower part of the diagram). Environmental conditions such as irradiation, ambient temperature, wind speed and direction were monitored as well as the collector inlet and outlet temperatures and the volume flow rate. All boundary conditions were fed into the simulation model in order to determine the (simulated) resulting collector outlet temperature.

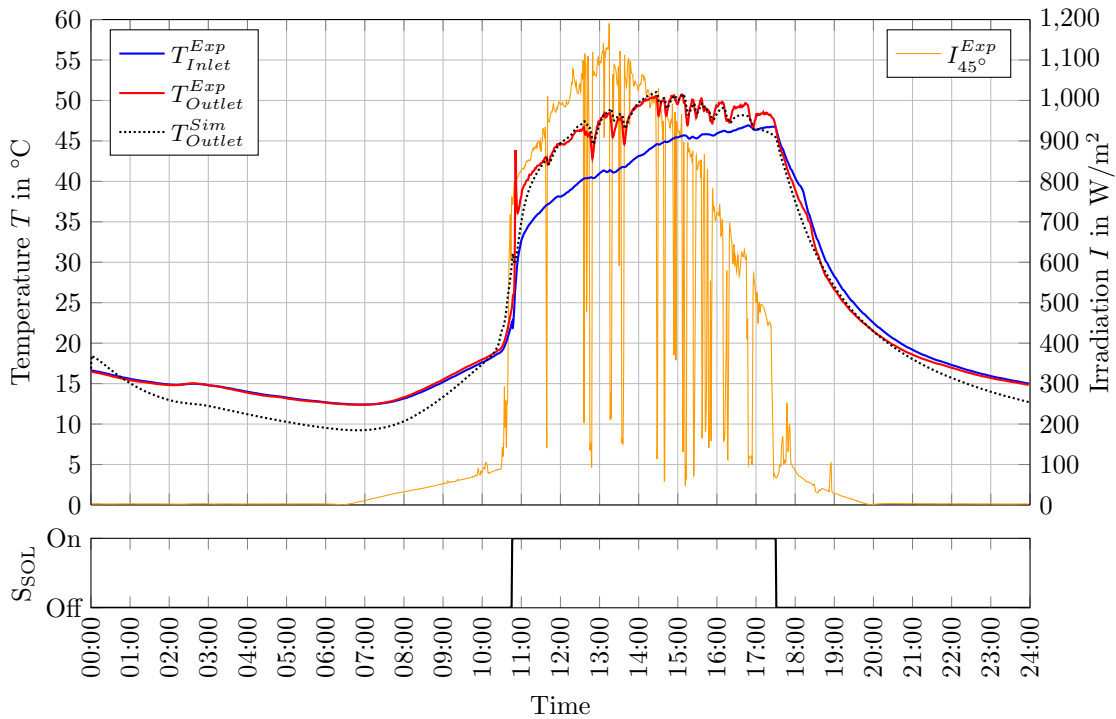


Figure 4.13: Dynamic validation of a collector array with four PP collectors with glasswool insulation and glass glazing under cloudy sky conditions. Deviation between simulated and measured solar yield: 4.9%.

To determine the quality of the simulation model, the solar thermal yield for both the measured as well as the simulated systems were compared according to equation 4.25:

$$\xi = \sqrt{\left(\frac{E^{Exp} - E^{Sim}}{E^{Exp}}\right)^2} \quad (4.25)$$

where:

- ξ = Difference between measured and simulated solar thermal yield
- E^{Exp} = Daily amount of energy (experiment) in kW h
- E^{Sim} = Daily amount of energy (simulation) in kW h

4 Collector Simulation

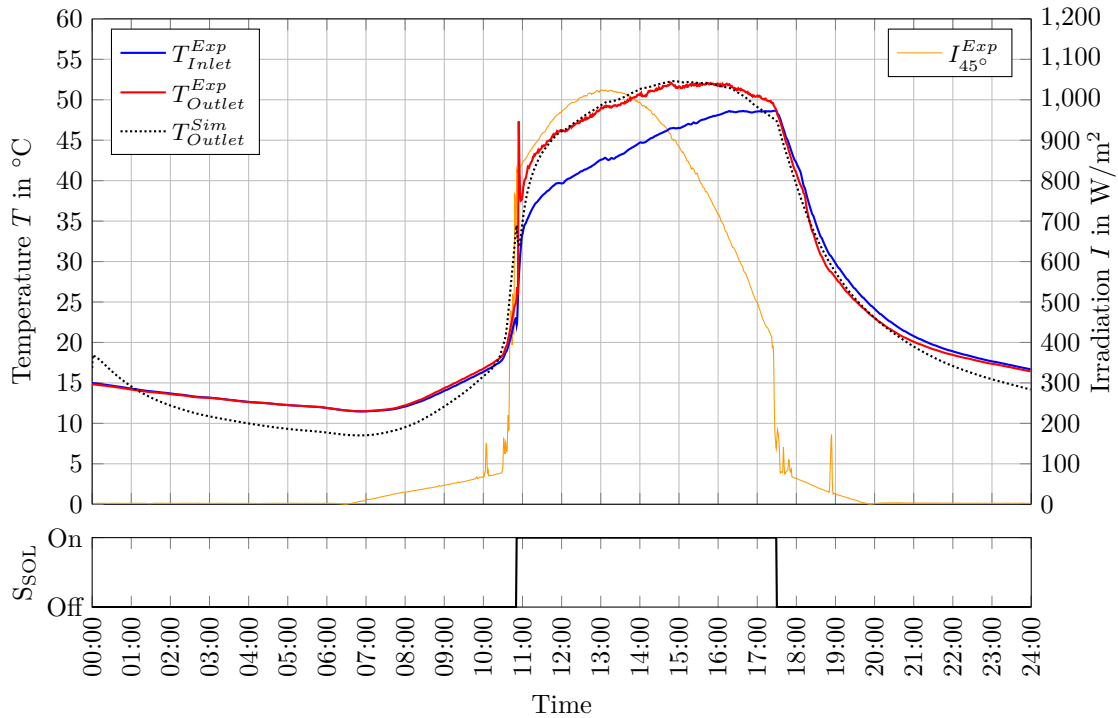


Figure 4.14: Dynamic validation of a collector array with four PP collectors with glasswool insulation and glass glazing in case of clear sky conditions. Deviation between simulated and measured solar yield: 2.2%.

For both days, a high degree of correlation between measured and simulated data was observed. For the first (cloudy) day, the developed collector model under-estimates the reality by 4.9%. For the second (cloudless) day, a difference of 2.2% can be observed. Comparing the simulated with the measured collector outlet temperature indicates that the model under-estimates the measurement data soon after the solar pump was activated (between 10:45 and 11:30 AM) and in the later afternoon hours (4:00 to 5:30 PM). The first effect can be attributed to the setup of the tested system: As this system is designed as a DBS, the collector array was empty before starting the pump. After switching on the pump, the overall thermal mass of the collector is affected by the incoming HTF.

In contrast to that, the simulation model assumes a constant thermal mass including the HTF. The resulting (higher) overall thermal mass yields a different heating-up performance. The under-estimation of the simulation model in the morning / evening hours can be attributed to optic properties of the absorber and / or the glazing material. To compensate this effect, more information regarding the angle-dependent material properties would be necessary. Between 12:00 AM and 4:00 PM, the simulation model slightly over-estimates the collector outlet temperature. The same effect could be observed at steady-state boundary conditions (cf. section 4.5.1), indicating that the simulation model does not account for all heat-loss effects which are present in reality.

When the solar pump is in stand-still, the simulated collector outlet temperature deviates from the measured value up to 5 °C. This effect can be attributed to the sky temperature (cf. section 4.3.3). To ensure compatibility with the results from the indoor measurements (cf.

section 4.5.1), the sky temperature of Swinbank (1963) was chosen. This model correlates the sky temperature solely with the ambient temperature. In reality, however, the sky temperature depends on several parameters (such as humidity or cloudiness degree). If this information was available, more complex models can be used for determining the sky temperature. An overview of different sky temperature models is given by Eicker (2012, p. 54). The effect of different sky temperature models to the resulting collector outlet temperature is shown in the appendix (cf. figures E.1 and E.2).

The results of the dynamic validation indicate a high correlation between the measured and simulated solar yield. Therefore, the developed collector model seems to be appropriate for application in more complex simulation models with dynamic boundary conditions.

4.6 Parametric Study

The evaluation of available literature (cf. chapter 2) revealed typical absorber areas of polymeric solar thermal FPCs ranging between 0.5 m^2 and 2.0 m^2 . According to Köhl, Meir and Papillon (2013, p. 56), the representative surface area for a standard, metal-based solar thermal FPC is 2.0 m^2 . Therefore, a 2 m long and 1 m wide collector made of PP is assumed for the subsequent parametric study.

In accordance with data available from literature, a 4 mm thick cover made of glass is assumed for all investigated variants. As the heat losses are mainly influenced by the thickness of the backside insulation as well as the distance between glazing and absorber, a parametric study was performed in order to obtain ideal values for both properties.

The thickness of the backside insulation was varied in 5 mm increments between 5 mm and 100 mm, the distance between glazing and absorber was varied in 1 mm increments, ranging between 1 mm and 40 mm. This results in a total number of 800 different combinations. The ambient temperature T_{Amb} was set to a constant value of $25 \text{ }^\circ\text{C}$, the irradiation was defined as $1,000 \text{ W/m}^2$. In accordance with the standard EN ISO 9806:2013 (p. 60), the specific mass flow rate was set to $0.02 \text{ kg/(s m}^2)$, yielding a mass flow rate of 144 kg/h . For inlet temperatures ranging between $10 \text{ }^\circ\text{C}$ and $0 \text{ }^\circ\text{C}$ (in $20 \text{ }^\circ\text{C}$ increments), the resulting efficiency curve was determined according to equation 2.4. In order to compare the different setups, the efficiency was evaluated at a reduced temperature of $0.05 \text{ K m}^2/\text{W}$, which is a representative operating point for FPCs (Kaltschmitt, 2013, p. 201).

With increasing thickness of the backside insulation and distance between glazing and absorber, the resulting efficiency increases, too (cf. figure 4.15). A maximum of the efficiency can be identified when the air gap between glazing and absorber is 12 mm (cf. figure 4.15, blue curve).

4 Collector Simulation

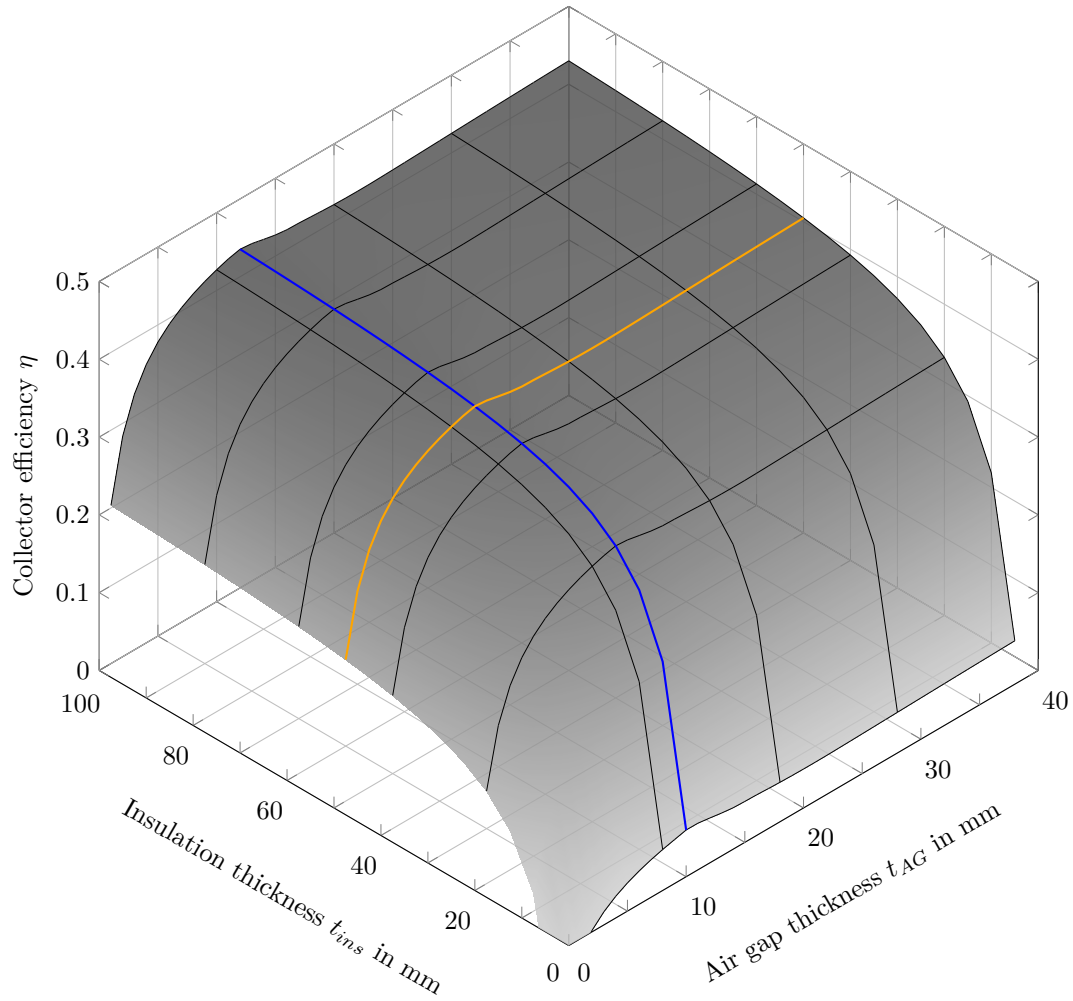


Figure 4.15: Results of a parametric study of a polymeric FPC with a PP absorber. Contour line for an air gap thickness of 12 mm (—), Contour line for an insulation thickness of 50 mm (—).

This can be attributed to the heat transfer between these two components due to natural convection (cf. section 4.3.2). For insulation thicknesses larger than 50 mm (cf. figure 4.15, red curve), a further increase of the efficiency is limited. As a result, an air gap distance between glazing and absorber of 12 mm in combination with a 50 mm thick backside insulation can be identified as suitable parameters.

The efficiency curve of this particular collector is plotted against data obtained from measurements (cf. figure 4.16). The results indicate that the simulated collector design has a significantly higher efficiency compared to the tested prototypes. Evaluating the efficiency at a representative operating point for DHW applications ($0.05 \text{ K m}^2/\text{W}$) yields a value of 37.9%. This value is 5.1 p.p. higher than the best tested prototype and 8.9 p.p. higher than the best market available polymeric collector (cf. table 3.4).

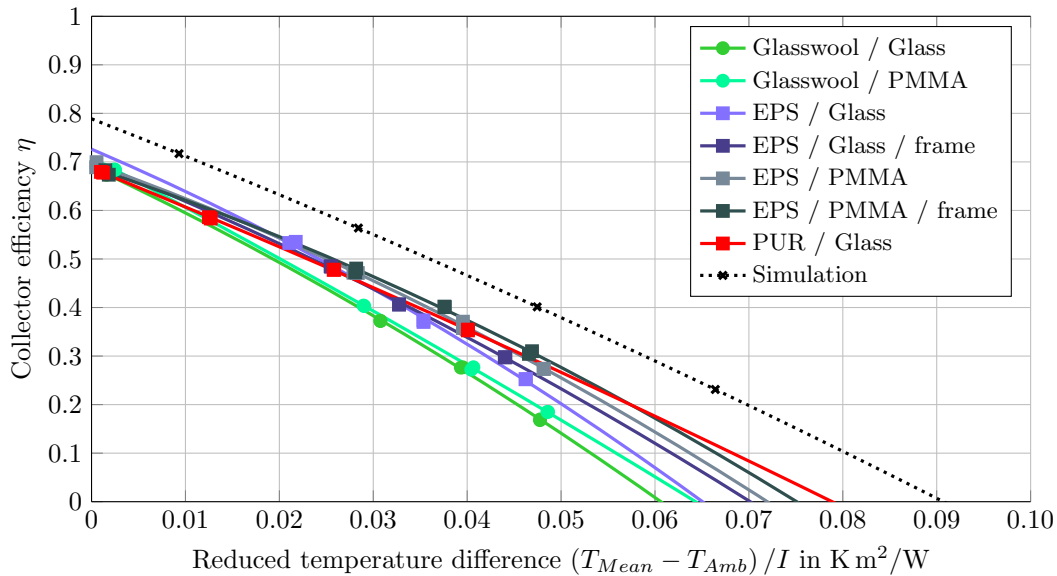


Figure 4.16: Comparison of measured and simulated collector prototypes. The data points indicate the measured / simulated values, the polynomials represent the resulting collector efficiency curves.

4.7 Summary

The developed simulation model was validated with measurement data from four different collector prototypes, which differ in size, material and setup. The results indicate a high correlation between measured and simulated data, both in case of steady-state and dynamic boundary conditions.

Based on this validation, a parametric study was performed in order to investigate ideal parameters for a 2 m² polymeric solar thermal FPC made of PP. The derived, optimised collector design shows a 5.1 p.p. higher efficiency compared to the best tested prototype. Therefore, it is advisable to incorporate the findings of the parametric study into the design of a polymeric solar thermal FPC.

The derived collector efficiency data are the basis for determining the technical performance of a DBS with such polymeric solar thermal FPCs (cf. chapter 6).

5 Experimental Analysis on System Level

In order to test the behaviour of the developed collector prototypes under realistic conditions, a system test rig was designed and set up. In contrast to the investigations on component level (cf. chapter 3), the system test rig is aiming at a holistic investigation of a solar thermal DBS with polymeric FPCs. Besides the determination of relevant component and system temperatures, the evaluation of the solar thermal yield is of major interest. The system test rig emulates the behaviour of a small DHW system. The hydraulic and the metrological setup are integrated into a 20 ft container, the collector array as well as a weather station (to monitor environmental boundary conditions) are mounted on top of the container. A schematic setup of the test rig is shown in figure 5.1, a photograph of the container can be found in the appendix (cf. figure A.2). The hydraulics of the test rig are shown in figure 5.2.

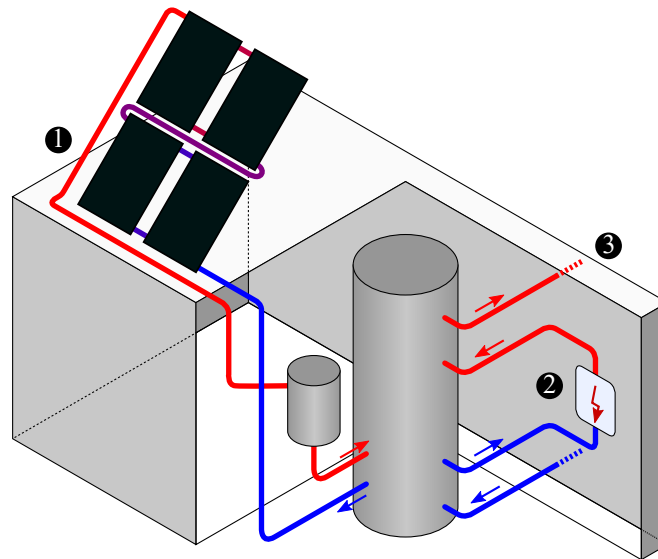


Figure 5.1: Schematic sketch of the system test rig. ① = Solar thermal collector array with drain back reservoir, ② = Electric backup heater, ③ = DHW tapping.

Central element of the test rig is a 500 l storage tank (cf. figure 5.2, centre) made of a fibre-plastic-composite material (Roth Werke GmbH, 2013, p. 21). The storage has two separate corrugated tube heat exchangers and can be charged with heat from a solar thermal collector array (cf. figure 5.2, left). If the amount of solar heat is not sufficient to cover the DHW demand, the heat storage can be charged by a conventional heat source (cf. figure 5.2, outer right). The energy stored inside the storage tank can be utilised to provide DHW (cf. figure 5.2, right). Four PT100 temperature sensors are equally distributed over the height of the heat storage (at $0/3$, $1/3$, $2/3$ and $3/3$ of the relative height). Every hydraulic loop is equipped with necessary sensors to evaluate the flow rate as well as the temperature into and out of the heat storage tank.

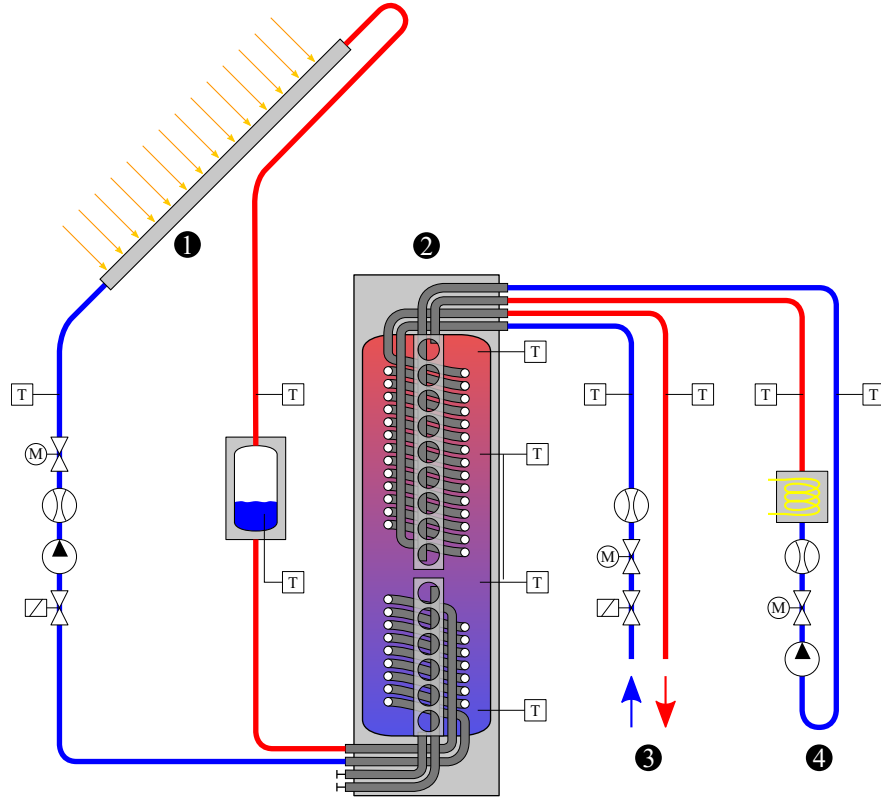


Figure 5.2: Hydraulic setup of the system test rig. ① = Solar thermal collector array with drain back reservoir, ② = Heat storage tank, ③ = Cold and hot water pipeline for DHW tapping, ④ = Backup heating loop with electric heater.

The temperature-dependent specific heat capacity c_p as well as the density ρ is obtained from a polynomial function according to EN ISO 9806:2013 (pp. 120-122) for the average temperature between inlet and outlet. As a result, the effective heat gain (provided by the backup heating and / or solar heating loop) and the consumption (due to DHW tapping) can be determined according to equation 5.1.

$$\dot{Q} = \dot{V} \cdot \rho \cdot c_p \cdot (T_H - T_C) \quad (5.1)$$

where:

| | |
|-----------|---|
| \dot{Q} | = Heat flux in W |
| \dot{V} | = Volume flow rate in m^3/s |
| ρ | = Density of the water in kg/m^3 |
| c_p | = Specific heat capacity of the water in $\text{J}/(\text{kg K})$ |
| T_H | = Hot water temperature in K |
| T_C | = Cold water temperature in K |

5.1 Solar Collector Loop

The system was set up as a DBS with four polymeric collectors. These collectors are identical prototypes compared to the collectors tested on the solar simulator (cf. chapter 3). Each collector has a gross surface area of 0.59 m^2 , yielding an overall collector array area of 2.36 m^2 . To minimise the backside heat losses, each collector has a 30 mm thick insulation made of glass wool. In addition, a 10 mm thick wooden plate was mounted to mechanically stabilise the collector. To minimise the front side heat losses, the collectors are covered with a 4 mm plate made of glass. Further details of the utilised collector prototypes can be found in table 3.2 (c). The four collector prototypes are serially connected, mounted under 45° and south-orientated (cf. figure 5.1). Two PT100 sensors are mounted upstream and downstream of the collector array to determine the useful temperature gain. To ensure a proper self-draining of the collector array in case of a pump standstill, all collectors are inclined approximately 5° to the horizontal. Two pumps connected in series were used to circulate the HTF (pure water) within the solar collector loop (cf. figure 5.2, left). Within the solar collector loop, two solenoid valves are installed to either operate one or both pumps. A motor control valve was installed to ensure a constant mass flow rate. This volume flow rate was set to approximately 150 l/h for the experiments performed on the system test rig. After leaving the collector array, the HTF flows into a drain back reservoir. The drain back reservoir is a 142.5 l , box-shaped storage tank which was insulated with a pour-in insulation. A PT100 sensor was used to measure the temperature of the HTF inside the reservoir. A photograph of the drain back reservoir can be found in the appendix (cf. figure A.5). A Coriolis mass flow meter with a measurement error lower than $\pm 0.5 \%$ (Krohne Messtechnik GmbH, 2013, p. 8) was used to determine the mass flow rate within the solar collector loop (cf. figure A.4). In contrast to a temperature difference controller (which is typically used to start / stop the solar pump within a conventional solar thermal system, cf. chapter 2), a mixed temperature- and irradiation-based algorithm was chosen to control the solar loop of the system test rig. As long as the system stays in idle mode, a pyranometer continuously measures the in-plane irradiation. In the case when the irradiation exceeds a threshold value of 700 W/m^2 , the controller switches on the pump. During normal operation, the temperature before and after the collector array is measured. As long as the outlet temperature is higher than the inlet temperature, the pump keeps operating.

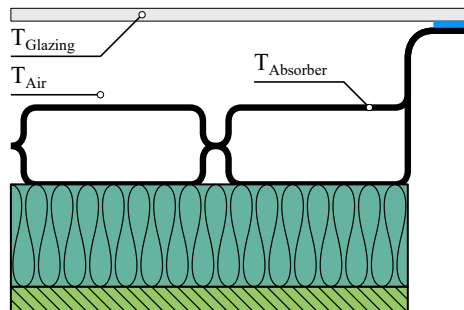


Figure 5.3: Position of temperature sensors mounted inside the collector prototype.

To account for the temperature of different components, three sensors (thermocouples) were mounted inside the collector. One sensor was connected to the inner side of the glazing

($T_{Glazing}$). The second sensor monitors the temperature of the upper part of the absorber ($T_{Absorber}$). The third sensor (T_{Air}) is mounted inside the gap between glazing and absorber and monitors the temperature of the air inside this gap. The position of the sensors are shown in figure 5.3.

5.2 Backup Heating Loop

In case of insufficient solar irradiation, the necessary heat for covering the DHW is provided from the backup heating loop (cf. figure 5.2, outer right). Here, a pump circulates water through a 9 kW electrical backup heater. The mass flow can be adjusted with a motor control valve, the resulting flow rate can be evaluated by means of an inductive flow meter with a measurement error lower than $\pm 1\%$ (Krohne Messtechnik GmbH, 1993, p. 53). The temperature-dependent density ρ as well as the specific heat capacity c_p are both obtained from a polynomial function according to EN ISO 9806:2013 (pp. 120-122) for the average temperature between inlet and outlet. The same procedure was chosen for the DHW loop. Together with the temperature upstream and downstream the backup heater (determined by means of two PT100 sensors), the resulting heating power can be determined according to equation 5.1. A photograph of the backup heating loop is shown in the appendix (cf. figure A.4). The control strategy of the backup heating loop is based on a two point hysteresis controller. As soon as the temperature inside the storage tanks drops below $45\text{ }^\circ\text{C}$, both the electric backup heater as well as the pump are switched on. Once the temperature in the storage tank exceeds a value of $48\text{ }^\circ\text{C}$, the backup heater and the pump are switched off by the controller.

5.3 Domestic Hot Water Loop

The open DHW loop is shown in figure 5.2 (right beside the heat storage). In case of a hot water demand, a solenoid valve is opened to release hot water out of the heat storage. At the same time, a second valve opens, allowing cold water to flow into the storage tank. This cold water is heated up afterwards (either by the solar thermal collector array or the backup heater). A motor control valve was installed within this loop to control the volume flow rate (which was set to a constant value of approximately 200 l/h). The flow rate is measured with an inductive flow meter which has a measurement error lower than $\pm 1\%$ (Krohne Messtechnik GmbH, 1993, p. 53). Both the inlet and outlet temperature is measured by means of a PT100 sensor. Due to the pressure from the water supply, no pump is needed within this loop. Based on several boundary conditions, the standard VDI 4655:2008 defines typical DHW demand profiles. This standard serves as a basis to emulate a realistic tapping behaviour at the system test rig. The daily amount of DHW adds up to approximately 6 kWh.

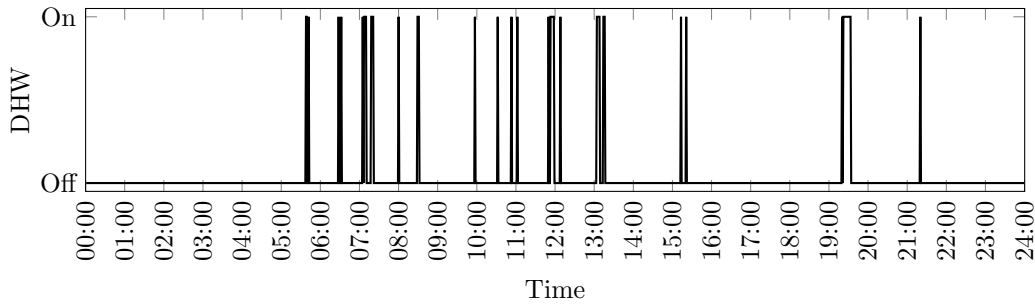


Figure 5.4: DHW tapping profile used in the system test rig.

Figure 5.4 shows the profile of the tapping throughout the day. Apart from larger heat demands in the morning, around noon and in the evening hours, minor tapplings are distributed over the day. In total, 23 individual tapplings are distributed over the day, where each tapping withdraws 1.9% – 22.2% of the daily DHW amount.

5.4 Test Results and Discussion

The results of testing on system level as described above shown on two representative, consecutive days. While the first day represents a sunny summer day with a maximum level of irradiation (in-plane of the collector array) of 942 W/m^2 and a maximum ambient temperature of $30.2 \text{ }^\circ\text{C}$, the second day was cloudy (maximum level of irradiation of 456 W/m^2) and cooler (maximum ambient temperature of $18.9 \text{ }^\circ\text{C}$). The weather conditions as well as the component temperatures present at these two days can be seen in figures 5.5 and 5.6.

On 25.06.2016, the level of irradiation increases significantly around 11 AM and decreases around 4:30 PM due to a passing field of clouds. The first phenomenon can be attributed to the location of the system test rig. Due to a small forest close to the container, the collector array gets shaded in the morning and evening hours. As soon as the collectors are exposed to the sun, the components heat up quickly ($T_{Absorber} = 77.0 \text{ }^\circ\text{C}$, $T_{Air} = 66.5 \text{ }^\circ\text{C}$, $T_{Glazing} = 44.7 \text{ }^\circ\text{C}$). At 11:06 AM, the incident irradiation is greater than the pre-defined threshold, leading the solar controller to circulate water through the hydraulic loop. As a result, the incoming irradiation is transferred to the HTF, causing a significant drop of the component temperatures. After 5 minutes of operation, the temperature difference between the inlet and outlet of the collector array is evaluated. As the temperature out of the collector array (T_{Outlet}) is lower than the temperature of the water flowing into the collector (T_{Inlet}), the controller switches off the pumps and stays in idle mode until 11:14 AM. As the amount of incident irradiation is still higher than the pre-defined threshold, the pumps are switched on again. As the collector array starts to produce heat ($T_{Outlet} > T_{Inlet}$) within the next 5 minutes, the pumps keep running throughout the day until 4:32 PM. During normal operation, the temperature of the absorber is lower than the temperature of the air inside the gap between absorber and glazing. The maximum temperatures are reached between 2 PM and 3 PM ($T_{Absorber} = 55.4 \text{ }^\circ\text{C}$, $T_{Air} = 59.3 \text{ }^\circ\text{C}$, $T_{Glazing} = 45.3 \text{ }^\circ\text{C}$). At 4:32 PM, the temperature out of the collector array drops below the inlet temperature ($T_{Outlet} < T_{Inlet}$), leading the pumps to be switched off.

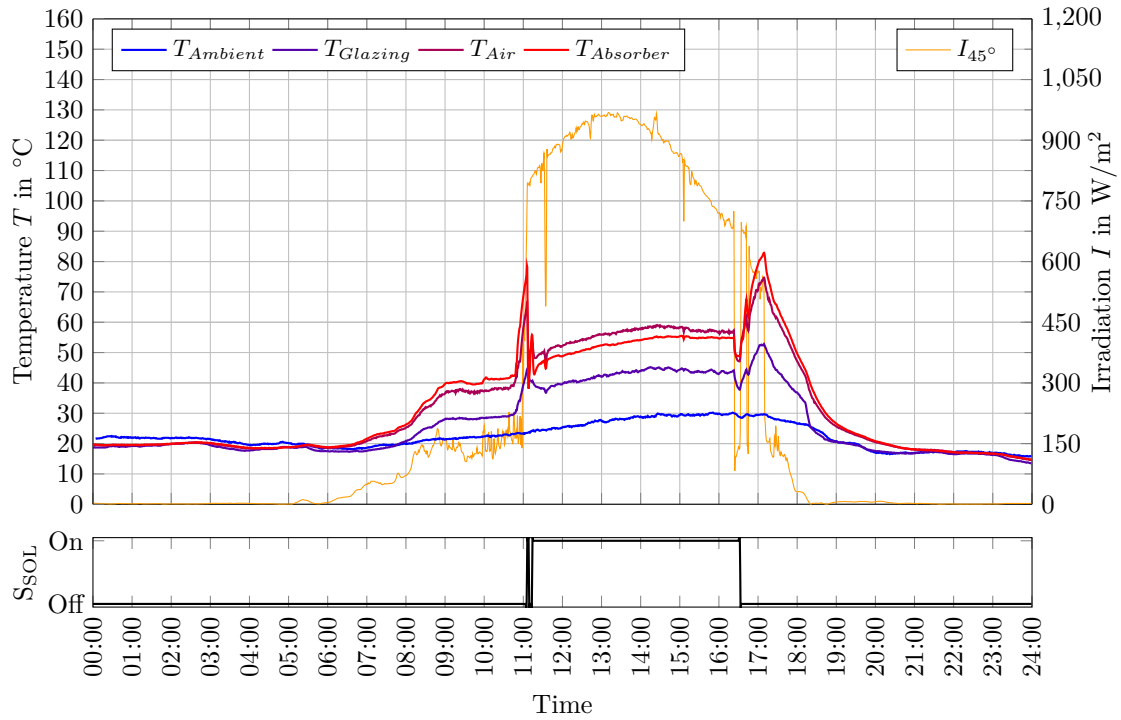


Figure 5.5: Temperatures inside the collector on 25.06.2016.

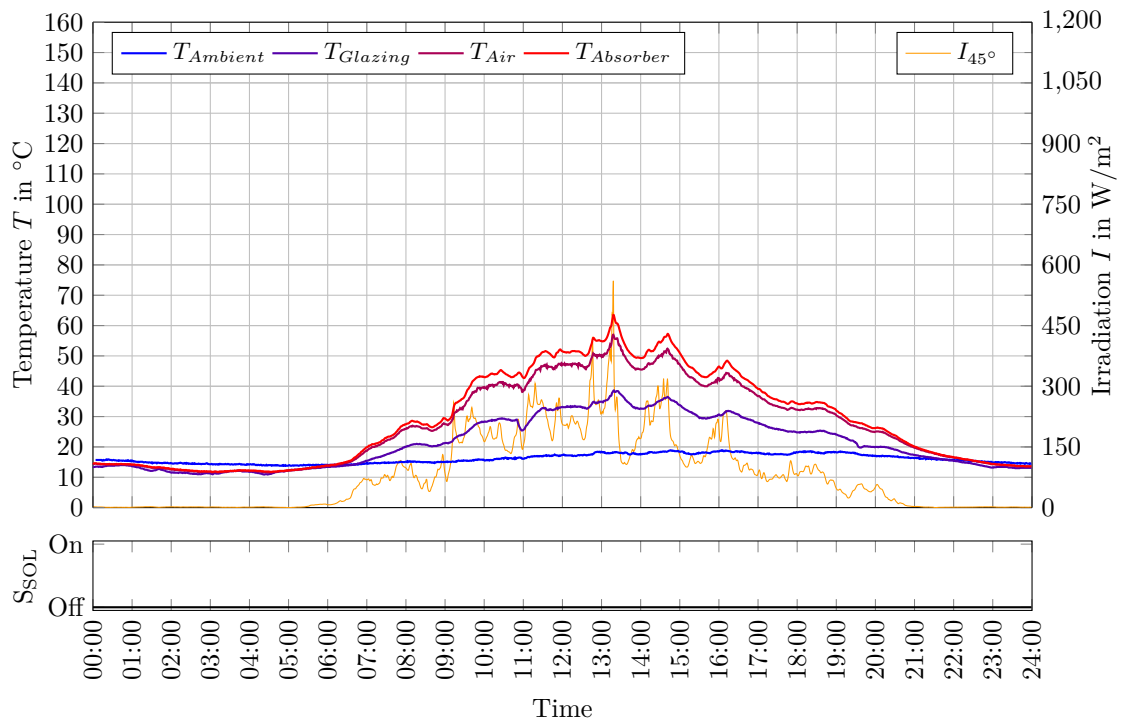


Figure 5.6: Temperatures inside the collector on 26.06.2016.

As the level of irradiation is lower than the pre-defined threshold for the rest of the day, the solar pumps remain in idle mode. As a result, the HTF flows back into the drain back

5 Experimental Analysis on System Level

reservoir. Similarly to the behaviour in the morning hours, the incident irradiation heats up the empty collector. However, the decreasing irradiation in the evening hours causes a less steep rise of the temperatures inside the collector.

On 26.06.2016, the level of incident irradiation is always lower than the threshold. Therefore, the pumps within the solar collector loop remained in idle mode throughout the whole day. The maximum temperatures occurred between 1 PM and 2 PM ($T_{Absorber} = 63.6^\circ\text{C}$, $T_{Air} = 57.5^\circ\text{C}$, $T_{Glazing} = 38.8^\circ\text{C}$).

The temperatures along the height of the storage are shown in figures 5.7 and 5.8. In addition to that, these diagrams show the signal of each hydraulic circuit (either on or off). Until 5:37 AM, the slope of the temperature sensors represent the thermal losses of the heat storage to the environment. It can be observed that the temperature of the drain back reservoir decreases faster than the temperature of the heat storage. This can be attributed to the worse insulation and higher area-to-volume-ratio of the drain back reservoir compared to the heat storage.

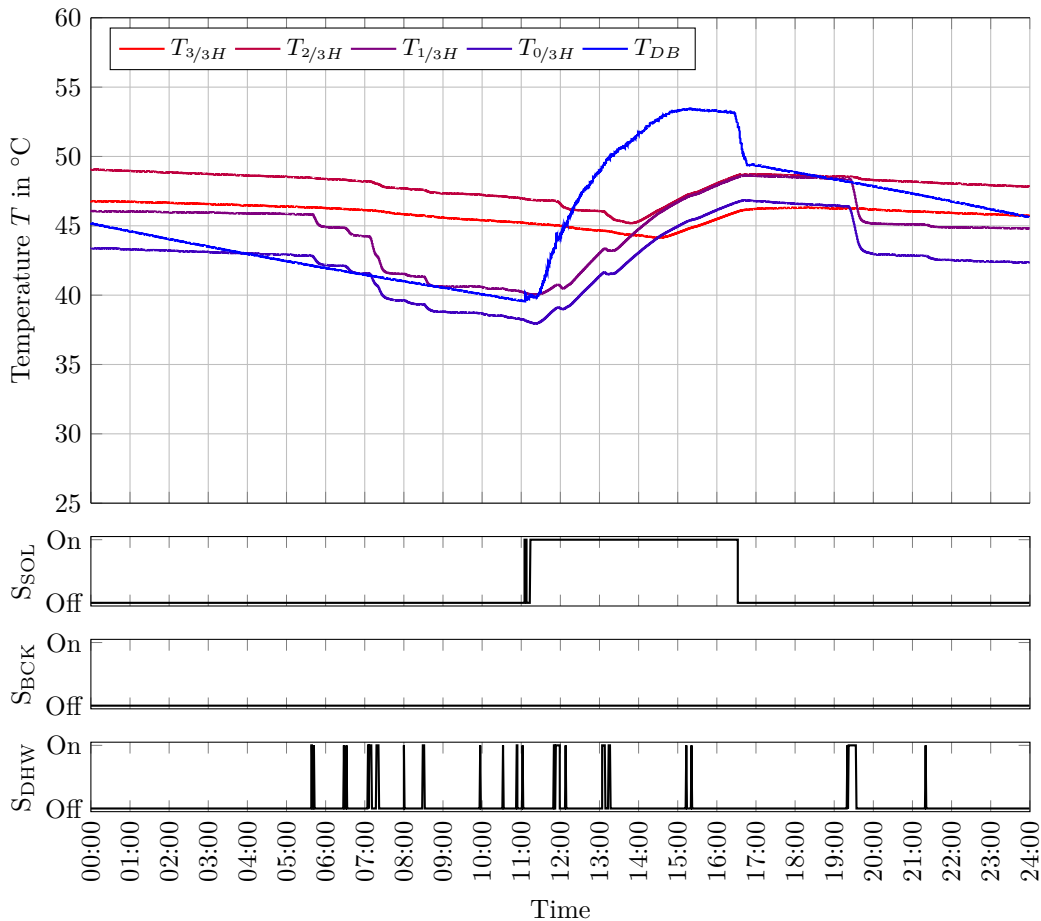


Figure 5.7: Temperatures inside the heat storage and states of the hydraulic loops on 25.06.2016. First diagram: Temperatures along the height of the storage tank ($T_{0/3H} - T_{3/3H}$) and inside the drain back reservoir (T_{DB}). Second diagram: Status of the solar loop. Third diagram: Status of the backup heating loop. Fourth diagram: Status of the DHW loop.

Assuming a uniform stratification of the water inside the storage tank, the temperature sensor located on top of the heat storage ($T_{3/3}$) should always be the highest one compared to the other sensors. For both days, figures 5.7 and 5.8 indicate that some air is trapped in the upper part of the heat storage. As a result, the temperature sensor located at the top of the heat storage monitors the temperature of the enclosed air (instead of the water inside the heat storage).

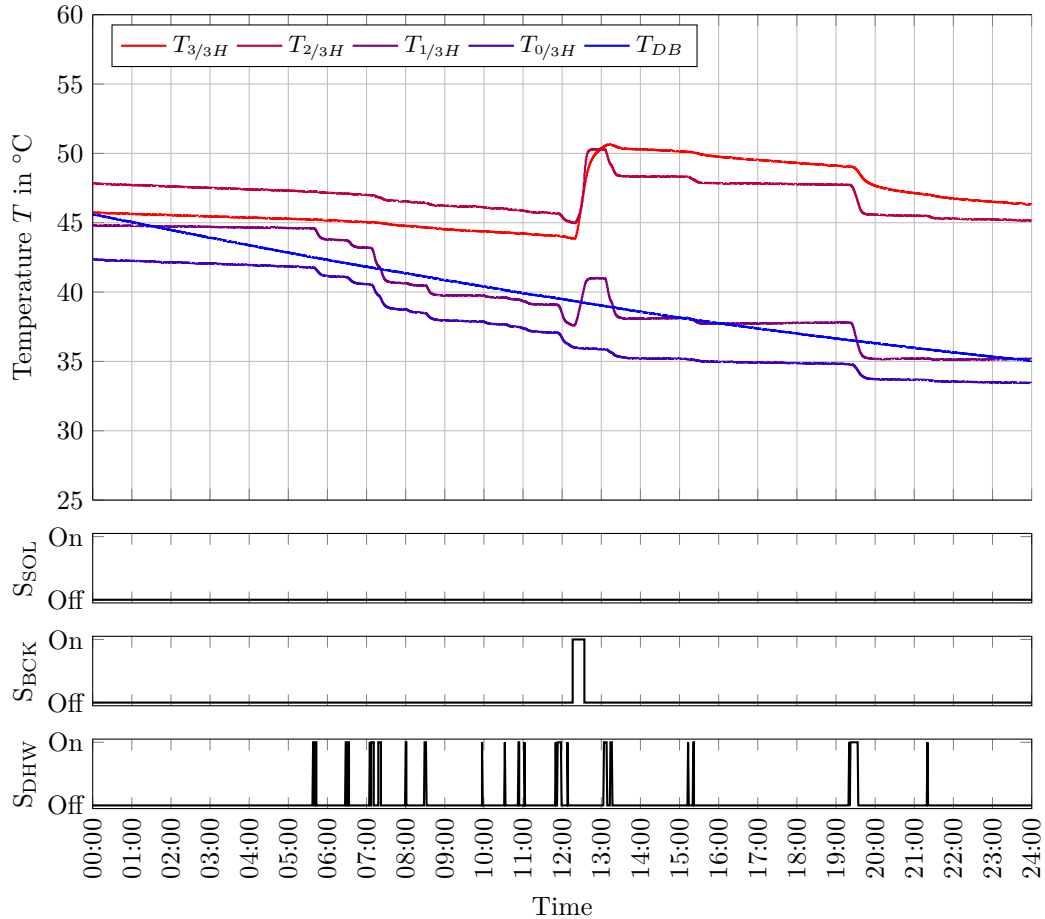


Figure 5.8: Temperatures inside the heat storage and states of the hydraulic loops on 26.06.2016. First diagram: Temperatures along the height of the storage tank ($T_{0/3H} - T_{3/3H}$) and inside the drain back reservoir (T_{DB}). Second diagram: Status of the solar loop. Third diagram: Status of the backup heating loop. Forth diagram: Status of the DHW loop.

Time and duration of the DHW tapplings are identical, as both days utilise the same profile (cf. section 5.3). However, the daily amount of heat which is drawn from the heat storage differs from 25.06.2016 (3.7 kW h) to 26.06.2016 (4.1 kW h). This can be attributed to the cold water supply of the system test rig: Before entering the test rig, the cold water pipe runs approximately 30 m close under the earth's surface. On sunny days (e.g. on 25.06.2016), the sun heats up the ground and consequently the water which enters the test rig. As a result, the daily amount of energy which is drawn from the heat storage on sunny days (such as the 25.06.2016) is smaller compared to cloudy days (such as 26.06.2016).

5 Experimental Analysis on System Level

Whenever hot water is drawn from the heat storage as a DHW tapping, cold water enters the heat storage, yielding a temperature drop at the bottom part of the storage tank (sensors $T_{0/3H}$ and $T_{1/3H}$). On 26.06.2016 at 12:16 PM, the temperature at $2/3$ of the storage height drops below $45\text{ }^{\circ}\text{C}$, yielding the electric backup heater as well as pump to be switched on. At 12:33 PM, the desired temperature of $48\text{ }^{\circ}\text{C}$ is reached. As a result, both the backup heater and the pump are switched off. On 25.06.2016, the heat demand for providing DHW (3.7 kW h) is completely covered by the solar thermal collector array (4.9 kW h). As the temperature of the sensor mounted at $2/3$ of the storage height never drops below $45\text{ }^{\circ}\text{C}$, the backup loop remains in idle mode on this day. Comparing the signals of the different temperature sensors indicates a much more noisy signal for the sensor mounted inside the drain back reservoir (T_{DB} , cf. figures 5.7 and 5.8). This behaviour is caused by the incoming water from the solar collector array that splashes into the water surface inside the drain back reservoir, yielding small spatial variations of the sensor position.

Data was monitored at the system test rig from end of June to end of October 2016. Within this 4-month period, a maximum collector outlet temperature of $55.5\text{ }^{\circ}\text{C}$ was measured. This value can be increased by adjusting the pump speed with a more sophisticated control algorithm. To enable a maximum temperature loading of the utilised collector prototypes, both solar pumps were shut off for two weeks with high levels of incident irradiation. A maximum temperature of $140\text{ }^{\circ}\text{C}$ was measured at the absorber, the sensor mounted at the inner side of the glazing monitored a maximum temperature of $112\text{ }^{\circ}\text{C}$. For the chosen absorber material PP, Domininghaus et al. (2012, p. 226) report a maximum permissible temperature for permanent operation of $100\text{ }^{\circ}\text{C}$ and $140\text{ }^{\circ}\text{C}$ for short-term operation. Kahlen, Wallner and Lang (2010) investigated the application of PP for solar thermal applications by means of material ageing experiments. Within a collector lifetime of 20 years, the authors identified an accumulated loading of PP with $80\text{ }^{\circ}\text{C}$ hot water (up to 16,000 h) and $140\text{ }^{\circ}\text{C}$ hot air (up to 500 h) as maximum operating conditions. Despite the short measurement period, the results obtained with the present system test rig support these figures. Within the 4-month period, no defects were found (neither on collector nor on system level). Instead, the proper functioning of the developed prototypes as well as the DBS was successfully demonstrated.

6 Simulation on System Level

In this chapter, a mathematical model for forecasting the system performance of a DBS with polymeric solar thermal FPCs is described. As the experimental results of the system test rig (cf. chapter 5) are limited to the measurement period, such a simulation model is necessary to assess the annual solar thermal yield. In addition, the solar thermal yield is an important prerequisite for determining the economic performance of a solar thermal system (cf. chapter 7).

6.1 Reference Models

The standard DIN EN 12977-2:2016 (p. 23) describes how solar thermal systems can be evaluated by means of simulation. The underlying evaluation criterion is the amount of fossil energy that can be saved by the solar thermal system with respect to a comparable, purely fossil-fuelled heating-system (cf. equation 6.1).

$$f_{sav} = \frac{Q_{Conv} - Q_{ST}}{Q_{Conv}} = 1 - \frac{Q_{ST}}{Q_{Conv}} \quad (6.1)$$

where:

| | |
|------------|--|
| f_{sav} | = Fractional energy savings |
| Q_{Conv} | = Fossil energy demand of a conventional heating system in kW h |
| Q_{ST} | = Fossil energy demand in case of using an additional solar thermal system in kW h |

The figure f_{sav} describes the technical efficiency of a solar thermal system with respect to a solely fossil-fuelled one. To obtain the system efficiency in case of solar thermal DBSs with polymeric FPCs, in a first step the fossil energy demand of a representative reference heating system (fossil-fuelled) has to be determined. Afterwards, the fractional energy savings f_{sav} of a solar thermal system with conventional, metal-based solar thermal FPCs are determined according to equation 6.1. In a third step, the fractional energy savings f_{sav} of a comparable solar thermal DBS with polymeric solar FPCs is evaluated. Comparing the fractional energy savings allows for a technical comparison of both solar thermal systems.

As the fossil energy demand of any heating system strongly depends on its location and the respective climate conditions, the aforementioned procedure is carried out at different reference locations. In this context, DIN EN 12977-2:2016 (p. 34) specifies Würzburg (Germany), Athens (Greece), Davos (Switzerland) and Stockholm (Sweden) as suitable reference locations in case of a simulation-based comparison of solar thermal systems. For these locations, relevant weather information (such as direct and diffuse irradiation, ambient temperatures etc.) were obtained in 1 h intervals from the software Meteonorm 7.3. The tapping cycle L was used to emulate realistic DHW tapplings (DIN EN 12977-2:2016 p.13). The profile of

6 Simulation on System Level

the space heating demand as well as relevant weather information for Würzburg can be seen in figure 6.1, the DHW profile applied can be seen in figure 6.2. Information regarding the other reference locations can be found in the appendix (cf. section F.1).

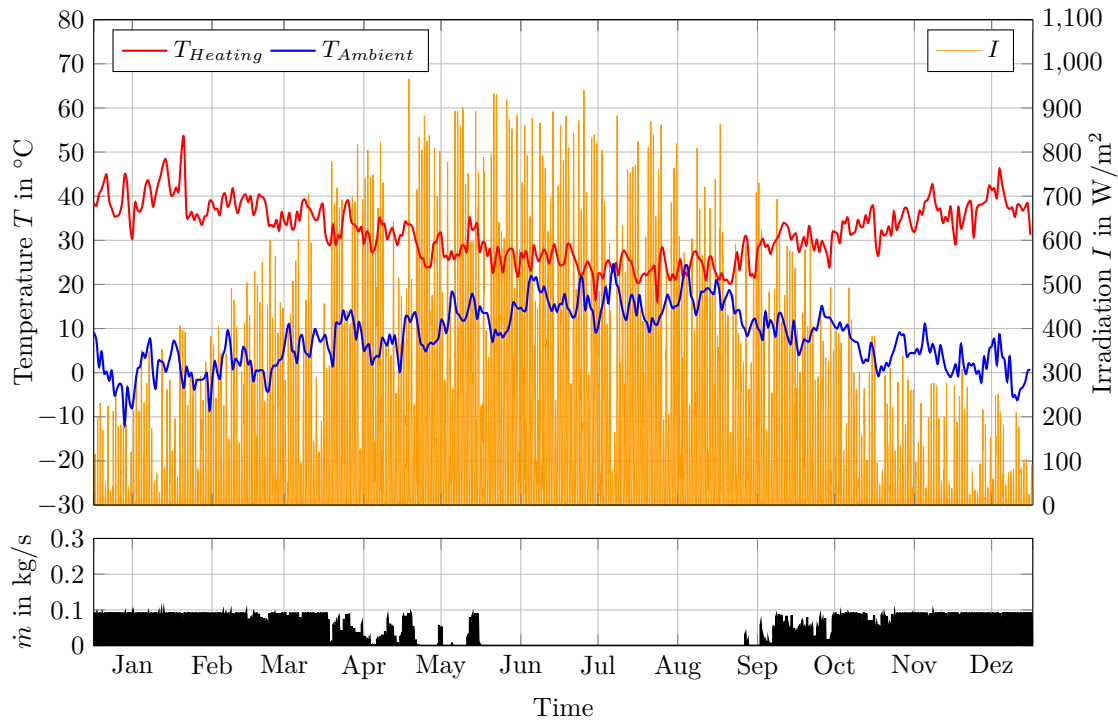


Figure 6.1: Weather conditions and heating parameters (flow temperature and mass flow rate) at the reference location Würzburg (Germany). Minimum / maximum ambient temperature: -12.2°C / 32.1°C . Maximum irradiation: $966 \text{ W}/\text{m}^2$. Maximum heating flow temperature: 54.4°C . Weather data source: Meteonorm 7.3, load profile data source: DIN EN 12977-2:2016 (pp. 30-39).

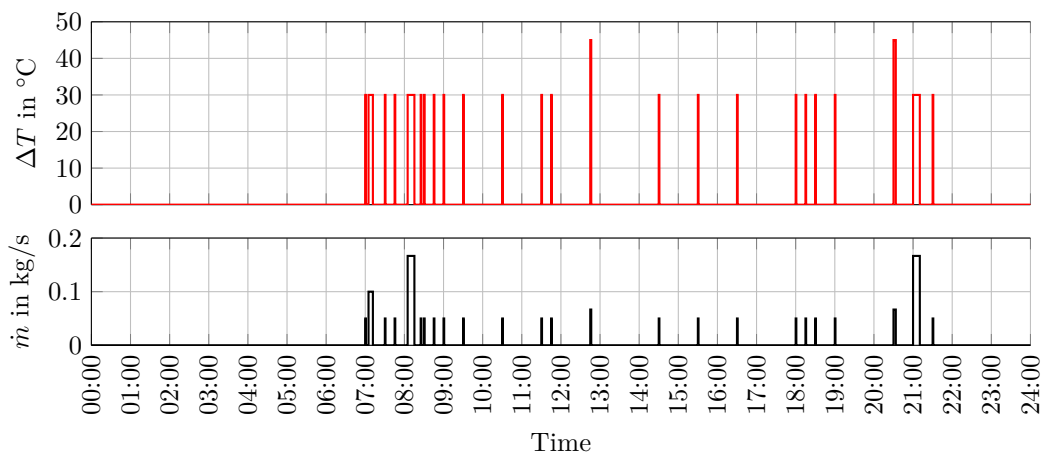


Figure 6.2: Tapping profile L according to DIN EN 13203-2:2015 (p. 13). The displayed temperature represents the difference between the hot water temperature and a cold water temperature (e.g. 10°C) that enters the system.

Within the framework of IEA SHC¹³ Task 54, both a characteristic conventional (i.e. fossil-fuelled) system as well as two different types of solar thermal systems were defined. These reference systems will be used as a benchmark for solar thermal DBSs with polymeric FPCs based on the concept of fractional energy savings f_{sav} (cf. equation 6.1). The reference models were set up using MATLAB / Simulink in combination with the CARNOT 5.3 toolbox.

6.1.1 Conventional Reference System

As mentioned above, the concept of fractional energy savings requires information regarding the energy demand of a solely fossil-fuelled heating system (cf. equation 6.1, Q_{Conv}). Figure 6.3 shows the hydraulic setup of a typical fossil-fuelled system located in Germany (Bachmann, Fischer and Hafner, 2018a). The core of the system is a 150l DHW storage tank, which is supplied with heat by a 19kW gas boiler. Once the temperature inside the storage tanks drops below the minimum temperature of 55 °C, the gas boiler heats up the storage tank until it reaches a temperature of 60 °C. Alternatively, the gas boiler covers the heat demand of the space heating. Two flow mixers are installed to mix the hot water from the upper part of the storage tank (in case of the DHW tapping) and / or from the furnace (in case of the space heating) to the respective temperature.

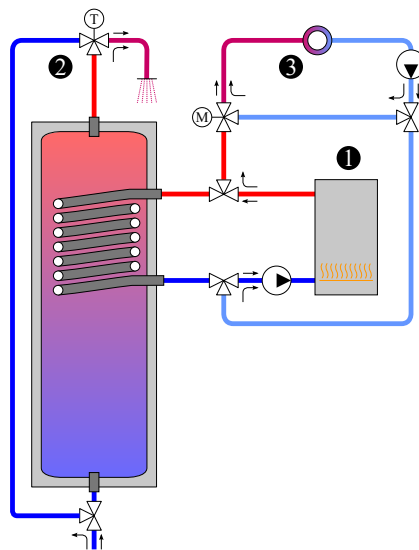


Figure 6.3: Hydraulic setup of the conventional reference system according to Bachmann, Fischer and Hafner (2018a). ① = Heater, ② = DHW tapping, ③ = Heat distribution (heating).

The results of the developed MATLAB / Simulink / CARNOT 5.3 simulation model in contrast to data provided by Bachmann, Fischer and Hafner (2018a) are shown in table 6.1. Comparing the overall fossil fuel demand of the furnace indicates a tolerable correlation between the developed MATLAB / Simulink / CARNOT 5.3 simulation model with the original results provided by Bachmann, Fischer and Hafner (2018a).

¹³ International Energy Agency Solar Heating & Cooling Programme

6 Simulation on System Level

Table 6.1: System properties of the conventional reference system (Task 54) and comparison with the developed MATLAB / Simulink / CARNOT 5.3 model. Positive / negative numbers indicate heat fluxes into / out of each subsystem, empty cells indicate that there is no information available.

| Physical quantity | Task 54 data | Simulation model | Deviation | |
|--|---------------------------|------------------|----------------|--------|
| Heat storage volume | | 1501 | | |
| Conventional heat source | 19 kW gas heating boiler | | | |
| Heat demand DHW ¹ | 4,254 kW h/a | | | |
| Heat demand space heating ² | 9,090 kW h/a | | | |
| Storage | Storage losses | -751 kW h/a | -920 kW h/a | 22.5 % |
| | DHW consumption | | -4,256 kW h/a | |
| | Gas boiler | | 5,177 kW h/a | |
| Boiler | Heat supply space heating | -9,090 kW h/a | -9,082 kW h/a | 0.1 % |
| | Heat supply storage | -5,009 kW h/a | -5,177 kW h/a | 3.4 % |
| | Heat generation | 14,099 kW h/a | -14,287 kW h/a | 1.3 % |
| | Fossil fuel demand | 15,666 kW h/a | 15,875 kW h/a | 1.3 % |

¹ according to DIN EN 13203-2:2015 (p. 13)

² according to DIN EN 12977-2:2016 (p. 36)

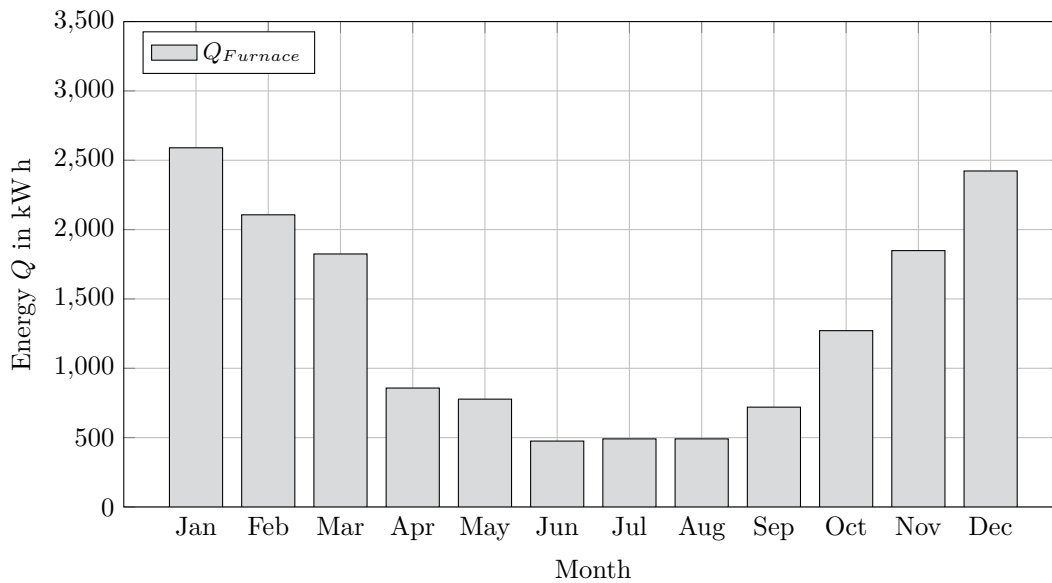


Figure 6.4: Distribution of the fossil fuel demand in case of the conventional reference system (Task 54) located in Würzburg (Germany).

Figure 6.4 shows the distribution of the fossil fuel demand throughout the observation period of one year. As expected, the highest energy demand occurs in the winter months, the least amount of energy is required during the summer months.

6.1.2 Solar Domestic Hot Water System

In this setup, the conventional reference system (cf. section 6.1.1) is supplemented with a 5 m^2 solar thermal collector array (cf. figure 6.5).

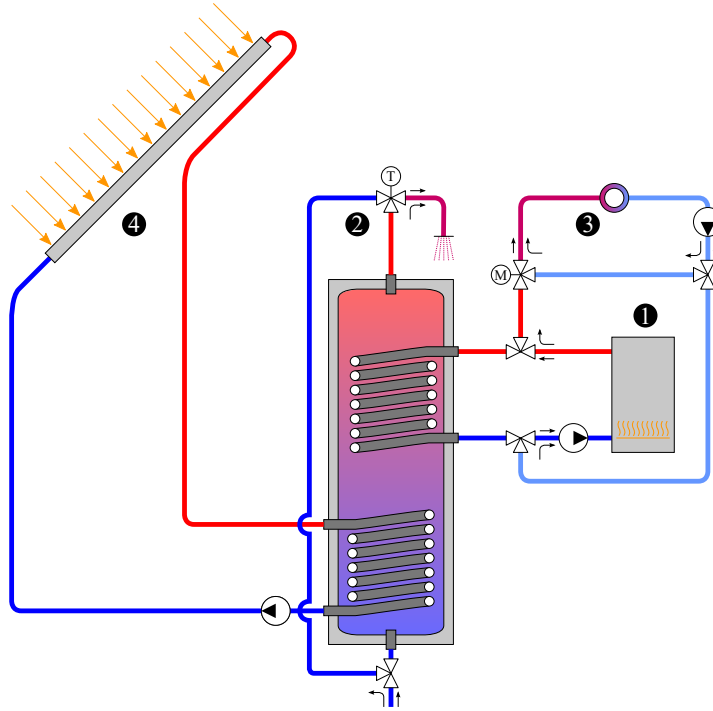


Figure 6.5: Hydraulic setup of the solar DHW system according to Bachmann, Fischer and Hafner (2018c). ① = Heater, ② = DHW tapping, ③ = Heat distribution (heating), ④ = Solar thermal collector array.

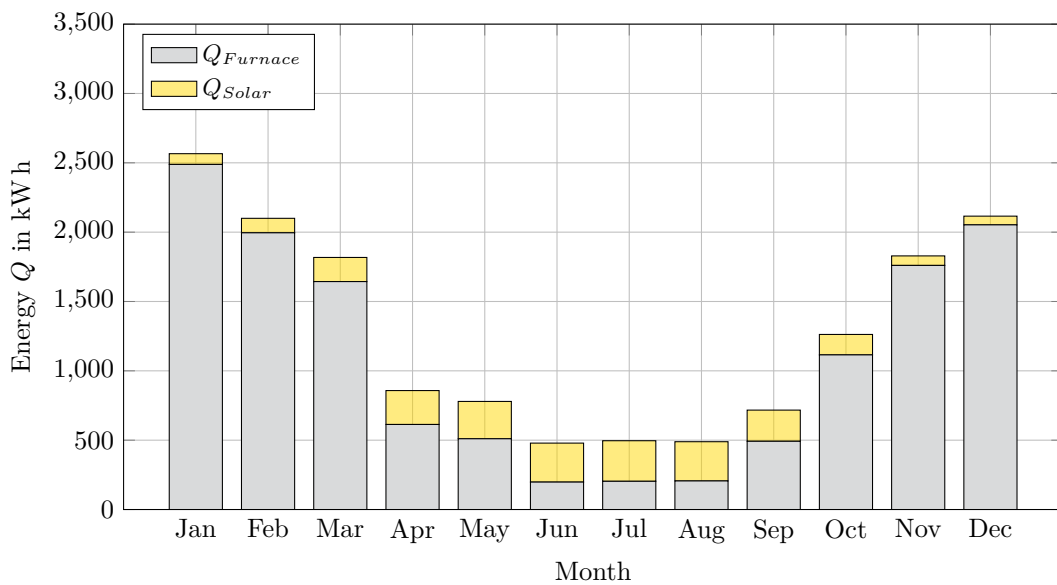


Figure 6.6: Distribution of the fossil fuel demand / solar yield in case of a solar DHW system with metal-based solar thermal FPCs (Task 54) located in Würzburg (Germany).

6 Simulation on System Level

In case of sufficient irradiation, the collector array will heat up the lower part of the 300 l storage tank. Due to the decreased density, the heated water rises inside the heat storage to the upper part, where it can either directly contribute to the DHW demand (especially during summer) or indirectly by preheating the water for the 19 kW fossil-fuelled furnace. The most relevant boundary conditions of the system are shown in the upper part of table 6.2, the lower part shows the results of the developed MATLAB / Simulink / CARNOT 5.3 simulation model in contrast to data provided by Bachmann, Fischer and Hafner (2018c).

Table 6.2: Results of the solar DHW system simulation with MATLAB / Simulink / CARNOT 5.3 in comparison to Task 54 results (metal-based solar thermal FPCs used). Positive / negative numbers indicate heat fluxes into / out of each subsystem, empty cells indicate that there is no information available.

| Physical quantity | Task 54 data | Simulation model | Deviation | |
|--|--|------------------|-----------------|-------|
| Heat storage volume | | 300 l | | |
| Conventional heat source | 19 kW gas heating boiler | | | |
| Collector array ¹ | $2 \times 2.5 \text{ m}^2 = 5.0 \text{ m}^2$ | | | |
| Heat demand DHW ² | 4,254 kW h/a | | | |
| Heat demand space heating ³ | 9,090 kW h/a | | | |
| Storage | Storage losses | -889 kW h/a | | |
| | DHW consumption | -4,256 kW h/a | | |
| | Collector array | 2,027 kW h/a | | |
| | Gas boiler | 3,114 kW h/a | | |
| Boiler | Heat supply space heating | -9,090 kW h/a | -9,082 kW h/a | 0.1 % |
| | Heat supply storage | -3,002 kW h/a | -3,114 kW h/a | 3.7 % |
| | Heat generation | 12,092 kW h/a | 12,214 kW h/a | 1.0 % |
| | Fossil fuel demand | 13,435 kW h/a | 13,571 kW h/a | 1.0 % |
| Solar | Collector yield | | 2,607 kW h/a | |
| | Pipe losses (indoor) | | -183 kW h/a | |
| | Pipe losses (outdoor) | | -195 kW h/a | |
| | Solar yield | 2,288 kW h/a | 2,230 kW h/a | 2.6 % |
| Energy saving ⁴ | 2,226 kW h/a | 2,304 kW h/a | 3.5 % | |
| f_{sav} | 14.2 % | 14.5 % | 0.3 p.p. | |

¹ Metal-based solar thermal FPCs: $\eta_0 = 0.683$, $a_1 = 3.51 \text{ W}/(\text{m}^2 \text{ K})$, $a_2 = 0.011 \text{ W}/(\text{m}^2 \text{ K}^2)$

² according to DIN EN 13203-2:2015 (p. 13)

³ according to DIN EN 12977-2:2016 (p. 36)

⁴ with respect to the conventional reference system

The installed collector array enables an energy saving of $> 2,200 \text{ kW h/a}$, yielding fractional energy savings f_{sav} of approximately 14%. Only a minor deviation between the simulation model and the reference data can be observed. Comparing figure 6.4 with figure 6.6 indicates, that fossil energy is mainly saved from April to September. This can be attributed to the fact that the solar thermal collector array provides most energy during these months.

6.1.3 Solar Combi System

Due to the hydraulic setup of this system, the 15 m² collector array can both contribute to the DHW and to the space heating demand of the system (cf. figure 6.7).

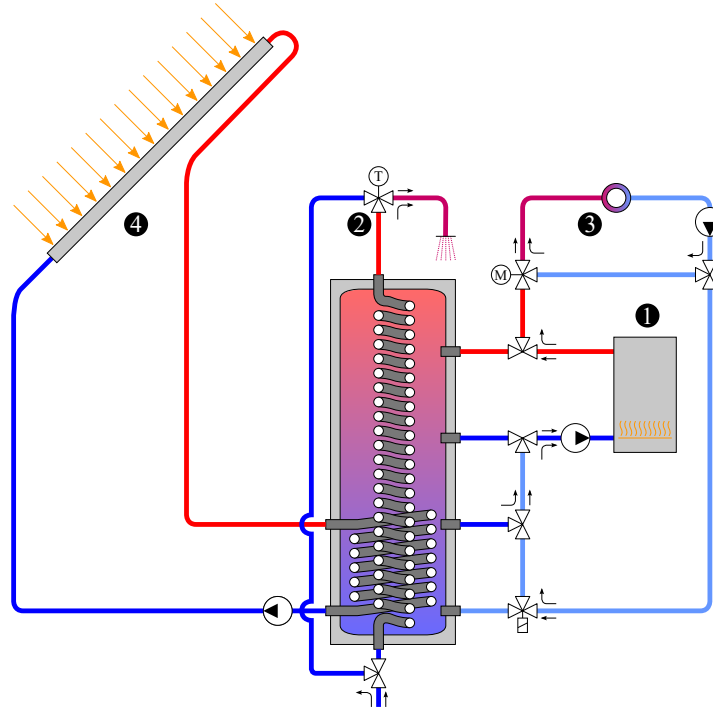


Figure 6.7: Hydraulic setup of the solar combi system according to Bachmann, Fischer and Hafner (2018b). ① = Heater, ② = DHW tapping, ③ = Heat distribution (heating), ④ = Solar thermal collector array.

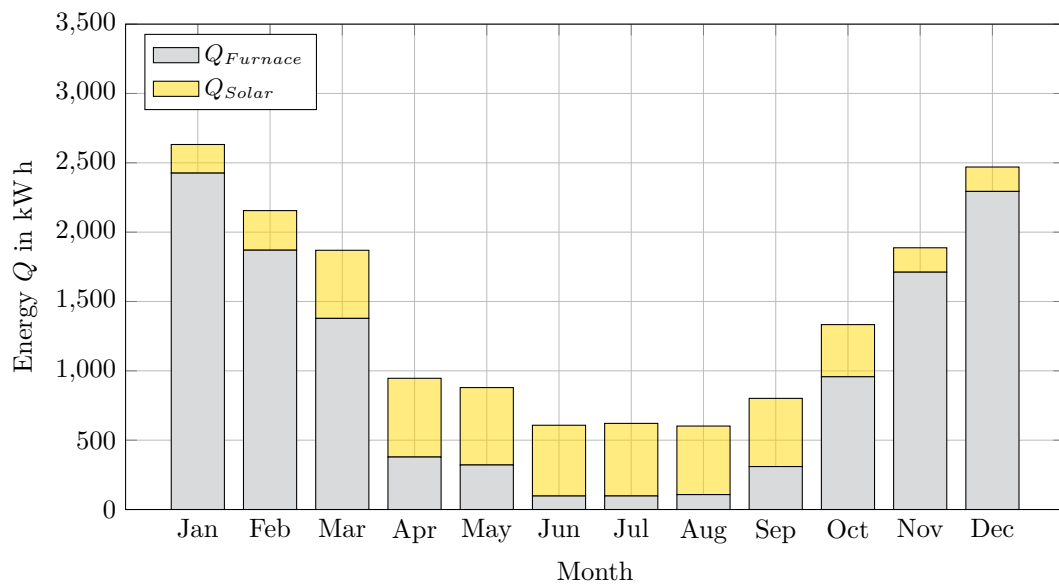


Figure 6.8: Distribution of the fossil fuel demand / solar yield in case of solar combi system with metal-based solar thermal FPCs (Task 54) located in Würzburg (Germany).

6 Simulation on System Level

In case of insufficient irradiation, the 19 kW furnace can directly heat up water from the 800 l storage tank to cover the necessary heat demand (similar to the setup described in section 6.1.2). In case of sufficient irradiation, the heat delivered from the collector array can be used to preheat the water flowing back to the gas boiler as well as to heat up the DHW inside the heat storage. The most relevant boundary conditions of the system are shown in the upper part of table 6.3, the lower part shows the results of the developed MATLAB / Simulink / CARNOT 5.3 simulation model in contrast to data provided by Bachmann, Fischer and Hafner (2018b). The installed collector array enables an energy saving of $> 3,100 \text{ kW h/a}$, yielding fractional energy savings f_{sav} of approximately 20%. Only a minor deviation between the simulation model and the reference data can be observed. A comparison of the monthly fossil energy consumption as well as the solar yield (cf. figures 6.6 and 6.8) indicates that the solar combi system allows for a utilisation of the solar heat not only in the summer, but also during the transitional periods in spring and autumn.

Table 6.3: Results of the solar combi system simulation with MATLAB / Simulink / CARNOT 5.3 in comparison to Task 54 results (metal-based solar thermal FPCs used). Positive / negative numbers indicate heat fluxes into / out off each subsystem, empty cells indicate that there is no information available.

| Physical quantity | Task 54 data | Simulation model | Deviation | |
|--|---|------------------|-----------------|-------|
| Heat storage volume | | 800 l | | |
| Conventional heat source | 19 kW gas heating boiler | | | |
| Collector array ¹ | $6 \times 2.5 \text{ m}^2 = 15 \text{ m}^2$ | | | |
| Heat demand DHW ² | 4,254 kW h/a | | | |
| Heat demand space heating ³ | 9,090 kW h/a | | | |
| Storage | Storage losses | -2,041 kW h/a | 2.7 % | |
| | DHW consumption | -4,258 kW h/a | | |
| | Collector array | 4,582 kW h/a | | |
| | Gas boiler | 3,422 kW h/a | | |
| | Return-flow boost | -1,762 kW h/a | | |
| Boiler | Heat supply space heating | -7,506 kW h/a | -7,321 kW h/a | 2.5 % |
| | Heat supply storage | -3,743 kW h/a | -3,422 kW h/a | 8.6 % |
| | Heat generation | 11,249 kW h/a | 10,753 kW h/a | 4.4 % |
| | Fossil fuel demand | 12,499 kW h/a | 11,948 kW h/a | 4.4 % |
| Solar | Collector yield | | 5,369 kW h/a | |
| | Pipe losses (indoor) | | -250 kW h/a | |
| | Pipe losses (outdoor) | | -262 kW h/a | |
| | Solar yield | 4,541 kW h/a | 4,857 kW h/a | 7.0 % |
| Energy saving ⁴ | 3,162 kW h/a | 3,927 kW h/a | 24.2 % | |
| f_{sav} | 20.2 % | 24.7 % | 4.5 p.p. | |

¹ Metal-based solar thermal FPCs: $\eta_0 = 0.683$, $a_1 = 3.51 \text{ W}/(\text{m}^2 \text{ K})$, $a_2 = 0.011 \text{ W}/(\text{m}^2 \text{ K}^2)$

² according to DIN EN 13203-2:2015 (p. 13)

³ according to DIN EN 12977-2:2016 (p. 36)

⁴ with respect to the conventional reference system

6.2 Simulation Model Validation

The evaluation of the annual energy savings shows a high correlation between the developed simulation models (both the solar DHW system as well as the solar combi system) with respect to data from literature. However, no reference data are available for a DBS with polymeric solar thermal FPC. To evaluate the validity of the MATLAB / Simulink / CARNOT 5.3 simulation model for such a setup, the model was adopted to the boundary conditions present at the system test rig (cf. chapter 5). The simulation model was set up according to the hydraulic scheme of the system test rig (cf. figure 5.2), the control algorithms for both the solar loop as well as the backup heating loop were integrated into the simulation model. The temperature distribution inside the storage was initialised with measurement data obtained from the system test rig. Further boundary conditions such as weather data (i.e. ambient temperature and irradiation) as well as DHW consumption and DHW demand were applied to the simulation model.

Two consecutive days in summer 2016 were chosen to validate the simulation model. Both days represent sunny days with comparable ambient temperatures and irradiation levels throughout the day. On both days, heat was fed into the storage tank by means of both the collector array as well as the backup heater. This heat was consumed throughout the day by means of several DHW tapplings. The ambient conditions recorded during the measurement can be seen in figures 6.9 and 6.10. The maximum ambient temperatures on these days were 27.3 °C (30.08.2016) and 28.7 °C (31.08.2016), the maximum horizontal irradiation reached values of 899 W/m² (30.08.2016) and 793 W/m² (31.08.2016). While the second day is completely cloudless (cf. figure 6.10), small cloud fields cause the incident irradiation to drop lower than < 300 W/m² on the first day (cf. figure 6.9). To assess the quality of the simulation model, the daily amount of energy produced by the collector array and the backup heating as well as the consumed amount of energy in terms of DHW were compared with the results of the simulation model.

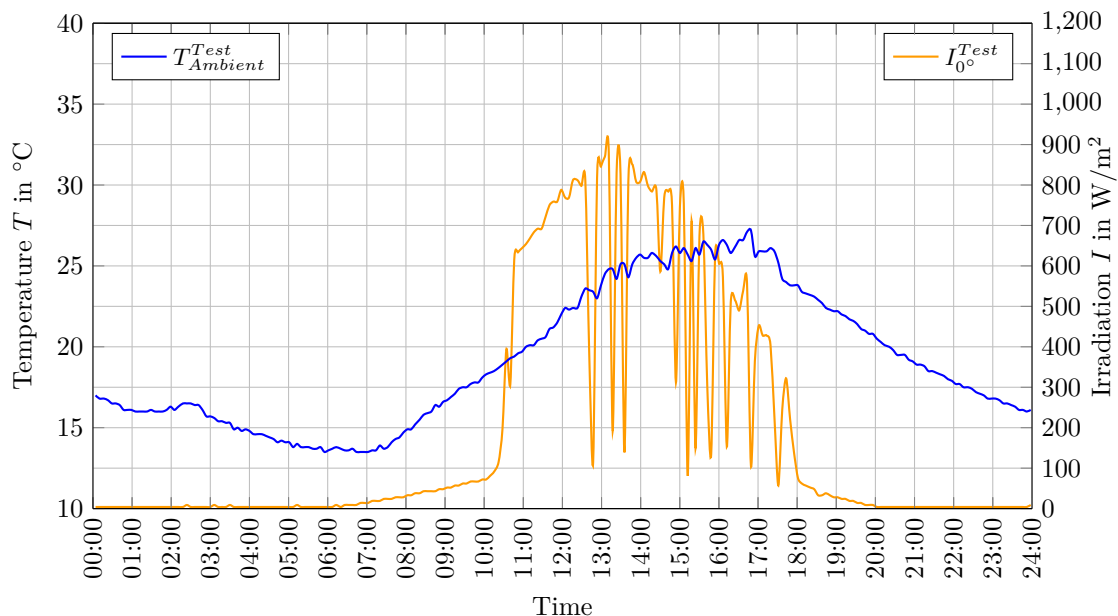


Figure 6.9: Weather conditions on 30.08.2016.

6 Simulation on System Level

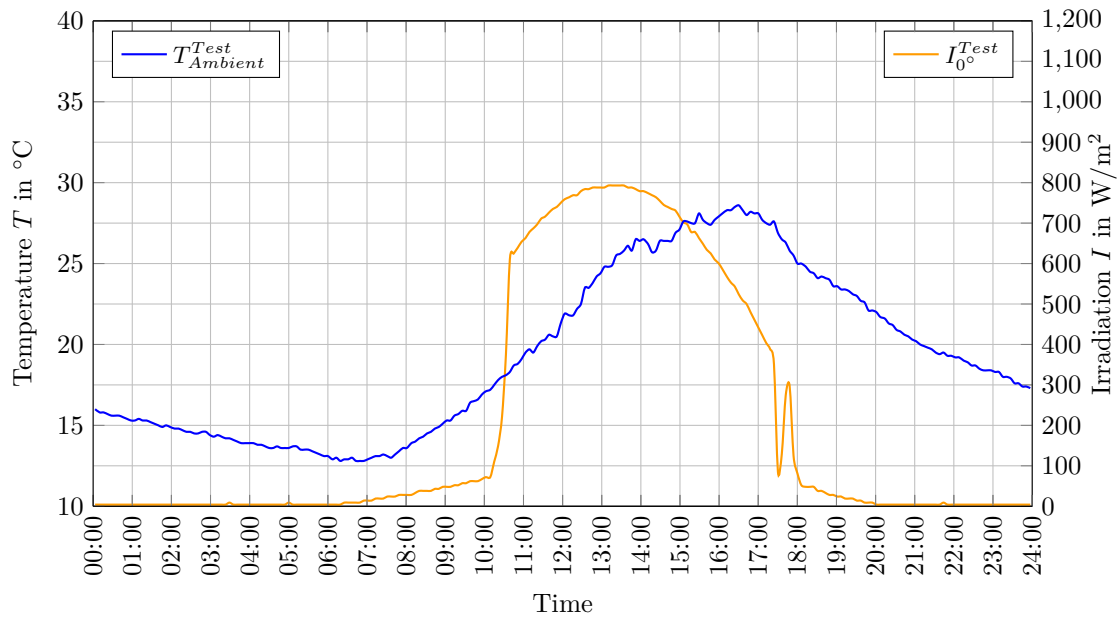


Figure 6.10: Weather conditions on August 31.08.2016.

Figure 6.11 shows the daily fluctuation of the heat generation and consumption. Starting at around 5 AM, DHW is drawn out from the heat storage throughout the day, ending at around 9:30 PM (blue / light blue curve).

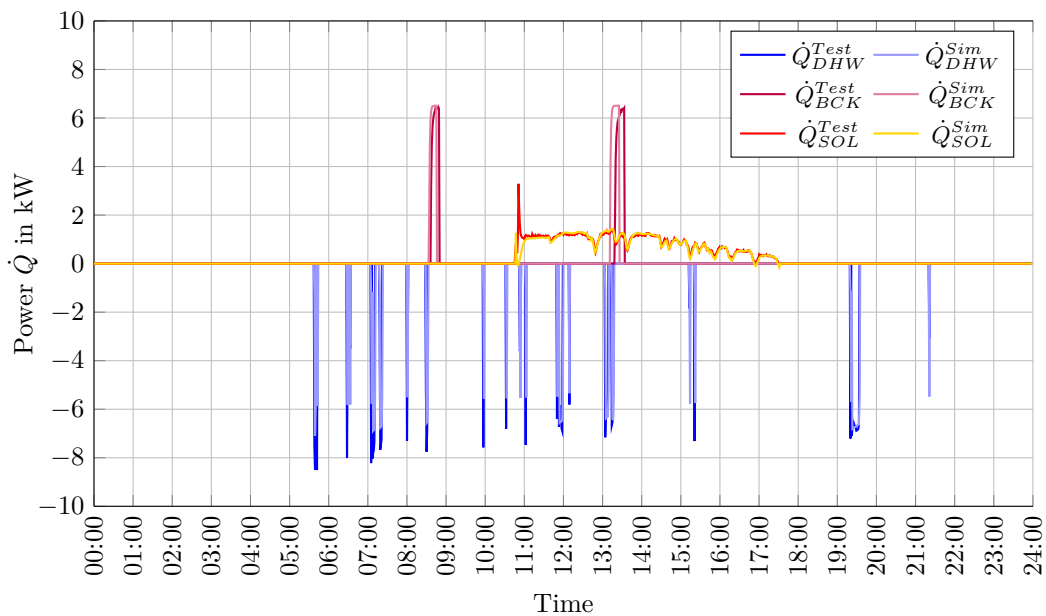


Figure 6.11: Heat production / demand on 30.08.2016.

At around 8:30 AM and shortly after 1 PM, the temperature inside the heat storage dropped below the minimum temperature, yielding the backup heater turning on and heating up the storage tank to the set temperature (purple / light purple curve). From 10:30 AM to 5:30 PM, the collector array (red / yellow curve) was in operation. The influence of the passing

clouds to the solar thermal power can be clearly seen. The deviations of the individual hydraulic circuits are ranging between 4.3 % and 5.1 % (cf. table 6.4). The good correlation between measurement and simulation data can also be observed on the subsequent day (31.08.2016) (cf. figure 6.12).

Table 6.4: Setup and results of the tested DBS with polymeric solar thermal FPCs in comparison to the MATLAB / Simulink / CARNOT 5.3 results on 30.08.2016.

| Physical quantity | Experiment | Simulation model | Deviation |
|------------------------------|--|------------------|-----------|
| Heat storage | | 500 l | |
| Conventional heat source | 9 kW electric heating rod | | |
| Collector array ¹ | $4 \times 0.59 \text{ m}^2 = 2.36 \text{ m}^2$ | | |
| Drain back storage | | 142.5 l | |
| Heat demand DHW ² | | approx. 6 kWh/d | |
| Heat generation (fossil) | 2.6 kWh/d | 2.7 kWh/d | 5.2 % |
| Heat generation (solar) | 5.9 kWh/d | 5.5 kWh/d | 5.8 % |
| Heat consumption (DHW) | 6.3 kWh/d | 6.0 kWh/d | 4.3 % |

¹ Polymeric solar thermal FPCs: $\eta_0 = 0.690$, $a_1 = 8.042 \text{ W}/(\text{m}^2 \text{ K})$, $a_2 = 0.034 \text{ W}/(\text{m}^2 \text{ K}^2)$, cf. chapter 3

² according to VDI 4655:2008

Since the test day on 31.08.2016 had no clouds, the power curve of the collector array is much smoother compared to the previous day (cf. figure 6.12). The corresponding amounts of energy for this test day are listed in table 6.5. The deviation between measured and simulated amount of heat for each hydraulic subsystem ranges between 3.9 % and 7.6 % (cf. table 6.5).

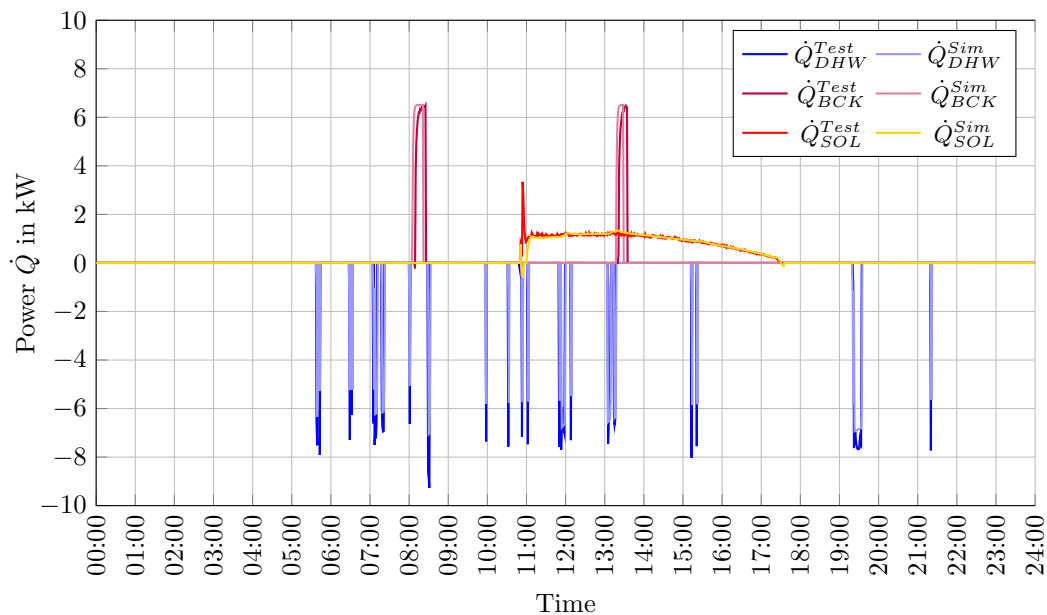


Figure 6.12: Heat production / demand on 31.08.2016.

On both days, a deviation in the start-up behaviour of the solar circuit can be seen. This can be attributed to the fact that the simulation model of the collector does not account for the initially empty collectors. Instead, the simulation model only accounts for one thermal mass (already including the HTF). To better meet the measured power output of the solar loop, a collector model with a time-variable thermal mass would be required. However, as the deviation only affects the start-up phase of the system and has only minor influence on the resulting amount of solar thermal heat, the chosen simulation model is considered to be appropriate for determining the annual amount of solar thermal heat.

Table 6.5: Setup and results of the tested DBS with polymeric solar thermal FPCs in comparison to the MATLAB / Simulink / CARNOT 5.3 results on 31.08.2016.

| Physical quantity | Experiment | Simulation model | Deviation |
|------------------------------|--|------------------|-----------|
| Heat storage | | 500 l | |
| Conventional heat source | 9 kW electric heating rod | | |
| Collector array ¹ | $4 \times 0.59 \text{ m}^2 = 2.36 \text{ m}^2$ | | |
| Drain back storage | | 142.5 l | |
| Heat demand DHW ² | | approx. 6 kW h/d | |
| Heat generation (fossil) | 2.7 kW h/d | 2.8 kW h/d | 3.9 % |
| Heat generation (solar) | 6.2 kW h/d | 6.0 kW h/d | 3.9 % |
| Heat consumption (DHW) | 6.5 kW h/d | 6.0 kW h/d | 7.6 % |

¹ Polymeric solar thermal FPCs: $\eta_0 = 0.690$, $a_1 = 8.042 \text{ W}/(\text{m}^2 \text{ K})$, $a_2 = 0.034 \text{ W}/(\text{m}^2 \text{ K}^2)$, cf. chapter 3

² according to VDI 4655:2008

The results indicate that the developed MATLAB / Simulink / CARNOT 5.3 simulation model can predict the system performance compared to both literature (in case of metal-based solar thermal FPCs) as well as experimental data (in case of polymeric solar thermal FPCs) with sufficient accuracy.

6.3 System Comparison

As the solar thermal system described in section 6.1.2 (solar DHW system) and 6.1.3 (solar combi system) were originally designed for metal-based FPCs, their suitability for DBSs equipped with polymeric solar thermal FPCs was investigated subsequently. Therefore, the validated simulation models of these system were supplemented by an appropriate drain back volume. At the same time, the efficiency curve for a characteristic, polymeric solar thermal FPC (cf. chapter 4) was implemented into the simulation model.

In order to evaluate the influence of the particular hydraulic setup of both systems, a representative configuration (i.e. a 800 l heat storage and a 15 m^2 collector array) was simulated in case of the solar DHW system as well as the solar combi system. Both systems were exposed to the same boundary conditions (i.e. weather conditions and heat demand) and therefore differ solely with regard to their particular hydraulic specifications. The results of

the comparison are shown in table 6.6 (first and second column). A direct comparison of both systems indicates, that both collector arrays supply approximately the same amount of heat to the heat storage (3,383 kW h/a in case of the solar DHW system, 3,386 kW h/a in case of the combi system). As both systems are equipped with the same type and size of solar thermal collectors, this observation is plausible.

Table 6.6: Comparison of a solar thermal DHW system with a solar combi system. Both systems contain a 800l heat storage tank and a 15 m² collector array consisting of polymeric solar thermal FPCs.

| Physical quantity | DHW system | Combi system | Combi system (mod.) | |
|--|---------------------------|--|---------------------|---------------|
| Hydraulic setup | cf. figure 6.5 | cf. figure 6.7 | cf. figure 6.13 | |
| Heat storage volume | | 800l | | |
| Conventional heat source | | 19 kW gas heating boiler | | |
| Collector array ¹ | | 6 × 2.5 m ² = 15 m ² | | |
| Drain back storage volume | | 45l | | |
| Heat demand DHW ² | | 4,254 kW h/a | | |
| Heat demand space heating ³ | | 9,090 kW h/a | | |
| Storage | Storage losses | −1,633 kW h/a | −1,851 kW h/a | −1,562 kW h/a |
| | DHW consumption | −4,261 kW h/a | −4,266 kW h/a | −4,261 kW h/a |
| | Collector array | 3,383 kW h/a | 3,386 kW h/a | 3,769 kW h/a |
| | Gas boiler | 2,491 kW h/a | 4,024 kW h/a | 3,029 kW h/a |
| | Return-flow boost | | −1,304 kW h/a | −994 kW h/a |
| Boiler | Heat supply space heating | −9,082 kW h/a | −7,778 kW h/a | −8,088 kW h/a |
| | Heat supply storage | −2,494 kW h/a | −4,027 kW h/a | −3,033 kW h/a |
| | Heat generation | 11,583 kW h/a | 11,814 kW h/a | 11,121 kW h/a |
| | Fossil fuel demand | 12,870 kW h/a | 13,127 kW h/a | 12,357 kW h/a |
| Solar | Collector yield | 4,175 kW h/a | 4,191 kW h/a | 4,563 kW h/a |
| | Pipe losses (indoor) | −183 kW h/a | −190 kW h/a | −194 kW h/a |
| | Pipe losses (outdoor) | −191 kW h/a | −201 kW h/a | −205 kW h/a |
| | Drain back storage losses | −213 kW h/a | −215 kW h/a | −198 kW h/a |
| | Solar yield | 3,588 kW h/a | 3,585 kW h/a | 3,966 kW h/a |

¹ Polymeric solar thermal FPCs: $\eta_0 = 0.789$, $a_1 = 7.570 \text{ W}/(\text{m}^2 \text{ K})$, $a_2 = 0.012 \text{ W}/(\text{m}^2 \text{ K}^2)$, cf. chapter 4

² according to DIN EN 13203-2:2015 (p. 13)

³ according to DIN EN 12977-2:2016 (p. 36)

Both system have to cover the same and space heating demand (9,090 kW h/a). In case of the solar DHW system, the space heating demand is solely covered by the gas heating boiler (9,082 kW h/a). In case of the solar combi system, only 7,778 kW h/a of the total space heating demand are directly covered by the gas heating boiler. Another 1,304 kW h/a are extracted by means of the return-flow boost (i.e. preheating the return flow of the space heating via the lower part of the heat storage).

6 Simulation on System Level

Extracting heat from the storage tank via the return-flow boost yields a temperature decrease in the lower and subsequently also in the middle part of the heat storage. In order to ensure the necessary minimum temperature for DHW preparation, the cooling of the heat storage is compensated by the gas heating boiler. Accordingly, the amount of heat delivered by the gas heating boiler into the heat storage (4,024 kW h/a) is significantly larger compared to the solar DHW system (2,491 kW h/a).

The higher losses of the heat storage in case of the solar combi system (1,851 kW h/a) in comparison the solar DHW system (1,633 kW h/a) can bet attributed to the particular hydraulic setup of this system: In case of the solar DHW system, the heat storage contains drinking water, which is heated by the gas heating boiler via a heat exchanger (inlet: 0.8 relative storage height / outlet: 0.5 relative storage height), cf. figure 6.5. As soon as the temperature in the upper part of the heat storage drops below 55 °C, the gas heating boiler heats up the upper part of the storage until the temperature reaches 60 °C. In case of the solar combi system, the fluid inside the heat storage is heating water. To ensure a proper separation between drinking and heating water, the DHW flows through a heat exchanger which extends the entire height of the heat storage tank (inlet: 0.05 relative storage height / outlet: 0.95 relative storage height), cf. figure 6.7. As the volume inside this heat exchanger is significantly smaller compared to the volume of the upper part of the heat storage in case of the solar DHW system, the gas heating boiler has to provide heat at a higher temperature level to the heat storage to provide sufficient DHW temperatures. Accordingly, the switch-on (60 °C) and switch-off (65 °C) temperature are (5 °C) above the values of the solar DHW system. As a result, the solar combi system ultimately requires more fossil energy (13,127 kW h/a) than the solar DHW system (12,870 kW h/a).

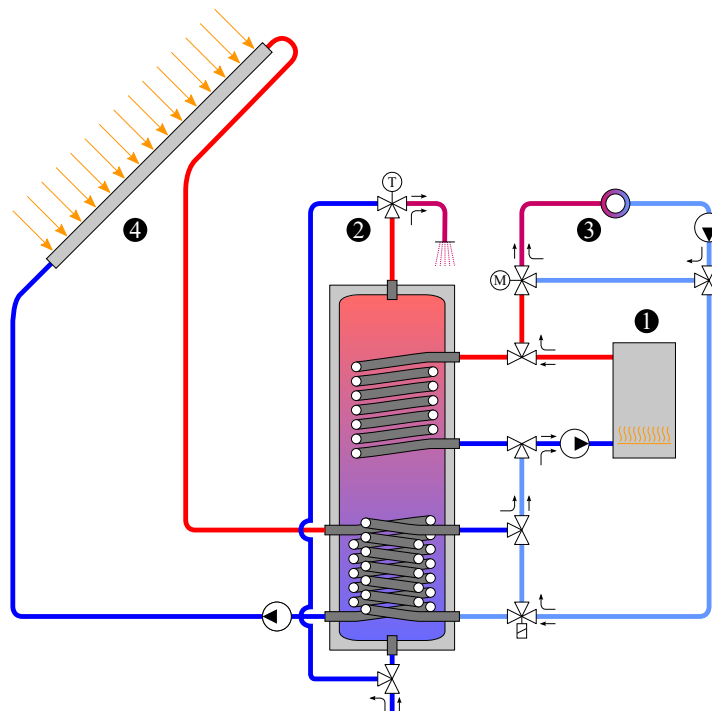


Figure 6.13: Hydraulic setup of the modified solar combi system. ① = Heater, ② = DHW tapping, ③ = Heat distribution (heating), ④ = Solar thermal collector array.

To integrate the advantages of a return-flow boost into a solar thermal DBSs equipped with polymeric FPCs, a modified version of the above-mentioned solar combi system was investigated. As in case of the solar DHW system, the heat storage contains drinking water. Therefore, the gas heating boiler can provide heat at the same temperature level ($T_{on} = 55\text{ }^{\circ}\text{C}$, $T_{off} = 60\text{ }^{\circ}\text{C}$). The return-flow boost is integrated into the heat storage by means of an additional heat exchanger, which has the same properties as the upper heat exchanger (cf. Bachmann, Fischer and Hafner, 2018c for further details). Figure 6.13 shows the modified solar combi system, the simulation results are shown in table 6.6 (third column). Comparing the results of the modified solar thermal combi system both with the original one as well as with the solar thermal DHW indicates, that the modified system has the least heat losses (1,562 kW h/a) and therefore requires the least amount of fossil energy (12,357 kW h/a). At the same time, the system yields the highest amount of solar thermal heat (3,966 kW h/a). Figure 6.14 shows the monthly distribution of both the fossil and solar thermal energy in case of the modified solar thermal combi and the solar thermal DHW system.

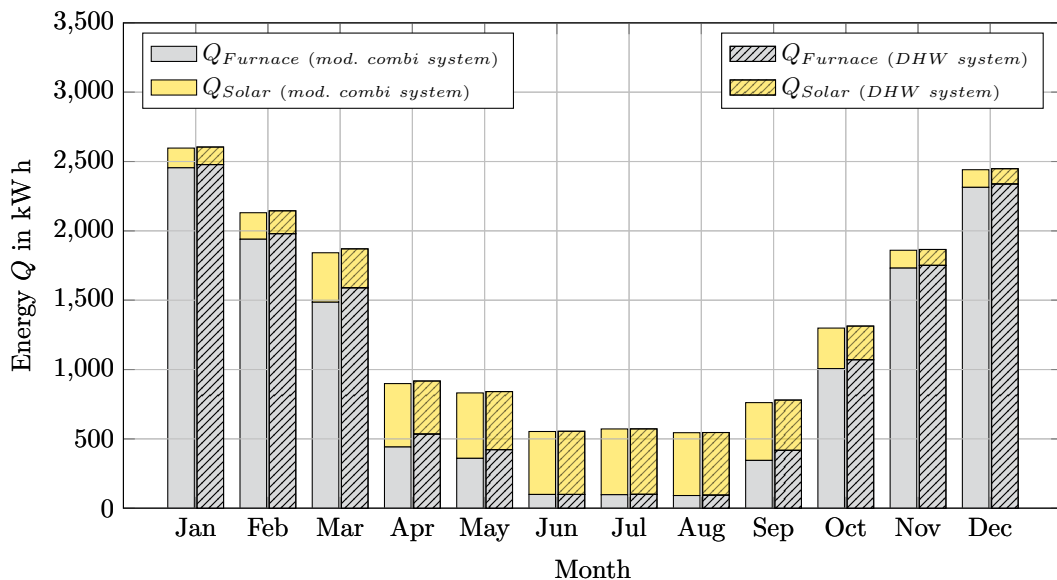


Figure 6.14: Distribution of the fossil fuel demand / solar yield in case of the modified solar combi system and a solar DHW system located in Würzburg (Germany). Both systems are equipped with a 800l heat storage volume and a 15m² collector array (polymeric solar thermal FPCs).

During the summer months June to August, the modified solar combi systems behaves identical to the solar DHW system. This seems plausible, as there is no space heating has to be covered during these months (cf. figure 6.1). As a result, the return-flow boost is deactivated, yielding the modified solar combi system to fall back to the default solar DHW system. In case of the seasonal transition months March to May as well as September and October, the modified solar combi systems outperforms the solar DHW system. This can be attributed to the fact that the space heating demand is at a favourable temperature level for the polymeric solar thermal FPCs, at the same time both ambient temperature as well as solar radiation are high enough to make a useful contribution towards the building's space heating demand. In the winter months (January, February, November and December), the

modified solar combi systems requires slightly less fossil energy than the solar DHW system. Due to the better performance of the modified solar combi system compared to the original one (as described by Bachmann, Fischer and Hafner (2018b)), the following paragraphs solely focus on this modified setup. Therefore, the term “solar combi system” subsequently refers to the modified solar combi system.

6.4 Simulation Results

To evaluate the influence of both the collector array size as well as the heat storage volume, a parametric study was performed. As the reference system (cf. section 6.1.2) has a 5 m^2 collector array in combination with a 300 l heat storage, the size of the collector array was varied between 4 m^2 and 20 m^2 , the heat storage volume ranged between 200 l and $1,000\text{ l}$.

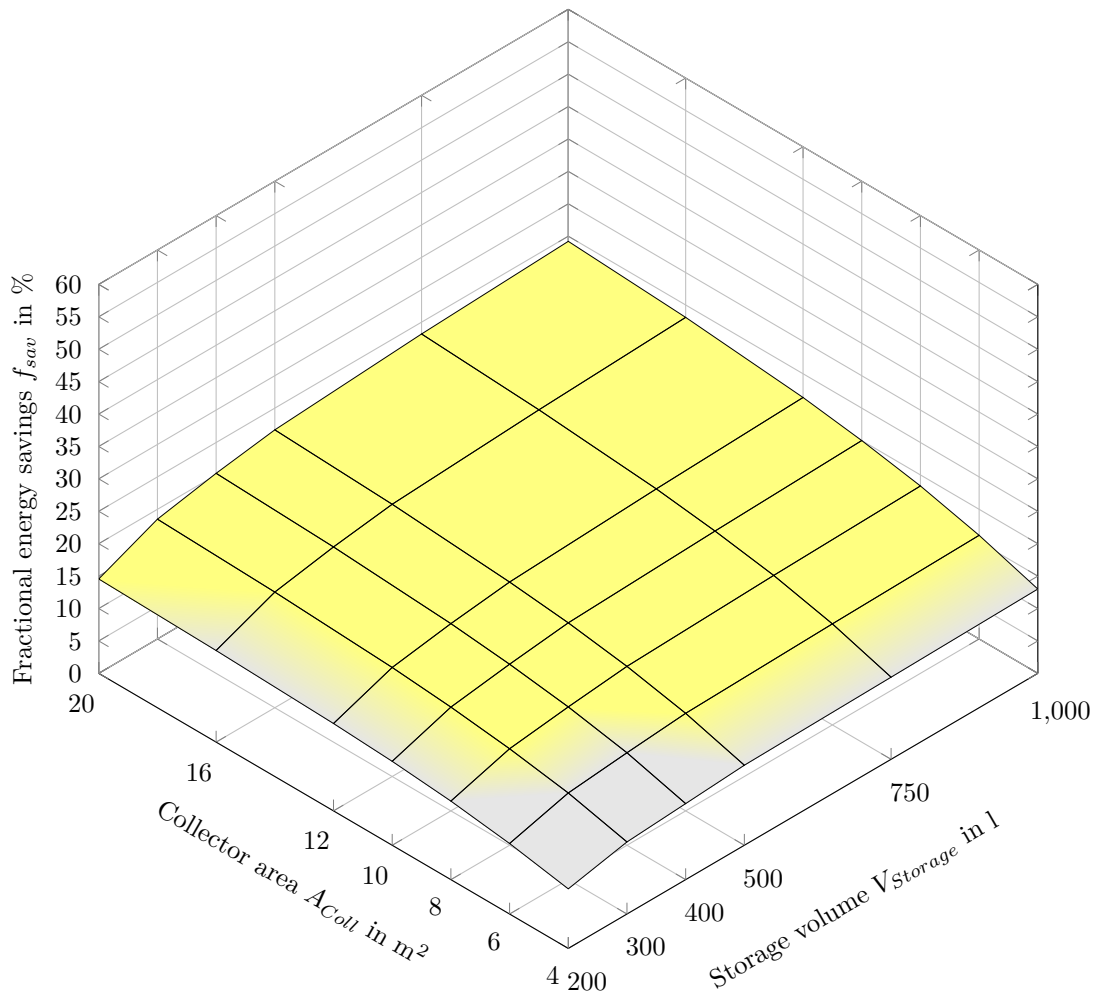


Figure 6.15: Correlation between collector area, heat storage volume and fractional energy savings f_{sav} in case of a solar DHW system located in Würzburg (Germany). The yellow-highlighted regions indicate systems with polymeric FPCs which yield higher fractional energy savings than the reference system with metal-based collectors (cf. section 6.1.2).

In case of the solar combi system (which has a 15 m^2 collector array in combination with a 800 l heat storage, cf. section 6.1.3), the size of the collector array was varied between 14 m^2 and 40 m^2 , the volume of the heat storage ranged between 600 l and $2,000\text{ l}$. With increasing collector array size, the capacity of the drain back volume was increased, too. For each square meter of polymeric collector area, a hypothetical volume of 3 l is assumed. In case of a 10 m^2 collector array, this yields a volume of the drain back vessel of 60 l .

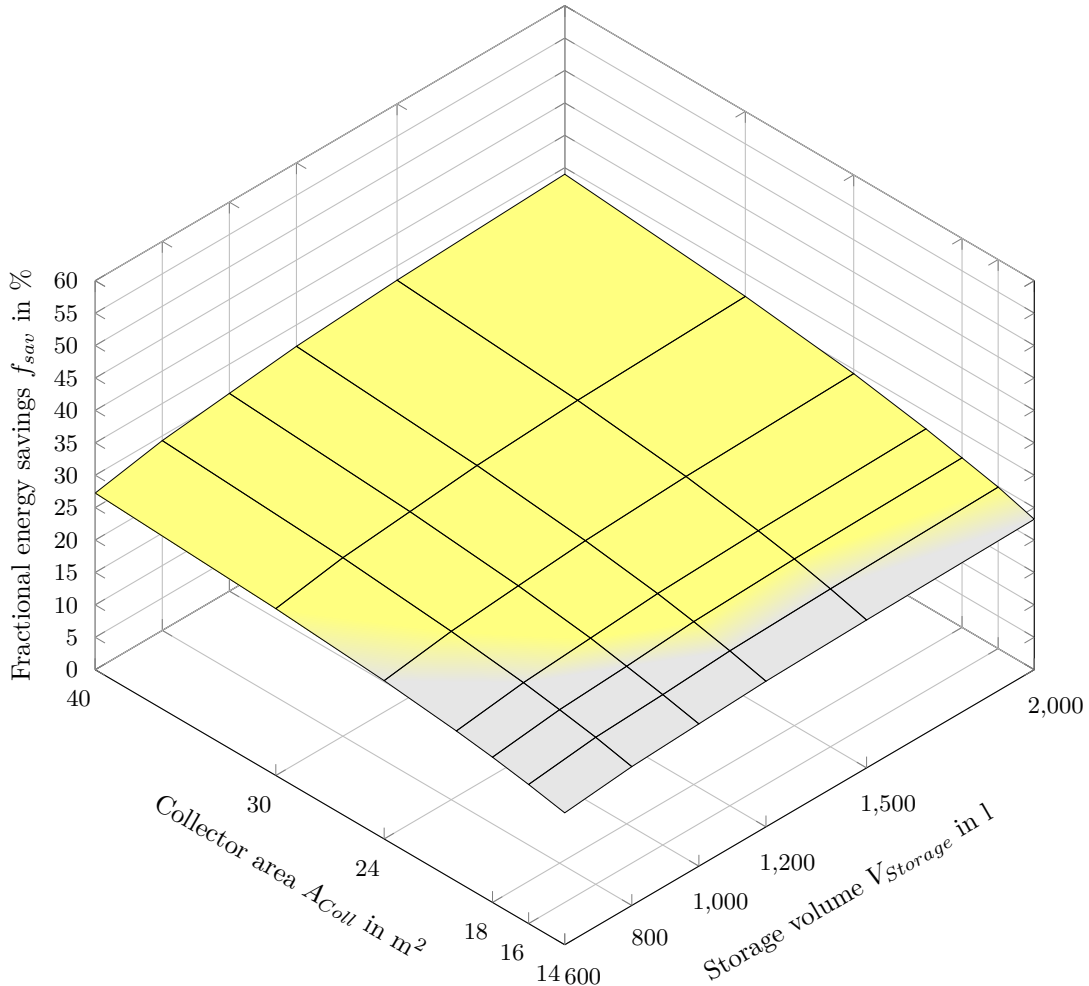


Figure 6.16: Correlation between collector area, heat storage volume and fractional energy savings f_{sav} in case of a solar combi system located in Würzburg (Germany). The yellow-highlighted regions indicate systems with polymeric FPCs which yield higher fractional energy savings than the reference system with metal-based collectors (cf. section 6.1.3).

The results of the parametric study can be seen in figure 6.15 (solar DHW system) and figure 6.16 (solar combi system). The results for the other reference locations can be found in the appendix (cf. section F.1). With both increasing collector array size and heat storage volume, the fractional energy savings f_{sav} are increasing, too. This can be attributed to the fact that an increased collector array yields higher fossil energy savings of the respective system. Comparing the results of the investigated solar DHW system (cf. figure 6.15) with those of the solar combi systems (cf. figure 6.16) indicates, that in the latter case

6 Simulation on System Level

significantly larger setups (e.g. 800l heat storage volume / 20 m² collector array → $f_{sav} = 24.6\%$ cf. table 6.2) are necessary to save approximately the same amount of fossil energy as the reference system with metal-based solar thermal collectors (800l heat storage volume / 15 m² collector array → $f_{sav} = 24.7\%$, cf. table 6.3). Due to lower efficiency of the polymeric solar thermal collectors compared to the metal-based ones, larger setups are also required in case of the solar DHW systems (e.g. 400l heat storage volume / 6 m² collector array → $f_{sav} = 14.3\%$) to reach comparable fractional energy savings as the reference system with metal-based collectors (300l heat storage volume / 5 m² collector area → $f_{sav} = 14.5\%$).

In addition to determining the fractional energy savings f_{sav} , the simulation models allow for an evaluation of the collector temperatures both in case of normal operation and idle mode. This is of particular importance for the polymeric solar thermal FPCs (which are made of PP in the present case, cf. section 4). The collector array's maximum temperatures inversely correlates with the system's heat storage volume. This can be attributed to the fact that potential solar yields cannot be further utilised in case of a fully loaded heat storage, leading to longer idle phases and therefore subsequently higher collector temperatures. As the system's minimal heat storage volume is 200l (in case of the solar DHW system) and 600l (in case of the solar combi system), maximum collector temperatures can be observed for these system configurations.

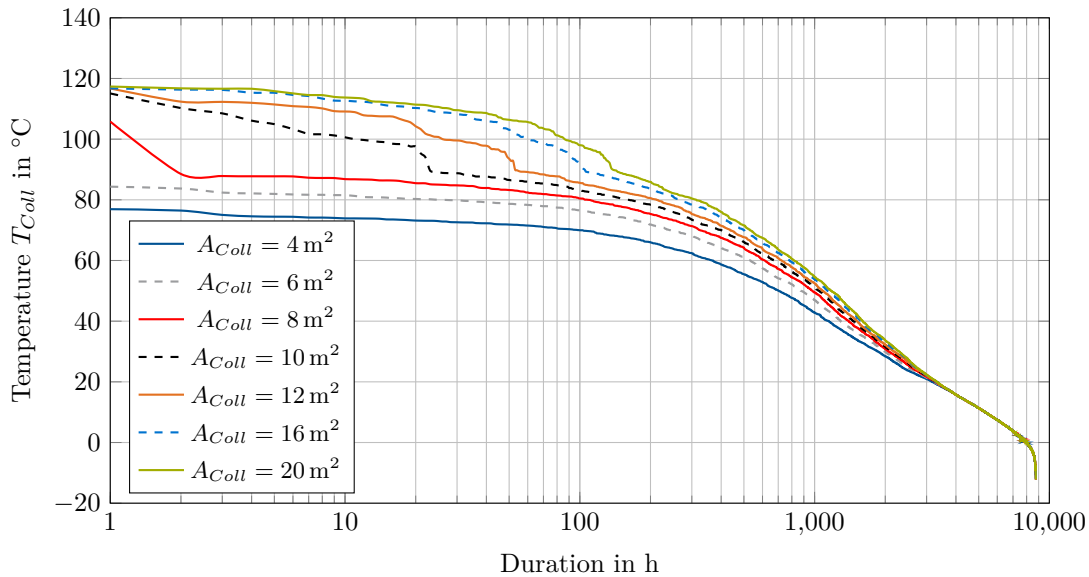


Figure 6.17: Collector temperatures T_{Coll} in case of solar DHW systems located in Würzburg (Germany). Each system is equipped with a 200l heat storage and a solar thermal collector array varying between 4 m² and 20 m².

Figures 6.17 and 6.18 show the resulting collector temperature. With increasing size of the collector array, the maximum temperatures increase as well. The overall maximum temperature of 120.48 °C can therefore be observed in case of the maximum collector array (i.e. 20 m² in the present case). Dominghaus et al. (2012, p. 228) specify a 100 °C long term and a 140 °C short term operation temperature for PP. Figure 6.17 indicates temperatures higher than 100 °C for less than 100 h per year. In case of the solar combi systems, temperatures higher than 100 °C can be observed for approximately 60 h per year

(cf. figure 6.18). In both systems, the maximum tolerable short term operation temperature of 140 h is never exceeded. The maximum collector temperatures at the other reference locations can be found in the appendix (cf. section F.1).

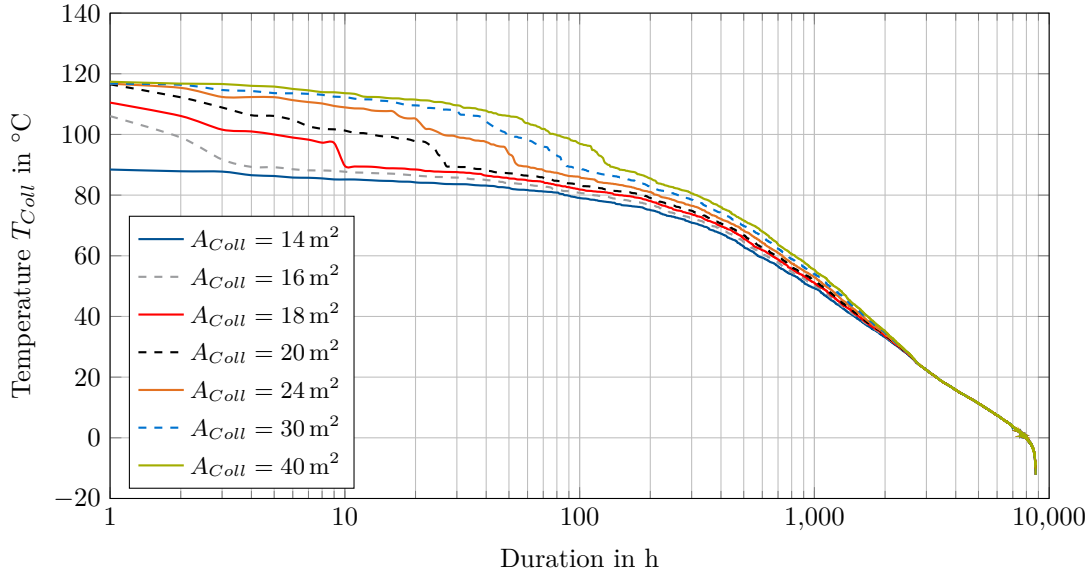


Figure 6.18: Collector temperatures T_{Coll} in case of solar combi systems located in Würzburg (Germany). Each system is equipped with a 600 l heat storage and a solar thermal collector array varying between 14 m^2 and 40 m^2 .

6.5 Summary

Comparing the simulation results with data available from literature indicates a deviation of the evaluated fractional energy savings f_{sav} smaller than 5 p.p.. In addition, the developed simulation model is able to precisely predict measurement results obtained from a DBS with polymeric solar thermal FPCs (maximum deviation 7.6 %).

Based on the validated models, a parametric study was performed at four different reference locations. The results indicate, that DBSs with polymeric solar thermal FPCs can reach comparable or even higher fractional energy savings f_{sav} than conventional solar thermal systems with metal-based collectors at all four reference locations. It is to emphasise that an appropriate hydraulic scheme is of major importance for DBSs equipped with polymeric solar thermal FPCs, as schemes originally developed for metal-based FPCs can have a negative effect on the system's performance.

The highest fractional energy savings can be achieved in Greece (Athens), the lowest ones in Stockholm (Sweden). Based on these findings, it can be deduced that DBSs with polymeric solar thermal FPCs can make a meaningful contribution to the DHW preparation, especially in milder climate zones. Independent from the chosen location, the maximum collector temperatures are raging around $120 \text{ }^\circ\text{C}$, which is an acceptable value for the chosen material PP.

6 Simulation on System Level

In any case, however, due to the lower efficiency of polymeric FPCs compared to metal-based ones, a larger collector array and / or heat storage volume is necessary to cover the same amount of heat. The simulation-based parametric study revealed solutions with lower fossil energy consumption than reference systems with metal-based solar thermal FPCs. To fairly evaluate these systems, the fossil energy saving of each system must be related to the associated costs over its lifetime. This will be done in the next chapter by means of an economic evaluation.

7 Economic Evaluation

In this chapter, the economic sustainability of the investigated solar thermal DBSs are elaborated. Next to the technical performance of these systems (i.e. the amount of fossil energy that can be saved by utilising the respective system, cf. chapter 6) and ecological aspects (e.g. lower CO₂ emissions compared to heating systems based on fossil fuels), the economic sustainability plays an important role for or against purchasing a solar thermal system. The concept of the levelised cost of heat (LCoH) is considered as an appropriate method to assess the economic sustainability of different (solar thermal) heating systems and is therefore applied subsequently.

For a better readability, all costs are rounded off to whole euros, the resulting LCoH are stated in €-Ct/(kW h) with one decimal place. The underlying calculations, however, were performed with unrounded numbers. In order to ensure a comparability of the LCoH independent from the respective solar thermal system's location, VAT rates and subsidies are neglected. This approach is also utilised e.g. by Weiss, Spörk-Dür and Mauthner (2017, p. 6) or Kaltschmitt (2013, p. 19). To determine end customer heat generation costs, the derived LCoH have to be scaled by the national VAT rates.

7.1 Methodology

At the most general level, heat generation costs / LCoH are defined as the cost per unit of energy. In the context of solar thermal systems, the standard VDI 6002-1:2014 (p. 60) states that heat generation cost should be calculated based on all expenses which arise from the installation, operation and maintenance of a solar thermal system.

$$LCoH = \frac{I_0 - S_0 + \sum_{t=1}^T \frac{C_t(1-TR) - DEP_t \cdot TR}{(1+r)^t} - \frac{RV}{(1+r)^T}}{\sum_{t=1}^T \frac{E_t}{(1+r)^t}} \quad (7.1)$$

where:

| | |
|---------|--|
| $LCoH$ | = Levelised cost of heat in €/(kW h) |
| I_0 | = Initial investment costs in € |
| S_0 | = Subsidies and incentives in € |
| C_t | = Operation and maintenance costs (for the respective year t) in € |
| TR | = Corporate tax in % |
| DEP_t | = Asset depreciation (for the respective year t) in € |
| RV | = Residual value in € |
| E_t | = Saved final energy (for the respective year t) in kW h |
| r | = Discount rate in % |
| t | = Year of consideration |
| T | = Evaluation horizon in a |

Depending on the methodology applied for calculating the LCoH, the observation period, the type of system (i.e. a solar DHW system or a solar combi system), as well as further boundary conditions (e.g. consideration of subsidies), different heat generation costs can be found in literature. In case of solar DHW systems (specific investment prices ranging between 600 €/m^2 and $1,500 \text{ €/m}^2$), Eicker (2012, p. 94) mentions heat generation costs of 14.0 €/Ct/(kWh) – 30.0 €/Ct/(kWh) ¹⁴. For a comparable system (i.e. specific investment prices ranging between 440 €/m^2 and $1,210 \text{ €/m}^2$, 6 m^2 collector array, 300 l heat storage), Weiss, Spörk-Dür and Mauthner (2017, p. 69) report LCoH between 7.8 €/Ct and 20.6 €/Ct ¹⁵. According to the same source, a solar combi system with 12 m^2 collector array and a $1,000 \text{ l}$ heat storage (specific investment prices ranging between 410 €/m^2 and $1,180 \text{ €/m}^2$) can provide heat for 8.1 €/Ct – 22.6 €/Ct under similar boundary conditions.

To cope with the problem of different formulae for calculating heat generation costs, Louvet et al. (2018, p. 1) postulated a very general form of LCoH (cf. equation 7.1). This formulation will be applied subsequently to determine the heat generation costs of solar thermal DBSs with polymeric FPCs.

7.2 Initial Investment Costs

The investment costs summarise all expenses which are necessary for the initial installation and operation of a solar thermal system. Besides the main components (such as solar thermal FPCs and the thermal heat storage), further necessary components are, for example, the solar controller, the pump necessary for circulating the HTF or the drain back volume. The investment costs of the individual components are explained subsequently.

7.2.1 Collectors

An analysis of 55 conventional (i.e. metal-based) solar thermal FPCs (gross collector area ranging between 2.10 m^2 and 2.51 m^2) indicated average specific costs of 243 €/m^2 (cf. table G.1) (Sonne, Wind & Wärme, 2018). This figure correlates with price ranges given by Quaschnig (2015, p. 396) (200 €/m^2 – 350 €/m^2), Kaltschmitt (2013, p. 235) (200 €/m^2 – 400 €/m^2) and Stieglitz and Heinzl (2012, p. 394) (300 €/m^2 – 400 €/m^2). Therefore, specific investment costs for conventional solar thermal FPCs of 300 €/m^2 are assumed subsequently.

In case of polymeric solar thermal FPC, only little information regarding their costs is available. This can be attributed to the fact that polymeric collectors are still in an early market stage and not yet widely manufactured. As a result, the final retail price strongly relies on the chosen manufacturing process, polymeric material and the number of produced items. Köhl (2015, p. 21) and Frick et al. (2014, p. 52) report specific costs of 197 €/m^2 . Lower costs (143 €/m^2)¹⁶ are given by Carlsson et al. (2014, p. 17), higher ones (243 €/m^2)

¹⁴ 20 a observation period, no subsidies.

¹⁵ 25 a observation period, system located in Würzburg (Germany).

¹⁶ 190 €/m^2 incl. 25% VAT.

by Ehrenwirth et al. (2016c, p. 89). To cope with these different figures, specific collector costs of 200 €/m^2 are assumed as realistic retail prices for polymeric solar thermal FPCs.

Independent from the type of collector (i.e. metal-based or polymeric), additional 61 €/m^2 must be taken into account for an appropriate substructure which connects the collector with the roof top (cf. table 7.1). The evaluation of the aforementioned (conventional) 55 collectors reveals a specific volume of 0.731 l/m^2 . This information is necessary for determining the required amount of HTF.

7.2.2 Heat Storages

The costs of thermal heat storages mainly depend on their volume as well as the amount and type of internal heat exchangers. According to Kaltschmitt (2013, p. 236), typical costs for DHW storages range between 3.50 €/l and 6.00 €/l , whereas simple buffer storages cost $2.00 \text{ €/l} - 3.50 \text{ €/l}$. Figure 7.1 shows the evaluation of 32 monovalent (i.e. one heat exchanger) and 29 bivalent (i.e. two heat exchangers) heat storages. The data indicates that the specific costs of heat storages decrease over-proportionally with increasing volume. To account for this observation, two appropriate cost functions were selected (cf. figure 7.1). For a typical heat storage volume of $1,000 \text{ l}$, the chosen functions yield costs of $2,667 \text{ €}$ (one heat exchanger) and $3,023 \text{ €}$ (two heat exchangers). The resulting difference of 356 € appears as a realistic value for the additional heat exchanger. Therefore, each additional heat exchanger was assumed to increase the specific heat storage costs by $2 \text{ €/l} \cdot V^{-0.25}$.

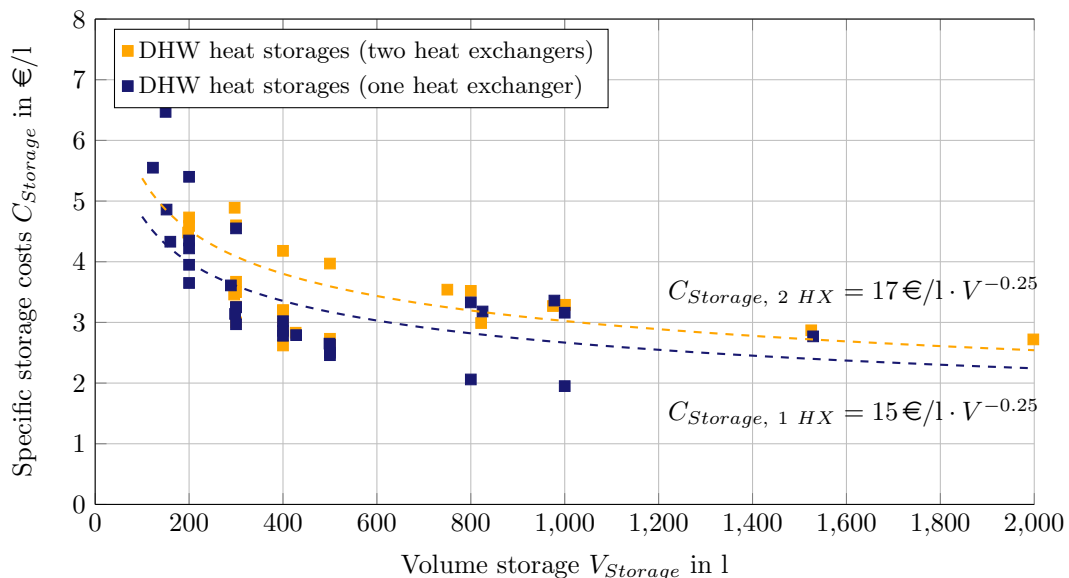


Figure 7.1: Evaluation of specific heat storage costs for DHW storages with one and two heat exchangers available from manufacturer’s price lists. Data source: CitrinSolar GmbH (2018), GASOKOL GmbH (2013), ThüSolar GmbH (2012), Wagner Solar GmbH (2017), Wikora GmbH (2017), WOLF GmbH (2018). Further information can be found in the appendix(cf. table G.2 and G.3).

In case of DBSs, further costs for the additional drain back volume must be considered. As the drain back vessel can be interpreted as a simple buffer storage without any heat exchangers, specific costs of 2 €/l were assumed.

7.2.3 Other Components

Apart from the collector array and the thermal heat storage, other necessary components (pipes, solar controller, membrane expansion vessel (MEV) etc.) are considered to determine the overall investment costs. To determine characteristic costs for these additional components, available price lists from 15 different manufacturers (located in Germany, Austria and Switzerland) were evaluated and averaged (cf. table 7.1). The available data covers a period from 2006 to 2018 and therefore inherently provides a temporal-averaging, too.

Table 7.1: Evaluation of component costs available from manufacturer’s price lists. Data source: Armacell GmbH (2018), Buderus Thermotechnik GmbH (2018), (price information available in CHF, assumed exchange rate: 1 € \cong 1.15 CHF (average exchange rate in 2018) (European Central Bank, 2020)), CitrinSolar GmbH (2018), Consolar GmbH (2006), GASOKOL GmbH (2013), ROTEX Heating Systems GmbH (2018), Roth Werke GmbH (2014), Sonnenkraft GmbH (2018), ThüSolar GmbH (2012), TiSUN GmbH (2018), Viessmann Werke GmbH & Co. KG (2017), Wagner Solar GmbH (2017), Wikora GmbH (2017), WOLF GmbH (2018). A detailed determination of the subsequent prices can be found in the appendix (cf. table G.4- G.9).

| Component | (Specific) investment costs ¹ | Sample size |
|------------------|--|-------------|
| MEV | 14 €/m ² | 82 |
| Piping | 41 €/m | 81 |
| Substructure | 61 €/m ² | 50 |
| Solar station | 618 € | 27 |
| Solar controller | 361 € | 41 |
| HTF | 4 €/m ² | 20 |

¹ without VAT.

The evaluation of available price lists reveals average costs of 41 €/m for corrugated stainless steel pipes (including thermal insulation, pipe length ranging between 6 m and 100 m, pipe diameter ranging between 14 mm and 25 mm). Within the scope of this study, an initial pipe length of 25 m is assumed for connecting the first two collectors of the array (located on the building’s rooftop) with the heat storage (located in the building’s basement). For each additional collector, a further pipe length of 0.5 m is assumed. In case of an overall collector area of 15 m² (i.e. 6 collectors with 2.5 m² gross area, cf. table 6.3), this results in a total pipe length¹⁷ of 27 m. The resulting specific costs¹⁸ (with respect to the overall collector array area) of approximately 74 €/m² are slightly higher than values given by Kaltschmitt

¹⁷ 25 m + 4 · 0.5 m = 28 m.

¹⁸ $\frac{27 \text{ m} \cdot 41 \text{ €/m}}{15 \text{ m}^2} \approx 74 \text{ €/m}^2$.

(2013, p. 236), who reports specific costs of $40 \text{ €/m}^2 - 70 \text{ €/m}^2$ for a thermally insulated, 25 m – 30 m long pipe.

The average costs for a solar station (including the pump necessary for circulating the HTF, thermometer, manometer, safety valve etc.) are 618 € (cf. table 7.1). The solar controller yields further costs of 361 € on average. In case of a conventional (i.e. pressurised) solar thermal system, a membrane expansion vessel is necessary to ensure a reliable and safe operation of the system. Assuming a minimum specific volume of the membrane expansion vessel of $41/\text{m}^2$ (cf. appendix, table G.1), average specific costs of 14 €/m^2 can be derived from the available price lists. To account for the proper amount of HTF, $0.251/\text{m}$ are assumed¹⁹ in addition to average volume of a solar thermal FPC of $0.731/\text{m}^2$ (cf. appendix, figure G.1). In case of the aforementioned example of an overall collector area of 15 m^2 these assumptions result in an overall HTF demand of 17.71 ²⁰.

7.2.4 Installation

In order to install all relevant components, Kaltschmitt (2013, p. 236) reports specific costs (with respect to the overall collector array area) ranging between 70 €/m^2 and 300 €/m^2 . Similar cost ranges are given by Eicker (2012, p. 93) ($126 \text{ €/m}^2 - 315 \text{ €/m}^2$). In case of the conventional system, 200 €/m^2 are considered as realistic installation costs. Assuming a significant lower weight of the polymeric FPCs compared to the metal-based ones, lower installation costs can be assumed in case of the DBSs. On the other hand, the proper installation of the pipes requires special attention in case of DBSs (cf. section 2.2.2). To cope with these two facts, specific installation costs of 200 €/m^2 are assumed, too.

7.2.5 Investment Costs of a Solar Domestic Hot Water System located in Würzburg (Germany)

Based on the component costs derived in the aforementioned sections, table 7.2 shows the initial investment costs of both a conventional solar DHW system as well as a comparable DBS located in Würzburg (Germany). To compensate the lower efficiency of the polymeric solar thermal FPCs, the overall collector array area must be larger in case of the DBS in order to achieve comparable fractional energy savings f_{sav} . The results indicate that, despite the significant lower specific costs of polymeric solar thermal FPCs, the overall costs for the DBS are 904 € higher. This can be attributed to the fact that a larger collector area yields further costs, mainly due to the increased installation expenditure. The overall specific systems costs (i.e. $1,220 \text{ €/m}^2$ in case of the conventional system and 876 €/m^2 in case of the DBS) are within the cost range given by Eicker (2012, p. 93) ($600 \text{ €/m}^2 - 1,500 \text{ €/m}^2$).

¹⁹ i.e. specific volume of a 1 m DN 18 pipe.

²⁰ $27 \text{ m} \cdot 0.251/\text{m} + 15 \text{ m}^2 \cdot 0.731/\text{m}^2 = 17.701$.

Table 7.2: Comparison of investment costs in case of a solar DHW system located in Würzburg (Germany).

| | Conventional system ¹ | DBS ² |
|-------------------------|--|--|
| Collector array area | $2 \times 2.5 \text{ m}^2 = 5 \text{ m}^2$ | $4 \times 2.0 \text{ m}^2 = 8 \text{ m}^2$ |
| Heat storage volume | | 300 l |
| Fossil energy demand | 13,572 kWh/a | 13,512 kWh/a |
| f_{sav} ³ | 14.5 % | 14.9 % |
| Collector array | 1,500 € | 1,600 € |
| Substructure | 305 € | 488 € |
| Heat storage | | 1,225 € |
| Drain back volume | — | 48 € |
| Piping | 1,025 € | 1,066 € |
| Solar station | | 618 € |
| Solar controller | | 361 € |
| MEV | 68 € | — |
| Mounting | 1,000 € | 1,600 € |
| Investment costs | 6,102 € | 7,006 € |

¹ with metal-based solar thermal FPCs (pressurised).

² with polymeric solar thermal FPCs (unpressurised).

³ with respect to the conventional reference system, cf. section 6.1.1.

7.3 Subsidies

Depending on the type of solar thermal system (i.e. for space heating and / or DHW preparation), final energy savings, building type etc., subsidies may be granted (Bundesamt für Wirtschaft und Ausfuhrkontrolle, 2020). Potential funding positively contributes to the LCoH of a solar thermal system and is therefore subtracted from the investment costs (cf. equation 7.1). As subsidies may significantly vary depending on the location (both nationally and regionally) and therefore hamper the comparability of the LCoH, subsidies are not considered subsequently.

7.4 Operation and Maintenance Costs

In contrast to the one-time installation costs, operation and maintenance costs reflect recurrent expenses which are either linked to the utilisation of solar thermal systems (e.g. to cover the electricity demand of the pump) or independent from the level of utilisation (e.g. in case of maintenance).

7.4.1 Operation-Related Costs

Operation-related costs occur independently of the annual operating hours of a solar thermal system and include expenditures for operating, inspection and maintenance. According to VDI 6002-1:2014 (p. 61), the overall operation-related costs range between 1%/a and 2%/a with respect to the initial investment costs I_0 . Therefore, operation-related costs equal to 2% of the investment costs are assumed in case of the conventional (i.e. pressurised) system. Due to the unpressurised setup of a DBS with polymeric FPCs, lower operation-related costs are considered: On the one hand, the system does not require regular checks regarding the pressure, accordingly, no efforts for refilling the HTF and / or re-pressurisation of the system needs to be considered. On the other hand, inspection and maintenance efforts regarding the HTF are of minor importance and typically limited to sporadically checking the water level in the drain back reservoir. In case of the conventional system, a water-glycol-mixture is used as HTF, requiring a regular check of the fluid's properties to prevent frost-damages from the system. Furthermore, the HTF must be exchanged at regular intervals. In this context, Jack and Rockendorf (2013, p. 175) report a typical exchange interval of seven years. To account for the reduced effort in case of the DBS with polymeric FPCs, operation-related costs of 1%/a with respect to the initial investment costs I_0 are considered as an appropriate assumption.

7.4.2 Demand-Related Costs

In contrast to the operation-related costs, demand-related costs are directly linked to the intensity of use of a solar thermal system. More specifically, this includes the electricity demand of both the pump and the solar controller. The latter one is assumed to continuously run throughout the year (i.e. 8,760 h) with an power consumption of 3 W, yielding an overall electricity demand of 26.3 kWh. VDI 6002-1:2014 (p. 62) states a typical value of 2% for the solar pump's electricity demand with respect to the solar gains of a solar thermal system. Slightly higher values (3% – 5%) are given by Oberzig (2014, p. 135) and Weyres-Borchert, Kasper and Drück (2015, p. 123) (2% – 5%). Subsequently, the solar pump's electricity demand is therefore assumed with 3% in both the conventional as well as the DBS. To determine the resulting demand-related costs, an electricity price of 25.1 €/Ct/(kWh) (excl. VAT) is assumed (Eurostat, 2018)²¹.

7.4.3 Operation and Maintenance Costs of a Solar Domestic Hot Water System located in Würzburg (Germany)

Table 7.3 summarises the overall operation and maintenance costs (i.e. the sum of annual operation-related and demand-related costs) for both the already mentioned conventional solar DHW system and the DBS located in Würzburg (Germany). The results indicate that the latter option has at least 47.61 €/a lower annual costs than the first one.

²¹ Electricity price in Germany in the first half-year of 2018.

Table 7.3: Operation and maintenance costs in case of a solar DHW system located in Würzburg (Germany).

| | Conventional system | DBS |
|--|--|--|
| Collector array area | $2 \times 2.5 \text{ m}^2 = 5 \text{ m}^2$ | $4 \times 2.0 \text{ m}^2 = 8 \text{ m}^2$ |
| Heat storage volume | 3001 | |
| Fossil energy demand | 13,572 kW h/a | 13,512 kW h/a |
| f_{sav} | 14.5 % | 14.9 % |
| Investment costs¹ | 6,102 € | 7,006 € |
| Inspection, maintenance | 122 €/a | 70 €/a |
| Operation (i.e HTF) | 56 €/7a | — |
| Operation-related costs² | 122 €/a | 70 €/a |
| Solar controller | 7 €/a | |
| Solar pump | 17 €/a | 18 €/a |
| Demand-related costs³ | 24 €/a | 25 €/a |

¹ cf. section 7.2.5.

² cf. section 7.4.1. In case of a price increase rate equal to 0%/a, the costs for the HTF may directly added up with the annual expenses for inspection and maintenance. In any other case (i.e. price increase rate \neq 0%/a), these expenses must be accounted at the time t when they were caused.

³ Assuming an electricity price of 25.1 €-Ct h/kW (Eurostat, 2018).

7.5 Further Parameters

The observation period T has a strong influence on the resulting LCoH of a solar thermal system. Depending on the location of such a system, typical values for the observation period range between 20 a and 35 a (Louvet et al., 2018, p. 4). In accordance with VDI 6002-1:2014 (p. 64), an observation period of 20 a is assumed within the scope of this study. The observation period does not necessarily match the service life T_L of the solar thermal systems components. In case that the observation period is greater than the service life of a component ($T > T_{L,C}$), the particular component has to be replaced. In case that $T_{L,C} > T$, the particular component has a residual value RV that positively contributes to the LCoH of the respective system. According to Louvet et al. (2018, p. 3), potential residual values may be neglected (i.e. $RV = 0$) in case of residential solar thermal applications and are therefore not considered within the scope of this study. VDI 2067:2012 (pp. 21-22) specifies characteristic service life times for components within a solar thermal system. The solar station as well as the solar controller must be replaced every 10 a, the MEV every 15 a. All other components do not have to be replaced within the observation period of 20 a. In accordance with Louvet et al. (2018, p. 3), a corporate tax rate TR and asset depreciation DEP_t are neglected, as the present study focuses on the residential sector ($TR = DEP_t = 0$). The discount rate r depends both on the inflation rate r_{Infl} as well as a characteristic interest rate r_{Int} (cf. equation 7.2). In case that the inflation rate is greater than the interest rate ($r_{Infl} > r_{Int}$), the resulting discount rate is less than zero, implying increasing costs over time. The opposite applies if the inflation rate is smaller than the interest rate ($r_{Infl} < r_{Int}$).

In this case, the resulting discount rate r is greater than zero, indicating that the system operator can expect decreasing costs over time. If the interest rate equals the inflation rate ($r_{Infl} = r_{Int}$), the interest earnings counterbalance the cash value reduction due to inflation. In that case, the system operator can expect constant costs over time.

$$r = \frac{r_{Int} - r_{Infl}}{1 + r_{Infl}} \quad (7.2)$$

where:

| | |
|------------|---|
| r | = Annual discount rate in % |
| r_{Int} | = Annual (risk free) interest rate in % |
| r_{Infl} | = Annual inflation rate in % |

Within the scope of this study, a risk free interest rate r_{Int} of 2% is assumed. As a comparison, the annual average return of a 10 a German Federal Bond equals 2.3%²² (European Central Bank, 2018). Furthermore, an annual inflation rate r_{Infl} of 1.5% is assumed. This figure coincidences with data from the German Federal Statistical Office, which reports an average increase of the consumer price index (i.e. inflation rate) of 1.4%²³ (Statistisches Bundesamt, 2018).

$$LCoH = \frac{I_0 + \sum_{t=1}^T \frac{C_{O,t} + C_{D,t} + C_{Rp,t}}{(1+r)^t}}{\sum_{t=1}^T \frac{E_t}{(1+r)^t}} \quad (7.3)$$

with

$$C_{D,t} = C_{D,0} \cdot (1 + r_E)^{(t-1)}$$

where:

| | |
|------------|--|
| $LCoH$ | = Levelised cost of heat in €/ (kW h) |
| I_0 | = Initial investment costs in € |
| $C_{O,t}$ | = Operation-related costs (for the respective year t) in € |
| $C_{D,t}$ | = Demand-related costs (for the respective year t) in € |
| $C_{Rp,t}$ | = Replacement costs (for the respective year t) in € |
| E_t | = Saved final energy (for the respective year t) in kW/h |
| r | = Annual discount rate in %, cf. equation 7.2 |
| r_E | = Annual electricity price increase rate in % |
| t | = Year of consideration |
| T | = Evaluation horizon in a |

The cost of electricity is assumed to equal 25.1 €-Ct/(kW h)²⁴ (Eurostat, 2018). The annual increase rate of electricity costs r_E is assumed with 3%, slightly lower than the long-term

²² 15 a monthly averaged value (10/2003 - 10/2018).

²³ 15 a yearly averaged value (2003 - 2017).

²⁴ Price-information for Germany in the first half-year of 2018 for consumption levels of 2,500 kW h/a – 5,000 kW h/a; VAT and other recoverable taxes and levies are excluded.

average (3.9%²⁵) in Germany over the last 10 a (Eurostat, 2018). Taking into account all above mentioned assumptions, the original definition of the LCoH (cf. equation 7.1) simplifies according to equation 7.3.

7.6 Resulting Levelised Cost of Heat of a Solar Domestic Hot Water System located in Würzburg (Germany)

Table 7.4 shows the resulting time series of cash and energy flows for an observation period of 20 a in case of the conventional (i.e. pressurised) solar DHW system. The system has to be filled with water-glycol-mixture, requiring initial demand-related costs C_D of 56.13 € (cf. table 7.4, 3rd column). This expenditure must be re-invested in a recurring 7 a interval (cf. section 7.4.1), yielding further costs in the 8th and 15th year of the observation period. After 10 a, the solar controller / station must be replaced, yielding replacement costs in the 11th year. The exchange of the MEV after 15 a causes further replacement costs C_{Rp} in the 16th year (cf. table 7.4, 4th column).

Table 7.4: Time series of cash and energy flows in case of a conventional solar DHW system located in Würzburg (Germany).

| t in a | I_0 | C_O | C_D | C_{Rp} | $\frac{\sum C}{(1+r)^t}$ | $\frac{E_t}{(1+r)^t}$ |
|----------|---------|-------|-------|----------|--------------------------|-----------------------|
| 0 | 6,102 € | | | | | |
| 1 | | 147 € | 56 € | | 202 € | 2,292 kW h |
| 2 | | 147 € | | | 146 € | 2,281 kW h |
| 3 | | 148 € | | | 146 € | 2,270 kW h |
| 4 | | 149 € | | | 146 € | 2,259 kW h |
| 5 | | 150 € | | | 146 € | 2,248 kW h |
| 6 | | 151 € | | | 147 € | 2,237 kW h |
| 7 | | 152 € | | | 147 € | 2,226 kW h |
| 8 | | 152 € | 56 € | | 200 € | 2,215 kW h |
| 9 | | 153 € | | | 146 € | 2,204 kW h |
| 10 | | 154 € | | | 147 € | 2,193 kW h |
| 11 | | 155 € | | 979 € | 1,074 € | 2,182 kW h |
| 12 | | 156 € | | | 147 € | 2,172 kW h |
| 13 | | 157 € | | | 147 € | 2,161 kW h |
| 14 | | 158 € | | | 147 € | 2,150 kW h |
| 15 | | 159 € | 56 € | | 200 € | 2,140 kW h |
| 16 | | 161 € | | 68 € | 212 € | 2,129 kW h |
| 17 | | 162 € | | | 149 € | 2,119 kW h |
| 18 | | 163 € | | | 149 € | 2,108 kW h |
| 19 | | 164 € | | | 149 € | 2,098 kW h |
| 20 | | 165 € | | | 150 € | 2,088 kW h |
| Σ | 6,102 € | | | | 4,097 € | 43,772 kW h |

²⁵ 2008 (first half-year): 18.0 €-Ct/(kW h), 2018 (first half-year): 25.1 €-Ct/(kW h).

Due to increasing electricity prices over the observation period, the operation-related costs C_O increase over time, too (cf. table 7.4, 2nd column). The sum of all annual expenses (i.e. $C_O + C_D + C_{Rp}$) is subject to the discount rate. As the risk free interest rate of 2%/a is higher than the inflation rate (1.5%/a), the annual expenses slightly decrease over time (cf. table 7.4, 5th row). The 6th row of table 7.4 reflects the discounted revenues of the conventional solar DHW system. Considering the initial costs I_0 , the sum of all annual costs $\sum C$ as well as the annual revenues yields LCoH of 23.3€-Ct/(kW h) for the observed period of 20 a in case of a conventional (metal-based) solar DHW system.

Table 7.5: Time series of cash and energy flows in case of a DBS with polymeric solar thermal FPCs located in Würzburg (Germany).

| t in a | I_0 | C_O | C_D | C_{Rp} | $\frac{\sum C}{(1+r)^t}$ | $\frac{E_t}{(1+r)^t}$ |
|----------------------------|----------------|-------|-------|----------|--------------------------|-----------------------|
| 0 | 7,006 € | | | | | |
| 1 | | 96 € | | | 96 € | 2,352 kW h |
| 2 | | 97 € | | | 96 € | 2,340 kW h |
| 3 | | 97 € | | | 96 € | 2,329 kW h |
| 4 | | 98 € | | | 96 € | 2,317 kW h |
| 5 | | 99 € | | | 97 € | 2,306 kW h |
| 6 | | 100 € | | | 97 € | 2,295 kW h |
| 7 | | 101 € | | | 98 € | 2,284 kW h |
| 8 | | 102 € | | | 98 € | 2,272 kW h |
| 9 | | 103 € | | | 99 € | 2,261 kW h |
| 10 | | 104 € | | | 99 € | 2,250 kW h |
| 11 | | 105 € | | 979 € | 1,027 € | 2,239 kW h |
| 12 | | 106 € | | | 100 € | 2,228 kW h |
| 13 | | 107 € | | | 100 € | 2,217 kW h |
| 14 | | 108 € | | | 101 € | 2,206 kW h |
| 15 | | 109 € | | | 101 € | 2,195 kW h |
| 16 | | 110 € | | | 102 € | 2,185 kW h |
| 17 | | 111 € | | | 102 € | 2,174 kW h |
| 18 | | 113 € | | | 103 € | 2,163 kW h |
| 19 | | 114 € | | | 104 € | 2,153 kW h |
| 20 | | 115 € | | | 104 € | 2,142 kW h |
| Σ | 7,006 € | | | | 2,916 € | 44,908 kW h |

Retaining all boundary conditions (i.e. the electricity price increase rates r_E , the discount rate r as well as the observation period of 20 a), the DBS with polymeric solar thermal FPC yields LCoH of 22.1€-Ct/(kW h) and has therefore a slightly higher economic performance than the conventional system. This can be attributed to the lower operation-related costs C_O , the non-existent demand-related costs C_D (due to the fact that the DBS can utilise pure water as a HTF) and to lower replacement costs C_{Rp} (due to the missing MEV). The cash and energy flows of the DBS with polymeric solar thermal FPCs are shown in table 7.5).

7.7 Parametric Study of the Levelised Cost of Heat

The parametric study described in section 6.4 is re-used to determine minimal LCoH for a solar DBS with polymeric FPCs located at different reference locations. For every combination of the heat storage ($200\text{ l} < V_{Storage} < 1,000\text{ l}$) and the collector array ($4\text{ m}^2 < A_{Coll} < 20\text{ m}^2$), the respective LCoH were determined. In case of Würzburg (Germany), an overall minimum of $20.8\text{ €-Ct}/(\text{kW h})$ can be determined for heat a storage volume of 500 l in combination with a 8 m^2 -collector array (cf. figure 7.2). However, the above-mentioned configuration ($V_{Storage} = 300\text{ l}$, $A_{Coll} = 8\text{ m}^2$, $\text{LCoH} = 22.1\text{ €-Ct}/(\text{kW h})$) still is economically more efficient than the reference system with metal-based solar thermal FPCs ($V_{Storage} = 300\text{ l}$, $A_{Coll} = 5\text{ m}^2$, $\text{LCoH} = 23.3\text{ €-Ct}/(\text{kW h})$).

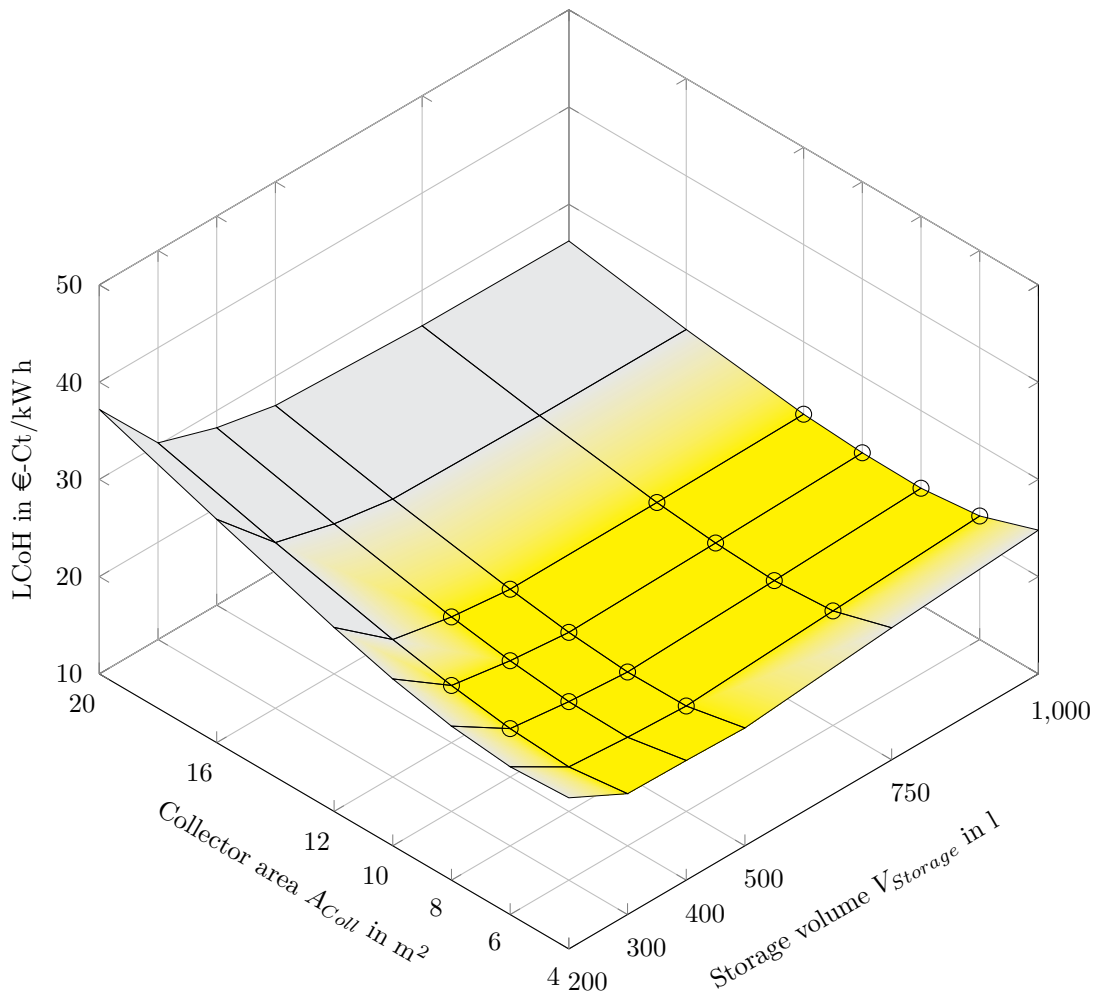


Figure 7.2: LCoH in case of a solar DBS with polymeric solar thermal FPCs located in Würzburg (Germany). The highlighted yellow area indicates system configurations which yield lower LCoH than the solar thermal reference system with metal-based FPCs (cf. section 6.1.2). In addition, the circular markers indicate system configurations with higher fractional energy savings than the solar thermal reference system with metal-based FPCs.

The methodology described above was also applied to determine the LCoH in case of a solar thermal combi system with three heat exchangers (cf. section 6.3). In this setup, the heat storage volume was varied between 600 l and 2,000 l while the collector array ranged between 14 m² and 40 m². The solar combi system described by Bachmann, Fischer and Hafner (2018b) with two heat exchangers (cf. figure 6.7) serves as a reference. In case of Würzburg (Germany), minimum costs of 24.8 €-Ct/(kW h) can be determined for heat storage volume of 1,200 l in combination with a 18 m²-collector array (cf. figure 7.3). Compared to the reference system with metal-based solar thermal FPC ($V_{Storage} = 800$ l, $A_{Coll} = 15$ m², LCoH = 27.7 €-Ct/(kW h)), this results in cost savings of approximately 10%.

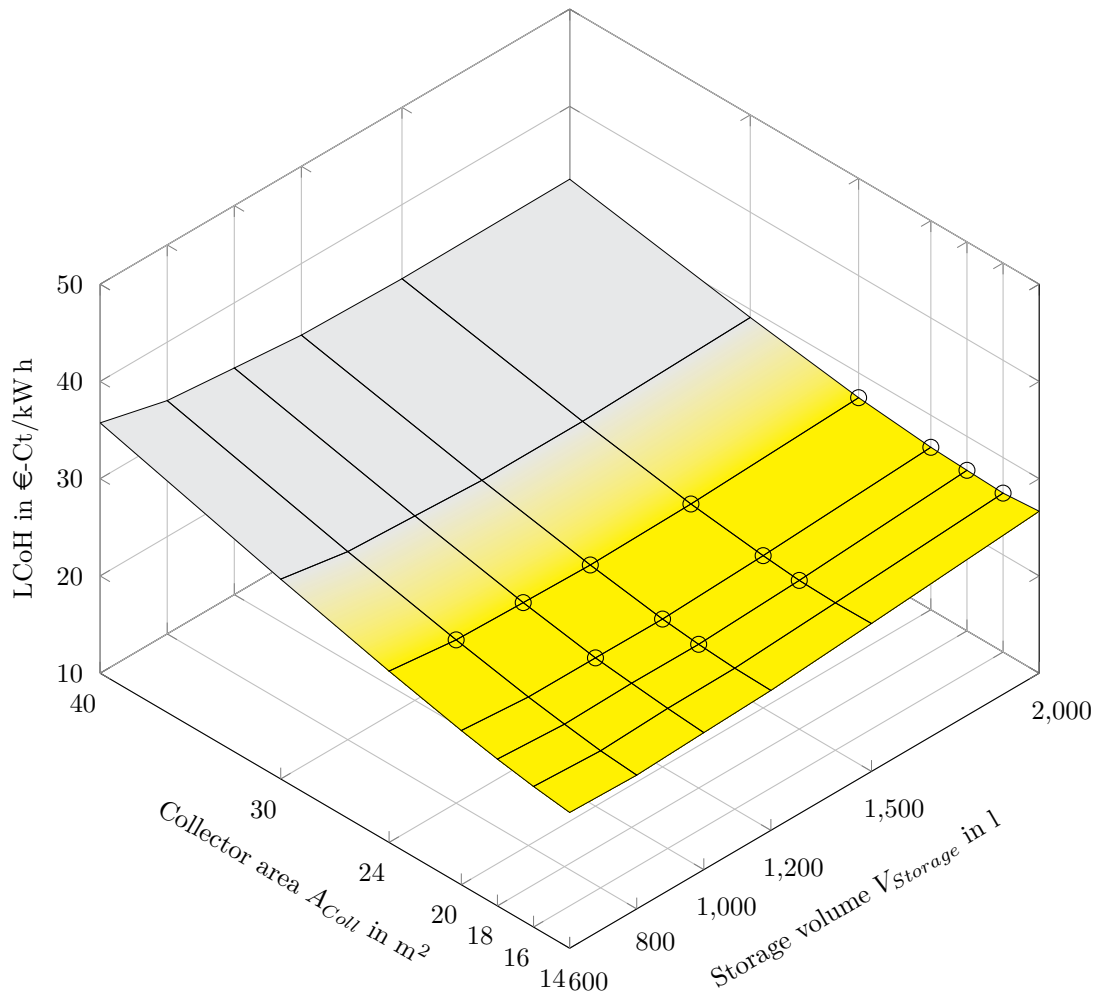


Figure 7.3: LCoH in case of a solar combi system with polymeric solar thermal FPCs located in Würzburg (Germany). The results indicate that no system configurations yields lower LCoH than the solar thermal reference system with metal-based FPCs (cf. section 6.1.3).

The results indicate, that DBSs with polymeric solar thermal FPCs can yield lower LCoH than the respective reference systems with metal-based FPC at all four locations. However, due to the lower efficiency of the investigated polymeric FPCs compared to the metal-based ones, suitable DBSs equipped with polymeric solar thermal FPCs demand for larger collector arrays and heat storages.

7.8 Cost Optimisation Potential for Polymeric Drain Back Systems

Figure 7.4 shows the cost distribution of the aforementioned discussed solar thermal DBS with a 8 m² polymeric solar thermal collector array and a 300l heat storage for DHW preparation located in Würzburg (Germany) (cf. table 7.3).

The underlying investment, installation, replacement, operation-related and demand-related costs are based on today’s available cost information and are thus a conservative – eventually too high – estimation of the resulting LCoH. This section therefore deals with the assessment of potential cost savings for polymeric solar thermal DBSs.

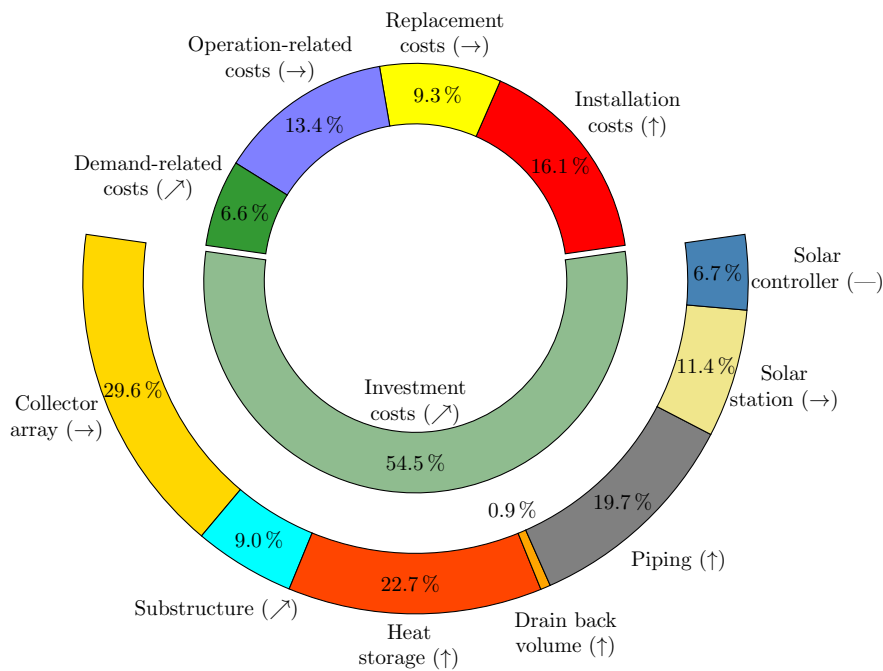


Figure 7.4: Cost distribution (in % of total cost in 20 a) of a solar thermal DBS with polymeric solar thermal FPCs located in Würzburg (Germany). Further details of the system can be found in table 7.3. The arrows indicate the estimated cost saving potential of each category (↑ = Significant cost saving potential, ↗ = Medium cost saving potential, → = Limited cost saving potential, — = No cost saving potential).

7.8.1 Installation Costs

A significant cost saving potential is assumed for installing a DBS with polymeric solar thermal FPCs. Due to their lower weight, the roof installation of the collector array can yield time and cost savings.

Metal-based solar thermal FPCs typically require more than one worker for the installation and handling of a single collector module. Although a weight reduction is also advantageous in case of metal-based FPCs, the associated time-saving is not directly linked to a cost

saving. This can be explained by the fact that the saved time cannot necessarily be invested elsewhere (e.g. at a different building site for installing another collector array). Such a parallelisation of individual tasks is therefore only possible if the solar thermal FPC's weight drops below a certain threshold. Polymeric solar thermal FPCs can address this optimisation target in such a way, that a single person can safely handle them on the roof. By enabling a one-person-installation of the overall collector array, polymeric solar thermal FPCs can exploit that "price threshold effect" and therefore positively contribute to lower costs of solar thermal systems.

Another cost saving potential with respect to the installation results from the unpressurised setup of the DBS. As the pipes do not have to withstand a high operation pressure, simple polymeric hoses can be considered to connect the heat storage with the collector array (and to connect the individual polymeric FPCs of the collector array). Flexible, polymeric hoses allow for an time-efficient installation and yield therefore a cost saving. However, it must be emphasised that "water pockets" must be prevented during installation (cf. section 2.2.2).

The unnecessary pressure resistance in case of DBSs positively also contributes to a reduction of the installation costs in case of the heat storage. Similar to the collector array, a reduced amount of workers is necessary to carry the heat storage into the basement, which yields a cost saving to the solar thermal system's owner as well as to an increased flexibility for the system's installer.

7.8.2 Investment / Replacement costs

Overall, DBSs with solar thermal FPCs offer a significant cost saving potential compared to conventional, metal-based solar thermal systems. In addition, the investment cost of such systems offer a further potential for lowering the resulting LCoH. As the costs of polymeric FPCs are strongly linked with the collector's design and the quantity of annually produced units, a reliable estimation regarding the development of future costs is hardly possible. However, the remaining system components offer a cost saving potential. Due to the unpressurised architecture of a DBS, cost-intensive, metal-based materials can be replaced by polymers, too. As the heat storage's outer shell does not have to withstand a certain operation pressure, the wall thickness can be reduced to only withstand the hydrostatic pressure inside the storage tank. By directly integrating the drain back reservoir into the heat storage (cf. section 2.2), the additional cost of the drain back reservoir can be eliminated.

Replacing metal-based pipes by polymeric hoses yields another significant cost saving potential with respect to the investment costs. In addition, the typically metal-based substructure can be replaced by polymeric materials, too. Due to the lower weight of the polymeric solar thermal FPCs, a polymeric substructure may be sufficient to withstand the static and dynamic loads due to wind and / or snow. Although the application of polymeric materials can also be extended to the solar station (e.g. by replacing certain metal components of the pump by polymers), a limited cost saving potential is assumed for this component. Considering the individual cost saving potentials of each component, a moderate overall cost saving can be estimated for investment costs in case of polymer-based DBSs.

Within the 20 a observation period, the solar station and controller have to be replaced after the 10th year (cf. section 7.5). The limited cost saving potential of these two components (with respect to the investment costs) also affects the limited cost saving potential of the replacement costs.

7.8.3 Operation-Related and Demand-Related Costs

As the annual operation-related costs (typically expressed as a portion of the investment costs, cf. section 7.4.1) of DBSs with polymeric solar thermal FPCs are already assumed to be lower than in case of conventional solar thermal systems, no further optimisation potential is estimated.

In case of the demand-related costs (cf. section 7.4.2), a moderate cost saving potential is assumed. Due to the volumetric riser channels of the polymeric absorber structure, a significant lower pressure drop compared to conventional, metal-based solar thermal FPCs may be considered (cf. section 3.1). This directly yields a lower power consumption of the solar pump and therefore lower operation-related costs.

7.8.4 Cost Saving Potential

Considering the aforementioned cost saving potentials, an overall reduction of the investment and installation costs up to 50 % is estimated as a realistic assumption. The replacement, operation-related and demand-related costs as well as all other parameters (i.e. a potential increase / decrease of electricity costs, interest rates, inflation rate, observation period etc.) are assumed to remain unchanged. The results of this parametric investigation is shown in table 7.6.

Table 7.6: Influence of investment / replacement cost saving potential on the resulting LCoH in case of a solar DHW with 300 l heat storage in combination with a 8 m² collector array (cf. table 7.2) located in Würzburg (Germany).

| Cost saving potential in % | Resulting change of LCoH in €-Ct/(kW h) | in % |
|----------------------------|---|------|
| 0 | 22.1 | — |
| 5 | 21.3 | 3.5 |
| 10 | 20.5 | 7.1 |
| 15 | 19.7 | 10.6 |
| 20 | 19.0 | 14.1 |
| 25 | 18.2 | 17.7 |
| 30 | 17.4 | 21.2 |
| 35 | 16.6 | 24.7 |
| 40 | 15.8 | 28.3 |
| 45 | 15.1 | 31.8 |
| 50 | 14.3 | 35.3 |

The results indicate a linear correlation between the cost saving potential of the investigated DBS with polymeric solar thermal FPCs on the resulting LCoH. This can be attributed to the underlying formulation of the LCoH (cf. equation 7.1). Assuming no cost saving potential (i.e. conservative scenario), the resulting LCoH coincident with the already derived value of 22.1 €-Ct/(kW h) (cf. section 7.3). In case of an overall cost saving of 30 % (i.e. optimistic scenario), the LCoH are reduced by 21.2 % to 17.4 €-Ct/(kW h) for the investigated solar thermal system. Although other systems (or other boundary conditions) yield a different cost distribution, a LCoH-reduction of 20 % is considered as a realistic value.

7.9 Summary

The results of the parametric study revealed economically feasible solutions for DBSs with polymeric solar thermal FPCs. Depending on the system type (i.e. solar DHW system or solar combi system) and the location, DBSs with polymeric solar thermal FPCs can yield 10 % lower LCoH compared to reference systems with metal-based FPCs. Independent from the particular setup, the lowest LCoH can be observed at Athens, the highest ones in Stockholm. As already discussed in chapter 6, the hydraulic setup of a solar thermal system with polymeric FPCs is crucial for its fractional energy savings f_{sav} and, subsequently, its economic viability. Integrating polymeric solar thermal FPCs into hydraulic setups which were originally developed for metal-based FPCs may yield systems which are less or even not economically compared to reference systems with metal-based FPCs.

Assessing technical potentials of solar thermal DBSs with polymeric FPCs promises further reductions of the LCoH up to 20 %. This figure also meets the results from Philippen et al. (2016, p. 37), who determined a cost saving potential of 25 % by utilising the drain back approach in combination with polymeric components.

It is to emphasize that the derived LCoH are based on conservative assumptions. Taking into account potential funding (e.g. a 30 % discount on the initial invest costs for solar thermal systems installed in Germany in 2020, Bundesamt für Wirtschaft und Ausfuhrkontrolle (2020)) and further discounts (which are typically given to the end customer when purchasing a complete solar thermal system instead of purchasing every component individually) can significantly reduce the LCoH. However, the focus of this study aims for a comparison of DBSs with polymeric FPCs with conventional solar thermal systems. Therefore, the absolute values of the derived LCoH are of secondary importance compared to their relative difference.

8 Conclusions and Outlook

8.1 Summary of Research Work

The overall objective of this thesis was to assess the levelised cost of heat (LCoH) of drain back systems (DBSs) with polymeric solar thermal flat plate collectors (FPCs) in the context of single family homes.

By reviewing relevant scientific literature, multiple drawbacks regarding the current manufacturing of polymeric absorbers (i.e. merging pre-fabricated, semi-finished components such as twin-wall or honeycombed plates) were identified. Therefore, a novel manufacturing process was adopted to fabricate an absorber prototype made of polypropylene (PP). The chosen twin-sheet-thermoforming (TST) process allows for a highly scalable, automated production of mass-producible polymeric absorbers and subsequently solar thermal FPCs.

The fabricated absorbers were subsequently used to set up four collector prototypes (which differ regarding the chosen cover materials, backside insulations and overall collector dimensions). The resulting polymeric FPCs were tested with respect to their thermal efficiency by means of an indoor solar simulator, indicating comparable efficiencies with respect to both market-available polymeric solar thermal FPCs and setups described in scientific publications. The derived test results were the basis for validating a physical model of a polymeric solar thermal FPC (maximum deviation between simulated and measured results: 5.8 p.p.).

To assess the behaviour of polymeric solar thermal FPCs within a solar thermal DBS under realistic conditions, an appropriate system test rig was set up including the previously developed polymeric collector prototypes. The results obtained from the outdoor test rig were used to validate a simulation model of an entire solar thermal system (maximum deviation between simulated and measured results: 7.6%). In addition, data available from scientific publications was used to validate the simulation model (maximum deviation of the fractional energy saving f_{sav} : < 4.5 p.p.).

Based on the developed system simulation model, a parametric study was performed to determine the system performance of both a solar thermal domestic hot water (DHW) system and a solar combi system at four different locations (i.e. Würzburg (Germany), Athens (Greece), Davos (Switzerland) and Stockholm (Sweden)). The results indicate that solar thermal DBSs with polymeric FPCs are able to yield similar (or even higher) fractional energy savings f_{sav} than the considered reference systems with metal-based solar thermal FPCs. However, DBSs with polymeric FPCs require significantly larger collector arrays and / or heat storage volumes to offset the lower thermal efficiency compared to metal-based solar thermal FPCs. In general, locations with higher values of solar radiation are better suited for DBSs with polymeric FPCs. Further criteria are the required temperatures for DHW preparation and space heating, as the suitability of DBSs with polymeric FPCs increases with decreasing system temperatures.

In the last step, economic parameters such as investment, maintenance and operation costs of polymeric solar thermal DBSs were identified to assess the LCoH of these systems. Evaluating the LCoH indicates, that solar thermal DBSs with polymeric FPCs are able to provide heat at 10 % lower costs (depending on the location) compared to the respective solar thermal reference system with metal-based FPCs.

8.2 Conclusions

The results of this study indicate, that DBSs with polymeric solar thermal FPCs can provide heat at a competitive cost level compared to conventional solar thermal systems. However, due to their limited thermal efficiency compared to metal-based solar thermal FPCs, the applicability of DBSs with polymeric solar thermal FPCs is strongly influenced by the respective climatic conditions and the necessary temperatures enquired by the heating system (both for space heating and DHW preparation). Nevertheless, the derived LCoH of DBSs with polymeric FPCs must be further reduced in order to reach cost competitiveness with other conventional and renewable energy sources. Although the collector costs can be significantly reduced by means of polymeric materials, the open, unpressurised architecture of DBSs allows for a wider application of these materials. For example, metal pipes can be replaced by polymeric (flexible) tubes, as they do not have to withstand the typical operating pressure of conventional solar thermal systems. Further cost savings can be realised by developing polymeric, low-cost heat storages based on polymers: As the cylinder walls only have to withstand the hydrostatic pressure of the water (but not the operation pressure), thin-walled polymeric heat storages (e.g. by utilising manufacturing processes such as extrusion blow moulding) can be utilised. In this case, the necessary drain back volume can be directly integrated into the heat storage. The utilisation of polymeric materials also allows for a re-design of unpressurised heat storages (e.g. cubic-shaped volumes), which better integrate into the building's basement than cylindrical-shaped volumes.

Another focus of cost reduction is the installation of DBSs with polymeric solar thermal FPCs. In case of using the aforementioned polymeric tubes, conventional connection technologies (i.e. welding, soldering or pressing) must be re-designed in a cost-effective manner. In this context, currently used approaches for connecting polymeric tubes can be adopted to develop plug-and-function solutions in the field of polymeric DBSs. Furthermore, the substructure must be adopted to the requirements of polymeric solar thermal FPCs.

It can furthermore be concluded that the hydraulic integration of polymeric FPCs into a particular solar thermal system is crucial. All summed up, replacing metal-based solar thermal FPC by polymeric ones can yield significant cost savings of solar thermal systems. However, it is to emphasise that this replacement has to be accompanied by further measures such as extending the application of polymers to other system components, re-designing the key components of the heating system and developing new hydraulic schemes which are particularly suited for such systems.

With respect to the chosen manufacturing process, the outcomes of this study indicate that the TST process is highly suitable for mass production of polymeric solar thermal FPCs made from standard plastics such as PP. Contrary to the currently chosen procedure of

fabricating polymeric solar thermal FPCs (i.e. merging together pre-fabricated components requiring high personal expenditures and / or supporting devices such as robotic arms), the TST process allows for a highly scalable manufacturing of such collectors. Although implementing the TST process might be too expensive for an individual manufacturer of solar thermal FPCs, the necessary facilities are typically available at manufactures of plastic components (e.g. for the automotive industry). Especially in times of lower production, these facilities can be used to produce a batch of polymeric solar thermal FPCs, allowing for a better utilisation of the available production facilities.

8.3 Outlook

Throughout this research, several scientific questions outside the primarily focus of this study were identified. To further promote DBSs with polymeric solar thermal FPCs, the most important research activities are proposed subsequently.

In the context of this study, polymeric absorbers were fabricated by utilising the TST process. Those absorbers were the basis for subsequently built prototypes of FPCs. In order to fully exploit the advantages of modern processing techniques, further research towards a fully automated collector manufacturing of solar thermal FPCs should be performed. This includes, for example, the further development of an appropriate framework / structure that both adopts the developed absorber concept and enables a proper mounting to the substructure. In case of a polymeric substructure, the influence of wind and / snow loads should be carefully evaluated. Especially at the interface between collector and substructure, connection mechanisms already developed and used in the field of plastics technology (e.g. a simple click mechanism) should be taken into consideration. The same applies for connecting polymeric tubes to a polymeric solar thermal FPC. Quick-mounting systems are already applied in other fields of application and should also be considered within solar thermal systems. Another possible application of polymers in the context of solar thermal systems are heat storages. Although simple storage tanks made from polymers are already available (e.g. oil tanks), further research activities should focus on polymeric heat exchangers and / or heat storage designs which do not require any heat exchangers (e.g. a multi-compartment heat storage). In any case, the direct integration of the drain back volume into such a polymeric heat storage should be considered to reduce the investment cost of a DBS.

The major benefit of the developed, physical model of a solar thermal FPC is its capability of predicting the temperatures of individual components such as absorber, frontside glazing or the backside insulation. However, integrating this collector model into a simulation model of a complete solar thermal system (e.g. to assess the individual thermal loads occurring throughout one year) requires a high computational effort (compared to a simple parameter model of a solar thermal FPC). Further research activities should therefore focus on combining the advantages of the developed physical model of a solar thermal FPC with those of a simple parameter model.

Within the scope of this study, the developed polymeric solar thermal FPC prototypes have been tested at an outdoor test rig that simulated a realistic solar thermal system. However, implementing such a polymeric solar thermal DBS into a real building allows for much deeper

insights into the operational behaviour of such a system. Ideally, a conventional solar thermal system with metal-based FPCs should be installed into a comparable building placed at a nearby location to allow for a direct comparison of those two systems. This approach will not only reveal differences from a technical point of view (e.g. stagnation temperatures, pump run-times etc.) but also shed more light on the respective operation and maintenance costs of each system. As a consequence, the economic performance of DBSs with polymeric solar thermal FPCs can be better assessed than in the present study.

With regard to the determination of the LCoH, further research should focus on the applicability of DBSs with polymeric solar thermal FPC at other locations to better identify suitable sites for such systems. In addition, country-specific cost information should be taken into account to better assess the economic performance of DBSs with polymeric solar thermal FPCs.

Last but not least, further research towards other application areas of DBSs with polymeric solar thermal FPCs should be performed. This includes, for example, solar district heating networks or low-temperature industrial heat applications. Another promising approach is the fully automated collector manufacturing of PV/T collectors by utilising the TST process. Furthermore, the suitability of the developed polymeric absorbers as a heat source for heat pumps should be examined.

Despite currently decreasing costs of other renewable energy technologies (e.g. PV, heat pumps), solar thermal heat will play an important role within a diverse, future energy system. Therefore, further research aiming towards cost reductions of solar thermal heat should be performed to remain competitive with alternative, renewable heat sources.

Bibliography

- Ariyawiriyanan, W., Meekaew, T., Yamphang, M., Tuenpusa, P., Boonwan, J., Euaphantasate, N., Muangchareon, P. and Chungpaibulpatana, S. (2013). Thermal Efficiency of Solar Collector Made from Thermoplastics. In: *Energy Procedia* 34, pp. 500–505. ISSN: 18766102. DOI: 10.1016/j.egypro.2013.06.778 (cf. pp. 13, 22, 49).
- Armacell GmbH (2018). *Preisliste 2018*. Münster (Germany) (cf. pp. 108, G13).
- Aventa AS (2016). *Solar thermal collector*. Fjellhamar (Norway). URL: <https://aventa.no/wp-content/uploads/2016/10/AventaSolar-solfanger.png> (cf. p. 18).
- Bachmann, S., Fischer, S. and Hafner, B. (2018a). *Conventional Heating System for Single-Family House: INFO Sheet A07*. Ed. by IEA SHC Task54. Freiburg (Germany). URL: <http://task54.iea-shc.org/Data/Sites/1/publications/A07-Info-Sheet--Ref-Conventional-Heating-System--Germany.pdf> (cf. p. 87).
- (2018b). *Solar Combisystem for Single-Family House: INFO Sheet A09*. Ed. by IEA SHC Task54. Freiburg (Germany). URL: <http://task54.iea-shc.org/Data/Sites/1/publications/A09-Info-Sheet--Ref-SF-Solar-Combisystem--Germany.pdf> (cf. pp. 91, 92, 100, 117).
- (2018c). *Solar Domestic Hot Water System for Single-Family House: INFO Sheet A08*. Ed. by IEA SHC Task54. Freiburg (Germany). URL: <http://task54.iea-shc.org/Data/Sites/1/publications/A08-Info-Sheet--Ref-SF-SDHW-System--Germany.pdf> (cf. pp. 89, 90, 99).
- Berner, J. (2012). Leere Kollektoren, voller Schutz. In: *Sonne Wind & Wärme* 9, pp. 58–61 (cf. p. 32).
- Bokhoven, T., van Dam, J. and Kratz, P. (2001). Recent experience with large solar thermal systems in The Netherlands. In: *Solar Energy* 71 (5), pp. 347–352. ISSN: 0038092X. DOI: 10.1016/S0038-092X(00)00124-9 (cf. pp. 23, 25, 34).
- Boltzmann, L. (1884). Ableitung des Stefan’schen Gesetzes, betreffend die Abhängigkeit der Wärmestrahlung von der Temperatur aus der electromagnetischen Lichttheorie. In: *Annalen der Physik* 258 (6), pp. 291–294. DOI: 10.1002/andp.18842580616 (cf. p. 60).
- Bonnet, M. (2014). *Kunststofftechnik: Grundlagen, Verarbeitung, Werkstoffauswahl und Fallbeispiele*. 2nd ed. Wiesbaden (Germany): Springer Vieweg. ISBN: 9783658031381. DOI: 10.1007/978-3-658-03139-8 (cf. p. 12).
- Bonten, C. (2014). *Kunststofftechnik: Einführung und Grundlagen*. München (Germany): Hanser. ISBN: 9783446441712. DOI: 10.3139/9783446441712 (cf. p. 42).
- Botpaev, R., Louvet, Y., Perers, B., Furbo, S. and Vajen, K. (2015). Drainback solar thermal systems: A Review. In: *Solar Energy* 128, pp. 41–60. ISSN: 0038092X. DOI: 10.1016/j.solener.2015.10.050 (cf. pp. 23–27, 30).
- Botpaev, R., Orozaliev, J. and Vajen, K. (2014). Experimental Investigation of the Filling and Draining Processes of the Drainback System (Part 1). In: *Energy Procedia* 57, pp. 2467–2476. ISSN: 18766102. DOI: 10.1016/j.egypro.2014.10.256 (cf. pp. 25, 30, 35).
- Botpaev, R. and Vajen, K. (2014a). *Drainback Systems: Market overview*. In: *24. Symposium Thermische Solarenergie*. Regensburg (Germany): Ostbayerisches Technologie-Transfer-Institut e.V. (OTTI), pp. 84–92 (cf. pp. 26, 32).

Bibliography

- Botpaev, R. and Vajen, K. (2014b). *Experimental investigation of the filling and draining processes of drainback systems (Part 2)*. In: *Proceedings of the EuroSun 2014*. Freiburg (Germany): International Solar Energy Society (ISES), pp. 2467–2476. ISBN: 9783981465938. DOI: 10.18086/eurosun.2014.03.03 (cf. pp. 29, 30).
- Brandemuehl, M. J. and Beckman, W. A. (1980). Transmission of diffuse radiation through CPC and flat plate collector glazings. In: *Solar Energy* 24 (5), pp. 511–513. ISSN: 0038092X. DOI: 10.1016/0038-092X(80)90320-5 (cf. p. 68).
- British Petrol (2019). *BP Energy Outlook 2040: February 2019*. London (United Kingdom). URL: <https://www.bp.com/content/dam/bp/business-sites/en/global/corporate/xlsx/energy-economics/energy-outlook/bp-energy-outlook-2019-summary-tables.xlsx> (cf. p. 1).
- Buchinger, R. and Berek, M. (2015). *Thermischer Solarkollektor*. Pat. WO2015135557A1. URL: <https://patentscope.wipo.int/search/en/detail.jsf?docId=W02015135557> (cf. p. 17).
- Buderus Thermotechnik GmbH (2018). *Katalog Wärmezeugung: Solarsysteme*. Wetzlar (Germany) (cf. pp. 108, G9, G13, G14, G17, G20, G21, G22).
- Bundesamt für Wirtschaft und Ausfuhrkontrolle, ed. (2020). *Förderübersicht: Heizen mit erneuerbaren Energien 2020*. Eschborn (Germany). URL: https://www.bafa.de/ShareDDocs/Downloads/DE/Energie/ee_foerderuebersicht_2020 (cf. pp. 110, 121).
- Bundesministerium für Wirtschaft und Energie (2019). *Zahlen und Fakten Energiedaten: Nationale und Internationale Entwicklung*. Berlin (Germany). URL: https://www.bmwi.de/Redaktion/DE/Binaer/Energiedaten/energiedaten-gesamt-xls.xlsx?__blob=publicationFile&v=95 (cf. p. 1).
- Bundesverband Solarwirtschaft e.V., ed. (2012). *Fahrplan Solarwärme: Strategie und Maßnahmen der Solarwärme-Branche für ein beschleunigtes Marktwachstum bis 2030*. Berlin (Germany). URL: https://www.solarwirtschaft.de/fileadmin/media/pdf/120854_bsw_studie_st.pdf (cf. p. 2).
- Cadafalch, J. (2009). A detailed numerical model for flat-plate solar thermal devices. In: *Solar Energy* 83 (12), pp. 2157–2164. ISSN: 0038092X. DOI: 10.1016/j.solener.2009.08.013 (cf. p. 69).
- Callister, W. D. and Rethwisch, D. G. (2020). *Fundamentals of materials science and engineering: An integrated approach*. 10th ed. Hoboken, NJ (USA): Wiley. ISBN: 9781119453918 (cf. pp. 10–12).
- Carlsson, B., Persson, H., Meir, M. and Rekstad, J. (2014). A total cost perspective on use of polymeric materials in solar collectors – Importance of environmental performance on suitability. In: *Applied Energy* 125, pp. 10–20. ISSN: 03062619. DOI: 10.1016/j.apenergy.2014.03.027 (cf. p. 106).
- Chen, G., Doroshenko, A., Koltun, P. and Shestopalov, K. (2015). Comparative field experimental investigations of different flat plate solar collectors. In: *Solar Energy* 115, pp. 577–588. ISSN: 0038092X. DOI: 10.1016/j.solener.2015.03.021 (cf. pp. 14, 20, 22).
- CitrinSolar GmbH (2018). *Preisliste 2018*. Moosburg (Germany). URL: www.e-sol-diffusion.com/download/cs-pl-de-bruttopreisliste-1801.pdf (cf. pp. 107, 108, G5, G7, G9, G14, G17, G20, G21, G22).

- Consolar GmbH (2006). *Preisliste Solare Heizungssysteme*. Lörrach (Germany). URL: https://www.oeko-energie.de/Preislisten/Consolar_Preise_2006.pdf (cf. pp. 108, G9, G14, G17, G20, G21).
- Cristofari, C., Notton, G., Poggi, P. and Louche, A. (2002). Modelling and performance of a copolymer solar water heating collector. In: *Solar Energy* 72 (2), pp. 99–112. ISSN: 0038092X. DOI: 10.1016/S0038-092X(01)00092-5 (cf. pp. 14, 22).
- Deutsche Gesellschaft für Sonnenenergie (2010). *Planning and installing solar thermal systems: A guide for installers, architects and engineers*. 2nd ed. London (United Kingdom): Earthscan. ISBN: 9781844077601 (cf. p. G1).
- DIN CERTO, ed. (2011). *Summary of EN 12975 Test Results, annex to Solar Keymark Certificate: Licence Number: 011-7S1599F* (cf. p. 19).
- ed. (2014). *Summary of EN 12975 Test Results, annex to Solar Keymark Certificate: Licence Number: 011-7S2409F* (cf. p. 19).
- ed. (2015). *Summary of EN ISO 9806 Test Results, annex to Solar Keymark Certificate: Licence Number: 011-7S2586F* (cf. p. 19).
- Dominghaus, H., Elsner, P., Eyerer, P. and Hirth, T. (2012). *Kunststoffe: Eigenschaften und Anwendungen*. 8th ed. Berlin (Germany): Springer. ISBN: 9783642161735. DOI: 10.1007/978-3-642-16173-5 (cf. pp. 42, 46, 84, 102).
- Duffie, J. A. and Beckman, W. A. (2013). *Solar engineering of thermal processes*. 4th ed. Hoboken, NJ (USA): Wiley. ISBN: 1118433483 (cf. pp. 7, 10, 18, 56, 60, 62, 64–68).
- VDI 2067:2012 (n.d.). *Economic efficiency of building installations: Fundamentals and economic calculation*. Berlin (Germany). URL: <https://www.vdi.de/richtlinien/details/vdi-2067-blatt-1-wirtschaftlichkeit-gebaeudetechnischer-anlagen-grundlagen-und-kostenberechnung-1> (cf. p. 112).
- Ehrenwirth, M., Beckenbauer, D., Klärner, M., Trinkl, C., Zörner, W. and Cheng, V. (2017a). *Theoretical and experimental investigation of polymeric solar-thermal flat-plate collectors*. In: *Conference Proceedings*. Freiburg (Germany): International Solar Energy Society (ISES). DOI: 10.18086/swc.2017.07.01 (cf. p. ii).
- Ehrenwirth, M., Brandmayr, S., Reiter, C., Trinkl, C. and Zörner, W. (2014). *Analysis of Polymeric Solar-thermal Collectors in Drain Back Systems by Simulation*. In: *Proceedings of the EuroSun 2014*. Freiburg (Germany): International Solar Energy Society (ISES). ISBN: 9783981465938. DOI: 10.18086/eurosun.2014.16.05 (cf. p. ii).
- Ehrenwirth, M., Klärner, M., Conti, F., Trinkl, C. and Zörner, W. (2016a). *Messtechnische Untersuchung solarthermischer Kunststoffkollektoren*. In: *26. Symposium Thermische Solarenergie*. Regensburg (Germany): Ostbayerisches Technologie-Transfer-Institut e.V. (OTTI) (cf. p. ii).
- (2016b). *Messtechnische Untersuchung solarthermischer Kunststoffkollektoren*. In: *Gleisdorf Solar 2016 - 12. Internationale Konferenz für Solares Heizen und Kühlen*. Gleisdorf: AEE INTEC, pp. 34–44 (cf. p. ii).
- Ehrenwirth, M., Klärner, M., Reiter, C., Trinkl, C., Zörner, W. and Hoellenriegel, W. (2016c). *Untersuchungen zur Fertigungstechnik und Kollektorkonstruktion für Vollkunststoff-Kollektoren: Abschlussbericht*. Ed. by Technische Hochschule Ingolstadt. Ingolstadt (Germany). DOI: 10.2314/GBV:887789994 (cf. pp. ii, 36, 37, 107).
- Ehrenwirth, M., Klärner, M., Trinkl, C. and Zörner, W. (2015). *Drain-Back-Systeme – Stand der Technik und Potenzial für Kunststoffkollektoren*. In: *25. Symposium Thermische*

Bibliography

- Solarenergie*. Regensburg (Germany): Ostbayerisches Technologie-Transfer-Institut e.V. (OTTI) (cf. p. ii).
- Ehrenwirth, M., Klärner, M., Trinkl, C. and Zörner, W. (2017b). *Technisch-wirtschaftliche Analyse eines solarthermischen Warmwasser-Systems mit Kunststoffkollektoren*. In: *27. Symposium Thermische Solarenergie*. Regensburg (Germany): Ostbayerisches Technologie-Transfer-Inst. e.V. (OTTI) (cf. p. ii).
- Eicker, U. (2012). *Solare Technologien für Gebäude*. 2nd ed. Wiesbaden (Germany): Vieweg + Teubner. ISBN: 9783834812810. DOI: 10.1007/978-3-8348-8237-0 (cf. pp. 2, 9, 24, 40, 56, 61–65, 67, 73, 106, 109, E1).
- Engeler, L. and Salerno, B. (2006). *SOLMAT Frostschutzmittelfreie Wassererwärmung: Schlussbericht*. Ed. by Salerno Engeler GmbH. Langenbruck (Switzerland) (cf. pp. 24, 30, 32, 35).
- European Central Bank (2020). *Euro foreign exchange reference rates*. Frankfurt (Germany). URL: <https://www.ecb.europa.eu/stats/eurofxref/eurofxref-hist.zip> (cf. pp. 11, 14, 24, 108).
- (2018). *Long-term interest rate for convergence purposes - 10 years maturity, denominated in Euro - Germany: IRS.M.DE.L.L40.CI.0000.EUR.N.Z*. Frankfurt (Germany). URL: http://sdw.ecb.europa.eu/quickview.do?SERIES_KEY=229.IRS.M.DE.L.L40.CI.0000.EUR.N.Z (cf. p. 113).
- Eurostat (2018). *Electricity prices for household consumers - bi-annual data (from 2007 onwards): nrg_pc_204*. Luxembourg City (Luxembourg). URL: appsso.eurostat.ec.europa.eu/nui/show.do?dataset=nrg_pc_204 (cf. pp. 111–114).
- Frick, S., Piekarczyk, A., Köhl, M., Volk, M. and Weiß, K.-A. (2014). *Kostenanalyse und Fertigungsoptimierung von Polymerkollektoren für den globalen Markt*. In: *Gleisdorf Solar 2014 - 11. Internationale Konferenz für Solares Heizen und Kühlen*. Gleisdorf (Austria): AEE INTEC, pp. 43–58 (cf. pp. 2, 106).
- Fuentes, M. K. (1987). *A simplified thermal model for Flat-Plate photovoltaic arrays*. Ed. by Sandia National Laboratories. Albuquerque, NM (USA). URL: <http://prod.sandia.gov/techlib/access-control.cgi/1985/850330.pdf> (cf. p. E1).
- DIN EN 13203-2:2015 (n.d.). *Gas-fired domestic appliances producing hot water - Part 2: Assessment of energy consumption*. Berlin (Germany). URL: <https://www.beuth.de/de/norm/din-en-13203-2/233887170> (cf. pp. 86, 88, 90, 92, 97).
- GASOKOL GmbH (2013). *Solar Preise 2013*. Saxen (Austria). URL: www.gasokol.be/upload/file/Prijслиjsten/PL_DE_1302_V1_1_VE.pdf (cf. pp. 107, 108, G5, G7, G9, G14, G17, G20, G21, G22).
- Gaspar, G. and Michalconok, G. (2016). *Proposal and simulation of control system for solar domestic water heating with drain-back*. In: *INES 2016 - 20th Jubilee IEEE International Conference on Intelligent Engineering Systems*. Piscataway, NJ (USA): Institute of Electrical and Electronics Engineers (IEEE), pp. 141–146. ISBN: 9781509012169. DOI: 10.1109/INES.2016.7555108 (cf. pp. 31, 34).
- Gladen, A. C., Davidson, J. H. and Mantell, S. C. (2014). Selection of thermotropic materials for overheat protection of polymer absorbers. In: *Solar Energy* 104, pp. 42–51. ISSN: 0038092X. DOI: 10.1016/j.solener.2013.10.026 (cf. p. 18).
- (2015). The Effect of a Thermotropic Material on the Optical Efficiency and Stagnation Temperature of a Polymer Flat Plate Solar Collector. In: *Journal of Solar Energy Engineering* 137 (2), pp. 1–6. DOI: 10.1115/1.4028366 (cf. p. 20).

- DIN EN 410:2011 (n.d.). *Glas im Bauwesen - Bestimmung der lichttechnischen und strahlungsphysikalischen Kenngrößen von Verglasungen*. Berlin (Germany). URL: <https://www.beuth.de/de/norm/din-en-410/138424295> (cf. p. C1).
- Gnielinski, V. (1975). Neue Gleichungen für den Wärme- und den Stoffübergang in turbulent durchströmten Rohren und Kanälen. In: *Forschung im Ingenieurwesen* 41 (1), pp. 8–16. DOI: 10.1007/BF02559682 (cf. p. 55).
- ASHRAE 1990 (n.d.). *Guide for preparing active solar heating systems operation and maintenance manuals*. Atlanta, GA (USA). URL: https://www.techstreet.com/ashrae/standards/guide-for-preparing-active-solar-heating-systems-operation-and-maintenance-manuals?gateway_code=ashrae&product_id=1718879 (cf. p. 30).
- Haaland, S. E. (1983). Simple and Explicit Formulas for the Friction Factor in Turbulent Pipe Flow. In: *Journal of Fluids Engineering* 105 (1), pp. 89–90. DOI: 10.1115/1.3240948 (cf. p. 55).
- Hausner, R. and Fechner, H. (1999). *Influence of the flow condition (laminar / turbulent) in the fluid tube on the collector efficiency factor of a fin absorber*. In: *Book of Proceedings Volume 2*. Birmingham (United Kingdom): Franklin, pp. 1–6. ISBN: 0952415038. URL: <http://www.aee-intec.at/0uploads/dateien116.pdf> (cf. p. 49).
- DIN EN 12828:2014 (n.d.). *Heating systems in buildings - Design for water-based heating systems*. Berlin (Germany). URL: <https://www.beuth.de/de/norm/din-en-12828/203258170> (cf. p. G1).
- Hermann, M. (2012). *BIONICOL: Project final report*. Ed. by Fraunhofer Institute for Solar Energy Systems. Freiburg (Germany). URL: http://www.bionicol.eu/Final_Report_BIONICOL.pdf/at_download/file (cf. p. 10).
- Herrero López, S., López Perez, S., del Hoyo Arce, I. and Mesonero Dávila, I. (2015). *Dynamic Modelling of a Flat-Plate Solar Collector for Control Purposes*. In: *The 11th International Modelica Conference*. Linköping (Sweden): Modelica Association, pp. 419–426. DOI: 10.3384/ecp15118419 (cf. pp. 50, 52).
- Hesselschwerdt, A. L. (1954). *Performance of the M.I.T. solar house*. In: *Space Heating with Solar Energy*. Cambridge, MA (USA): Massachusetts Institute of Technology (M.I.T), pp. 99–107 (cf. pp. 23, 31, 34).
- Hintringer, C., Richtfeld, A. and Hauer, N. (2014). *Ein Beitrag zur Simulation und Messung eines Kunststoffkollektors mit integriertem Überhitzungsschutz*. In: *24. Symposium Thermische Solarenergie*. Regensburg (Germany): Ostbayerisches Technologie-Transfer-Institut e.V. (OTTI) (cf. p. 20).
- Hollands, K. G. T., Unny, T. E., Raithby, G. D. and Konicek, L. (1976). Free Convective Heat Transfer Across Inclined Air Layers. In: *Journal of Heat Transfer* 98 (2), pp. 189–193. DOI: 10.1115/1.3450517 (cf. p. 59).
- Hollands, K. (1965). Honeycomb devices in flat-plate solar collectors. In: *Solar Energy* 9 (3), pp. 159–164. ISSN: 0038092X. DOI: 10.1016/0038-092X(65)90089-7 (cf. p. 17).
- Hopmann, C. and Michaeli, W. (2015). *Einführung in die Kunststoffverarbeitung*. 7th ed. München (Germany): Hanser. ISBN: 9783446446274 (cf. p. 36).
- Hottel, H. C. and Woertz, B. B. (1942). The Performance of Flat Plate Solar-Heat Collectors. In: *Transactions of the ASME* 64, pp. 64–91 (cf. p. 7).
- Idel’cik, I. E. (1996). *Handbook of hydraulic resistance*. 3rd ed. New York, NY (USA): Begell House. ISBN: 1567000746 (cf. p. 38).

Bibliography

- DIN EN 60751:2009 (n.d.). *Industrial platinum resistance thermometers and platinum temperature sensors*. Berlin (Germany). URL: <https://www.beuth.de/de/norm/din-en-60751/115799593> (cf. p. 45).
- Intergovernmental Panel on Climate Change, ed. (2014). *Climate Change 2014: Mitigation of Climate Change: Contribution of Working Group III to the Fifth Assessment Report of the Intergovernmental Panel on Climate Change*. Cambridge (United Kingdom). URL: https://www.ipcc.ch/site/assets/uploads/2018/02/ipcc_wg3_ar5_full.pdf (cf. p. 1).
- Internationales Design Zentrum Berlin e. V. (2015). *Eine-Welt-Solar-Kollektor: Sunlumo Technology GmbH*. Berlin (Germany). URL: <https://www.bundespreis-ecodesign.de/img/big2404.jpg> (cf. p. 17).
- Jack, S. and Rockendorf, G. (2013). *Wärmerohre in Sonnenkollektoren - Wärmetechnische Grundlagen und Bewertung sowie neue Ansätze für die Integration: Abschlussbericht zum Vorhaben*. Ed. by Institut für Solarenergieforschung GmbH. Hameln / Emmerthal (Germany). DOI: 10.2314/GBV:788667017 (cf. p. 111).
- Kahlen, S., Wallner, G. M. and Lang, R. W. (2010). Aging behavior of polymeric solar absorber materials – Part 1. In: *Solar Energy* 84 (9), pp. 1567–1576. ISSN: 0038092X. DOI: 10.1016/j.solener.2010.03.021 (cf. p. 84).
- Kalogirou, S. A. (2004). Solar thermal collectors and applications. In: *Progress in Energy and Combustion Science* 30 (3), pp. 231–295. ISSN: 03601285. DOI: 10.1016/j.pecs.2004.02.001 (cf. pp. 7, 9, 10).
- Kaltschmitt, M. (2013). *Erneuerbare Energien: Systemtechnik, Wirtschaftlichkeit, Umweltaspekte*. 5th ed. Berlin (Germany): Springer. ISBN: 9783642032493 (cf. pp. 2, 8, 9, 73, 105–109).
- Kearney, M., Davidson, J. H. and Mantell, S. (2005). Polymeric Absorbers for Flat Plate Collectors: Can Venting Provide Adequate Overheat Protection?. In: *Journal of Solar Energy Engineering* 127 (3), pp. 421–414. DOI: 10.1115/1.1979518 (cf. p. 19).
- Kessentini, H., Castro, J., Capdevila, R. and Oliva, A. (2014). Development of flat plate collector with plastic transparent insulation and low-cost overheating protection system. In: *Applied Energy* 133, pp. 206–223. ISSN: 03062619. DOI: 10.1016/j.apenergy.2014.07.093 (cf. p. 19).
- Kim, S. I., Kissick, J., Spence, S. and Boyle, C. (2016). Design, analysis and performance of a polymer-carbon nanotubes based economic solar collector. In: *Solar Energy* 134, pp. 251–263. ISSN: 0038092X. DOI: 10.1016/j.solener.2016.04.019 (cf. pp. 15, 22, 48).
- Köhl, M. (2015). *Konzeption von extrudierten Polymerkollektoren und Komponenten: Schlussbericht*. Ed. by Fraunhofer Institute for Solar Energy Systems. Freiburg (Germany). DOI: 10.2314/GBV:865648514 (cf. p. 106).
- Köhl, M., Meir, M. G. and Papillon, P. (2013). *Polymeric materials for solar thermal applications*. Weinheim (Germany): Wiley. ISBN: 9783527332465. DOI: 10.1002/9783527659609 (cf. pp. 16, 24, 73).
- Krohne Messtechnik GmbH, ed. (1993). *Compact magnetic inductive flowmeters IFM 1080: Installation and operating instructions IFM 1080*. Duisburg (Germany) (cf. p. 79).
- ed. (2004). *IFC 300: Technisches Datenblatt*. Duisburg (Germany) (cf. p. 46).
- ed. (2013). *OPTIMASS 6000: Technisches Datenblatt*. Duisburg (Germany) (cf. p. 78).

- Kutscher, C., Davenport, R., Farrington, R., Jorgensen, G., Lewandowski, A. and Vineyard, C. (1984). *Low-Cost Collectors / Systems Development Progress Report*. Ed. by Solar Energy Research Institute. Golden, CO (USA) (cf. pp. 23, 26, 27, 29, 30).
- Kutscher, C. (1985). *Low Cost Solar Water and Space Heating Systems*. Ed. by Solar Energy Research Institute. Golden, CO (USA). URL: <http://www.nrel.gov/docs/legosti/old/2672.pdf> (cf. pp. 25, 27).
- Louvet, Y., Botpaev, R. and Vajen, K. (2015). *Evaluation of a large solar thermal drainback system for hay bales drying*. In: *Conference Proceedings*. Freiburg (Germany): International Solar Energy Society (ISES). ISBN: 9783981465952. DOI: 10.18086/swc.2015.10.39 (cf. pp. 24, 28, 29, 31, 34).
- Louvet, Y., Fischer, S., Furbo, S., Köhl, M., Mauthner, F. and Philippen, D. (2018). *LCoH for Solar Thermal Applications: INFO Sheet A01*. Ed. by IEA SHC Task54. Freiburg (Germany). URL: <http://task54.iea-shc.org/Data/Sites/1/publications/A01-Info-Sheet--LCOH-for-Solar-Thermal-Applications.pdf> (cf. pp. 106, 112).
- MacAdams, W. H. (1954). *Heat transmission*. 3rd ed. New York, NY (USA): McGraw-Hill. ISBN: 0070447993 (cf. p. 56).
- Martin, M. and Berdahl, P. (1984). Characteristics of infrared sky radiation in the United States. In: *Solar Energy* 33 (3-4), pp. 321–336. ISSN: 0038092X. DOI: 10.1016/0038-092X(84)90162-2 (cf. p. E1).
- Martinopoulos, G., Missirlis, D., Tsilingiridis, G., Yakinthos, K. and Kyriakis, N. (2010). CFD modeling of a polymer solar collector. In: *Renewable Energy* 35 (7), pp. 1499–1508. ISSN: 09601481. DOI: 10.1016/j.renene.2010.01.004 (cf. pp. 13, 14, 22, 48).
- Mathioulakis, E., Voropoulos, K. and Belessiotis, V. (1999). Assessment of uncertainty in solar collector modeling and testing. In: *Solar Energy* 66 (5), pp. 337–347. ISSN: 0038092X. DOI: 10.1016/S0038-092X(99)00034-1 (cf. p. 46).
- Matuska, T. and Zmrhal, V. (2009). *KOLEKTOR 2.2 - Reference handbook: A mathematical model and design tool*. Ed. by Czech Technical University. Prague (Czech Republic). URL: http://users.fs.cvut.cz/tomas.matuska/wordpress/wp-content/uploads/2015/02/Reference_Handbook_KOLEKTOR_012009.pdf (cf. p. 68).
- Mauthner, F., Weiss, W. and Spörk-Dür, M. (2015). *Solar Heat Worldwide: Markets and Contribution to the Energy Supply 2013*. Ed. by IEA Solar Heating & Cooling Programme. Gleisdorf (Austria). URL: <http://www.iea-shc.org/data/sites/1/publications/Solar-Heat-Worldwide-2015.pdf> (cf. pp. 2, 7).
- Meteotest AG (2018). *Meteonorm*. Bern (Switzerland). URL: https://meteonorm.com/assets/downloads/mn73_software.pdf (cf. pp. 85, 86, F1, F7, F13).
- ASHRAE 93-1986 (n.d.). *Methods of Testing to Determine the Thermal Performance of Solar Collectors*. Atlanta, GA (USA) (cf. p. 15).
- Mills, A. F. (1999). *Heat transfer*. 2nd ed. Upper Saddle River, NJ (USA): Prentice Hall. ISBN: 0139476245 (cf. pp. 54, 55, 57, 61).
- Mintsa Do Ango, A. C., Medale, M. and Abid, C. (2013). Optimization of the design of a polymer flat plate solar collector. In: *Solar Energy* 87, pp. 64–75. ISSN: 0038092X. DOI: 10.1016/j.solener.2012.10.006 (cf. pp. 13, 22).
- Missirlis, D., Martinopoulos, G., Tsilingiridis, G., Yakinthos, K. and Kyriakis, N. (2014). Investigation of the heat transfer behaviour of a polymer solar collector for different manifold configurations. In: *Renewable Energy* 68, pp. 715–723. ISSN: 09601481. DOI: 10.1016/j.renene.2014.03.008 (cf. pp. 13, 22, 49).

Bibliography

- Myers, D. (2013). *Solar radiation: Practical modeling for renewable energy applications*. Boca Raton, FL (USA): Taylor & Francis. ISBN: 9781466502949 (cf. p. 45).
- Myers, D. R., Stoffel, T. L., Reda, I., Wilcox, S. M. and Andreas, A. M. (2002). Recent Progress in Reducing the Uncertainty in and Improving Pyranometer Calibrations. In: *Journal of Solar Energy Engineering* 124 (1), pp. 44–50. DOI: 10.1115/1.1434262 (cf. p. 45).
- Oberzig, K. (2014). *Solarwärme: Heizen mit der Sonne*. 2nd ed. Berlin (Germany): Stiftung Warentest. ISBN: 9783868514070 (cf. p. 111).
- Oku Obermaier GmbH (2018). *OKU-Absorber, schwarz, mit 2 Anschlußstutzen 1000*. Geretsried (Germany). URL: <https://www.okuonline.com/oku-absorber-schwarz-mit-2-anschlussstutzen-1000.html> (cf. p. 16).
- Oliva, A., Costa, M. and Segarra, C. (1991). Numerical simulation of solar collectors: The effect of nonuniform and nonsteady state of the boundary conditions. In: *Solar Energy* 47 (5), pp. 359–373. ISSN: 0038092X. DOI: 10.1016/0038-092X(91)90030-Z (cf. p. 50).
- Palyvos, J. A. (2008). A survey of wind convection coefficient correlations for building envelope energy systems' modeling. In: *Applied Thermal Engineering* 28 (8-9), pp. 801–808. ISSN: 13594311. DOI: 10.1016/j.applthermaleng.2007.12.005 (cf. pp. 56, 57).
- PAW GmbH & Co. KG (2017). *DrainBloC DN20 Drainback-System*. Hameln (Germany). URL: https://www.ohrej.se/zbozi-prilohy/paw_drainbloc_gb.pdf (cf. p. 32).
- Perers, B., Furbo, S., Fan, J., Kong, W. and Chen, Z. (2015). Drain Back Systems in Laboratory and in Practice. In: *Energy Procedia* 70, pp. 300–310. ISSN: 18766102. DOI: 10.1016/j.egypro.2015.02.127 (cf. pp. 25, 27, 30–32, 34).
- Peuser, F. A., Remmers, K.-H. and Schnauss, M. (2002). *Solar thermal systems: Successful planning and construction*. Berlin (Germany): Solarpraxis. ISBN: 3934595243 (cf. p. 2).
- Philippen, D., Calfisch, M., Brunold, S. and Haller, M. (2016). *ReSoTech – Reduktion der Marktpreise solarthermischer Anlagen durch neue technologische Ansätze: Teil 1: Potenzialanalyse und Lösungsansätze*. Ed. by SPF Institut für Solartechnik. Rapperswil (Switzerland). URL: http://www.spf.ch/fileadmin/user_upload/Forschung/Projekte/ReSoTech_2016_BFE_Schlussbericht_ReSoTech_Teil1.pdf (cf. p. 121).
- Piekarczyk, A., Volk, M., Heck, M., Wiesmeier, S., Weiß, K.-A. and Köhl, M. (2016). Field Test for Polymeric Collector Models in Different Climatic Locations. In: *Energy Procedia* 91, pp. 384–391. ISSN: 18766102. DOI: 10.1016/j.egypro.2016.06.281 (cf. p. 19).
- Quaschnig, V. (2015). *Regenerative Energiesysteme: Technologie - Berechnung - Simulation*. 9th ed. München (Germany): Hanser. ISBN: 9783446443334. DOI: 10.3139/9783446443334 (cf. pp. 1, 3, 7, 40, 106).
- Reda, I. (2011). *Method to Calculate Uncertainty Estimate of Measuring Shortwave Solar Irradiance using Thermopile and Semiconductor Solar Radiometers*. Ed. by National Renewable Energy Laboratory. Golden, CO (USA). DOI: 10.2172/1021250 (cf. p. 45).
- VDI 4655:2008 (n.d.). *Reference load profiles of single-family and multi-family houses for the use of CHP systems*. Düsseldorf (Germany). URL: <https://www.vdi.de/richtlinien/details/vdi-4655-referenzlastprofile-von-ein-und-mehrfamilienhausern-fuer-den-einsatz-von-kwk-anlagen> (cf. pp. 79, 95, 96).
- Reiter, C., Brandmayr, S., Trinkl, C., Zörner, W. and Hanby, V. I. (2014). Performance Optimisation of Polymeric Collectors by Means of Dynamic Simulation and Sensitivity Analysis. In: *Energy Procedia* 48, pp. 181–191. ISSN: 18766102. DOI: 10.1016/j.egypro.2014.02.023 (cf. p. 2).

- Reiter, C. N., Trinkl, C., Zörner, W. and Hanby, V. I. (2015). A Dynamic Multinode Model for Component-Oriented Thermal Analysis of Flat-Plate Solar Collectors. In: *Journal of Solar Energy* 2015 (1), pp. 1–16. ISSN: 2356-7635. DOI: 10.1155/2015/280694 (cf. pp. 50, 56, 63, 65, 67, 68).
- Rekstad, J., Henden, L., Imenes, A. G., Ingebretsen, F. and Meir, M. (2000). *Effective solar energy utilisation - More dependent on system design than solar collector efficiency*. In: *ISES 1999 Solar World Congress*. Kidlington (United Kingdom): Elsevier, pp. 265–270. ISBN: 9780080951782 (cf. pp. 23, 32, 35).
- Rekstad, J. (2012). *Arrangement for a solar collector plate, solar collector plate, solar collector module, and solar collector system*. Pat. WO2012067515A1. URL: <https://patentscope.wipo.int/search/en/detail.jsf?docId=W02012067515> (cf. p. 18).
- Resch, K., Wallner, G. M. and Hausner, R. (2009). Phase separated thermotropic layers based on UV cured acrylate resins – Effect of material formulation on overheating protection properties and application in a solar collector. In: *Solar Energy* 83 (9), pp. 1689–1697. ISSN: 0038092X. DOI: 10.1016/j.solener.2009.06.006 (cf. p. 20).
- ROTEX Heating Systems GmbH (2018). *Preisliste und technische Daten*. Güglingen (Germany) (cf. pp. 108, G9, G14, G17, G20, G21, G22).
- Roth Werke GmbH (2014). *Preisliste 2014: Solarsysteme*. Dautphetal-Buchenau (Germany) (cf. pp. 108, G1, G10, G15, G17, G20, G21, G22).
- ed. (2013). *Thermotank Quadroline: The new generation of plastic storage tanks*. Dautphetal-Buchenau (Germany). URL: http://www.roth-werke.de/en/files/WS_Thermotank_2013_EN.pdf (cf. p. 76).
- Sandnes, B. and Rekstad, J. (2002). A photovoltaic/thermal (PV/T) collector with a polymer absorber plate. Experimental study and analytical model. In: *Solar Energy* 72 (1), pp. 63–73. ISSN: 0038092X. DOI: 10.1016/S0038-092X(01)00091-3 (cf. pp. 14, 15, 22).
- Sessler, M., Waisman, A. and Plaschkes, M. (2011). *Solar Collector*. Pat. WO 2011//48367 A3. URL: <https://patentscope.wipo.int/search/en/detail.jsf?docId=W02011148367> (cf. p. 17).
- Sillmann, R. and Rockendorf, G. (2001). *Meß- und verfahrenstechnische Unsicherheiten bei Leistungsprüfungen an Sonnenkollektoren*. In: *11. Symposium Thermische Solarenergie*. Regensburg (Germany): Ostbayerisches Technologie-Transfer-Institut e.V. (OTTI), pp. 256–262 (cf. p. 46).
- Slaman, M. and Griessen, R. (2009). Solar collector overheating protection. In: *Solar Energy* 83 (7), pp. 982–987. ISSN: 0038092X. DOI: 10.1016/j.solener.2009.01.001 (cf. p. 20).
- EN ISO 9806:2013 (n.d.). *Solar energy - Solar thermal collectors - Test methods*. Berlin (Germany). URL: <https://www.iso.org/standard/59879.html> (cf. pp. 15, 17, 19, 43–46, 49, 73, 77, 79).
- ISO 9060:1990 (n.d.). *Solar energy - Specification and classification of instruments for measuring hemispherical solar and direct solar radiation*. Geneva (Switzerland). URL: <https://www.iso.org/standard/16629.html> (cf. p. 45).
- VDI 6002-1:2014 (n.d.). *Solar heating for potable water: Basic principles*. Düsseldorf (Germany). URL: <https://www.vdi.de/richtlinien/details/vdi-6002-blatt-1-solare-trinkwassererwaermung-allgemeine-grundlagen-systemtechnik-und-anwendung-im-wohnungsbau> (cf. pp. 105, 111, 112).

Bibliography

- Solar-Institut Jülich (1999). *Conventional And Renewable energy systems Optimization Toolbox*. Jülich (Germany). URL: <https://fh-aachen.sciebo.de/index.php/s/0hxb0iIJrui3ED> (cf. pp. 87, 88, 90, 92, 93, 95, 96).
- Sonne, Wind & Wärme (2018). *Energie-Datenbank*. Offenbach am Main (Germany). URL: <http://www.sonnewindwaerme.de/energie-datenbank> (cf. pp. 106, G2, G3, G4).
- Sonnenkraft GmbH (2018). *Produkte & Preise 2018*. St. Veit/Glan (Austria) (cf. pp. 108, G1, G10, G15, G18, G20, G21, G22).
- Sparrow, E. M., Ramsey, J. W. and Mass, E. A. (1979). Effect of Finite Width on Heat Transfer and Fluid Flow about an Inclined Rectangular Plate. In: *Journal of Heat Transfer* 101 (2), pp. 199–204. DOI: 10.1115/1.3450946 (cf. p. 56).
- Spitzner, M. H., Rodolphi, A., Pfundstein, M. and Gellert, R. (2007). *Dämmstoffe: Grundlagen, Materialien, Anwendungen*. München (Germany): De Gruyter. ISBN: 9783920034188. URL: http://www.degruyter.com/search?f_0=isbnissn&q_0=9783955530211&searchTitles=true (cf. p. 42).
- Statistisches Bundesamt (2018). *Verbraucherpreisindex (inkl. Veränderungsdaten): 61111-0001*. Wiesbaden (Germany). URL: <https://www-genesis.destatis.de/genesis/online/link/tabelleErgebnis/61111-0001?type=dataset> (cf. p. 113).
- Stefan, J. (1879). Über die Beziehung zwischen der Wärmestrahlung und der Temperatur. In: *Sitzungsberichte der mathematisch-naturwissenschaftlichen Classe der kaiserlichen Akademie der Wissenschaften* 79, pp. 391–428 (cf. p. 60).
- STI Solar-Technologie-International GmbH (2017). *SolBox*. Meerane (Germany). URL: https://www.alpha-solar.info/images/product_images/info_images/SolBox-STI-GmbH.jpg (cf. p. 32).
- Stieglitz, R. and Heinzl, V. (2012). *Thermische Solarenergie: Grundlagen, Technologie, Anwendungen*. Berlin (Germany): Springer. ISBN: 9783642294747. DOI: 10.1007/978-3-642-29475-4 (cf. p. 106).
- Swinbank, W. C. (1963). Long-wave radiation from clear skies. In: *Quarterly Journal of the Royal Meteorological Society* 89 (381), pp. 339–348. DOI: 10.1002/qj.49708938105 (cf. pp. 62, 73, E1).
- Tagliafico, L. A., Scarpa, F. and Rosa, M. de (2014). Dynamic thermal models and CFD analysis for flat-plate thermal solar collectors – A review. In: *Renewable and Sustainable Energy Reviews* 30, pp. 526–537. ISSN: 13640321. DOI: 10.1016/j.rser.2013.10.023 (cf. p. 50).
- The MathWorks Inc. (2016a). *MATLAB*. Natick, MA (USA). URL: <https://mathworks.com/products/matlab.html> (cf. pp. 38, 52, 87, 88, 90, 92, 93, 95, 96).
- (2016b). *Simscape*. Natick, MA (USA). URL: <https://mathworks.com/products/simscape.html> (cf. pp. 38, 52, 54).
- (2016c). *Simulink*. Natick, MA (USA). URL: <https://mathworks.com/products/simulink.html> (cf. pp. 87, 88, 90, 92, 93, 95, 96).
- DIN EN 12977-2:2016 (2016). *Thermal solar systems and components - Custom built systems - Part 2: Test methods for solar water heaters and combisystems*. Berlin (Germany). URL: <https://www.beuth.de/de/norm-entwurf/din-en-12977-2/253128226> (cf. pp. 85, 86, 88, 90, 92, 97, F1, F7, F13).
- DIN EN 12975-2:2006 (n.d.). *Thermal solar systems and components - Solar collectors - Part 2: Test methods*. Berlin (Germany). URL: <https://www.beuth.de/de/norm/din-en-12975-2/83764314> (cf. pp. 15, 18, 19).

- Thornton, J. P. and Shannon, L. J. (1984). *Survey of failure modes from 122 residential solar water heaters*. Ed. by ESG Inc. Atlanta, GA (USA). DOI: 10.2172/5955956 (cf. p. 31).
- Thür, A., Neyer, J. and Streicher, W. (2014). *Collector efficiency calculation tool for polymer collectors with temperature limitation*. In: *Proceedings of the EuroSun 2014*. Freiburg (Germany): International Solar Energy Society (ISES). ISBN: 9783981465938. DOI: 10.18086/eurosun.2014.16.23 (cf. p. 20).
- ThüSolar GmbH (2012). *Preisliste Solarthermie 2012*. Rudolstadt (Germany). URL: https://www.thuesolar.de/fileadmin/Download/Preisliste_2012.pdf (cf. pp. 107, 108, G5, G10, G15, G18, G20, G21, G22).
- TiSUN GmbH (2018). *Solar-, Speicher- & Wärmesysteme*. Söll (Austria) (cf. pp. 108, G11, G15, G18, G20, G21, G22).
- UMA Solar (2016). *SunStar Pool heating collector*. Altamonte Springs, FL (USA). URL: https://advancesolar.com/wp-content/uploads/photo-gallery/hc_panel3.jpg (cf. p. 16).
- United Nations, ed. (2015). *Adoption of the Paris Agreement: Proposal by the President: Draft decision -/CP.21*. Paris (France). URL: <http://unfccc.int/resource/docs/2015/cop21/eng/109.pdf> (cf. p. 1).
- Vaillant GmbH (2017). *auroFLOW plus VPM 15 D*. Remscheid (Germany). URL: http://www.gsukr.com.ua/gs/imgs/b/baz_modul.jpg (cf. p. 32).
- Verein Deutscher Ingenieure (2010). *VDI Heat Atlas*. 2nd ed. Berlin (Germany): Springer. ISBN: 9783540778769. DOI: 10.1007/978-3-540-77877-6 (cf. pp. 5, 12, 39, 42, 46, 53, 55–60).
- Viessmann Werke GmbH & Co. KG (2017). *Preisliste 2017 DE: Heizsysteme*. Allendorf (Germany) (cf. pp. 108, G11, G16, G19, G20, G21, G22).
- Wagner Solar GmbH (2017). *Preisliste 03/2017: Solarwärme / Wärmerückgewinnung*. Kirchhain (Germany). URL: www.pv-solartechnik.de/Infos/solarthermie.pdf (cf. pp. 107, 108, G7, G11, G16, G19, G21, G22).
- Wallner, G. M., Resch, K. and Hausner, R. (2008). Property and performance requirements for thermotropic layers to prevent overheating in an all polymeric flat-plate collector. In: *Solar Energy Materials and Solar Cells* 92 (6), pp. 614–620. ISSN: 09270248. DOI: 10.1016/j.solmat.2007.12.005 (cf. p. 20).
- Weiss, W. (2003). *Solar heating systems for houses: A design handbook for solar combisystems*. London (United Kingdom): James & James. ISBN: 1902916468 (cf. pp. 25, 28).
- Weiss, W., Spörk-Dür, M. and Mauthner, F. (2017). *Solar Heat Worldwide: Global Market Development and Trends in 2016*. Ed. by IEA Solar Heating & Cooling Programme. Gleisdorf (Austria). URL: <http://www.iea-shc.org/Data/Sites/1/publications/Solar-Heat-Worldwide-2017.pdf> (cf. pp. 105, 106).
- Wesselak, V., Schabbach, T., Link, T. and Fischer, J. (2013). *Regenerative Energietechnik*. 2nd ed. Berlin (Germany): Springer. ISBN: 9783642241642. DOI: 10.1007/978-3-642-24165-9 (cf. pp. 40, 49).
- Weyres-Borchert, B., Kasper, B.-R. and Drück, H. (2015). *Solare Wärme: Technik - Planung - Hausanlage*. Stuttgart (Germany): Fraunhofer IRB. ISBN: 9783816791492 (cf. p. 111).
- Wikora GmbH (2017). *Preisliste 2017*. Hermaringen (Germany). URL: www.wikora.de/fileadmin/wikoratheme/assets/documents/print_material/preisliste_2017_de.pdf (cf. pp. 107, 108, G5, G6, G7, G8, G12, G19, G20, G21, G22).

Bibliography

- WOLF GmbH (2018). *Preisliste*. Mainburg (Germany) (cf. pp. 107, 108, G6, G8, G12, G19, G20, G21, G22).
- World Meteorological Organization (2012). *Guide to meteorological instruments and methods of observation*. Geneva (Switzerland): World Meteorological Organization. ISBN: 9789263100085. URL: https://library.wmo.int/pmb_ged/wmo_8_en-2012.pdf (cf. p. 45).
- Zhang, K., Hao, L., Du, M., Mi, J., Wang, J.-N. and Meng, J.-p. (2017). A review on thermal stability and high temperature induced ageing mechanisms of solar absorber coatings. In: *Renewable and Sustainable Energy Reviews* 67, pp. 1282–1299. ISSN: 13640321. DOI: 10.1016/j.rser.2016.09.083 (cf. p. 10).

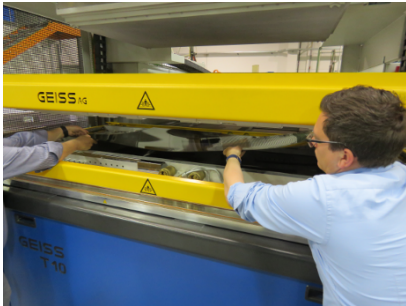
Contents (Appendices)

| | | |
|----------|---|-----------|
| A | Supplementary Photos | A1 |
| B | Measurement Data of the Collector Efficiency Testing | B1 |
| C | Spectroscopy Measurement | C1 |
| D | Numerical Data Obtained with the Collector Model | D1 |
| E | Sky Temperature Modelling | E1 |
| F | Further Results of the Parametric Study | F1 |
| | F.1 Athens (Greece) | F1 |
| | F.2 Davos (Switzerland) | F7 |
| | F.3 Stockholm (Sweden) | F13 |
| G | Component Costs | G1 |

A Supplementary Photos



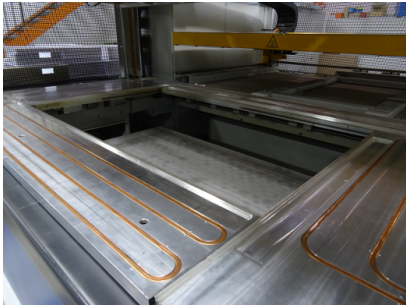
(a) TST-machine (type *Geiss T10*)



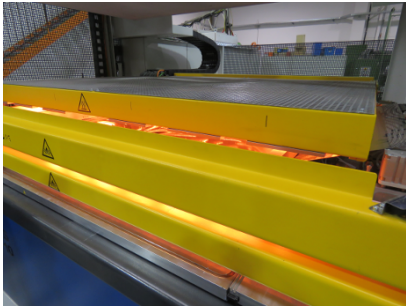
(b) Manual inserting of polymeric sheets



(c) Upper mold half



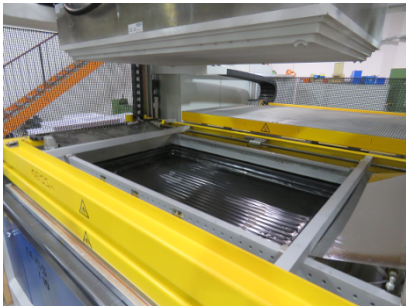
(d) Lower mold half



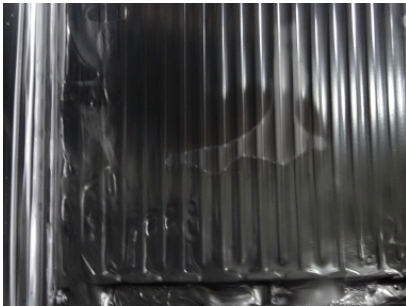
(e) Heat-up of the polymeric sheets



(f) Heated-up polymeric sheets



(g) Reopening the mold halves



(h) Reject part

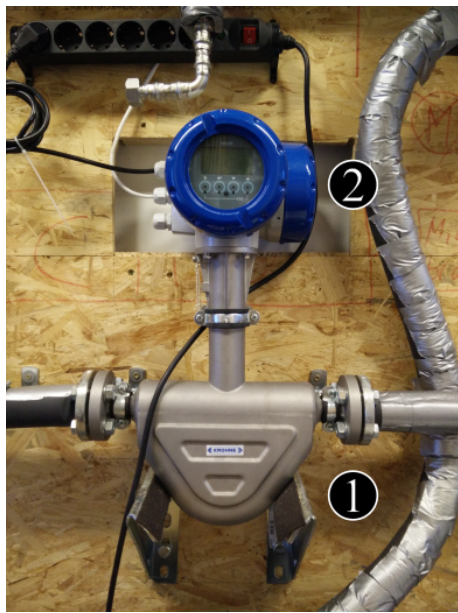
Figure A.1: Photographs of the TST-process.



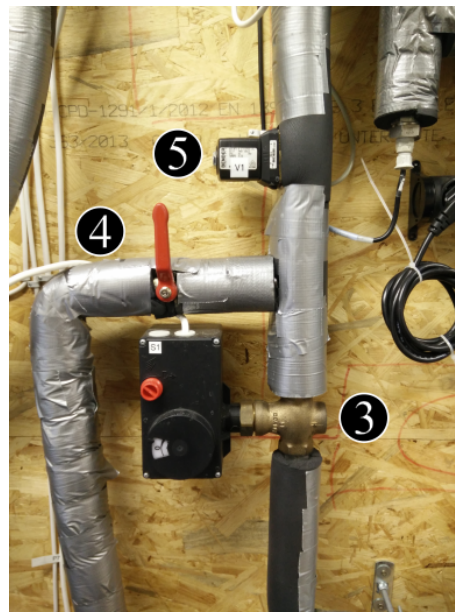
Figure A.2: External view of the system test rig. ① = Container, ② = Collector array, ③ = Pyranometer (horizontally mounted), ④ = Pyranometer (mounted under 45°), ⑤ = Weather station.



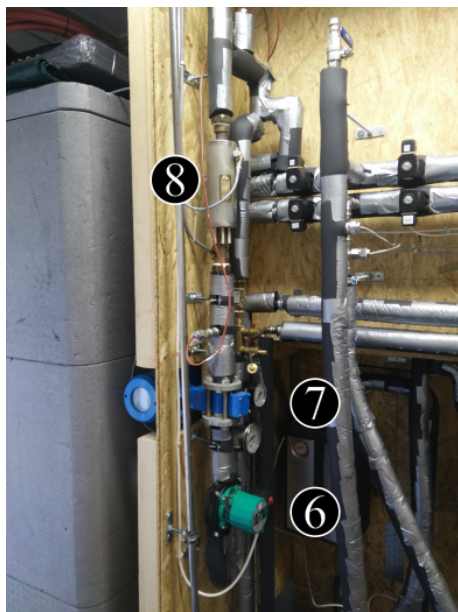
Figure A.3: Collector array. The four polymeric solar thermal FPCs are inclined approximately 5° to the horizontal to ensure a proper self-draining.



(a) Coriolis mass flow meter



(b) Different types of valves



(c) Electric backup heater



(d) Data acquisition / control unit

Figure A.4: Measuring and control equipment used at the system test rig. ① = Coriolis mass flow meter (sensor), ② = Coriolis mass flow meter (sensor head), ③ = Motor control valve, ④ = Ball valve, ⑤ = Magnetic valve, ⑥ = Pump, ⑦ = Volume flow meter, ⑧ = Electric backup heater, ⑨ = Data acquisition / control unit.

A Supplementary Photos



Figure A.5: Drain back reservoir of the system test rig. ① = Uncovered drain back reservoir, ② = Covered drain back reservoir. In order to minimise heat losses to the ambient, a pour-in insulation was filled in between the drain back reservoir and the wooden cover.

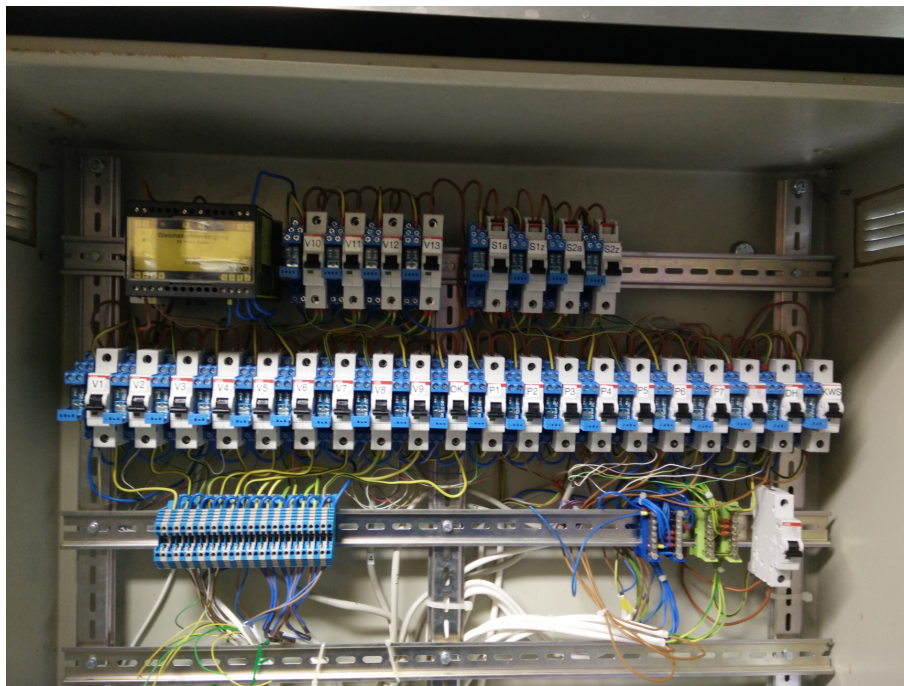


Figure A.6: Control cabinet inside the system test rig. The control cabinet provides both a 230 V AC as well as a 24 V DC voltage source for the electric consumers of the test rig (e.g. pumps, motor control valves, check valves etc.). All components can either be controlled by manual switches or remotely by the external control units (cf. figure A.4).



Figure A.7: Indoor solar simulator. 228 lamps provide a uniform level of irradiation ranging between 600 W/m^2 and $1,100 \text{ W/m}^2$ with a light spectrum comparable to the sunlight. A solar thermal FPC (maximum possible dimensions 1.4 m (width) \times 2.3 m (height), not shown in the photograph) is placed below the lamp field at an angle of inclination of 45° . Fans above the lamp field provide an airflow to prevent the lamps from overheating. During operation, the test rig demands an electric power of approximately 30 kW .

B Measurement Data of the Collector Efficiency Testing

Table B.1: Measurement results for PP-collector with EPS-insulation and glass-glazing (Date of measurement: 22.09.2015). The sub- / superscripts indicate the minimum / maximum deviation from the mean value over the measurement period.

| T_{in} in °C | T_{out} in °C | T_{amb} in °C | \dot{V} in l/h | I in W/m ² |
|---|---|---|---|--|
| 19.16 ^{+0.01} _{-0.00} | 27.13 ^{+0.03} _{-0.02} | 23.23 ^{+0.23} _{-0.22} | 40.13 ^{+0.24} _{-0.30} | 867.63 ^{+0.81} _{-0.89} |
| 19.17 ^{+0.01} _{-0.00} | 27.17 ^{+0.02} _{-0.02} | 23.32 ^{+0.13} _{-0.25} | 39.95 ^{+0.32} _{-0.34} | 867.48 ^{+0.62} _{-0.72} |
| 40.05 ^{+0.01} _{-0.01} | 45.95 ^{+0.02} _{-0.02} | 21.26 ^{+0.36} _{-0.25} | 40.29 ^{+0.36} _{-0.71} | 869.05 ^{+0.58} _{-0.74} |
| 40.06 ^{+0.03} _{-0.02} | 45.99 ^{+0.02} _{-0.03} | 21.97 ^{+0.59} _{-0.72} | 39.90 ^{+0.43} _{-0.45} | 868.76 ^{+0.62} _{-0.56} |
| 58.15 ^{+0.02} _{-0.03} | 62.19 ^{+0.05} _{-0.05} | 24.82 ^{+0.30} _{-0.33} | 41.00 ^{+0.58} _{-0.47} | 869.52 ^{+1.06} _{-1.37} |
| 58.13 ^{+0.03} _{-0.03} | 62.25 ^{+0.02} _{-0.02} | 24.86 ^{+0.28} _{-0.33} | 40.65 ^{+0.44} _{-0.63} | 870.31 ^{+1.22} _{-0.86} |
| 69.10 ^{+0.01} _{-0.02} | 71.94 ^{+0.02} _{-0.01} | 24.26 ^{+0.32} _{-0.31} | 39.91 ^{+0.83} _{-0.69} | 869.49 ^{+0.95} _{-0.70} |
| 69.10 ^{+0.02} _{-0.02} | 71.96 ^{+0.03} _{-0.02} | 24.32 ^{+0.30} _{-0.33} | 39.61 ^{+0.59} _{-0.75} | 869.20 ^{+0.72} _{-0.71} |

Table B.2: Measurement results for PP-collector with EPS-insulation and glass-glazing (including additional frame) (Date of measurement: 11.02.2016). The sub- / superscripts indicate the minimum / maximum deviation from the mean value over the measurement period.

| T_{in} in °C | T_{out} in °C | T_{amb} in °C | \dot{V} in l/h | I in W/m ² |
|---|---|---|---|--|
| 22.48 ^{+0.01} _{-0.01} | 30.04 ^{+0.04} _{-0.04} | 26.46 ^{+0.11} _{-0.12} | 42.71 ^{+0.23} _{-0.29} | 907.68 ^{+0.53} _{-0.61} |
| 22.47 ^{+0.01} _{-0.00} | 29.98 ^{+0.04} _{-0.05} | 26.55 ^{+0.10} _{-0.12} | 43.12 ^{+0.42} _{-0.35} | 907.77 ^{+0.74} _{-0.56} |
| 50.09 ^{+0.01} _{-0.01} | 55.42 ^{+0.01} _{-0.02} | 27.24 ^{+0.12} _{-0.11} | 42.32 ^{+0.48} _{-0.35} | 908.09 ^{+0.59} _{-0.66} |
| 50.09 ^{+0.00} _{-0.01} | 55.41 ^{+0.02} _{-0.02} | 27.29 ^{+0.10} _{-0.10} | 42.45 ^{+0.39} _{-0.38} | 907.91 ^{+0.51} _{-0.49} |
| 60.08 ^{+0.01} _{-0.01} | 64.53 ^{+0.01} _{-0.01} | 29.56 ^{+0.10} _{-0.09} | 42.42 ^{+0.36} _{-0.57} | 902.36 ^{+1.08} _{-0.78} |
| 60.08 ^{+0.01} _{-0.01} | 64.53 ^{+0.01} _{-0.01} | 29.56 ^{+0.17} _{-0.15} | 42.43 ^{+0.40} _{-0.46} | 902.30 ^{+0.78} _{-0.43} |
| 70.13 ^{+0.02} _{-0.01} | 73.34 ^{+0.01} _{-0.02} | 27.66 ^{+0.17} _{-0.14} | 43.48 ^{+0.57} _{-0.84} | 905.81 ^{+0.92} _{-0.83} |
| 70.14 ^{+0.02} _{-0.02} | 73.35 ^{+0.02} _{-0.02} | 27.74 ^{+0.14} _{-0.09} | 43.52 ^{+0.49} _{-0.66} | 905.79 ^{+0.53} _{-0.55} |

B Measurement Data of the Collector Efficiency Testing

Table B.3: Measurement results for PP-collector with EPS-insulation and PMMA-glazing (Date of measurement: 18.02.2016). The sub- / superscripts indicate the minimum / maximum deviation from the mean value over the measurement period.

| T_{in} in °C | T_{out} in °C | T_{amb} in °C | \dot{V} in l/h | I in W/m ² |
|---|---|---|---|--|
| 20.97 ^{+0.01} _{-0.03} | 28.31 ^{+0.10} _{-0.20} | 24.15 ^{+0.22} _{-0.20} | 42.02 ^{+0.20} _{-0.32} | 881.85 ^{+1.25} _{-0.95} |
| 20.99 ^{+0.00} _{-0.01} | 28.44 ^{+0.02} _{-0.01} | 24.18 ^{+0.36} _{-0.66} | 42.03 ^{+0.22} _{-0.21} | 882.04 ^{+0.62} _{-0.55} |
| 50.19 ^{+0.02} _{-0.03} | 55.24 ^{+0.01} _{-0.01} | 24.35 ^{+0.50} _{-0.41} | 42.21 ^{+0.28} _{-0.42} | 882.04 ^{+1.13} _{-3.28} |
| 50.18 ^{+0.01} _{-0.02} | 55.23 ^{+0.01} _{-0.01} | 24.82 ^{+0.47} _{-0.31} | 42.18 ^{+0.34} _{-0.40} | 881.10 ^{+1.30} _{-0.91} |
| 59.76 ^{+0.15} _{-0.04} | 63.59 ^{+0.12} _{-0.27} | 22.13 ^{+0.54} _{-0.28} | 42.24 ^{+1.24} _{-0.77} | 876.16 ^{+2.49} _{-2.26} |
| 59.72 ^{+0.03} _{-0.01} | 63.69 ^{+0.02} _{-0.02} | 22.16 ^{+0.40} _{-0.37} | 42.22 ^{+0.57} _{-0.75} | 876.75 ^{+2.26} _{-2.89} |
| 69.14 ^{+0.02} _{-0.01} | 72.05 ^{+0.01} _{-0.02} | 22.42 ^{+0.39} _{-0.59} | 42.84 ^{+0.69} _{-0.65} | 879.87 ^{+0.81} _{-0.65} |
| 69.13 ^{+0.02} _{-0.03} | 72.04 ^{+0.02} _{-0.01} | 22.46 ^{+0.39} _{-1.39} | 42.81 ^{+0.93} _{-0.63} | 879.56 ^{+0.78} _{-0.62} |

Table B.4: Measurement results for PP-collector with EPS-insulation and PMMA-glazing (including additional frame) (Date of measurement: 22.02.2016). The sub- / superscripts indicate the minimum / maximum deviation from the mean value over the measurement period.

| T_{in} in °C | T_{out} in °C | T_{amb} in °C | \dot{V} in l/h | I in W/m ² |
|---|---|---|---|--|
| 20.09 ^{+0.02} _{-0.02} | 27.30 ^{+0.05} _{-0.10} | 21.85 ^{+0.58} _{-0.36} | 41.95 ^{+0.34} _{-0.28} | 884.42 ^{+1.53} _{-2.10} |
| 20.08 ^{+0.01} _{-0.00} | 27.32 ^{+0.02} _{-0.02} | 22.23 ^{+0.35} _{-0.33} | 42.38 ^{+0.26} _{-0.27} | 885.67 ^{+0.98} _{-0.83} |
| 48.17 ^{+0.02} _{-0.04} | 53.10 ^{+0.07} _{-0.05} | 22.56 ^{+0.20} _{-0.19} | 43.52 ^{+0.60} _{-0.32} | 885.20 ^{+1.05} _{-0.80} |
| 48.19 ^{+0.00} _{-0.01} | 53.20 ^{+0.02} _{-0.04} | 22.51 ^{+0.21} _{-0.21} | 43.47 ^{+0.44} _{-0.44} | 884.81 ^{+0.84} _{-0.94} |
| 58.99 ^{+0.02} _{-0.01} | 63.25 ^{+0.02} _{-0.02} | 23.50 ^{+0.24} _{-0.31} | 42.48 ^{+0.74} _{-0.38} | 885.48 ^{+0.65} _{-0.55} |
| 58.98 ^{+0.01} _{-0.01} | 63.25 ^{+0.01} _{-0.01} | 23.54 ^{+0.16} _{-0.13} | 42.88 ^{+0.51} _{-0.52} | 885.34 ^{+0.82} _{-0.76} |
| 68.25 ^{+0.02} _{-0.01} | 71.55 ^{+0.01} _{-0.01} | 23.00 ^{+0.19} _{-0.21} | 43.08 ^{+0.79} _{-0.68} | 885.28 ^{+0.91} _{-0.85} |
| 68.24 ^{+0.02} _{-0.02} | 71.49 ^{+0.03} _{-0.03} | 23.29 ^{+0.48} _{-0.24} | 42.89 ^{+0.93} _{-0.74} | 885.96 ^{+0.85} _{-0.78} |

Table B.5: Measurement results for PP-collector with glasswool-insulation and glass-glazing (Date of measurement: 26.02.2016). The sub- / superscripts indicate the minimum / maximum deviation from the mean value over the measurement period.

| T_{in} in °C | T_{out} in °C | T_{amb} in °C | \dot{V} in l/h | I in W/m ² |
|---|---|---|---|--|
| 19.42 ^{+0.01} _{-0.01} | 26.64 ^{+0.03} _{-0.04} | 21.43 ^{+0.55} _{-0.33} | 41.86 ^{+0.22} _{-0.24} | 885.38 ^{+0.87} _{-0.92} |
| 19.43 ^{+0.00} _{-0.01} | 26.68 ^{+0.02} _{-0.01} | 21.60 ^{+0.46} _{-0.25} | 41.93 ^{+0.22} _{-0.22} | 884.30 ^{+0.76} _{-0.63} |
| 50.96 ^{+0.02} _{-0.01} | 54.92 ^{+0.01} _{-0.02} | 22.19 ^{+0.44} _{-0.50} | 42.86 ^{+0.39} _{-0.44} | 886.10 ^{+1.11} _{-0.96} |
| 50.96 ^{+0.02} _{-0.01} | 54.91 ^{+0.02} _{-0.02} | 22.16 ^{+0.29} _{-0.37} | 42.85 ^{+0.42} _{-0.39} | 886.22 ^{+0.99} _{-0.74} |
| 60.32 ^{+0.02} _{-0.03} | 63.27 ^{+0.02} _{-0.03} | 22.26 ^{+0.48} _{-0.38} | 42.72 ^{+0.94} _{-0.75} | 885.71 ^{+0.68} _{-0.92} |
| 60.28 ^{+0.02} _{-0.03} | 63.26 ^{+0.03} _{-0.01} | 22.45 ^{+0.32} _{-0.28} | 42.22 ^{+0.86} _{-0.70} | 885.30 ^{+0.76} _{-0.77} |
| 69.61 ^{+0.01} _{-0.02} | 71.42 ^{+0.02} _{-0.01} | 22.77 ^{+0.15} _{-0.13} | 42.48 ^{+0.65} _{-1.02} | 886.34 ^{+1.17} _{-0.74} |
| 69.61 ^{+0.01} _{-0.01} | 71.44 ^{+0.02} _{-0.01} | 22.76 ^{+0.17} _{-0.16} | 42.44 ^{+0.86} _{-0.76} | 886.32 ^{+0.72} _{-0.65} |

Table B.6: Measurement results for PP-collector with glasswool-insulation and PMMA-glazing (Date of measurement: 23.02.2016). The sub- / superscripts indicate the minimum / maximum deviation from the mean value over the measurement period.

| T_{in} in °C | T_{out} in °C | T_{amb} in °C | \dot{V} in l/h | I in W/m ² |
|---|---|---|---|--|
| 20.33 ^{+0.00} _{-0.01} | 27.55 ^{+0.02} _{-0.02} | 21.43 ^{+0.32} _{-0.21} | 42.64 ^{+0.29} _{-0.30} | 887.97 ^{+1.09} _{-0.73} |
| 20.32 ^{+0.01} _{-0.01} | 27.52 ^{+0.01} _{-0.03} | 21.47 ^{+0.22} _{-0.22} | 42.85 ^{+0.50} _{-0.37} | 888.05 ^{+0.89} _{-0.80} |
| 49.61 ^{+0.01} _{-0.01} | 53.98 ^{+0.02} _{-0.03} | 22.83 ^{+0.60} _{-0.20} | 42.00 ^{+0.53} _{-0.58} | 885.44 ^{+0.76} _{-0.90} |
| 49.60 ^{+0.01} _{-0.02} | 53.96 ^{+0.03} _{-0.02} | 22.74 ^{+0.41} _{-0.23} | 41.91 ^{+0.63} _{-0.94} | 884.23 ^{+1.13} _{-0.84} |
| 60.17 ^{+0.02} _{-0.03} | 63.15 ^{+0.04} _{-0.03} | 21.15 ^{+0.47} _{-0.59} | 41.67 ^{+0.76} _{-0.85} | 884.64 ^{+1.26} _{-0.83} |
| 60.18 ^{+0.01} _{-0.01} | 63.19 ^{+0.02} _{-0.04} | 21.08 ^{+0.44} _{-0.41} | 41.75 ^{+0.67} _{-0.79} | 884.95 ^{+0.92} _{-0.88} |
| 69.56 ^{+0.02} _{-0.03} | 71.57 ^{+0.03} _{-0.02} | 21.94 ^{+0.39} _{-0.33} | 42.11 ^{+0.57} _{-0.80} | 887.16 ^{+0.83} _{-0.86} |
| 69.54 ^{+0.01} _{-0.01} | 71.56 ^{+0.03} _{-0.04} | 22.02 ^{+0.51} _{-0.42} | 41.97 ^{+0.66} _{-0.75} | 886.82 ^{+0.53} _{-1.20} |

B Measurement Data of the Collector Efficiency Testing

Table B.7: Measurement results for ABS-collector with PUR-insulation and PMMA-glazing (Date of measurement: 07.07.2017). The sub- / superscripts indicate the minimum / maximum deviation from the mean value over the measurement period.

| T_{in} in °C | T_{out} in °C | T_{amb} in °C | \dot{V} in l/h | I in W/m ² |
|---|---|---|--|--|
| 23.32 ^{+0.01} _{-0.02} | 30.55 ^{+0.02} _{-0.01} | 28.60 ^{+0.16} _{-0.21} | 96.27 ^{+0.72} _{-0.85} | 876.52 ^{+0.78} _{-0.93} |
| 23.32 ^{+0.02} _{-0.01} | 30.56 ^{+0.03} _{-0.02} | 28.61 ^{+0.15} _{-0.19} | 96.27 ^{+0.65} _{-0.63} | 877.63 ^{+1.18} _{-1.56} |
| 35.86 ^{+0.02} _{-0.01} | 41.79 ^{+0.01} _{-0.01} | 25.44 ^{+0.16} _{-0.18} | 100.32 ^{+0.63} _{-0.58} | 878.64 ^{+0.74} _{-0.58} |
| 35.86 ^{+0.01} _{-0.01} | 41.80 ^{+0.01} _{-0.02} | 25.45 ^{+0.23} _{-0.12} | 100.31 ^{+0.48} _{-0.50} | 879.46 ^{+0.84} _{-0.88} |
| 50.47 ^{+0.03} _{-0.02} | 55.54 ^{+0.03} _{-0.02} | 26.07 ^{+0.21} _{-0.17} | 98.25 ^{+0.62} _{-0.57} | 881.26 ^{+1.01} _{-0.77} |
| 50.48 ^{+0.03} _{-0.02} | 55.55 ^{+0.01} _{-0.02} | 26.23 ^{+0.11} _{-0.16} | 98.27 ^{+0.84} _{-0.62} | 879.81 ^{+1.42} _{-0.99} |
| 65.11 ^{+0.03} _{-0.03} | 68.97 ^{+0.01} _{-0.01} | 27.29 ^{+0.14} _{-0.14} | 102.34 ^{+0.62} _{-0.91} | 881.96 ^{+1.04} _{-0.99} |
| 65.11 ^{+0.03} _{-0.04} | 68.98 ^{+0.02} _{-0.01} | 27.38 ^{+0.18} _{-0.13} | 102.32 ^{+0.48} _{-0.65} | 882.10 ^{+0.89} _{-0.78} |

C Spectroscopy Measurement

Transmittance properties of glazing materials strongly depend on the chemical composition of each specimen and the wavelength considered. In order to precisely account for the transmittance property of the different glazings used within this project, a spectroscopy measurement was performed. The schematic layout is shown in figure C.1, a photo of the test arrangement can be seen in figure C.2.

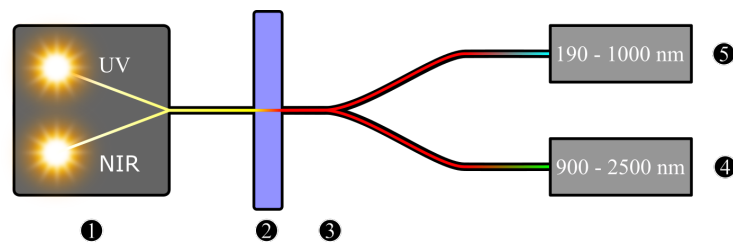


Figure C.1: Schematic layout of the spectroscopy measurement. ① = light source, ② = specimen, ③ = switch, ④ / ⑤ = light sensor.

A light source ① emits light from two different bulbs. A deuterium lamp emits light within the ultraviolet (UV) spectrum of the light ($\lambda = 180 \text{ nm} - 380 \text{ nm}$), whereas a halogen lamp provides radiation within the visible and near-infrared (NIR) spectrum of the light ($\lambda = 300 \text{ nm} - 2,500 \text{ nm}$). The light is being transferred to the specimen ② with a fibre optic cable. Here, the light gets either reflected, scattered or transmitted through the specimen. The transmitted part of the light is split up by means of a switch ③ which is connected to two different spectrometers ④, ⑤. The first one ④ is able to detect radiation within 190 nm – 1,000 nm, the second one ⑤ measures radiation between 900 nm and 2,500 nm. The transmission was determined at three different locations and subsequently averaged. The results are shown in figure C.3. The glass-cover shows a more or less constant transmittance in the UV, visible and NIR regime, ranging between 0.85 and 0.90. However, the PMMA-cover has a significantly lower transmittance in the NIR range. In addition to the wavelength-dependent transmittance, the average transmittance within the visible range (380 nm – 780 nm) was determined according to DIN EN 410:2011 (p. 9). The visual transmittance τ_{vis} of glass is 0.90 and 0.92 in case of PMMA, respectively.

C Spectroscopy Measurement

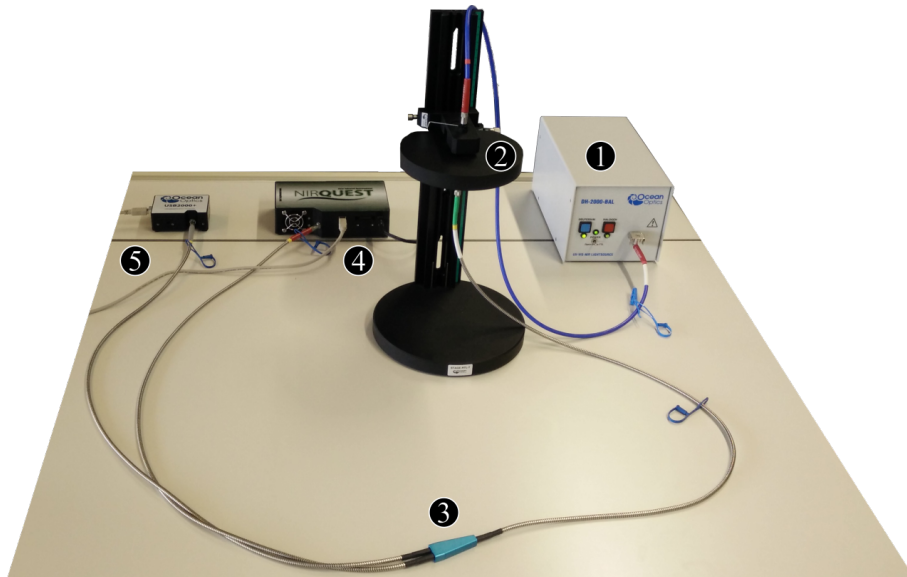


Figure C.2: Setup of the spectroscopy measurement. ① = light source, ② = specimen, ③ = switch, ④, ⑤ = light sensor.

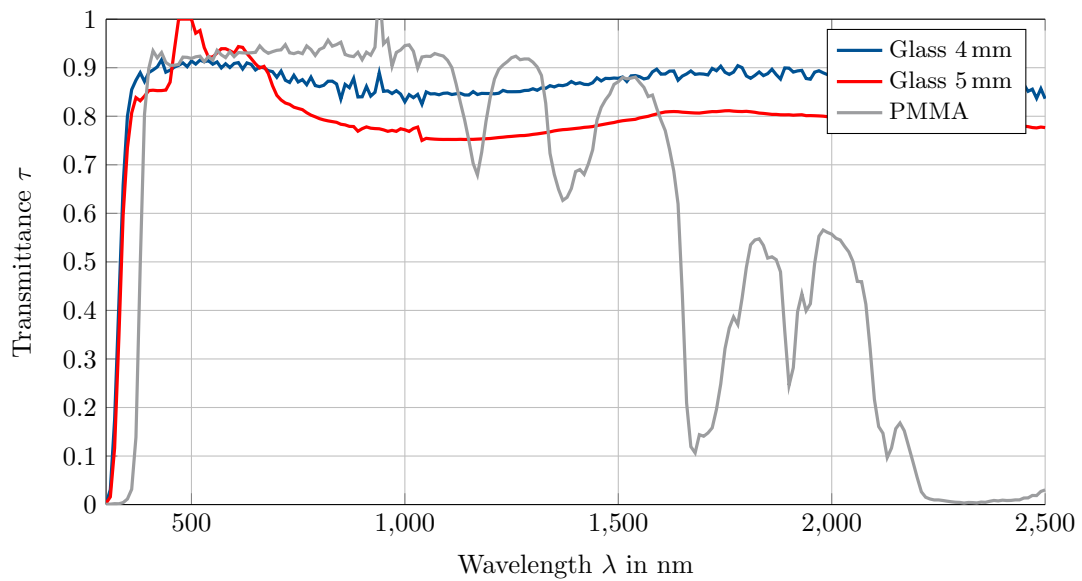


Figure C.3: Wavelength-dependent transmittance τ of glass and PMMA.

D Numerical Data Obtained with the Collector Model

Table D.1: Measured and simulated results for ABS-collector with PUR-insulation and PMMA-glazing.

| T_{in} in °C | T_{out}^{meas} in °C | T_{out}^{sim} in °C | T_{amb} in °C | \dot{V} in l/h | I in W/m ² |
|----------------|------------------------|-----------------------|-----------------|------------------|-------------------------|
| 23.32 | 30.55 | 31.16 | 28.60 | 96.27 | 876.52 |
| 23.32 | 30.56 | 31.16 | 28.61 | 96.27 | 877.63 |
| 35.86 | 41.79 | 42.31 | 25.44 | 100.32 | 878.64 |
| 35.86 | 41.80 | 42.32 | 25.45 | 100.31 | 879.46 |
| 50.47 | 55.54 | 55.97 | 26.07 | 98.25 | 881.26 |
| 50.48 | 55.55 | 55.97 | 26.23 | 98.27 | 879.81 |
| 65.11 | 68.97 | 69.35 | 27.29 | 102.34 | 881.96 |
| 65.11 | 68.98 | 69.36 | 27.38 | 102.32 | 882.10 |

Table D.2: Measured and simulated results for PP-collector with glasswool-insulation and glass-glazing.

| T_{in} in °C | T_{out}^{meas} in °C | T_{out}^{sim} in °C | T_{amb} in °C | \dot{V} in l/h | I in W/m ² |
|----------------|------------------------|-----------------------|-----------------|------------------|-------------------------|
| 19.42 | 26.64 | 27.05 | 21.43 | 41.86 | 885.38 |
| 19.43 | 26.68 | 27.06 | 21.60 | 41.93 | 884.30 |
| 50.96 | 54.92 | 55.23 | 22.19 | 42.86 | 886.10 |
| 50.96 | 54.91 | 55.23 | 22.16 | 42.85 | 886.22 |
| 60.32 | 63.27 | 63.57 | 22.26 | 42.74 | 885.71 |
| 60.28 | 63.26 | 63.59 | 22.45 | 42.22 | 885.30 |
| 69.61 | 71.42 | 71.87 | 22.77 | 42.48 | 886.34 |
| 69.61 | 71.44 | 71.88 | 22.76 | 42.44 | 886.32 |

D Numerical Data Obtained with the Collector Model

Table D.3: Measured and simulated results for PP-collector with EPS-insulation and glass-glazing.

| T_{in} in °C | T_{out}^{meas} in °C | T_{out}^{sim} in °C | T_{amb} in °C | \dot{V} in l/h | I in W/m ² |
|----------------|------------------------|-----------------------|-----------------|------------------|-------------------------|
| 19.16 | 27.13 | 27.29 | 23.23 | 40.13 | 867.63 |
| 19.17 | 27.17 | 27.34 | 23.32 | 39.95 | 867.48 |
| 40.05 | 45.95 | 45.87 | 21.26 | 40.29 | 869.05 |
| 40.06 | 45.99 | 46.00 | 21.97 | 39.90 | 868.76 |
| 58.15 | 62.19 | 62.35 | 24.82 | 41.00 | 869.52 |
| 58.13 | 62.25 | 62.38 | 24.86 | 40.65 | 870.31 |
| 69.10 | 71.94 | 72.12 | 24.26 | 39.91 | 869.49 |
| 69.10 | 71.96 | 72.14 | 24.32 | 39.61 | 869.20 |

Table D.4: Measured and simulated results for PP-collector with EPS-insulation and glass-glazing (including additional frame).

| T_{in} in °C | T_{out}^{meas} in °C | T_{out}^{sim} in °C | T_{amb} in °C | \dot{V} in l/h | I in W/m ² |
|----------------|------------------------|-----------------------|-----------------|------------------|-------------------------|
| 22.48 | 30.04 | 30.53 | 26.46 | 42.71 | 907.68 |
| 22.47 | 29.98 | 30.47 | 26.55 | 43.12 | 907.77 |
| 50.09 | 55.42 | 55.64 | 27.24 | 42.32 | 908.09 |
| 50.09 | 55.41 | 55.63 | 27.29 | 42.45 | 907.91 |
| 60.08 | 64.53 | 64.77 | 29.56 | 42.42 | 902.36 |
| 60.08 | 64.53 | 64.77 | 29.56 | 42.43 | 902.30 |
| 70.13 | 73.34 | 73.55 | 27.66 | 43.48 | 905.81 |
| 70.14 | 73.35 | 73.57 | 27.74 | 43.52 | 905.79 |

E Sky Temperature Modelling

The dynamic behaviour of the developed collector model (cf. chapter 4) during idle mode depends on the sky temperature T_{Sky} . An overview of different sky temperature models is given by Eicker (2012, p. 54) (cf. table E.1).

Table E.1: Overview of different formulations for the sky temperature T_{Sky} according to Eicker (2012, p. 54). T_{Sky} = Sky temperature, T_{Amb} = Ambient temperature, T_{DP} = dew point temperature.

| Source | Sky temperature |
|---------------------------|--|
| Swinbank (1963) | $T_{Sky} = 0.0552 \cdot T_{Amb}^{1.5}$ |
| Fuentes (1987) | $T_{Sky} = 0.037536 \cdot T_{Amb}^{1.5} + 0.32 \cdot T_{Amb}$ |
| Martin and Berdahl (1984) | $T_{Sky} = \left(0.711 + 0.56 \frac{T_{DP}}{100} + 0.73 \left(\frac{T_{DP}}{100}\right)^2\right)^{0.25} \cdot T_{Amb}$ |

The influence of different sky temperature models to the resulting collector outlet temperature are shown in figures E.1 and E.2. Comparing the measured collector outlet temperature (red curve) with simulated values based on different sky temperature models (dotted curves) indicates the highest deviation between 6:00 and 7:00 AM. During normal operation (e.g. at 1:00 PM) the influence of different sky temperature models to the resulting collector outlet temperature is negligible.

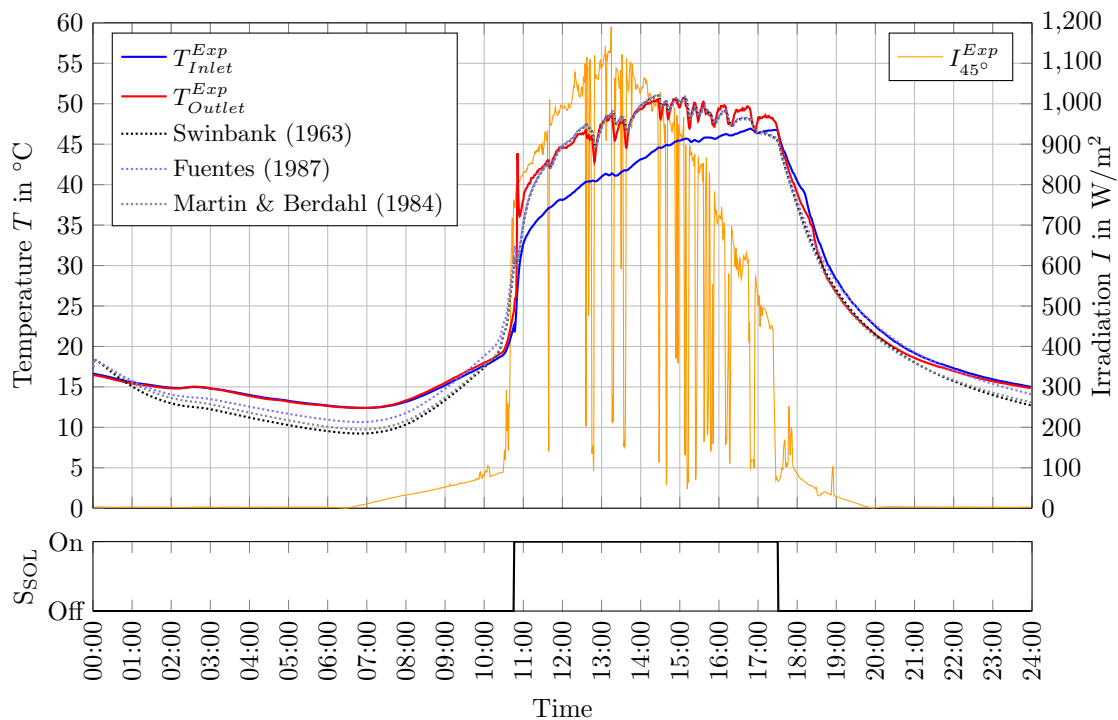


Figure E.1: Influence of different sky temperature models to the simulated collector outlet temperature in case of cloudy sky conditions (Date of measurement 30.08.2016).

E Sky Temperature Modelling

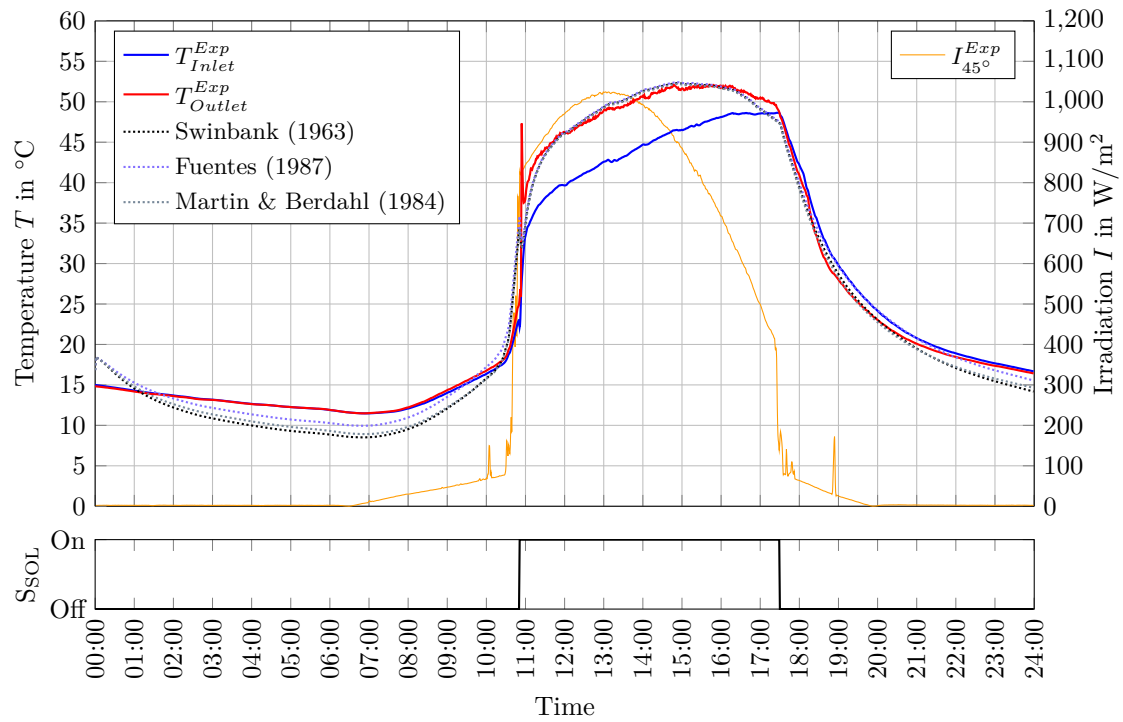


Figure E.2: Influence of different sky temperature models to the simulated collector outlet temperature in case of clear sky conditions (Date of measurement 31.08.2016).

F Further Results of the Parametric Study

F.1 Athens (Greece)

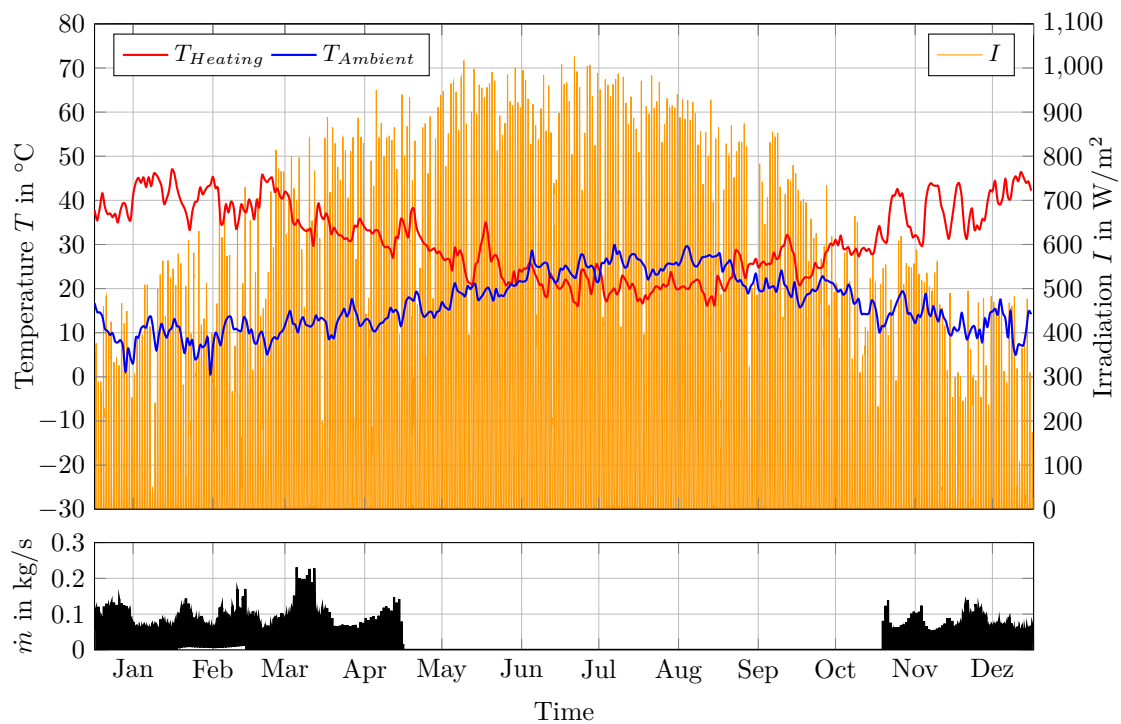


Figure F.1: Weather conditions and heating parameters (flow temperature and mass flow rate) at the reference location Athens (Greece). Minimum / maximum ambient temperature: 0.5°C / 38.3°C . Maximum irradiation: $1,026 \text{ W}/\text{m}^2$. Maximum heating flow temperature: 48.6°C . Weather data source: Meteonorm 7.3, load profile data source: DIN EN 12977-2:2016 (pp. 30-39).

F Further Results of the Parametric Study

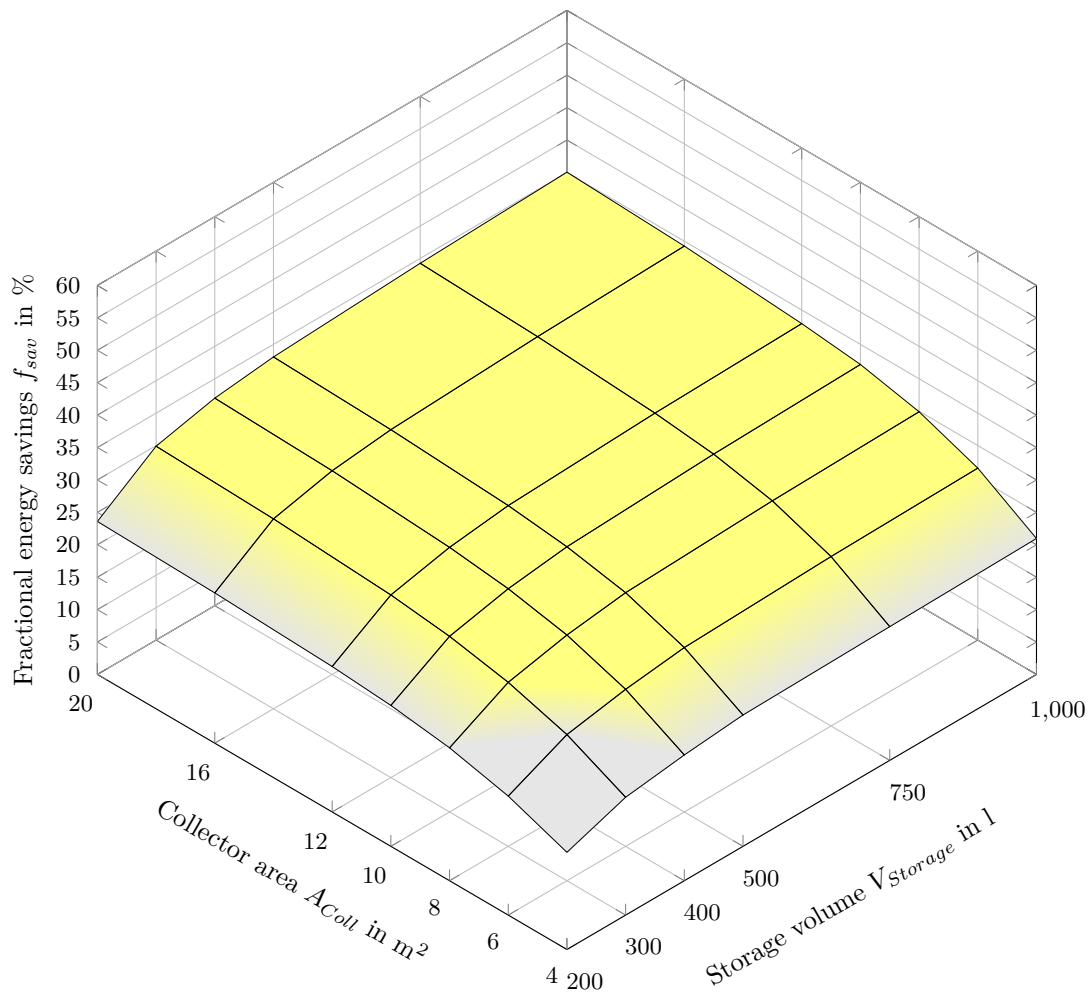


Figure F.2: Correlation between collector area, heat storage volume and fractional energy savings f_{sav} in case of a solar DHW system located in Athens (Greece). The yellow-highlighted regions indicate systems with polymeric FPCs which yield higher fractional energy savings than the reference system with metal-based collectors (cf. section 6.1.2).

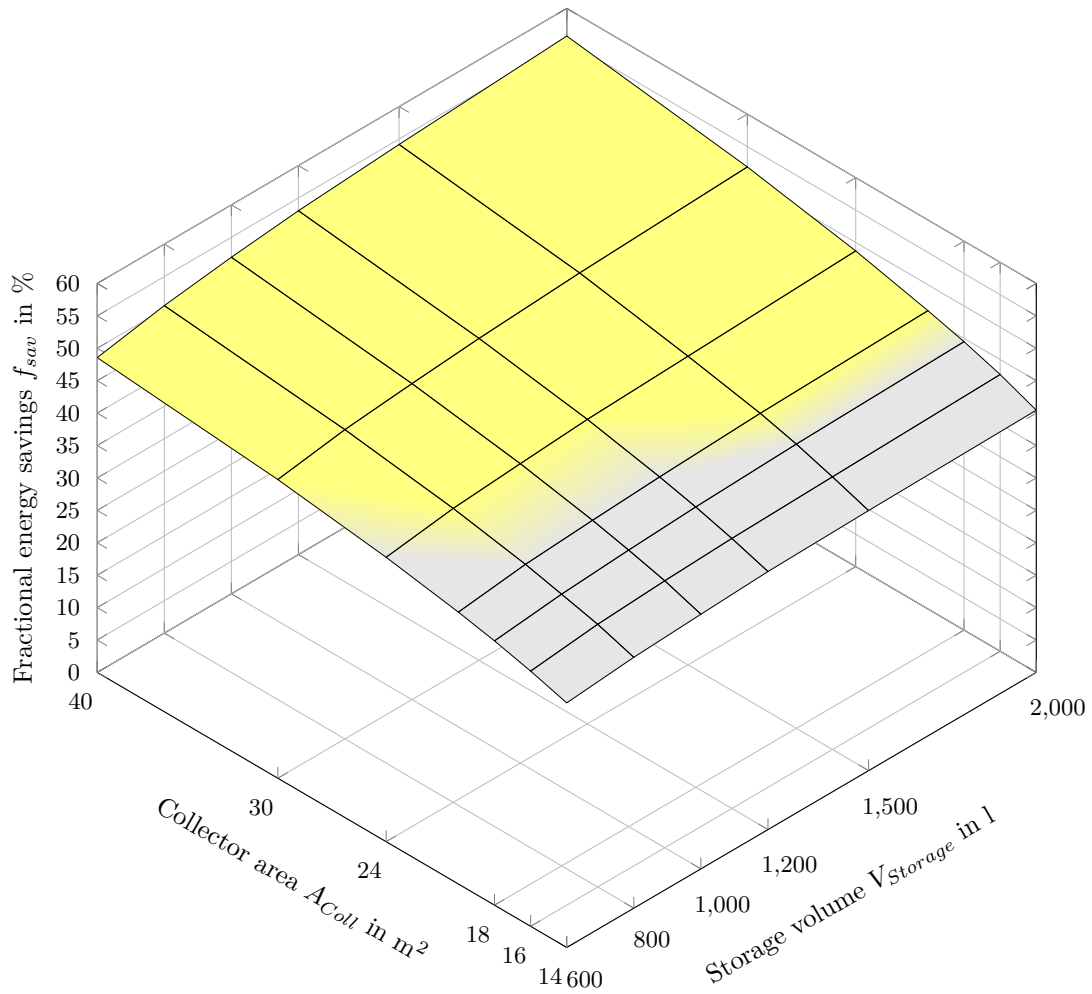


Figure F.3: Correlation between collector area, heat storage volume and fractional energy savings f_{sav} in case of a solar combi system located in Athens (Greece). The yellow-highlighted regions indicate systems with polymeric FPCs which yield higher fractional energy savings than the reference system with metal-based collectors (cf. section 6.1.3).

F Further Results of the Parametric Study

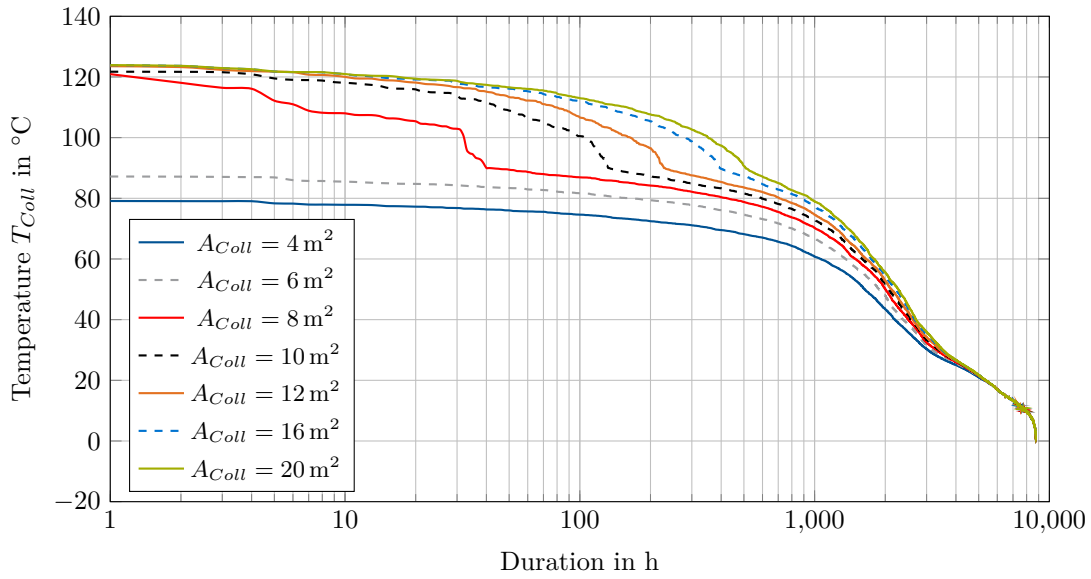


Figure F.4: Collector temperatures T_{Coll} in case of solar DHW systems located in Athens (Greece). Each system is equipped with a 200l heat storage and a solar thermal collector array varying between 4 m^2 and 20 m^2 . Maximum collector temperature: 124.7 $^{\circ}\text{C}$.

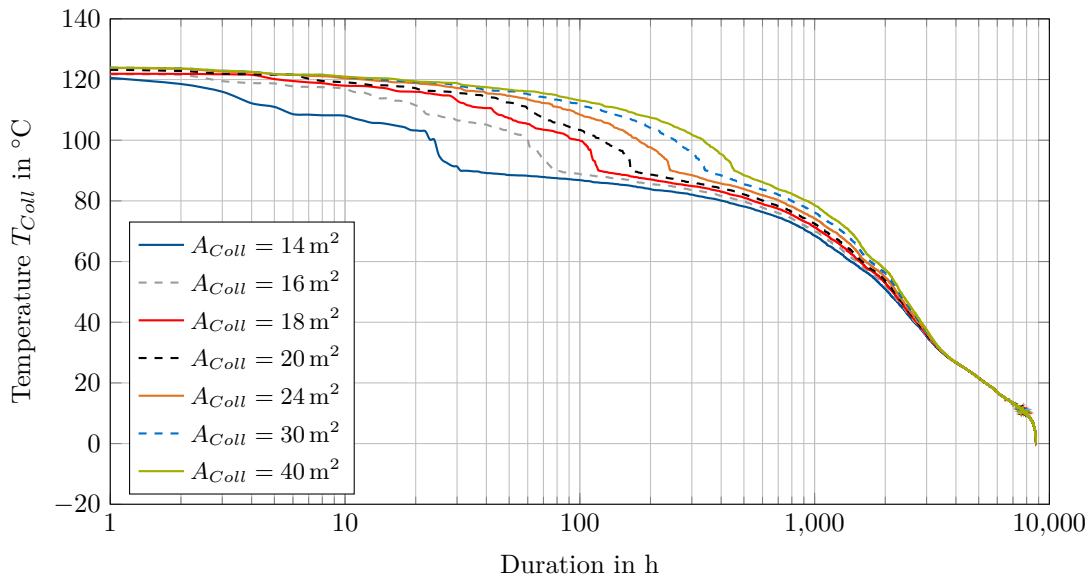


Figure F.5: Collector temperatures T_{Coll} in case of solar combi systems located in Athens (Greece). Each system is equipped with a 600l heat storage and a solar thermal collector array varying between 14 m^2 and 40 m^2 . Maximum collector temperature: 124.7 $^{\circ}\text{C}$.

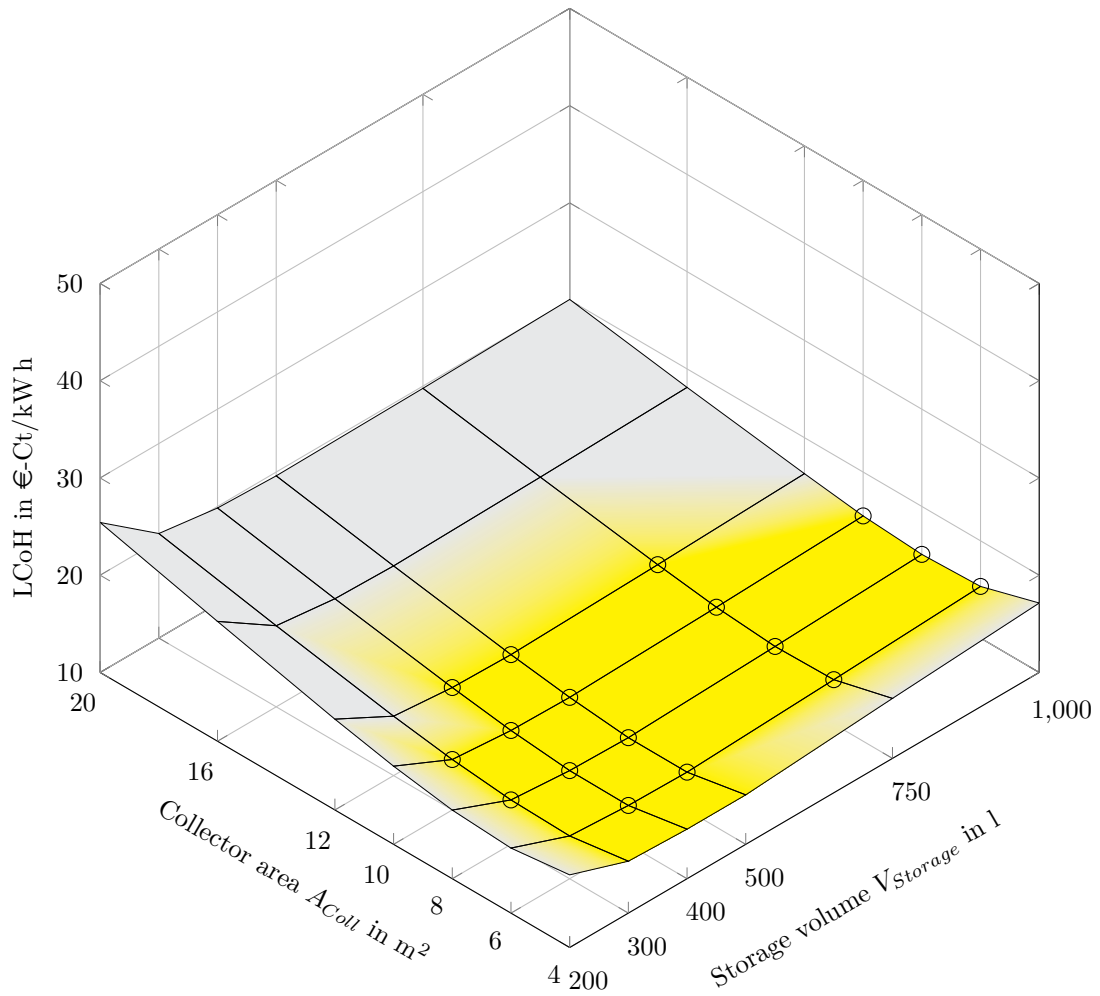


Figure F.6: LCoH in case of a solar DHW system with polymeric solar thermal FPCs located in Athens (Greece). The highlighted yellow area indicates system configurations which yield lower LCoH than the solar thermal reference system with metal-based FPCs (cf. section 6.1.2). In addition, the circular markers indicate system configurations with higher fractional energy savings than the solar thermal reference system with metal-based FPCs.

F Further Results of the Parametric Study

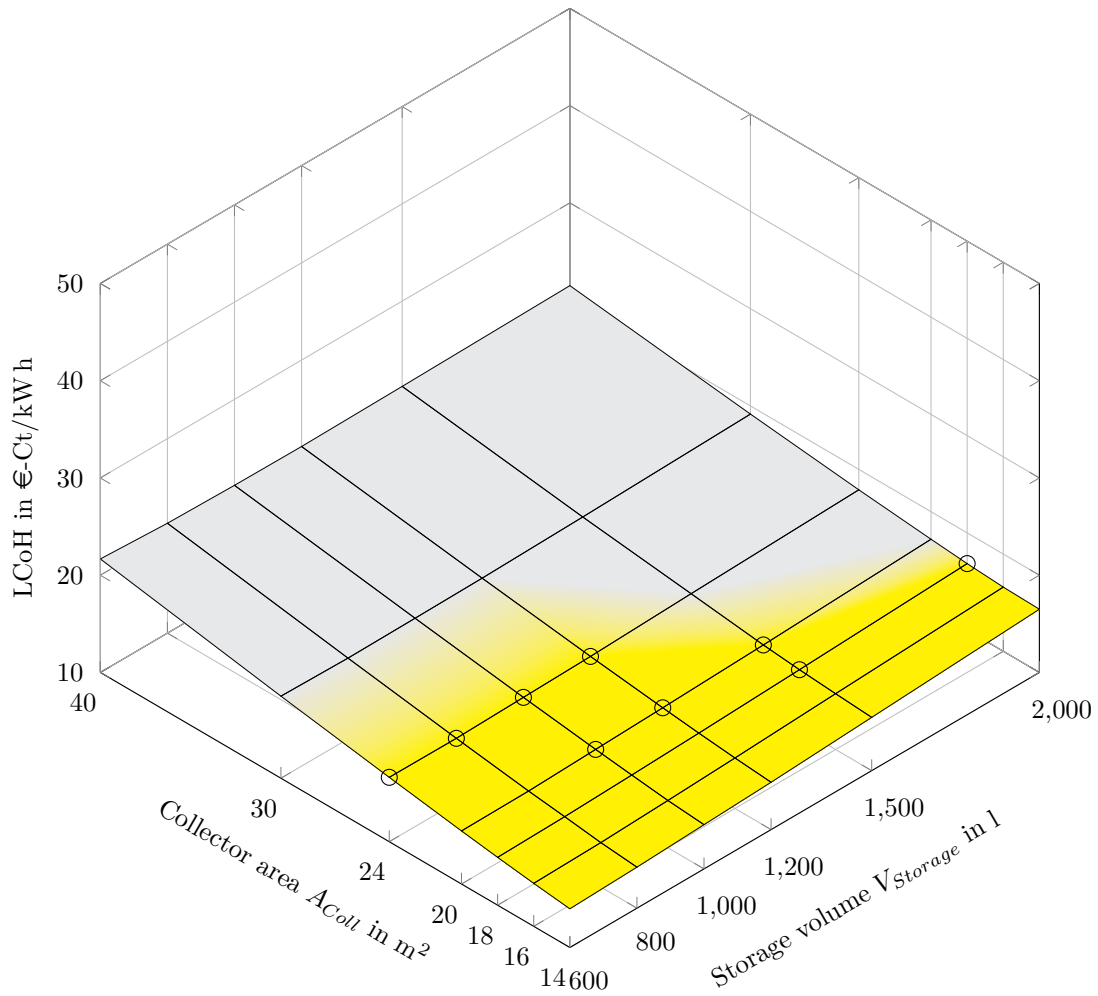


Figure F.7: LCoH in case of a solar combi system with polymeric solar thermal FPCs located in Athens (Greece). The highlighted yellow area indicates system configurations which yield lower LCoH than the solar thermal reference system with metal-based FPCs (cf. section 6.1.3). In addition, the circular markers indicate system configurations with higher fractional energy savings than the solar thermal reference system with metal-based FPCs.

F.2 Davos (Switzerland)

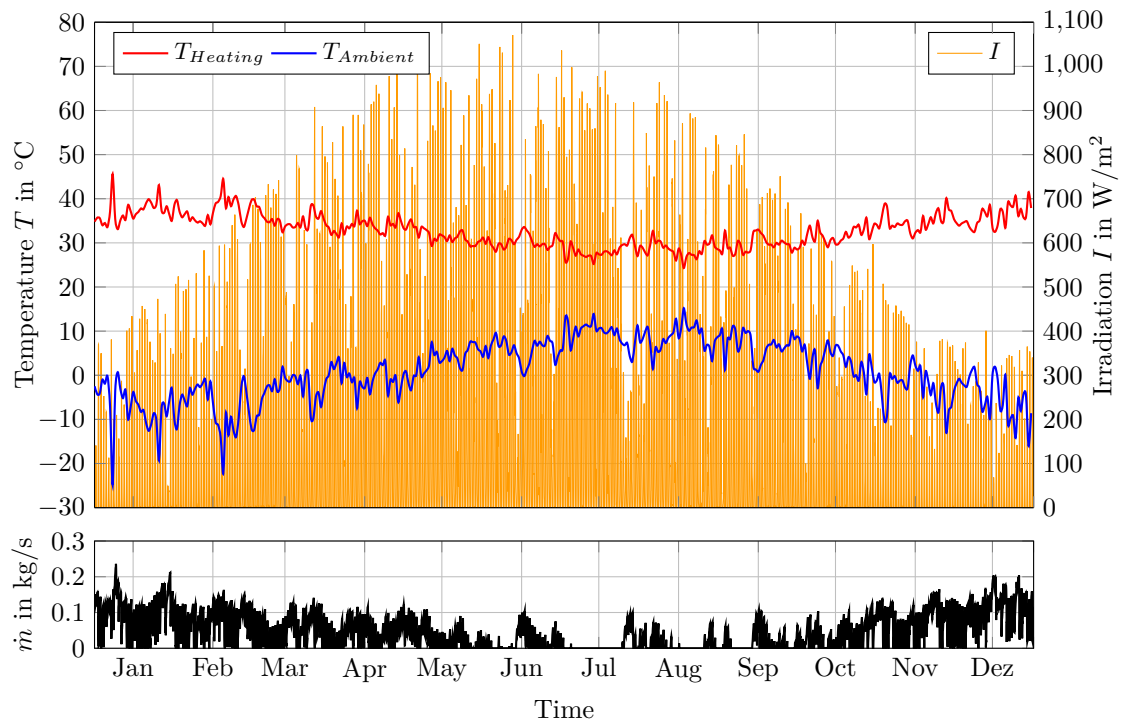


Figure F.8: Weather conditions and heating parameters (flow temperature and mass flow rate) at the reference location Davos (Switzerland). Minimum / maximum ambient temperature: $-26.6\text{ }^{\circ}\text{C}$ / $27.8\text{ }^{\circ}\text{C}$. Maximum irradiation: $1,071\text{ W/m}^2$. Maximum heating flow temperature: $46.5\text{ }^{\circ}\text{C}$. Weather data source: Meteonorm 7.3, load profile data source: DIN EN 12977-2:2016 (pp. 30-39).

F Further Results of the Parametric Study

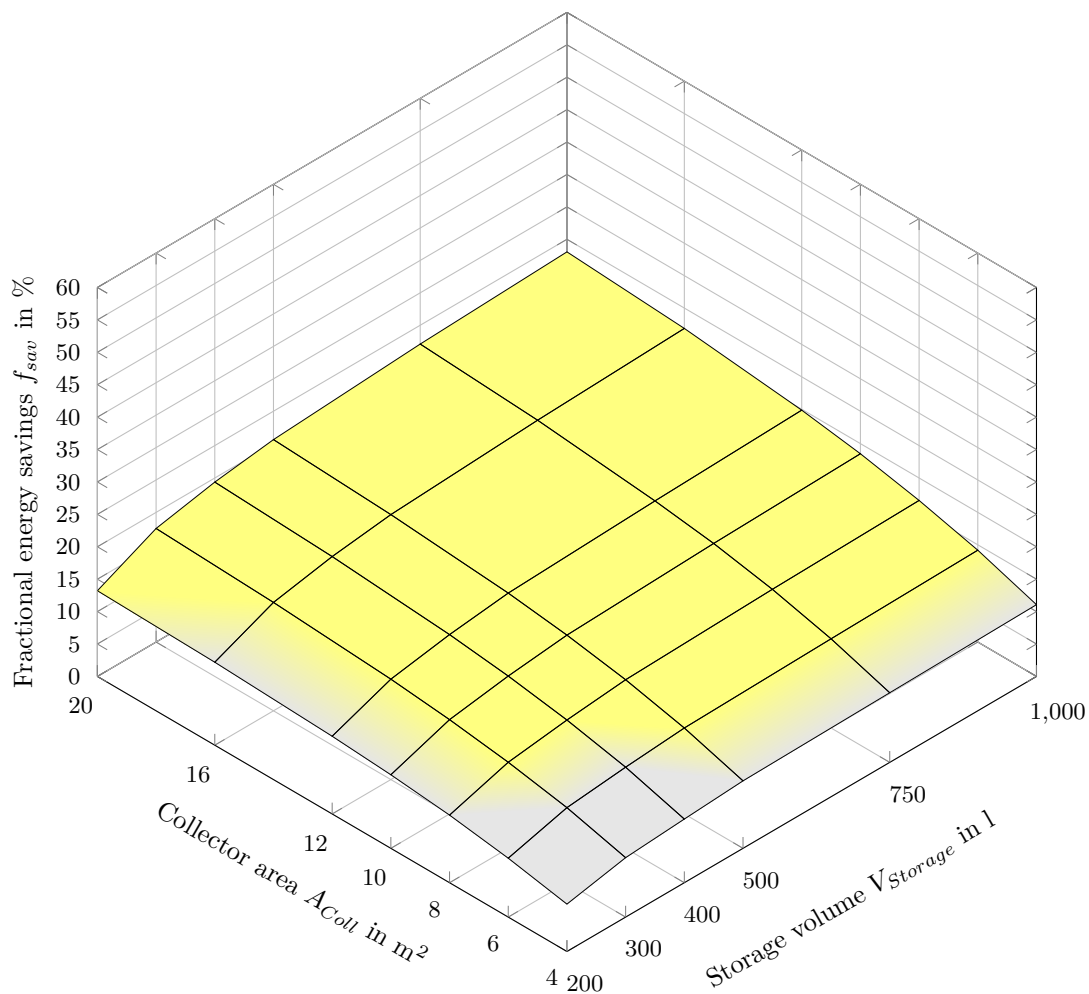


Figure F.9: Correlation between collector area, heat storage volume and fractional energy savings f_{sav} in case of a solar DHW system located in Davos (Switzerland). The yellow-highlighted regions indicate systems with polymeric FPCs which yield higher fractional energy savings than the reference system with metal-based collectors (cf. section 6.1.2).

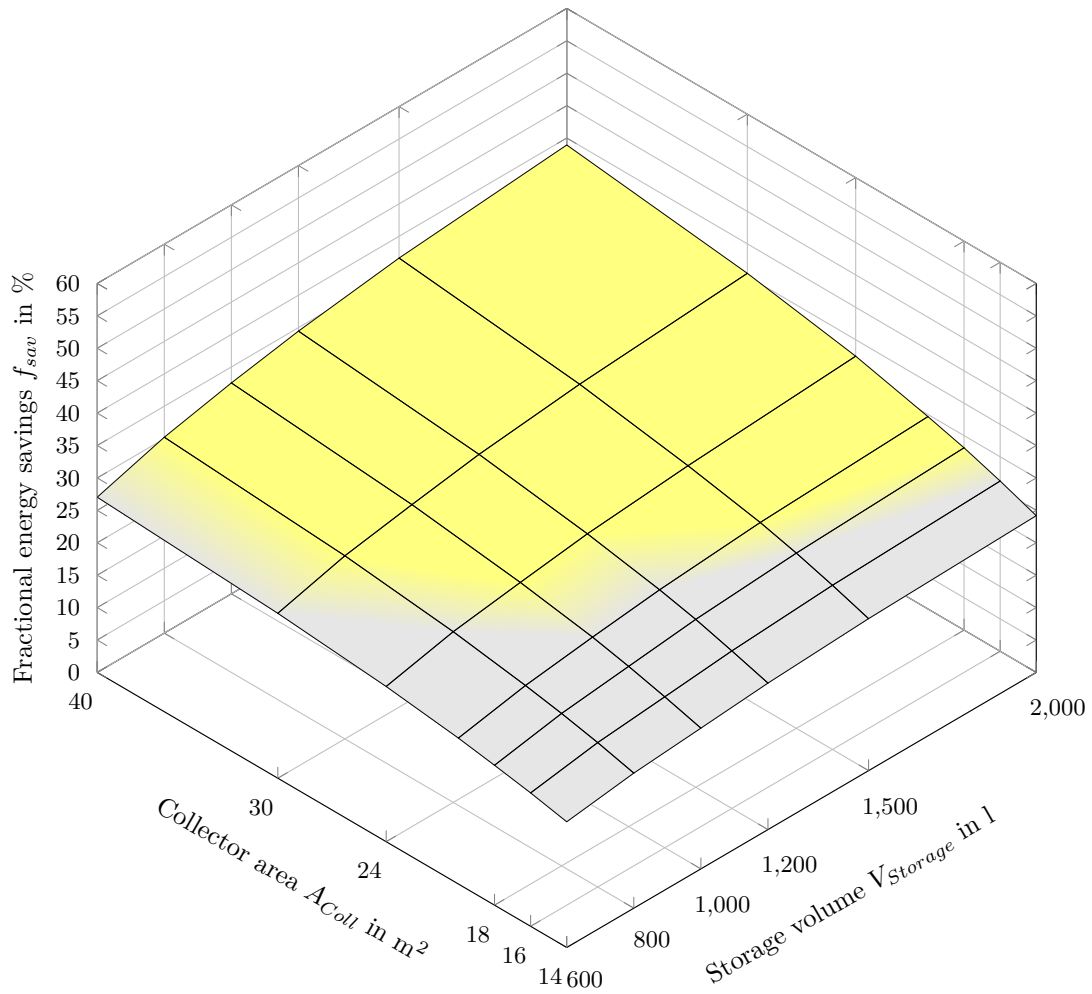


Figure F.10: Correlation between collector area, heat storage volume and fractional energy savings f_{sav} in case of a solar combi system located in Davos (Switzerland). The yellow-highlighted regions indicate systems with polymeric FPCs which yield higher fractional energy savings than the reference system with metal-based collectors (cf. section 6.1.3).

F Further Results of the Parametric Study

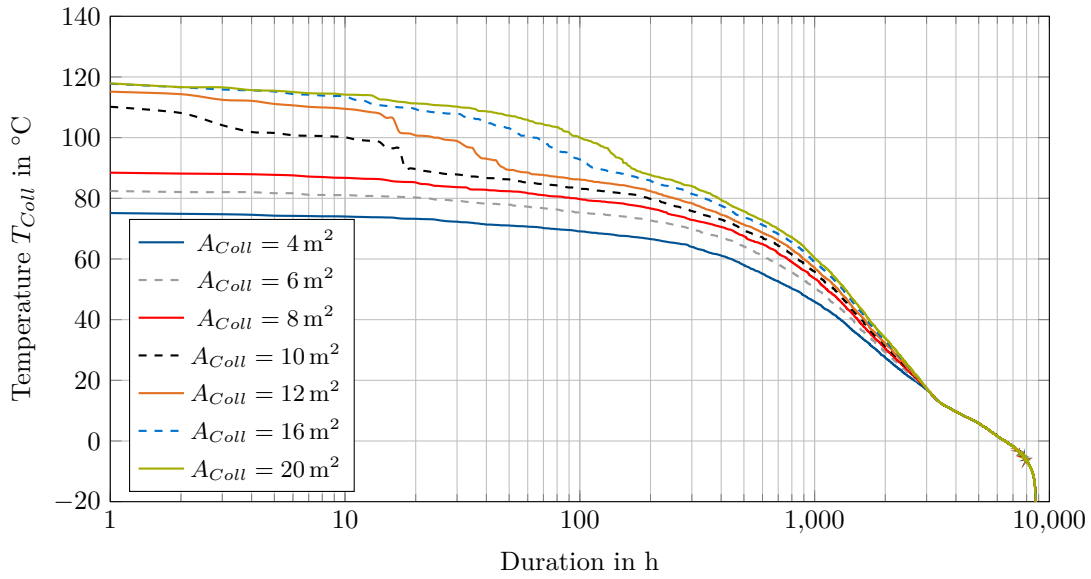


Figure F.11: Collector temperatures T_{Coll} in case of solar DHW systems located in Davos (Switzerland). Each system is equipped with a 200l heat storage and a solar thermal collector array varying between 4 m^2 and 20 m^2 . Maximum collector temperature: $117.9 \text{ }^{\circ}\text{C}$.

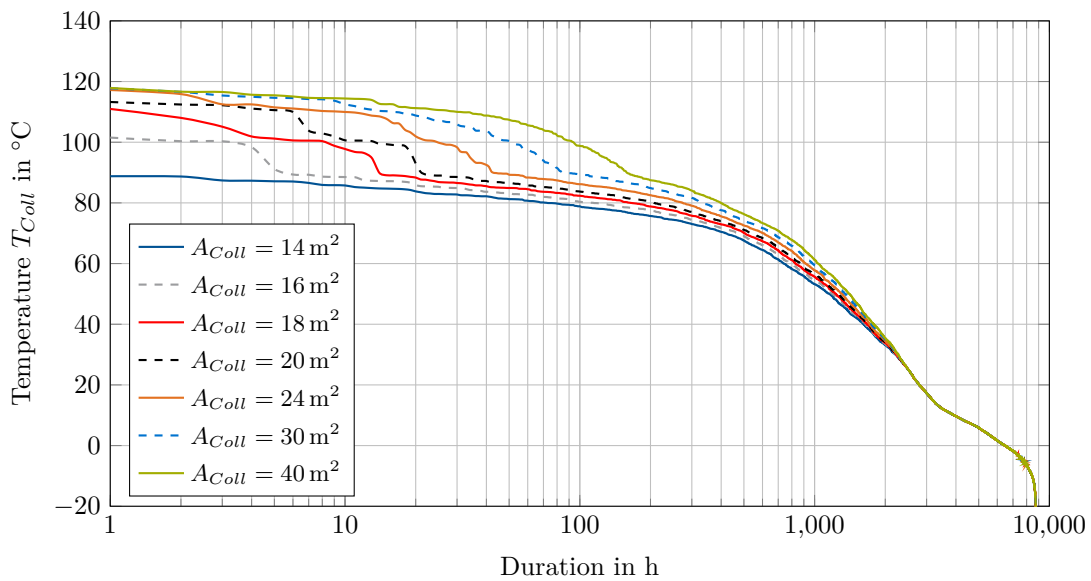


Figure F.12: Collector temperatures T_{Coll} in case of solar combi systems located in Davos (Switzerland). Each system is equipped with a 600l heat storage and a solar thermal collector array varying between 14 m^2 and 40 m^2 . Maximum collector temperature: $117.9 \text{ }^{\circ}\text{C}$.

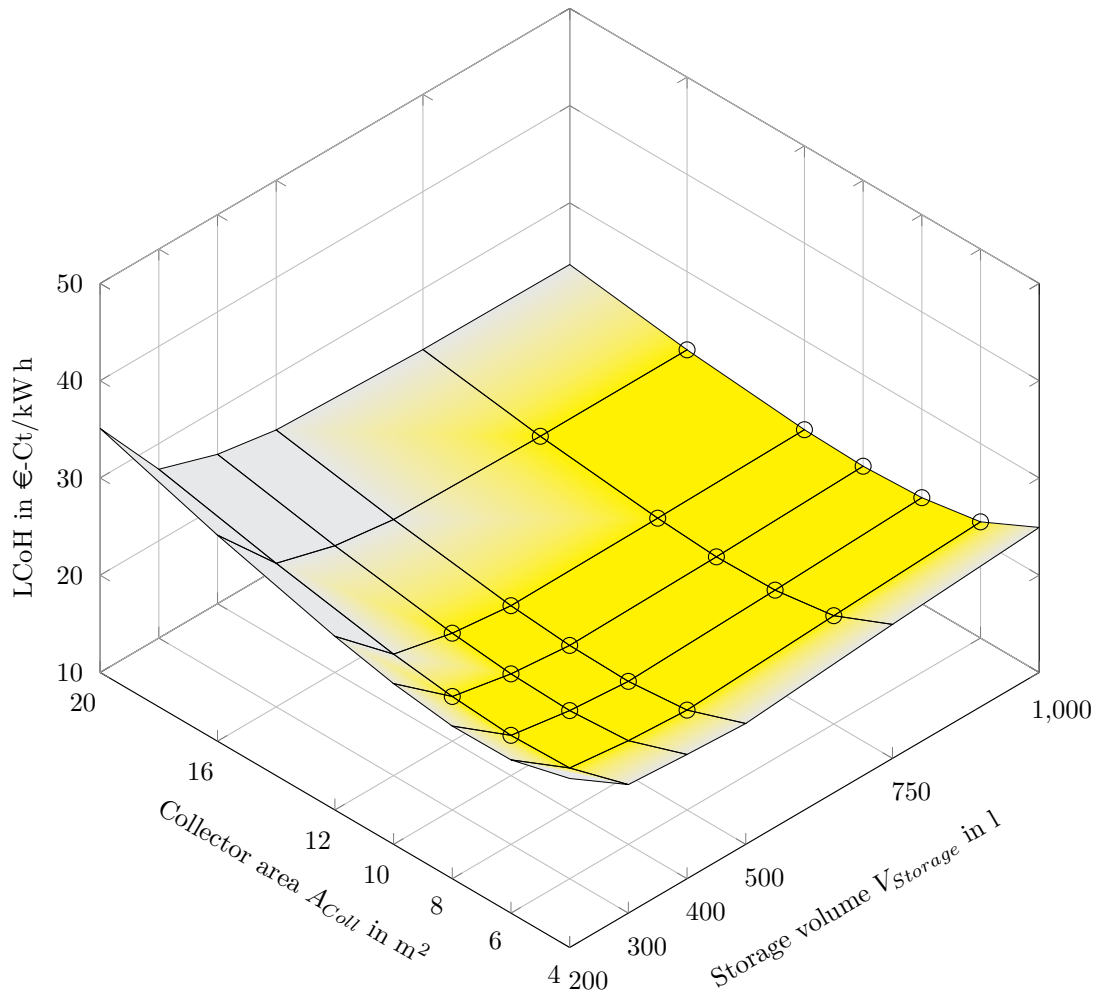


Figure F.13: LCoH in case of a solar DHW system with polymeric solar thermal FPCs located in Davos (Switzerland). The result indicate that no systems with polymeric FPC yields higher fractional energy savings than the reference system with metal-based FPCs (cf. section 6.1.2). In addition, the circular markers indicate system configurations with higher fractional energy savings than the solar thermal reference system with metal-based FPCs.

F Further Results of the Parametric Study

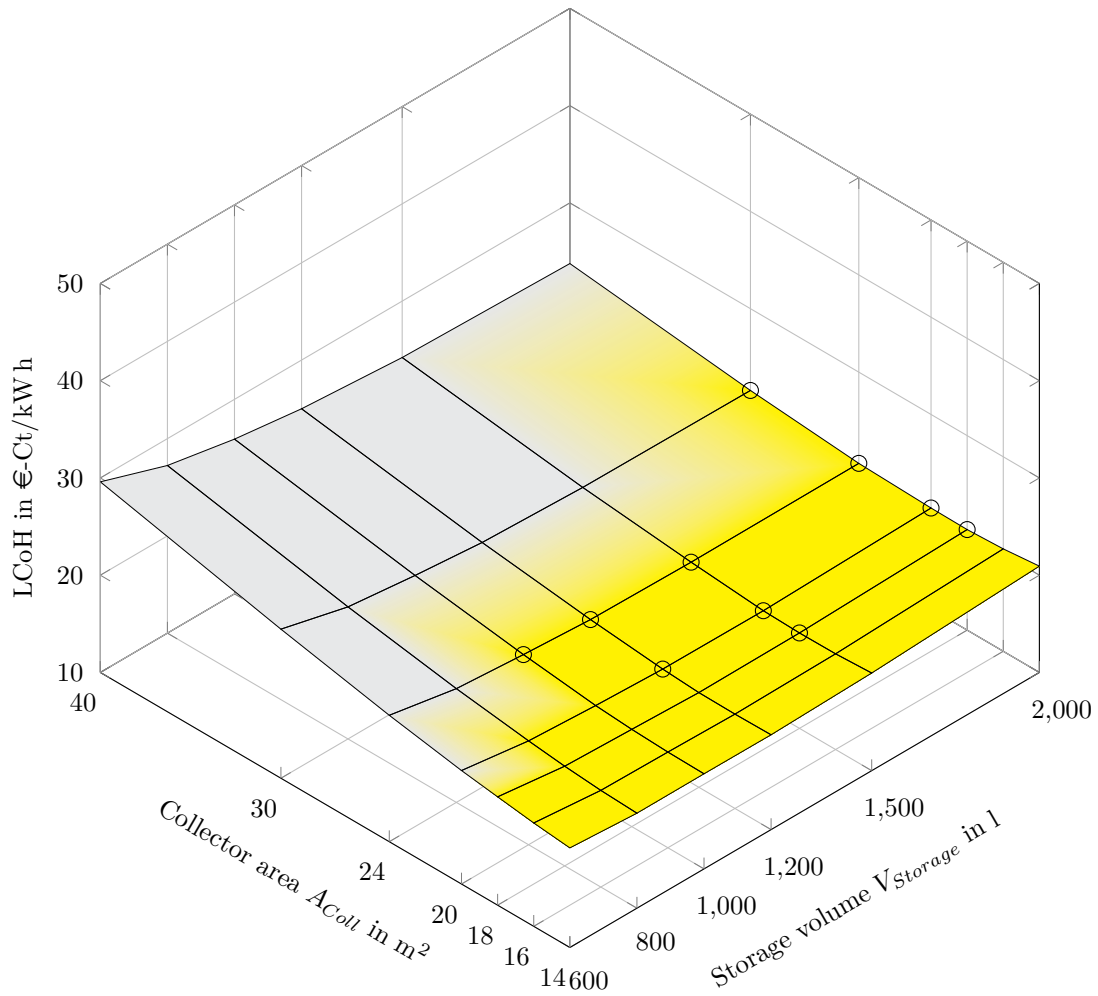


Figure F.14: LCoH in case of a solar combi system with polymeric solar thermal FPCs located in Davos (Switzerland). The highlighted yellow area indicates system configurations which yield lower LCoH than the solar thermal reference system with metal-based FPCs (cf. section 6.1.3). In addition, the circular markers indicate system configurations with higher fractional energy savings than the solar thermal reference system with metal-based FPCs.

F.3 Stockholm (Sweden)

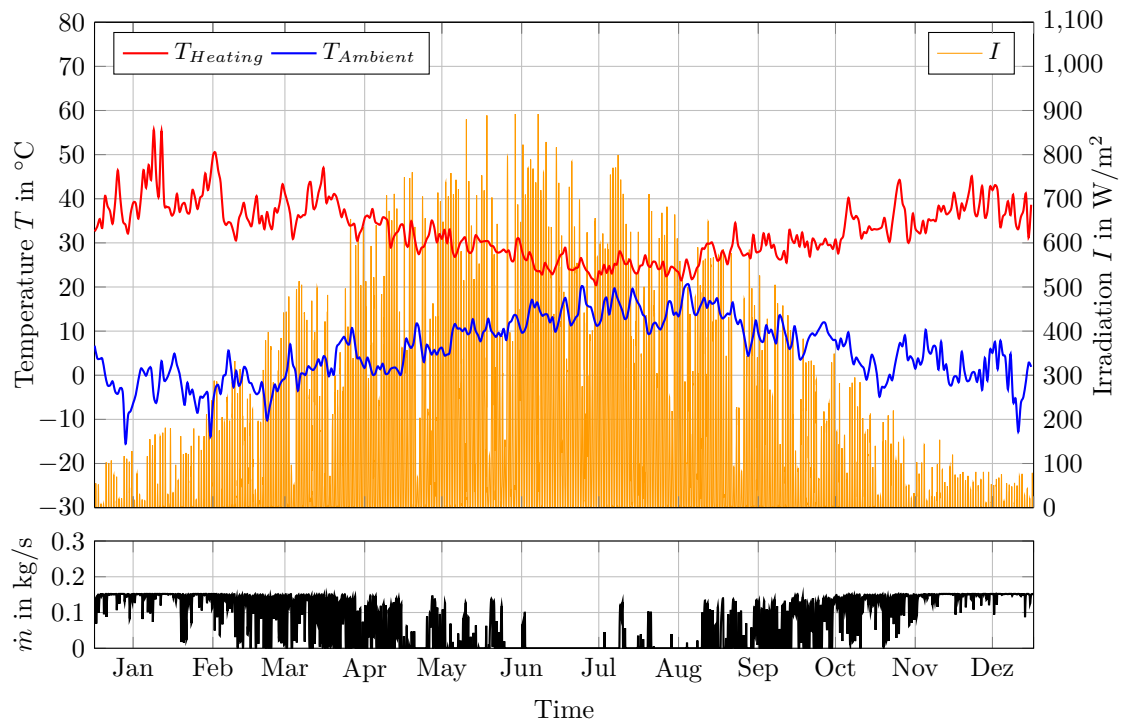


Figure F.15: Weather conditions and heating parameters (flow temperature and mass flow rate) at the reference location Stockholm (Sweden). Minimum / maximum ambient temperature: -15.9°C / 30.2°C . Maximum irradiation: 892 W/m^2 . Maximum heating flow temperature: 60.7°C . Weather data source: Meteonorm 7.3, load profile data source: DIN EN 12977-2:2016 (pp. 30-39).

F Further Results of the Parametric Study

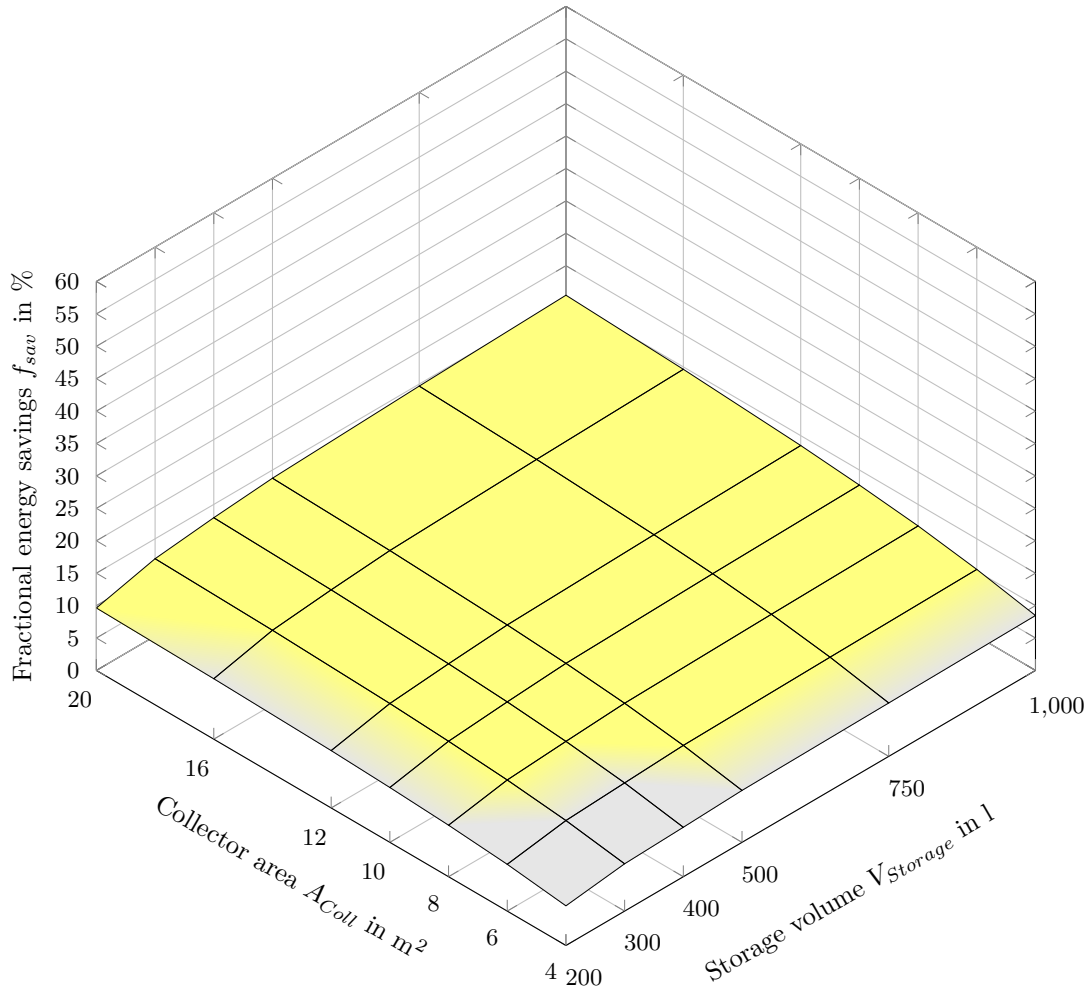


Figure F.16: Correlation between collector area, heat storage volume and fractional energy savings f_{sav} in case of a solar domestic hot water system located in Stockholm (Sweden). The yellow-highlighted regions indicate systems with polymeric FPC which yield higher fractional energy savings than the reference system with metal-based collectors (cf. section 6.1.2).

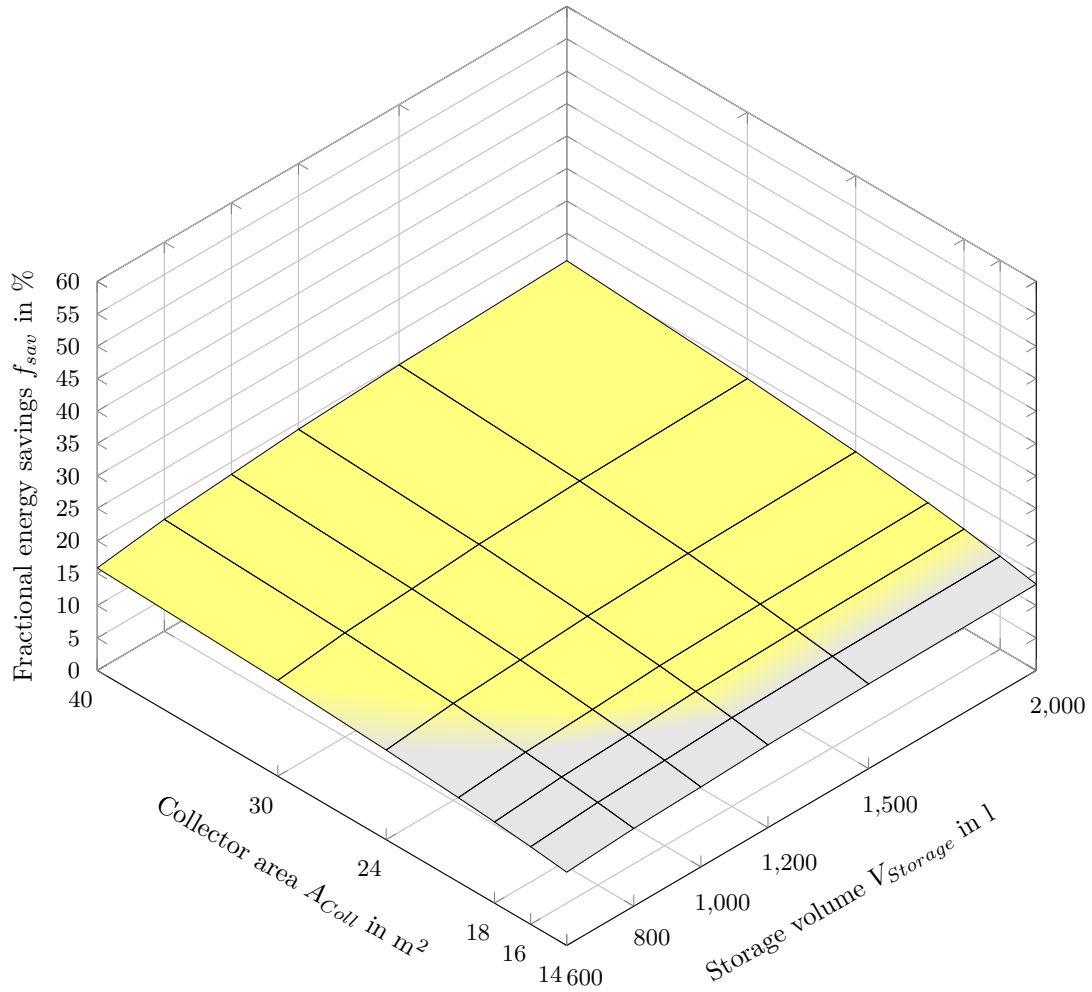


Figure F.17: Correlation between collector area, heat storage volume and fractional energy savings f_{sav} in case of a solar combi system located in Stockholm (Sweden). The result indicate that no systems with polymeric FPC yields higher fractional energy savings than the reference system with metal-based collectors (cf. section 6.1.3).

F Further Results of the Parametric Study

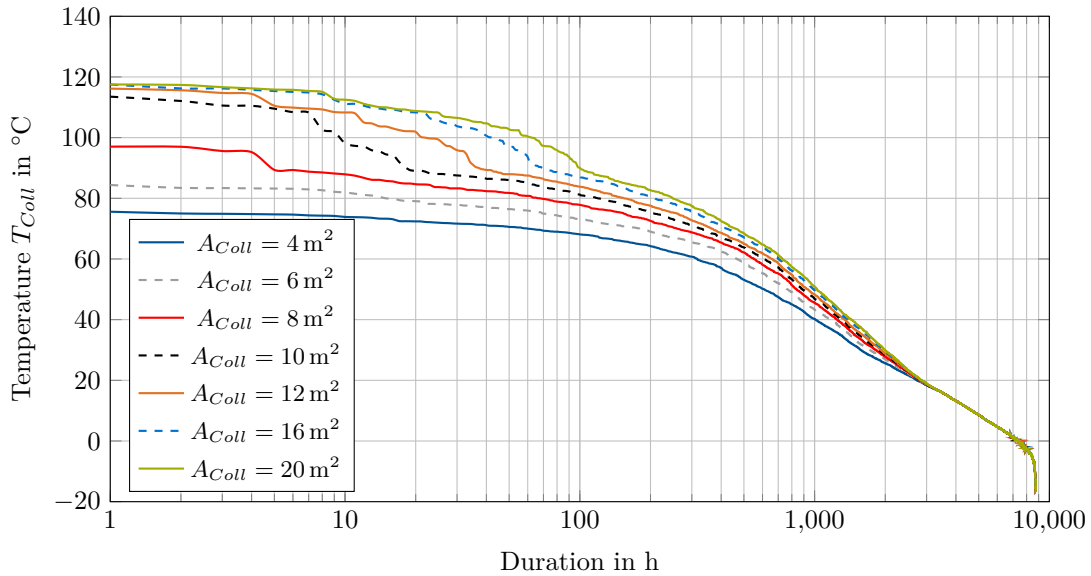


Figure F.18: Collector temperatures T_{Coll} in case of solar DHW systems located in Stockholm (Sweden). Each system is equipped with a 200l heat storage and a solar thermal collector array varying between 4 m^2 and 20 m^2 . Maximum collector temperature: $118.4 \text{ }^{\circ}\text{C}$.

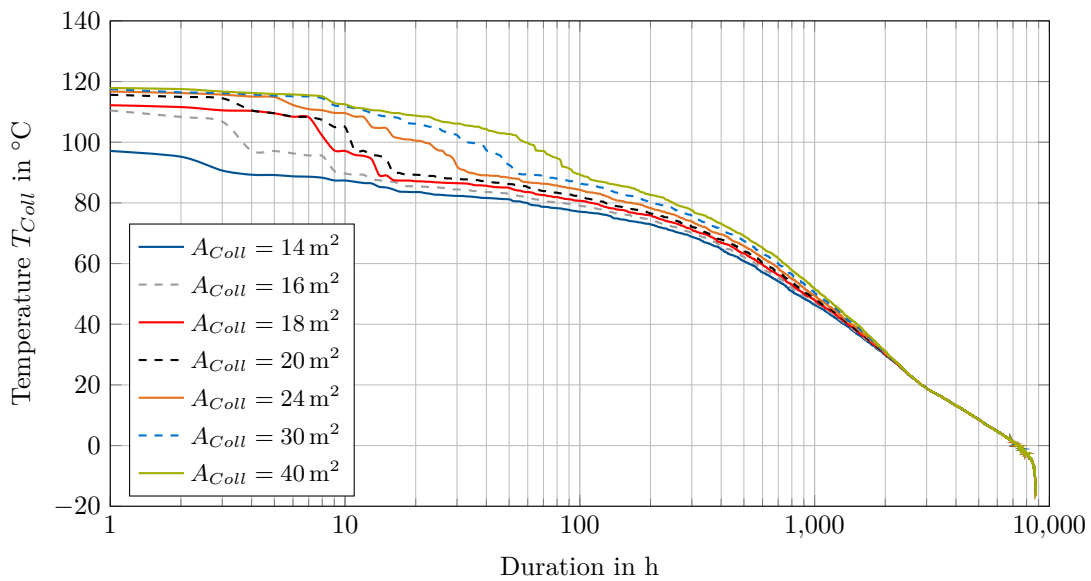


Figure F.19: Collector temperatures T_{Coll} in case of solar combi systems located in Stockholm (Sweden). Each system is equipped with a 600l heat storage and a solar thermal collector array varying between 14 m^2 and 40 m^2 . Maximum collector temperature: $118.4 \text{ }^{\circ}\text{C}$.

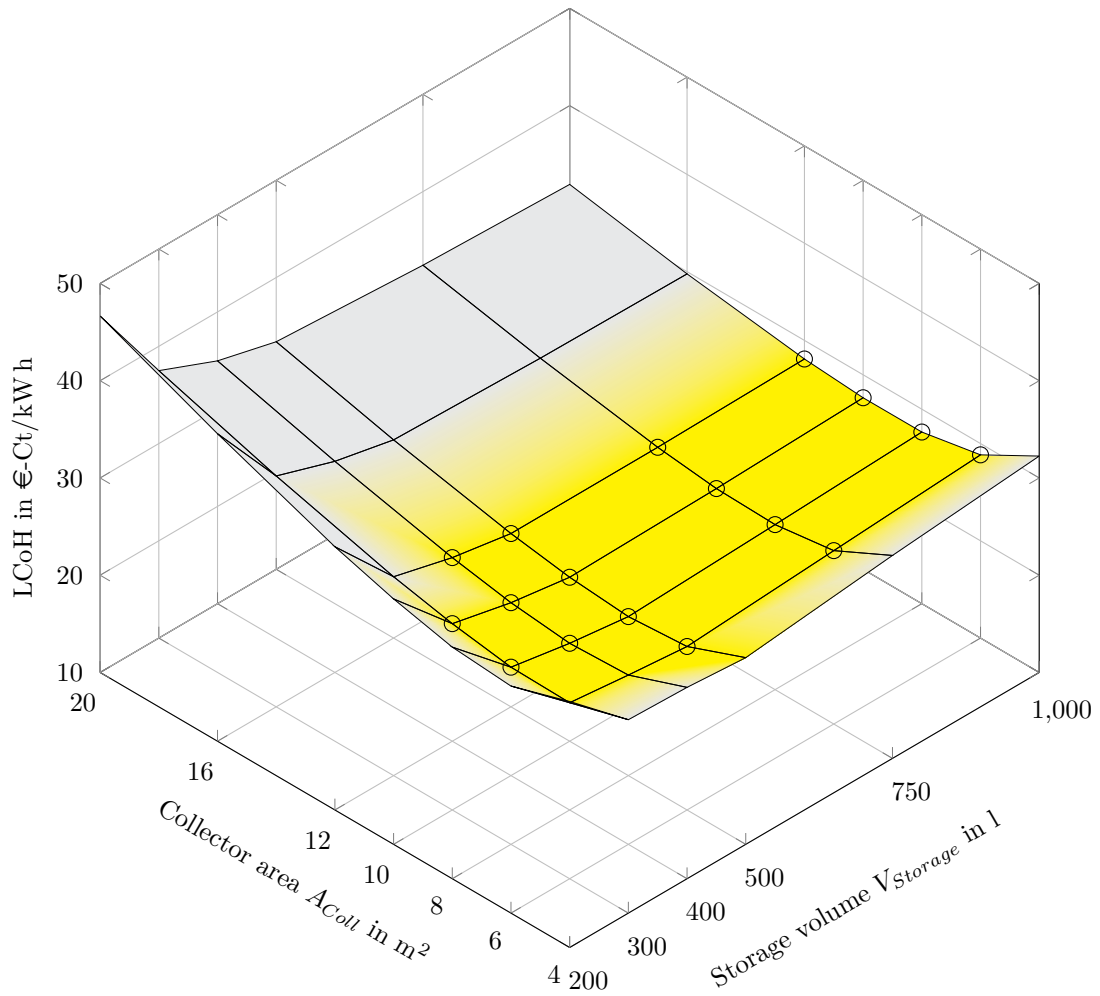


Figure F.20: LCoH in case of a solar DHW system with polymeric solar thermal FPCs located in Stockholm (Sweden). The highlighted yellow area indicates system configurations which yield lower LCoH than the solar thermal reference system with metal-based FPCs (cf. section 6.1.2). In addition, the circular markers indicate system configurations with higher fractional energy savings than the solar thermal reference system with metal-based FPCs.

F Further Results of the Parametric Study

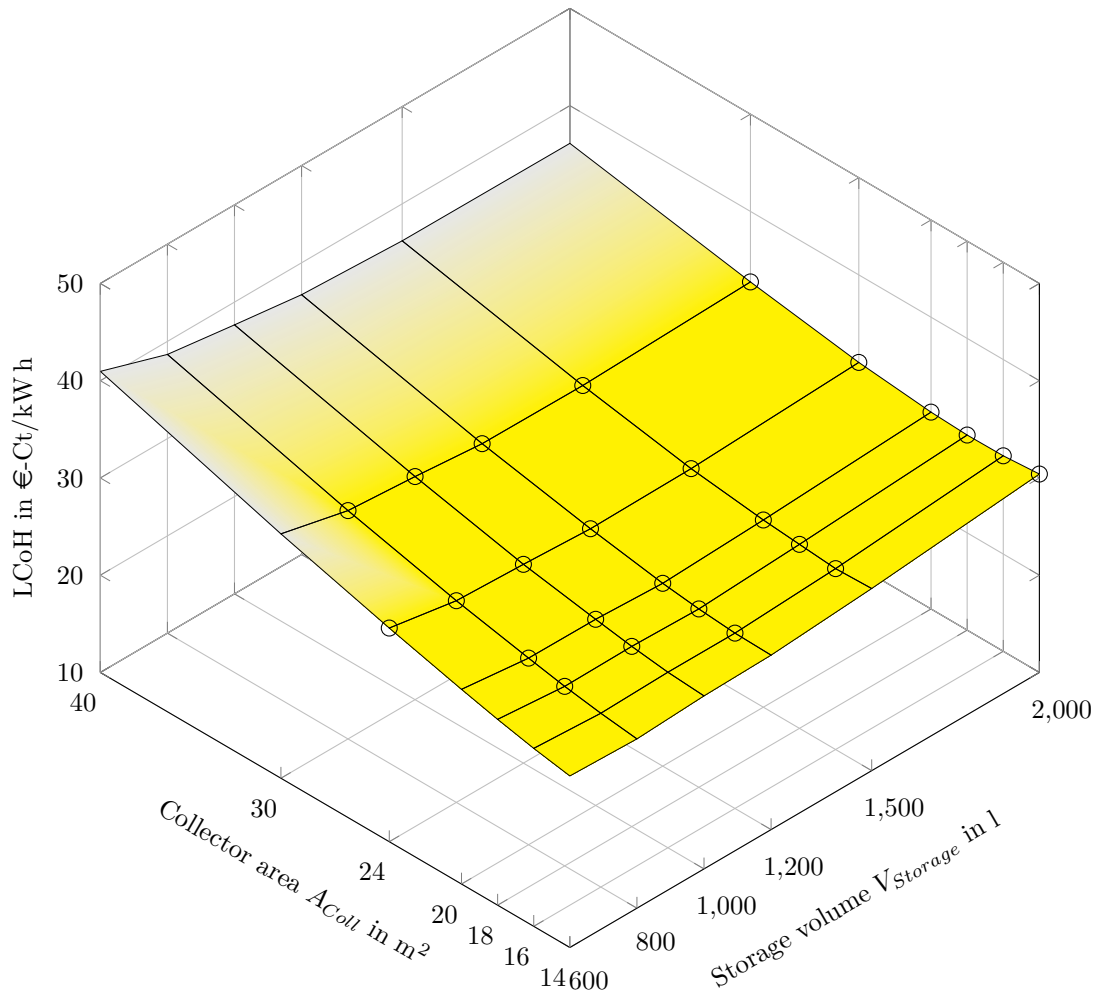


Figure F.21: LCoH in case of a solar combi system with polymeric solar thermal FPCs located in Stockholm (Sweden). The highlighted yellow area indicates system configurations which yield lower LCoH than the solar thermal reference system with metal-based FPCs (cf. section 6.1.3). In addition, the circular markers indicate system configurations with higher fractional energy savings than the solar thermal reference system with metal-based FPCs.

G Component Costs

To determine characteristic component costs for solar thermal systems, available price lists from 15 different manufacturers (located in Germany, Austria and Switzerland) were evaluated and averaged (cf. table 7.1).

The necessary volume of a membrane expansion vessel correlates with the volume of the HTF inside the solar collector loop (and therefore with the overall area of the solar thermal collector array), the system pressure, length and diameter of the pipes as well as further parameters. In order to ensure a reliable and safe operation of a solar thermal system, the membrane expansion vessel shall be sized according to DIN EN 12828:2014 (pp. 39 - 42). However, to estimate specific costs of membrane expansion vessels (with respect to the corresponding area of the collector array), a specific value of 4l/m^2 is assumed (cf. figure G.1).

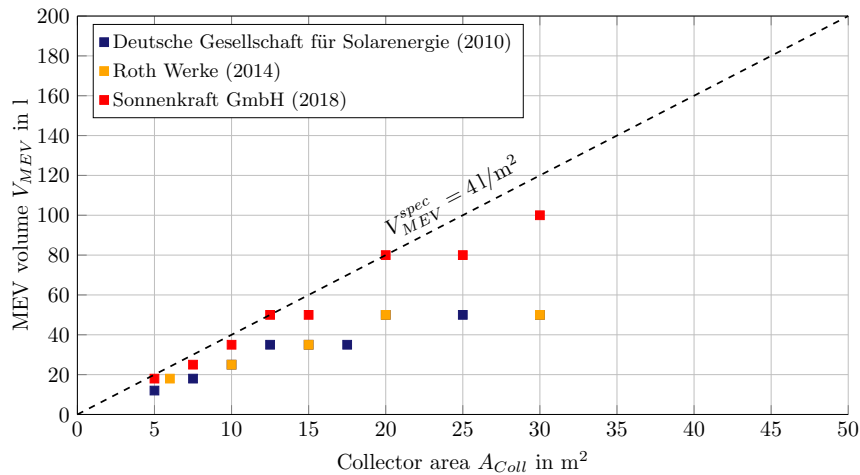


Figure G.1: Ratio between collector area and related membrane expansion volume according to literature and manufacturer's data. Data source: Deutsche Gesellschaft für Sonnenenergie (2010, p. 83), Sonnenkraft GmbH (2018, p. 42), Roth Werke GmbH (2014, p. 162).

As indicated in figure G.1, the assumed specific volume for membrane expansion vessels over-estimate the necessary volumes available from both solar thermal manufacturers as well as literature data. Therefore, the aforementioned value of 4l/m^2 represents a conservative assumption.

Table G.1: Specific costs (without VAT) and volumes of solar thermal FPCs. Data source: Sonne, Wind & Wärme (2018), gross collector area ranging between 2.10 m² and 2.51 m². Empty cells indicate that there is no information available.

| Manufacturer | Product | Gross collector area in m ² | List price in € | Specific price in €/m ² | Volume in l | Specific volume in l/m ² |
|--------------|---------------------|--|-----------------|------------------------------------|-------------|-------------------------------------|
| OEG | 2plus | 2.10 | 258.30 | 123.00 | 1.3 | 0.62 |
| OEG | 4plus Harfe | 2.53 | 301.00 | 118.97 | 2.5 | 0.99 |
| OEG | 4Plus Mäander | 2.53 | 301.00 | 118.97 | | |
| Rennergy | AK2300 | 2.25 | 454.00 | 201.78 | | |
| AS Solar | ASFk 2.5 WLT | 2.53 | 487.00 | 192.49 | | |
| Remeha | C250V / C250H | 2.51 | 604.00 | 240.64 | 1.7 | 0.68 |
| Capito | CCPCW 252 | 2.52 | 631.00 | 250.40 | | |
| Wolf | CFK-1 | 2.30 | 575.00 | 250.00 | 1.1 | 0.48 |
| Remeha | D 230 | 2.30 | 604.00 | 262.61 | 2.3 | 1.00 |
| Ufe | Eco Star III blue | 2.20 | 345.00 | 156.82 | | |
| Wagner Solar | EURO L20 MH AR | 2.61 | 805.00 | 308.43 | 2.2 | 0.84 |
| Brötje | FK 25 R C | 2.55 | 441.00 | 172.94 | | |
| Brötje | FK 26 W B | 2.59 | 482.00 | 186.10 | | |
| Brötje | FK 26 WL B | 2.59 | 561.00 | 216.60 | | |
| Estec | FK 8210 4H Prestige | 2.02 | 380.00 | 188.12 | | |
| Estec | FK 8250 H Prestige | 2.52 | 462.00 | 183.33 | | |
| Estec | FK 8250 Prestige | 2.52 | 460.00 | 182.54 | | |
| Estec | Fk 8250 Q Prestige | 2.52 | 462.00 | 183.33 | | |
| Westfalen | FK23 | 2.34 | 455.00 | 194.44 | 1.6 | 0.68 |
| Westfalen | FK23 AR | 2.32 | 495.00 | 213.36 | 1.7 | 0.73 |
| s-power | FK251 BlueLine | 2.51 | 499.00 | 198.80 | 1.7 | 0.68 |
| STI | FKF 200 V Cu/Cu | 2.13 | 855.00 | 401.41 | 2.1 | 0.99 |
| STI | FKF 240 V Al/Al | 2.52 | 1,044.00 | 414.29 | 1.9 | 0.75 |

Table G.1: Specific costs (without VAT) and volumes of solar thermal FPCs. Data source: Sonne, Wind & Wärme (2018), gross collector area ranging between 2.10 m² 2.51 m². Empty cells indicate that there is no information available. **(Continued)**

| Manufacturer | Product | Gross collector area in m ² | List price in € | Specific price in €/m ² | Volume in l | Specific volume in l/m ² |
|------------------|---------------------|--|-----------------|------------------------------------|-------------|-------------------------------------|
| Estec | IDKM Integra 1.25 | 1.25 | 380.00 | 304.00 | | |
| Estec | IDKM Integra 2.5 | 2.52 | 499.00 | 198.02 | | |
| Sonnenkraft | IDMK12AL | 1.25 | 485.00 | 388.00 | | |
| Sonnenkraft | IDMK25Al | 2.52 | 370.00 | 146.83 | | |
| Brötje | IK 25 K | 2.52 | 445.00 | 176.59 | | |
| Buderus | Logasol SKT1.0-s | 2.55 | 886.00 | 347.45 | 1.61 | 0.63 |
| Solarbayer | PremiumPlus AL 2.86 | 2.86 | 471.00 | 164.69 | 2.1 | 0.73 |
| Reinhard Solarte | RST Sol 4 Niox | 2.21 | 669.00 | 302.71 | | |
| Solar-Steiner | Sanos L40 | 2.61 | 490.00 | 187.74 | | |
| NAU | SAPHIRLINE | 2.35 | 612.00 | 260.43 | 1.25 | 0.53 |
| Siko Solar | Sikosun 1200 | 2.08 | 740.00 | 355.77 | 1.6 | 0.77 |
| NAU | SILVERLINE | 2.15 | 550.00 | 255.81 | 1.15 | 0.53 |
| Sonnenkraft | SK500L-ECO-AL | 2.57 | 540.00 | 210.12 | | |
| Sonnenkraft | SK500N-ECO-AL | 2.57 | 540.00 | 210.12 | | |
| Sonnenkraft | SKR500 | 2.57 | 600.00 | 233.46 | | |
| Sonnenkraft | SKR500L | 2.57 | 600.00 | 233.46 | | |
| Westfalen | Solacept FK22 | 2.25 | 433.00 | 192.44 | | |
| Westfalen | Solacept FK22AR | 2.25 | 550.00 | 244.44 | | |
| MHG | Solarmat FL | 2.37 | 1,079.00 | 455.27 | | |
| Solvis | SolvisCala 254 AR | 2.56 | 860.20 | 336.02 | 2.52 | 0.98 |
| Oertli | SUN D 230 | 2.30 | 766.00 | 333.04 | | |
| Orange Energy | Sun2 / Sun2Q | 2.57 | 660.00 | 256.81 | 2.2 | 0.86 |
| Sunset | SUNblue 25 | 2.51 | 739.00 | 294.42 | | |
| Sunset | SUNblue 25 -TA | 2.51 | 739.00 | 294.42 | 1.3 | 0.52 |

Table G.1: Specific costs (without VAT) and volumes of solar thermal FPCs. Data source: Sonne, Wind & Wärme (2018), gross collector area ranging between 2.10 m² and 2.51 m². Empty cells indicate that there is no information available. **(Continued)**

| Manufacturer | Product | Gross collector area in m ² | List price in € | Specific price in €/m ² | Volume in l | Specific volume in l/m ² |
|-----------------|-------------------------|--|-----------------|------------------------------------|-------------|-------------------------------------|
| Wolf | TopSon F3-1 | 2.30 | 755.00 | 328.26 | 1.7 | 0.74 |
| Wolf | TopSon F3-1Q | 2.30 | 755.00 | 328.26 | 1.9 | 0.83 |
| Helvetic Energy | Valor | 2.40 | 467.00 | 194.58 | | |
| Viessmann | Vitosol 100-FM Typ SH1F | 2.51 | 649.00 | 258.57 | 2.4 | 0.96 |
| Immosolar | XLS | 2.69 | 600.60 | 223.27 | 2.2 | 0.82 |
| Immosolar | XLW | 2.69 | 613.60 | 228.10 | 2.2 | 0.82 |
| Zewotherm | ZewoSol Premium AC200 | 2.09 | 465.00 | 222.49 | | |
| Zewotherm | ZewoSol Premium AC250 | 2.51 | 609.00 | 242.63 | | |
| | | | | Ø243.05 €/m² | | Ø0.73 l/m² |

Table G.2: Specific costs (without VAT) of monovalent heat storages.

| Source | Product | Volume in l | List price in € | Specific price in €/m ² |
|--------------------------------|-------------|----------------|--------------------|---------------------------------------|
| CitrinSolar GmbH (2018, p. 82) | 306002 | 160 | 692.00 | 4.33 |
| CitrinSolar GmbH (2018, p. 82) | 306004 | 200 | 729.00 | 3.65 |
| CitrinSolar GmbH (2018, p. 82) | 306006 | 300 | 892.00 | 2.97 |
| CitrinSolar GmbH (2018, p. 82) | 306008 | 400 | 1,143.00 | 2.86 |
| CitrinSolar GmbH (2018, p. 82) | 306010 | 500 | 1,250.00 | 2.50 |
| CitrinSolar GmbH (2018, p. 82) | 321805 | 800 | 2,666.00 | 3.33 |
| CitrinSolar GmbH (2018, p. 82) | 321905 | 1,000 | 3,157.00 | 3.16 |
| GASOKOL GmbH (2013, p. 21) | 610804-24 | 200 | 870.00 | 4.35 |
| GASOKOL GmbH (2013, p. 21) | 610806-84 | 300 | 975.00 | 3.25 |
| GASOKOL GmbH (2013, p. 21) | 610808-84 | 400 | 1,206.00 | 3.02 |
| GASOKOL GmbH (2013, p. 21) | 610810-84 | 500 | 1,317.00 | 2.63 |
| ThüSolar GmbH (2012, p. 15) | 1099 | 200 | 843.00 | 4.22 |
| ThüSolar GmbH (2012, p. 15) | 1100 | 300 | 975.00 | 3.25 |
| ThüSolar GmbH (2012, p. 15) | 1101 | 289 | 1,044.00 | 3.61 |
| ThüSolar GmbH (2012, p. 15) | 1102 | 400 | 1,112.00 | 2.78 |
| ThüSolar GmbH (2012, p. 15) | 1103 | 500 | 1,230.00 | 2.46 |
| ThüSolar GmbH (2012, p. 15) | 1104 | 800 | 1,649.00 | 2.06 |
| ThüSolar GmbH (2012, p. 15) | 1105 | 1,000 | 1,946.00 | 1.95 |
| Wikora GmbH (2017, p. 10) | 55120000110 | 123 | 683.00 | 5.55 |
| Wikora GmbH (2017, p. 10) | 55155000191 | 152 | 738.00 | 4.86 |
| Wikora GmbH (2017, p. 10) | 55210000191 | 200 | 789.00 | 3.95 |
| Wikora GmbH (2017, p. 10) | 55310000191 | 298 | 936.00 | 3.14 |
| Wikora GmbH (2017, p. 10) | 55410000191 | 428 | 1,194.00 | 2.79 |

Table G.2: Specific costs (without VAT) of monovalent heat storages. **(Continued)**

| Source | Product | Volume in l | List price in € | Specific price in €/m ² |
|----------------------------|-------------|----------------|--------------------|---------------------------------------|
| Wikora GmbH (2017, p. 10) | 55510000191 | 499 | 1,321.00 | 2.65 |
| Wikora GmbH (2017, p. 11) | 55810000101 | 825 | 2,626.00 | 3.18 |
| Wikora GmbH (2017, p. 11) | 55101000101 | 978 | 3,285.00 | 3.36 |
| Wikora GmbH (2017, p. 11) | 55151000101 | 1,529 | 4,233.00 | 2.77 |
| Wikora GmbH (2017, p. 11) | 55201000101 | 2,002 | 5,162.00 | 2.58 |
| Wikora GmbH (2017, p. 11) | 55301000101 | 2,938 | 6,118.00 | 2.08 |
| WOLF GmbH (2018, p. 06.25) | 2444170 | 150 | 970.00 | 6.47 |
| WOLF GmbH (2018, p. 06.25) | 2444171 | 200 | 1,080.00 | 5.40 |
| WOLF GmbH (2018, p. 06.25) | 2444172 | 300 | 1,365.00 | 4.55 |
| | | | | ∅3.43 €/l |

Table G.3: Specific costs (without VAT) of bivalent heat storages.

| Source | Product | Volume in l | List price in € | Specific price in €/m ² |
|---------------------------------|-------------|----------------|--------------------|---------------------------------------|
| CitrinSolar GmbH (2018, p. 83) | 306020 | 200 | 917.00 | 4.59 |
| CitrinSolar GmbH (2018, p. 83) | 306022 | 300 | 977.00 | 3.26 |
| CitrinSolar GmbH (2018, p. 83) | 306024 | 400 | 1,189.00 | 2.97 |
| CitrinSolar GmbH (2018, p. 83) | 306026 | 500 | 1,322.00 | 2.64 |
| CitrinSolar GmbH (2018, p. 83) | 322805 | 800 | 2,816.00 | 3.52 |
| CitrinSolar GmbH (2018, p. 83) | 322905 | 1,000 | 3,286.00 | 3.29 |
| GASOKOL GmbH (2013, p. 21) | 620804-24 | 200 | 945.00 | 4.73 |
| GASOKOL GmbH (2013, p. 21) | 620806-84 | 300 | 1,050.00 | 3.50 |
| GASOKOL GmbH (2013, p. 21) | 620808-84 | 400 | 1,281.00 | 3.20 |
| GASOKOL GmbH (2013, p. 21) | 620810-84 | 500 | 1,365.00 | 2.73 |
| Wagner Solar GmbH (2017, p. 52) | 130 103 04 | 300 | 1,100.00 | 3.67 |
| Wagner Solar GmbH (2017, p. 52) | 130 103 02 | 400 | 1,280.00 | 3.20 |
| Wagner Solar GmbH (2017, p. 53) | 130 141 14 | 300 | 900.00 | 3.00 |
| Wagner Solar GmbH (2017, p. 53) | 130 141 15 | 400 | 1,050.00 | 2.62 |
| Wagner Solar GmbH (2017, p. 53) | 130 141 13 | 500 | 1,270.00 | 2.54 |
| Wikora GmbH (2017, p. 12) | 55212000191 | 198 | 888.00 | 4.48 |
| Wikora GmbH (2017, p. 12) | 55312000191 | 296 | 1,024.00 | 3.46 |
| Wikora GmbH (2017, p. 12) | 55412000191 | 427 | 1,209.00 | 2.83 |
| Wikora GmbH (2017, p. 12) | 55512000191 | 297 | 1,452.00 | 4.89 |
| Wikora GmbH (2017, p. 13) | 55812000101 | 822 | 2,460.00 | 2.99 |
| Wikora GmbH (2017, p. 13) | 55101200101 | 975 | 3,185.00 | 3.27 |
| Wikora GmbH (2017, p. 13) | 55151200101 | 1,525 | 4,376.00 | 2.87 |
| Wikora GmbH (2017, p. 13) | 55201200101 | 1,998 | 5,438.00 | 2.72 |

Table G.3: Specific costs (without VAT) of bivalent heat storages. **(Continued)**

| Source | Product | Volume in l | List price in € | Specific price in €/m ² |
|----------------------------|-------------|----------------|--------------------|---------------------------------------|
| Wikora GmbH (2017, p. 13) | 55301200101 | 2,894 | 6,496.00 | 2.24 |
| WOLF GmbH (2018, p. 06.22) | 2483737 | 300 | 1,380.00 | 4.60 |
| WOLF GmbH (2018, p. 06.22) | 2483738 | 400 | 1,670.00 | 4.18 |
| WOLF GmbH (2018, p. 06.21) | 2444850 | 500 | 1,985.00 | 3.97 |
| WOLF GmbH (2018, p. 06.21) | 2444875 | 750 | 2,655.00 | 3.54 |
| WOLF GmbH (2018, p. 06.21) | 2444810 | 1,000 | 3,290.00 | 3.29 |
| | | | | ∅3.41 €/l |

Table G.4: Specific costs (without VAT) of MEVs.

| Source | Product | Volume in l | List price in € | Specific price in €/m ² |
|--|--------------|----------------|--------------------|---------------------------------------|
| Buderus Thermotechnik GmbH (2018, p. 7087) | 12 222 080 | 18 | 76.73 | 17.05 |
| Buderus Thermotechnik GmbH (2018, p. 7087) | 12 222 081 | 25 | 98.31 | 15.73 |
| CitrinSolar GmbH (2018, p. 14) | 196018 | 18 | 80.00 | 17.78 |
| CitrinSolar GmbH (2018, p. 14) | 196025 | 25 | 91.00 | 14.56 |
| CitrinSolar GmbH (2018, p. 14) | 196035 | 35 | 120.00 | 13.71 |
| CitrinSolar GmbH (2018, p. 23) | 196050 | 50 | 169.00 | 13.52 |
| CitrinSolar GmbH (2018, p. 28) | 196080 | 80 | 387.00 | 19.35 |
| CitrinSolar GmbH (2018, p. 28) | 196100 | 100 | 498.00 | 19.92 |
| Consolar GmbH (2006, p. 20) | PS050 | 18 | 60.00 | 13.33 |
| Consolar GmbH (2006, p. 20) | PS052 | 25 | 81.00 | 12.96 |
| Consolar GmbH (2006, p. 20) | PS053 | 35 | 93.00 | 10.63 |
| Consolar GmbH (2006, p. 20) | PS056 | 50 | 120.00 | 9.60 |
| GASOKOL GmbH (2013, p. 35) | 7504 | 18 | 48.40 | 10.76 |
| GASOKOL GmbH (2013, p. 35) | 7506 | 25 | 54.90 | 8.78 |
| GASOKOL GmbH (2013, p. 35) | 7508 | 40 | 88.00 | 8.80 |
| GASOKOL GmbH (2013, p. 35) | 7510 | 60 | 125.60 | 8.37 |
| GASOKOL GmbH (2013, p. 35) | 7511 | 80 | 173.60 | 8.68 |
| GASOKOL GmbH (2013, p. 35) | 7512 | 100 | 237.20 | 9.49 |
| GASOKOL GmbH (2013, p. 35) | 7516 | 200 | 412.80 | 8.26 |
| GASOKOL GmbH (2013, p. 35) | 7520 | 300 | 608.00 | 8.11 |
| ROTEX Heating Systems GmbH (2018, p. 197) | 16 20 70 | 12 | 88.87 | 29.62 |
| ROTEX Heating Systems GmbH (2018, p. 198) | 16 20 50 | 25 | 109.78 | 17.56 |
| ROTEX Heating Systems GmbH (2018, p. 198) | 16 20 51-RTX | 35 | 134.89 | 15.42 |

Table G.4: Specific costs (without VAT) of MEVs. **(Continued)**

| Source | Product | Volume in l | List price in € | Specific price in €/m ² |
|--------------------------------|------------|----------------|--------------------|---------------------------------------|
| Roth Werke GmbH (2014, p. 162) | 1135006675 | 18 | 90.05 | 20.01 |
| Roth Werke GmbH (2014, p. 162) | 1135006676 | 25 | 101.00 | 16.16 |
| Roth Werke GmbH (2014, p. 162) | 1135006633 | 35 | 154.00 | 17.60 |
| Roth Werke GmbH (2014, p. 162) | 1135006601 | 50 | 207.00 | 16.56 |
| Roth Werke GmbH (2014, p. 162) | 1135006602 | 80 | 313.00 | 15.65 |
| Sonnenkraft GmbH (2018, p. 42) | AG18 | 18 | 40.00 | 8.89 |
| Sonnenkraft GmbH (2018, p. 42) | AG25 | 25 | 50.00 | 8.00 |
| Sonnenkraft GmbH (2018, p. 42) | AG35 | 35 | 60.00 | 6.86 |
| Sonnenkraft GmbH (2018, p. 42) | AG50 | 50 | 90.00 | 7.20 |
| Sonnenkraft GmbH (2018, p. 42) | AG80 | 80 | 150.00 | 7.50 |
| Sonnenkraft GmbH (2018, p. 42) | AG100 | 100 | 174.00 | 6.96 |
| Sonnenkraft GmbH (2018, p. 42) | AG150 | 150 | 203.00 | 5.41 |
| Sonnenkraft GmbH (2018, p. 42) | AG200 | 200 | 268.00 | 5.36 |
| Sonnenkraft GmbH (2018, p. 42) | AG300 | 300 | 465.00 | 6.20 |
| Sonnenkraft GmbH (2018, p. 42) | AG500 | 500 | 695.00 | 5.56 |
| ThüSolar GmbH (2012, p. 31) | SP12 | 12 | 55.50 | 18.50 |
| ThüSolar GmbH (2012, p. 31) | SP18 | 18 | 59.70 | 13.27 |
| ThüSolar GmbH (2012, p. 31) | SP25 | 25 | 74.40 | 11.90 |
| ThüSolar GmbH (2012, p. 31) | SP35 | 35 | 108.00 | 12.34 |
| ThüSolar GmbH (2012, p. 31) | SP50 | 50 | 172.00 | 13.76 |
| ThüSolar GmbH (2012, p. 31) | SP80 | 80 | 252.00 | 12.60 |
| ThüSolar GmbH (2012, p. 31) | SP105 | 105 | 320.20 | 12.20 |
| ThüSolar GmbH (2012, p. 31) | SP150 | 150 | 472.00 | 12.59 |

Table G.4: Specific costs (without VAT) of MEVs. **(Continued)**

| Source | Product | Volume in l | List price in € | Specific price in €/m ² |
|--|------------|----------------|--------------------|---------------------------------------|
| TiSUN GmbH (2018, p. 24) | AG18 | 18 | 40.00 | 8.89 |
| TiSUN GmbH (2018, p. 24) | AG25 | 25 | 50.00 | 8.00 |
| TiSUN GmbH (2018, p. 24) | AG35 | 35 | 60.00 | 6.86 |
| TiSUN GmbH (2018, p. 24) | AG50 | 50 | 90.00 | 7.20 |
| TiSUN GmbH (2018, p. 24) | AG80 | 80 | 150.00 | 7.50 |
| TiSUN GmbH (2018, p. 24) | AG100 | 100 | 174.00 | 6.96 |
| TiSUN GmbH (2018, p. 24) | AG150 | 150 | 203.00 | 5.41 |
| TiSUN GmbH (2018, p. 24) | AG200 | 200 | 268.00 | 5.36 |
| TiSUN GmbH (2018, p. 24) | AG300 | 300 | 465.00 | 6.20 |
| TiSUN GmbH (2018, p. 24) | AG500 | 500 | 695.00 | 5.56 |
| Viessmann Werke GmbH & Co. KG (2017, p. 5.4-3) | 7248241 | 18 | 111.00 | 24.67 |
| Viessmann Werke GmbH & Co. KG (2017, p. 5.4-3) | 7248242 | 25 | 139.00 | 22.24 |
| Viessmann Werke GmbH & Co. KG (2017, p. 5.4-3) | 7248243 | 40 | 180.00 | 18.00 |
| Viessmann Werke GmbH & Co. KG (2017, p. 5.4-3) | 7248244 | 50 | 269.00 | 21.52 |
| Viessmann Werke GmbH & Co. KG (2017, p. 5.4-3) | 7248245 | 80 | 375.00 | 18.75 |
| Wagner Solar GmbH (2017, p. 60) | 150 450 10 | 12 | 92.65 | 30.88 |
| Wagner Solar GmbH (2017, p. 60) | 150 450 11 | 18 | 112.14 | 24.92 |
| Wagner Solar GmbH (2017, p. 60) | 150 450 13 | 24 | 150.64 | 25.11 |
| Wagner Solar GmbH (2017, p. 60) | 150 450 14 | 35 | 164.34 | 18.78 |
| Wagner Solar GmbH (2017, p. 60) | 150 450 15 | 50 | 228.61 | 18.29 |

Table G.4: Specific costs (without VAT) of MEVs. **(Continued)**

| Source | Product | Volume in l | List price in € | Specific price in €/m ² |
|----------------------------|----------------|----------------|--------------------|---------------------------------------|
| Wikora GmbH (2017, p. 55) | 01 5318 0 0101 | 18 | 90.00 | 20.00 |
| Wikora GmbH (2017, p. 55) | 01 5325 0 0101 | 25 | 100.00 | 16.00 |
| Wikora GmbH (2017, p. 55) | 01 5340 0 0101 | 40 | 140.00 | 14.00 |
| Wikora GmbH (2017, p. 55) | 01 5350 0 0101 | 50 | 160.00 | 12.80 |
| Wikora GmbH (2017, p. 55) | 01 5380 0 0101 | 80 | 180.00 | 9.00 |
| Wikora GmbH (2017, p. 55) | 01 5310 0 0101 | 100 | 270.00 | 10.80 |
| Wikora GmbH (2017, p. 55) | 01 5320 0 0101 | 200 | 510.00 | 10.20 |
| WOLF GmbH (2018, p. 04.22) | 2444210 | 12 | 66.00 | 22.00 |
| WOLF GmbH (2018, p. 04.22) | 2444211 | 18 | 82.00 | 18.22 |
| WOLF GmbH (2018, p. 04.22) | 2444212 | 25 | 100.00 | 16.00 |
| WOLF GmbH (2018, p. 04.22) | 2483075 | 35 | 126.00 | 14.40 |
| WOLF GmbH (2018, p. 04.22) | 2444223 | 50 | 182.00 | 14.56 |
| WOLF GmbH (2018, p. 04.22) | 2483608 | 80 | 301.00 | 15.05 |
| WOLF GmbH (2018, p. 04.22) | 2482818 | 100 | 472.00 | 18.88 |
| WOLF GmbH (2018, p. 04.22) | 2484096 | 150 | 775.00 | 20.67 |
| WOLF GmbH (2018, p. 04.22) | 2484097 | 200 | 905.00 | 18.10 |
| | | | | Ø13.60 €/m² |

Table G.5: Specific costs (without VAT) for piping. Empty cells indicate that there is no information available.

| Source | Product | Diameter in mm | Length in m | List price in € | Specific price in €/m |
|--|-----------------|-------------------|----------------|--------------------|--------------------------|
| Armacell GmbH (2018, p. 58) | SO-DV-14X16/100 | DN 14 | 100 | | 48.11 |
| Armacell GmbH (2018, p. 58) | SO-DV-14X16/E10 | DN 14 | 10 | | 48.11 |
| Armacell GmbH (2018, p. 58) | SO-DV-14X16/E15 | DN 14 | 15 | | 48.11 |
| Armacell GmbH (2018, p. 58) | SO-DV-14X16/E20 | DN 14 | 20 | | 48.11 |
| Armacell GmbH (2018, p. 58) | SO-DV-14X16/E25 | DN 14 | 25 | | 48.11 |
| Armacell GmbH (2018, p. 58) | SO-DV-14X16/E50 | DN 14 | 50 | | 48.11 |
| Armacell GmbH (2018, p. 58) | SO-DV-14X20/100 | DN 14 | 100 | | 56.76 |
| Armacell GmbH (2018, p. 58) | SO-DV-14X20/E10 | DN 14 | 10 | | 56.76 |
| Armacell GmbH (2018, p. 58) | SO-DV-14X20/E15 | DN 14 | 15 | | 56.76 |
| Armacell GmbH (2018, p. 58) | SO-DV-14X20/E20 | DN 14 | 20 | | 56.76 |
| Armacell GmbH (2018, p. 58) | SO-DV-14X20/E25 | DN 14 | 25 | | 56.76 |
| Armacell GmbH (2018, p. 58) | SO-DV-14X20/E50 | DN 14 | 50 | | 56.76 |
| Armacell GmbH (2018, p. 58) | SO-DV-14X25/100 | DN 14 | 100 | | 64.15 |
| Armacell GmbH (2018, p. 58) | SO-DV-14X25/E15 | DN 14 | 15 | | 64.15 |
| Armacell GmbH (2018, p. 58) | SO-DV-14X25/E25 | DN 14 | 25 | | 64.15 |
| Armacell GmbH (2018, p. 58) | SO-DV-20X16/E15 | DN 20 | 15 | | 55.50 |
| Armacell GmbH (2018, p. 58) | SO-DV-20X16/E25 | DN 20 | 25 | | 55.50 |
| Armacell GmbH (2018, p. 58) | SO-DV-20X20/E15 | DN 20 | 15 | | 65.22 |
| Armacell GmbH (2018, p. 58) | SO-DV-20X20/E25 | DN 20 | 25 | | 65.22 |
| Buderus Thermotechnik GmbH (2018, p. 7090) | 12 055 320 | DN 12 | 15 | 562.89 | 37.53 |
| Buderus Thermotechnik GmbH (2018, p. 7090) | 12 055 321 | DN 12 | 20 | 749.94 | 37.50 |
| Buderus Thermotechnik GmbH (2018, p. 7090) | 12 055 322 | DN 12 | 25 | 936.99 | 37.48 |

Table G.5: Specific costs (without VAT) for piping. Empty cells indicate that there is no information available. **(Continued)**

| Source | Product | Diameter in mm | Length in m | List price in € | Specific price in €/m |
|--|------------|-------------------|----------------|--------------------|--------------------------|
| Buderus Thermotechnik GmbH (2018, p. 7090) | 12 055 323 | DN 16 | 15 | 621.18 | 41.41 |
| Buderus Thermotechnik GmbH (2018, p. 7090) | 12 055 324 | DN 16 | 20 | 828.24 | 41.41 |
| Buderus Thermotechnik GmbH (2018, p. 7090) | 12 055 325 | DN 16 | 25 | 1,036.17 | 41.45 |
| Buderus Thermotechnik GmbH (2018, p. 7091) | 12 055 326 | DN 20 | 15 | 708.18 | 47.21 |
| Buderus Thermotechnik GmbH (2018, p. 7091) | 12 055 327 | DN 20 | 20 | 943.08 | 47.15 |
| Buderus Thermotechnik GmbH (2018, p. 7091) | 12 055 328 | DN 20 | 25 | 1,178.85 | 47.15 |
| Buderus Thermotechnik GmbH (2018, p. 7091) | 12 055 329 | DN 25 | 15 | 950.04 | 63.34 |
| Buderus Thermotechnik GmbH (2018, p. 7091) | 12 055 330 | DN 25 | 20 | 1,265.85 | 63.29 |
| Buderus Thermotechnik GmbH (2018, p. 7091) | 12 055 331 | DN 25 | 25 | 1,582.53 | 63.30 |
| CitrinSolar GmbH (2018, p. 54) | 191844 | DN 16 | 15 | 352.00 | 23.47 |
| CitrinSolar GmbH (2018, p. 54) | 191848 | DN 16 | 20 | 587.00 | 29.35 |
| CitrinSolar GmbH (2018, p. 54) | 191849 | DN 16 | 25 | 1,173.00 | 46.92 |
| CitrinSolar GmbH (2018, p. 54) | 191850 | DN 20 | 15 | 421.00 | 28.07 |
| CitrinSolar GmbH (2018, p. 54) | 191854 | DN 20 | 20 | 699.00 | 34.95 |
| CitrinSolar GmbH (2018, p. 54) | 191857 | DN 20 | 25 | 1,397.00 | 55.88 |
| CitrinSolar GmbH (2018, p. 54) | 191886 | DN 25 | 15 | 566.00 | 37.73 |
| CitrinSolar GmbH (2018, p. 54) | 191888 | DN 25 | 20 | 939.00 | 46.95 |
| CitrinSolar GmbH (2018, p. 54) | 191890 | DN 25 | 25 | 1,877.00 | 75.08 |
| Consolar GmbH (2006, p. 18) | LE005 | DN 12 | 15 | 430.00 | 28.67 |
| Consolar GmbH (2006, p. 18) | LE015 | DN 15 | 15 | 480.00 | 32.00 |
| Consolar GmbH (2006, p. 18) | LE025 | DN 18 | 15 | 560.00 | 37.33 |
| GASOKOL GmbH (2013, p. 36) | 35031 | DN 16 | 10 | | 42.90 |
| GASOKOL GmbH (2013, p. 36) | 35032 | DN 16 | 15 | | 42.90 |
| GASOKOL GmbH (2013, p. 36) | 35036 | DN 20 | 10 | | 51.90 |
| GASOKOL GmbH (2013, p. 36) | 35037 | DN 20 | 15 | | 51.90 |
| ROTEX Heating Systems GmbH (2018, p. 197) | 16 20 73 | DN 16 | 15 | 469.45 | 31.30 |
| ROTEX Heating Systems GmbH (2018, p. 197) | 16 20 74 | DN 20 | 15 | 594.91 | 39.66 |

Table G.5: Specific costs (without VAT) for piping. Empty cells indicate that there is no information available. **(Continued)**

| Source | Product | Diameter in mm | Length in m | List price in € | Specific price in €/m |
|--------------------------------|------------|-------------------|----------------|--------------------|--------------------------|
| Roth Werke GmbH (2014, p. 163) | 1135004131 | DN 16 | 15 | 568.00 | 37.87 |
| Roth Werke GmbH (2014, p. 163) | 1135004132 | DN 20 | 15 | 729.00 | 48.60 |
| Roth Werke GmbH (2014, p. 163) | 1135004551 | DN 16 | 25 | 984.00 | 39.36 |
| Roth Werke GmbH (2014, p. 163) | 1135004552 | DN 20 | 25 | 1,215.00 | 48.60 |
| Sonnenkraft GmbH (2018, p. 41) | EWRID16/10 | DN 16 | 10 | 205.00 | 20.50 |
| Sonnenkraft GmbH (2018, p. 41) | EWRID20/10 | DN 20 | 10 | 260.00 | 26.00 |
| Sonnenkraft GmbH (2018, p. 41) | EWRID16/15 | DN 16 | 15 | 310.00 | 20.67 |
| Sonnenkraft GmbH (2018, p. 41) | EWRID20/15 | DN 20 | 15 | 370.00 | 24.67 |
| Sonnenkraft GmbH (2018, p. 41) | EWRID16/20 | DN 16 | 20 | 410.00 | 20.50 |
| Sonnenkraft GmbH (2018, p. 41) | EWRID20/20 | DN 20 | 20 | 495.00 | 24.75 |
| Sonnenkraft GmbH (2018, p. 41) | EWRID25/20 | DN 25 | 20 | 550.00 | 27.50 |
| Sonnenkraft GmbH (2018, p. 41) | EWRID16/50 | DN 16 | 50 | 1,020.00 | 20.40 |
| Sonnenkraft GmbH (2018, p. 41) | EWRID20/50 | DN 20 | 50 | 1,230.00 | 24.60 |
| Sonnenkraft GmbH (2018, p. 41) | EWRID25/50 | DN 25 | 50 | 1,590.00 | 31.80 |
| ThüSolar GmbH (2012, p. 37) | wws202010 | DN 16 | 10 | | 57.50 |
| ThüSolar GmbH (2012, p. 37) | wws203010 | DN 20 | 10 | | 62.50 |
| TiSUN GmbH (2018, p. 13) | EWRID16/10 | DN 16 | 10 | 205.00 | 20.50 |
| TiSUN GmbH (2018, p. 13) | EWRID20/10 | DN 16 | 15 | 310.00 | 20.67 |
| TiSUN GmbH (2018, p. 13) | EWRID16/15 | DN 16 | 20 | 410.00 | 20.50 |
| TiSUN GmbH (2018, p. 13) | EWRID20/15 | DN 16 | 50 | 1,020.00 | 20.40 |
| TiSUN GmbH (2018, p. 13) | EWRID16/20 | DN 20 | 10 | 260.00 | 26.00 |
| TiSUN GmbH (2018, p. 13) | EWRID20/20 | DN 20 | 15 | 370.00 | 24.67 |
| TiSUN GmbH (2018, p. 13) | EWRID25/20 | DN 20 | 20 | 495.00 | 24.75 |
| TiSUN GmbH (2018, p. 13) | EWRID16/50 | DN 20 | 50 | 1,230.00 | 24.60 |
| TiSUN GmbH (2018, p. 13) | EWRID20/50 | DN 25 | 20 | 550.00 | 27.50 |
| TiSUN GmbH (2018, p. 13) | EWRID25/50 | DN 25 | 50 | 1,590.00 | 31.80 |

Table G.5: Specific costs (without VAT) for piping. Empty cells indicate that there is no information available. **(Continued)**

| Source | Product | Diameter in mm | Length in m | List price in € | Specific price in €/m |
|--|------------|-------------------|----------------|--------------------|--------------------------|
| Viessmann Werke GmbH & Co. KG (2017, p. 5.4-3) | 7419567 | DN 16 | 15 | 557.00 | 37.13 |
| Viessmann Werke GmbH & Co. KG (2017, p. 5.4-3) | 7373478 | DN 16 | 12 | 482.00 | 40.17 |
| Viessmann Werke GmbH & Co. KG (2017, p. 5.4-3) | 7373477 | DN 16 | 6. | 265.00 | 44.17 |
| Wagner Solar GmbH (2017, p. 67) | 150 301 33 | DN 16 | 15 | 354.64 | 23.64 |
| Wagner Solar GmbH (2017, p. 67) | 150 304 10 | DN 16 | 15 | 449.38 | 29.96 |
| Wagner Solar GmbH (2017, p. 67) | 150 301 34 | DN 20 | 15 | 429.08 | 28.61 |
| | | | | | ∅41.35 €/m |

Table G.6: Specific costs (without VAT) of the substructure for solar thermal FPCs.

| Source | Product | Collector area in m ² | List price in € | Specific price in €/m ² |
|--|----------------------------|-------------------------------------|--------------------|---------------------------------------|
| Buderus Thermotechnik GmbH (2018, p. 7016) | 7 736 614 796 | 2.37 | 165.30 | 69.75 |
| Buderus Thermotechnik GmbH (2018, p. 7016) | 7 736 614 799 | 2.37 | 159.21 | 67.18 |
| CitrinSolar GmbH (2018, p. 41) | 114010 | 2.57 | 254.00 | 98.83 |
| CitrinSolar GmbH (2018, p. 41) | 115010 | 2.57 | 281.00 | 109.3 |
| CitrinSolar GmbH (2018, p. 41) | 114020 | 5.14 | 387.00 | 75.29 |
| CitrinSolar GmbH (2018, p. 41) | 114080 | 5.14 | 345.00 | 67.12 |
| CitrinSolar GmbH (2018, p. 41) | 114090 | 2.57 | 174.00 | 67.70 |
| CitrinSolar GmbH (2018, p. 41) | 115090 | 2.57 | 237.00 | 92.22 |
| Consolar GmbH (2006, p. 14) | KF331 | 2.55 | 155.00 | 60.78 |
| Consolar GmbH (2006, p. 14) | KF330 | 5.10 | 227.00 | 44.51 |
| Consolar GmbH (2006, p. 14) | KF325 | 7.65 | 341.00 | 44.58 |
| GASOKOL GmbH (2013, p. 8) | 03081 2R | 2.25 | 163.40 | 72.62 |
| GASOKOL GmbH (2013, p. 8) | 03081 2R | 4.50 | 381.30 | 84.73 |
| GASOKOL GmbH (2013, p. 8) | 03081 2R | 6.75 | 599.30 | 88.79 |
| GASOKOL GmbH (2013, p. 8) | 03081 2R | 9.00 | 762.60 | 84.73 |
| GASOKOL GmbH (2013, p. 8) | 03081 2R | 11.25 | 980.60 | 87.16 |
| GASOKOL GmbH (2013, p. 8) | 03081 2R | 13.50 | 1,198.60 | 88.79 |
| GASOKOL GmbH (2013, p. 8) | 03081 2R | 15.75 | 1,362.00 | 86.48 |
| GASOKOL GmbH (2013, p. 8) | 03081 2R | 18.00 | 1,580.00 | 87.78 |
| GASOKOL GmbH (2013, p. 8) | 03081 2R | 20.25 | 1,798.00 | 88.79 |
| GASOKOL GmbH (2013, p. 8) | 03081 2R | 22.50 | 1,961.30 | 87.17 |
| ROTEX Heating Systems GmbH (2018, p. 195) | 16 20 66 / 16 20 85 | 1.79 | 95.95 | 53.60 |
| Roth Werke GmbH (2014, pp. 129-130) | 1115008698 / 1135004083 | 5.04 | 312.00 | 61.90 |
| Roth Werke GmbH (2014, pp. 129-130) | 1115008699 / 1135004084 | 2.52 | 119.20 | 47.30 |

Table G.6: Specific costs (without VAT) of the substructure for solar thermal FPCs. **(Continued)**

| Source | Product | Collector area in m ² | List price in € | Specific price in €/m ² |
|--------------------------------|----------------------|-------------------------------------|--------------------|---------------------------------------|
| Sonnenkraft GmbH (2018, p. 19) | DBPN/L / SKR0/1 | 2.52 | 139.00 | 55.16 |
| Sonnenkraft GmbH (2018, p. 19) | DBPN/L / SKR0/2 | 5.04 | 200.00 | 39.68 |
| Sonnenkraft GmbH (2018, p. 19) | DBPN/L / SKR0/3 | 7.56 | 343.00 | 45.37 |
| Sonnenkraft GmbH (2018, p. 19) | DBPN/L / SKR0/4 | 10.08 | 406.00 | 40.28 |
| Sonnenkraft GmbH (2018, p. 19) | DBPN/L / SKR0/5 | 12.60 | 517.00 | 41.03 |
| Sonnenkraft GmbH (2018, p. 19) | DBPN/L / SKR0/6 | 15.12 | 612.00 | 40.48 |
| Sonnenkraft GmbH (2018, p. 19) | DBPN/L / SKR0/7 | 17.64 | 723.00 | 40.99 |
| Sonnenkraft GmbH (2018, p. 19) | DBPN/L / SKR0/8 | 20.16 | 818.00 | 40.58 |
| Sonnenkraft GmbH (2018, p. 19) | DBPN/L / SKR0/9 | 22.68 | 929.00 | 40.96 |
| Sonnenkraft GmbH (2018, p. 19) | DBPN/L / SKR0/10 | 25.20 | 1,024.00 | 40.63 |
| ThüSolar GmbH (2012, p. 6) | 1075 | 2.50 | 40.17 | 16.07 |
| TiSUN GmbH (2018, p. 4, p. 10) | 1430720 / 1430914 | 2.55 | 182.00 | 71.37 |
| TiSUN GmbH (2018, p. 4, p. 10) | 1421398 / 1430914 | 5.10 | 313.00 | 61.37 |

Table G.6: Specific costs (without VAT) of the substructure for solar thermal FPCs. **(Continued)**

| Source | Product | Collector area in m ² | List price in € | Specific price in €/m ² |
|---|------------------------------------|-------------------------------------|--------------------|---------------------------------------|
| Viessmann Werke GmbH & Co. KG (2017, p. 5.1-10) | 008464 | 2.51 | 126.00 | 50.20 |
| Viessmann Werke GmbH & Co. KG (2017, p. 5.1-10) | 008465 | 5.02 | 221.00 | 44.02 |
| Viessmann Werke GmbH & Co. KG (2017, p. 5.1-10) | 008466 | 7.53 | 321.00 | 42.63 |
| Viessmann Werke GmbH & Co. KG (2017, p. 5.1-10) | 008467 | 10.04 | 449.00 | 44.72 |
| Viessmann Werke GmbH & Co. KG (2017, p. 5.1-10) | 008468 | 12.55 | 549.00 | 43.75 |
| Viessmann Werke GmbH & Co. KG (2017, p. 5.1-10) | 008469 | 15.06 | 654.00 | 43.43 |
| Viessmann Werke GmbH & Co. KG (2017, p. 5.1-10) | 008470 | 20.08 | 882.00 | 43.92 |
| Viessmann Werke GmbH & Co. KG (2017, p. 5.1-10) | 008471 | 25.10 | 1,102.00 | 43.90 |
| Wagner Solar GmbH (2017, p. 34) | 192 001 42 | 5.22 | 133.08 | 25.49 |
| Wagner Solar GmbH (2017, p. 34) | 192 001 46 | 2.61 | 93.25 | 35.73 |
| Wagner Solar GmbH (2017, p. 34) | 192 001 44 | 2.61 | 59.28 | 22.71 |
| Wikora GmbH (2017, pp. 47, 49) | 01 2221 6 0102 / 01 2121 2 0102 | 1.98 | 90.00 | 45.45 |
| WOLF GmbH (2018, p. 04.04) | 7701592 | 4.60 | 785.00 | 170.65 |
| | | | | ∅60.95 €/m² |

G Component Costs

Table G.7: Costs (without VAT) for solar stations.

| Source | Product | List price in € |
|--|----------------|--------------------|
| Buderus Thermotechnik GmbH (2018, p. 7080) | 7 735 600 041 | 651.63 |
| Buderus Thermotechnik GmbH (2018, p. 7080) | 7 735 600 049 | 992.67 |
| Buderus Thermotechnik GmbH (2018, p. 7080) | 7 735 600 051 | 1,547.73 |
| CitrinSolar GmbH (2018, p. 60) | 195097 | 574.00 |
| CitrinSolar GmbH (2018, p. 60) | 195100 | 627.00 |
| Consolar GmbH (2006, p. 19) | PS022 | 331.00 |
| Consolar GmbH (2006, p. 19) | PS082 | 331.00 |
| GASOKOL GmbH (2013, p. 32) | 07103 | 410.50 |
| GASOKOL GmbH (2013, p. 32) | 07104 | 442.70 |
| GASOKOL GmbH (2013, p. 32) | 07107-130 | 707.50 |
| ROTEX Heating Systems GmbH (2018, p. 197) | 16 20 49 | 479.91 |
| Roth Werke GmbH (2014, p. 161) | 1135002274 | 440.00 |
| Roth Werke GmbH (2014, p. 161) | 1135004442 | 480.00 |
| Roth Werke GmbH (2014, p. 161) | 1135006101 | 982.00 |
| Sonnenkraft GmbH (2018, p. 31) | SSTX25/2E | 430.00 |
| Sonnenkraft GmbH (2018, p. 31) | SST25/2E | 610.00 |
| Sonnenkraft GmbH (2018, p. 31) | SST25VME | 670.00 |
| ThüSolar GmbH (2012, p. 32) | 1431 | 285.00 |
| ThüSolar GmbH (2012, p. 32) | 1432 | 329.00 |
| TiSUN GmbH (2018, p. 21) | SSTX25/2E | 430.00 |
| TiSUN GmbH (2018, p. 21) | SSTX100/E | 790.00 |
| Viessmann Werke GmbH & Co. KG (2017, p. 5.4-1) | Z012020 | 763.00 |
| Viessmann Werke GmbH & Co. KG (2017, p. 5.4-1) | Z012027 | 858.00 |
| Wikora GmbH (2017, p. 54) | 01 5200 7 0101 | 630.00 |
| Wikora GmbH (2017, p. 54) | 01 5200 8 0101 | 650.00 |
| WOLF GmbH (2018, p. 04.21) | 2484991 | 610.00 |
| WOLF GmbH (2018, p. 04.21) | 2484992 | 630.00 |
| | | ∅617.88 € |

Table G.8: Costs (without VAT) for solar controllers.

| Source | Product | List price in € |
|--|----------------|--------------------|
| Buderus Thermotechnik GmbH (2018, p. 7084) | 7 747 004 406 | 303.63 |
| Buderus Thermotechnik GmbH (2018, p. 7084) | 7 735 600 069 | 370.62 |
| Buderus Thermotechnik GmbH (2018, p. 7084) | 7 739 602 105 | 716.88 |
| CitrinSolar GmbH (2018, p. 58) | 192132 | 369.00 |
| CitrinSolar GmbH (2018, p. 58) | 192017 | 262.00 |
| CitrinSolar GmbH (2018, p. 58) | 192008 | 178.00 |
| Consolar GmbH (2006, p. 21) | RE003 | 300.00 |
| Consolar GmbH (2006, p. 21) | RE035 | 460.00 |
| Consolar GmbH (2006, p. 21) | RE037 | 620.00 |
| GASOKOL GmbH (2013, p. 27) | 06016 | 147.00 |
| GASOKOL GmbH (2013, p. 27) | 06017 | 147.00 |
| GASOKOL GmbH (2013, p. 27) | 06062 | 259.40 |
| GASOKOL GmbH (2013, p. 27) | 06064 | 359.00 |
| GASOKOL GmbH (2013, p. 27) | 06093 | 406.80 |
| GASOKOL GmbH (2013, p. 27) | 06091 | 369.60 |
| GASOKOL GmbH (2013, p. 27) | 06063 | 278.30 |
| GASOKOL GmbH (2013, p. 28) | 06000 | 564.00 |
| ROTEX Heating Systems GmbH (2018, p. 197) | 16 20 84 | 173.53 |
| Roth Werke GmbH (2014, p. 159) | 1135003975 | 249.00 |
| Roth Werke GmbH (2014, p. 159) | 1135003976 | 395.00 |
| Roth Werke GmbH (2014, p. 159) | 1135006102 | 275.00 |
| Roth Werke GmbH (2014, p. 160) | 1135006103 | 435.00 |
| Roth Werke GmbH (2014, p. 160) | 1135007151 | 500.00 |
| Sonnenkraft GmbH (2018, p. 39) | STRGO | 159.00 |
| Sonnenkraft GmbH (2018, p. 39) | STRGBXPLUS | 419.00 |
| ThüSolar GmbH (2012, p. 22) | 11541020 | 248.00 |
| ThüSolar GmbH (2012, p. 23) | 11542040 | 320.00 |
| ThüSolar GmbH (2012, p. 24) | 11542210 | 354.00 |
| ThüSolar GmbH (2012, p. 25) | 11566130 | 470.00 |
| ThüSolar GmbH (2012, p. 26) | 11599020 | 557.00 |
| TiSUN GmbH (2018, p. 20) | STRGO | 159.00 |
| TiSUN GmbH (2018, p. 20) | STRGBXPLUS | 419.00 |
| Viessmann Werke GmbH & Co. KG (2017, p. 5.5-1) | Z007387 | 331.00 |
| Viessmann Werke GmbH & Co. KG (2017, p. 5.5-2) | Z007388 | 584.00 |
| Wagner Solar GmbH (2017, p. 70) | 150 115 11 | 233.60 |
| Wagner Solar GmbH (2017, p. 70) | 150 115 12 | 433.41 |
| Wagner Solar GmbH (2017, p. 71) | 150 115 13 | 776.48 |
| Wikora GmbH (2017, p. 54) | 01 7820 0 0101 | 180.00 |
| Wikora GmbH (2017, p. 54) | 01 7840 0 0101 | 310.00 |
| WOLF GmbH (2018, p. 04.19) | 2745936 | 300.00 |
| WOLF GmbH (2018, p. 04.19) | 2745869 | 423.00 |
| | | ∅361.35 € |

Table G.9: Specific costs (without VAT) for HTF. The necessary amount of water-glycol-mixture per square metre collector area is determined by considering an average volume of 0.731/m² (cf. table G.1).

| Source | Product | Volume in l | List price in € | Specific price in €/m ² |
|--|----------------|----------------|--------------------|---------------------------------------|
| Buderus Thermotechnik GmbH (2018, p. 7089) | 8 718 660 947 | 20 | 160.08 | 5.84 |
| CitrinSolar GmbH (2018, p. 62) | 194015 | 10 | 61.00 | 4.45 |
| CitrinSolar GmbH (2018, p. 62) | 194030 | 20 | 105.00 | 3.83 |
| CitrinSolar GmbH (2018, p. 62) | 194050 | 200 | 705.00 | 2.57 |
| GASOKOL GmbH (2013, p. 35) | 07822 | 10 | | 5.04 |
| GASOKOL GmbH (2013, p. 35) | 07824 | 25 | | 5.04 |
| GASOKOL GmbH (2013, p. 35) | 07826 | 200 | | 5.07 |
| ROTEX Heating Systems GmbH (2018, p. 198) | 16 20 52-RTX | 20 | 78.41 | 2.86 |
| Roth Werke GmbH (2014, p. 162) | 1135002277 | 25 | 77.25 | 2.26 |
| Sonnenkraft GmbH (2018, p. 42) | FSM25 | 25 | 85.00 | 2.48 |
| ThüSolar GmbH (2012, p. 33) | 1440 | 10 | 46.50 | 3.39 |
| TiSUN GmbH (2018, p. 25) | FSM25 | 25 | 85.00 | 2.48 |
| Viessmann Werke GmbH & Co. KG (2017, p. 5.4-5) | 7159727 | 25 | 120.00 | 3.50 |
| Viessmann Werke GmbH & Co. KG (2017, p. 5.4-5) | 7159729 | 200 | 966.00 | 3.53 |
| Wagner Solar GmbH (2017, p. 64) | 150 304 23 | 5 | 34.65 | 5.06 |
| Wagner Solar GmbH (2017, p. 64) | 150 304 24 | 10 | 63.17 | 4.61 |
| Wagner Solar GmbH (2017, p. 64) | 150 304 25 | 25 | 157.60 | 4.60 |
| Wikora GmbH (2017, p. 55) | 01 5420 0 0101 | 20 | 114.00 | 4.16 |
| WOLF GmbH (2018, p. 05.31) | 2484552 | 3 | 24.80 | 6.03 |
| WOLF GmbH (2018, p. 05.31) | 2483422 | 20 | 166.00 | 6.06 |
| | | | | ∅4.14 €/m² |